PREDICTION OF IMPACT SOUND TRANSMISSION WITH HEAVY IMPACT SOURCES IN HEAVYWEIGHT BUILDINGS

By

Susumu HIRAKAWA

Submitted to

School of Architecture, University of Liverpool

Thesis submitted in accordance with the requirements of the University of Liverpool for the degree of Doctor in Philosophy by

Susumu HIRAKAWA

<NOVEMBER 2018>

ABSTRACT

In heavyweight buildings, impact sound insulation from heavy impacts such as footsteps in bare feet, or children running and jumping can be a significant problem. Hence it is useful to be able to predict the Fast time-weighted maximum sound pressure level ($L_{p,Fmax}$) in a room due a transient impact on the floor above. This thesis extends an existing prediction model using Transient Statistical Energy Analysis (TSEA) to include the effect of a floating floor on top of the concrete base floor, and through comparison with measurements. Time-domain Finite Element Methods (FEM) have been used to incorporate the rubber ball (a heavy impact source) within the model and to investigate the accuracy of TSEA and measurement procedures in the low-frequency range.

Experimental and lump parameter models have been used to investigate the structural dynamics of the rubber ball, and the blocked force on impact. Experimental determination of modal parameters identified the fundamental frequency in order to estimate the Young's modulus of the rubber for FEM models. A single degree-of-freedom (dof) model for the ball gave reasonable estimates of the blocked force but for modelling purposes more accurate data was needed from force plate measurements. An idealised floating floor was investigated using small mass-spring systems that would fit on top of a force plate for which experiments and two dof models indicated a single peak or a double peak in the time domain blocked force depending on whether the resilient material was soft or stiff respectively.

To incorporate the effect of a floating floor on a heavyweight base floor in a TSEA model, an inverse approach to TSEA (ITSEA) has been developed. Using laboratory measurements this gives the normalised transient power input into the base floor for a heavy impact source impacting the floating floor. Experimental assessment of ITSEA was carried out in test laboratories using small mass-spring systems and a full-size floating floor which validated the approach to experimentally quantify transient power with ITSEA and incorporate this in TSEA to predict $L_{p,Fmax}$ in a receiving room.

FEM models were validated against measurements from which comparisons of TSEA and FEM at low-frequencies show sufficiently close agreement (i.e. <2.5dB) to recommend that TSEA be used in design work due to its fast computation time. FEM was also used to investigate and suggest improvements to measurement procedures by using corner measurement positions of $L_{p,Fmax}$.

ACKNOWLEDGEMENT

The author would like to express his appreciation to Professor Carl Hopkins who offered continuing support and constant encouragement through my research in the Acoustic Research Unit.

The author would like to thank Dr Pyoung-Jik Lee, Dr Gary Seiffert and Professor Emeritus Barry Gibbs and colleagues of Acoustics Research Unit who made my research enjoyable and gave me their valuable experience.

The author would also like to express many thanks to Dr Junichi Yoshimura (Kobayasi Institute of Physical Research), Dr Atsuo Hiramitsu (National Institute for Land and Infrastructure Management), Dr Hiroshi Sato (National Institute of Advanced Industrial Technology) and Dr Takashi Koga (Kajima Technical Research Institute) for continuous support through my research from Japan. I also appreciated their encouragement for my work.

My sincere gratitude goes to my family, for their support.

I gratefully acknowledge the funding for this research which has been carried out at the Acoustics Research Unit at the University of Liverpool with financial support by grants (16REP-B082204-05) and (18REP-B082204-05) from Residential Environment Research Program funded by Ministry of Land, Infrastructure and Transport of Korean Government.

For assistance with the measurements, the author is grateful to Dr Byung Kwon Lee for providing access to the LH laboratory in Korea and collecting the raw time domain data for the ondol floating floor, to Gary Timmins for providing access to the BRE laboratory in the UK, and to Kobayasi Institute of Physical Research and RION Co., Ltd for discussions regarding the standard impact sources.

The author is grateful for the MATLAB code made available by Dr Matthew Robinson for the TSEA model that was adapted for this thesis.

.

TABLE OF CONTENTS

Page

LIST OF TABLES

Page

LIST OF FIGURES

Page

LIST OF SYMBOLS

b	Integer constant for optimum value for prediction of $L_{\mathrm{p,Fmax}}$ (-)
c	Damping coefficient (Ns/m)
c_0	Speed of sound (m/s)
$c_{\mathrm{g(B)}}$	Group velocity of bending waves (m/s)
c_{B}	Bending wave speed (m/s)
c_{d}	Dilatational wave speed (m/s)
c_{L}	Quasi-longitudinal wave speed (m/s)
d_{mfp}	Mean free path (m)
e	Restitution coefficient (-)
f	Frequency (Hz)
f_{c}	Critical frequency
f_{cut}	Cut-off frequency (Hz)
f_{r}	Resonance frequency (Hz)
f_{limit}	Limit of lower branch mode frequency (Hz)
h	Thickness (m)
i	Imaginary number, $\sqrt{(-1)}$
m	Mass (kg)
p	Instantaneous sound pressure (Pa)
p_0	Reference sound pressure level (Pa)
p_{rms}	Root-Mean-Square (RMS) sound pressure (Pa)
t	Time array (-) or instantaneous time (s)
t_{n}	Time step (s)
t_{peak}	Time at first peak of mean-square velocity (s)
$< v^2 >_{\mathrm{t,s}}$	Spatial and time average mean-square velocity (m/s)
v_0	Instantaneous velocity (m/s)
y	Displacement (m)
$\dot{y}$	Velocity (m/s)
$\ddot{y}$	Acceleration (m/s^2)
A_{T}	Total absorption area (m^2)

$[C]$	Damping matrix (Ns/m)
E	Young's modulus (N/m^2), Energy (J)
F	Force (N)
F_{rms}	Root-mean-square force (N)
[K]	Stiffness matrix (N/m)
L	Smallest element size of the global model (m)
$L_{\mathrm{p,Fmax}}$	Fast time-weighted maximum sound pressure level (dB)
$L_{\mathrm{v,Fmax}}$	Fast time-weighted maximum velocity level (dB)
L_x, L_y, L_z	x-, y-, z- dimensions (m)
[M]	Mass matrix (-)
N	Integer number of time steps (-), Modal density (Hz^{-1})
R	Externally applied loads (N), Reflection coefficient (-)
S	Surface area (m^2)
S_{T}	Total surface area (m^2)
T_{x}	Reverberation time with evaluation range of x dB (s)
U	Perimeter (m)
[U]	Displacement matrix (m)
[$\dot{\mathrm{U}}$]	Velocity matrix (m/s)
[$\ddot{\mathrm{U}}$]	Acceleration matrix (m/s^2)
V	Volume (m^3)
W_{ij}	Power transfer from subsystem i to j (W)
W_{in}	Transient power input (W)
W'_{in}	Normalised transient power input (W)
Y_{dp}	Driving-point mobility (m/Ns)
Z	Driving-point impedance (Ns/m)
$Z_{\mathrm{a,s}}$	Specific acoustic impedance (-)
α	Rayleigh damping (-)
β	Rayleigh damping (-)
$\beta_{\mathrm{a,s}}$	Specific acoustic admittance (-)
η_i	Total loss factor (-)

η_{ii}	Internal loss factor (-)
η_{ij}	Coupling loss factor (-)
λ	Wavelength of sound of air (m)
λ_B	Wavelength of bending wave (m)
ν	Poisson's ratio (-)
ρ	Density (kg/m^3)
ρ_0	Density of air (kg/m^3)
ρ_s	Mass per unit area (kg/m^2)
σ	Radiation efficiency (-)
τ	Exponential time constant (s)
ω	Angular frequency (radians/s)
ω_d	Damped natural angular frequency (radians/s)
$\psi_{p,q,(r)}$	Local mode shape/eigenfunction (-)
Δt	Step time (s), Size of time increment (s)
ΔT	Duration of the rubber ball force input (s)
ξ	Dummy variable of time integration, constant damping ratio (-)

1. INTRODUCTION

In this chapter, section 1.1 gives the background for heavy impact sound insulation in the heavyweight buildings. Section 1.2 reviews the standard impact forces, measurement procedures and existing prediction models. Section 1.3 discusses the outline of the thesis.

1.1 Background

Surveys show that impact sound insulation in the dwellings is an essential factor for a comfortable living environment [1–6]. In Europe, the main aim of building regulations is to minimise annoyance or disturbance due to footsteps or other impacts on floors such as the scraping of chairs. This is similar to regulations in Japan and Korea [7–9], where there have also been incidents leading to murder or assault [10,11] due to impact sound.

Impact sound insulation measurements are described in International [12,13], Japanese [14] and Korean [15] standards for laboratory or field situations. In Europe and the USA, the tapping machine described in International standards is commonly used to excite the floor. In Japan and Korea, there are two heavy impact sources that are also used. These are the rubber ball and tyre source. In recent years the rubber ball source has been included in the International standards.

The tapping machine attempts to simulate impact sources like human footsteps when a person is wearing shoes [12]. In contrast, the tyre source and rubber ball simulate "heavy" impact sources with strong low-frequency components, such as human footsteps (bare feet) or children jumping [14]. The tapping machine can be considered as a steady-state source whereas the tyre source and rubber ball are used to provide a single impact. This has implications for the measurement parameters that are used. The tapping machine is measured using a continuous equivalent sound pressure level. However, the tyre source and rubber ball are measured using Fast time-weighted maximum sound pressure level ($L_{p,Fmax}$). For Fast time-weighted maximum sound pressure level, there are only a few prediction models available.

At the design stage of a heavyweight building, there is a need for validated prediction models to assess impact sound insulation performance from heavy impacts in terms of Fast time-weighted maximum sound pressure levels. This thesis investigates the prediction models, and measurement procedures for the impact sound insulation of floors with heavy impact sources. In particular, it extends previous prediction models to allow the inclusion of floating floors, and assesses and develops an improvement for the measurement method. In Japan and Korea, the majority of the buildings are of heavyweight construction with solid concrete base floors; hence only this type of construction is considered in this thesis.

1.2 Literature review

1.2.1 Standard impact sources

1.2.1.1 Tapping machine

Figure 1-1. ISO tapping machine (image reproduced with permission from RION Co., Ltd).

The tapping machine was designed to simulate light and hard impacts on the floor such as the walking sound from shoes with hard rubber or plastic heel.

The measurement and rating system for impacts on floors originated in experimental work between 1927 and 1928 at the US National Bureau of Standards. A machine was developed with five ≈2lb hammers dropped at 0.2s intervals to excite the floor [16]. In 1938, Germany standardised a measurement procedure in DIN 4110 using a wooden tapping machine where the impact sound pressure level was measured in Phon as a broadband level applying a frequency weighting filter B [17]. Two years later, Lindahl and Sabine published a new method of measuring the impact sound generated by a

mechanical tapper. This measured the sound pressure level reduction in decibels at each octave frequency from 128 to 4096Hz, with the overall rating for each construction taken as the average of these decibel reductions [18]. In 1947, Ingerslev *et al.* [19] published the practice of measuring the impact sound in one-third octave bands from 100 to 2000Hz using a tapping machine, with five hammers each weighing 500g that deliver two impacts per second. These hammers were operated by a motor-driving camshaft that enabled free drop of the hammer from 0.04m. Ingerslev *et al.* indicated that the tapping machine they used was similar to the one that Lindahl and Sabine tested.

In the 1960s, International Standard recommendations were published to establish minimum requirements, the ranking of impact sound insulation, and the comparison of the impact sound insulation of different floors. These recommendations were in ISO/R 140:1960 for the measurement of floor impact sound insulation, and ISO/R 717:1968 for the rating of floor impact sound insulation and used the tapping machine as an impact source.

Despite the poor correlation between the real-life impacts and tapping machine impact on the same floor in subjective analysis [20–23], ISO/R 140:1960 became a standard in the ISO140:1978 series, and ISO/R 717 formed the ISO 717:1982 series. ISO 140:1997 was updated to ISO10140-3:2010 for laboratory measurements and ISO16283-2:2000 for field measurements.

The ISO tapping machine described in International standards [12,13] has a line of five equally spaced hammers that impact on the floor ten times every second with 100ms interval between the impacts. The requirement for each tapping machine hammer is that the momentum of each hammer impact should represent a free-falling mass of 0.5kg with a drop-height of 0.04m. In practice, the mass will not be free-falling, and there will be some friction losses in the guidance device used to minimise lateral movement of the hammer. The relevant ISO Standard gives tolerances on the masses of the hammer, and the velocity at impact, hence, where necessary, slightly greater drop-heights than 0.04m can be used to compensate for friction losses [24].

1.2.1.2 Tyre source

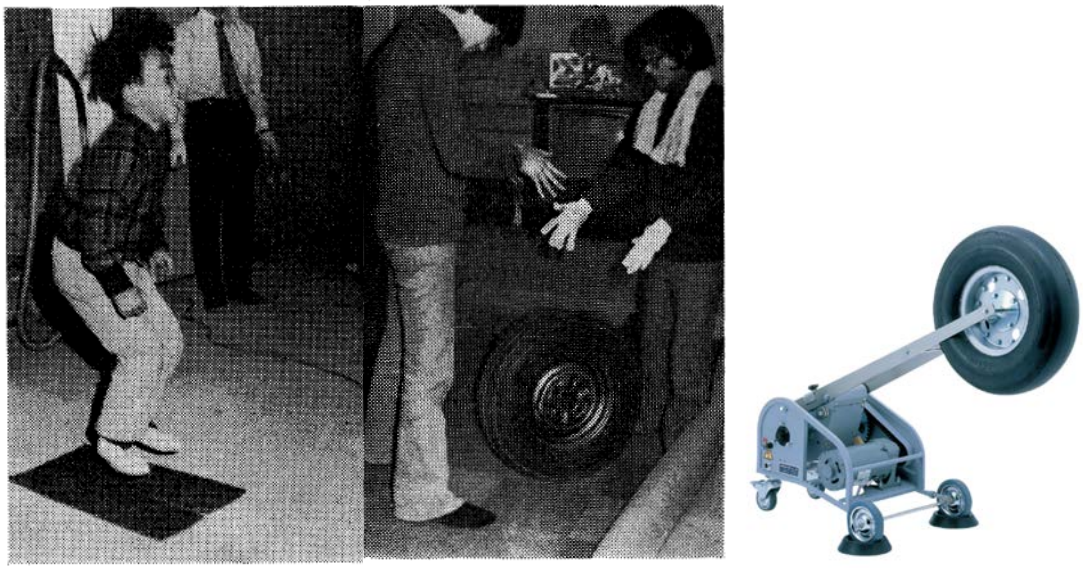

Figure 1-2. Child jumping on the floor (left), tyre dropped by two men (centre) (images reproduced with permission from Acoustical Materials Association of Japan, Onkyo Gijutsu No.20). Tyre source (right) (image reproduced with permission from RION Co., Ltd).

In Japan, people do not usually wear shoes at home, and there is a particular problem with barefoot walking sound as well as and children running and jumping on the floor in multi-story dwellings [25–27]. Hence, the tapping machine, which was primarily designed to assess walking in shoes, was not deemed adequate to assess floor impact sound insulation in Japan.

The work to investigate floor impact sound insulation problems in Japan began in the early 1970s. Kimura and Yasuoka [28,29] suggested that dropping a car tyre from a height of 85cm could simulate a child jumping off from the chair (Figure 1-2, left). This tyre source was initially dropped by two men (Figure 1-2, centre), but later the drop was automated by using a mechanical arm (Figure 1-2, right).

In 1974, JIS A 1418:1974 was formed as an impact sound insulation measurement standard in Japan. It only referred to the tapping machine as an excitation source since there was an urgent need for standardised floor impact sound insulation measurements [30].

In 1978, the tyre source (also known as the ‘bang machine’) was added as a heavy impact source to JIS A 1418:1978. This excitation source is designed to simulate a

child jumping [31]. The impact force was ≈4000N with a 20ms half-sine shape when the tyre was dropped from 85cm [32].

Currently, the tyre source is still used in Japan. However, there are numerous on-going discussions about the choice of excitation source [e.g. 33,34]. One aspect concerns the excessive impact force that sometimes damages wooden structures, and sometimes leads to a non-linear response. However, it is difficult for Japan to change because of historical research data that is not closely related to the rubber ball introduced in JIS A 1418-2:2000. Also, there is a simple prediction model based on regression analysis and statistics from measurements of the tyre source in Japanese buildings [35].

1.2.1.3 Rubber ball

Figure 1-3. Rubber ball source (image reproduced with permission from RION Co., Ltd).

The high force applied by the tyre source can cause damage on the wooden structure, light-weight reinforced concrete buildings and, sometimes causes rattling noise due to the high force input. Also, the 'tyre' is described in an associated standard, JIS D 4204; hence, the definition of the excitation source depends on this tyre standard. For these reasons, a new excitation source for the measurement of the heavy impact sound insulation was developed. The rubber ball was designed as a new excitation source that simulates the impact force of human walking in bare feet as well as children jumping [36].

The first paper on the development of the new measurement method for the heavy impact sound insulation of building floors was published by the floor impact sound insulation working group in Architectural Institute of Japan in 1997 [37]. This paper examined seven different impact sources from a usability aspect. It suggested a ball with the contact duration of 10ms and a peak contact force of 2600N. However, their research indicated that there were differences in the Fast time-weighted maximum sound pressure level with 10ms and 20ms contact duration. In addition, there was a compatibility issue with existing tyre source data; hence to emulate real impact sounds (i.e. children jumping), a ball with 20ms contact duration was proposed. A subsequent study was published in 1998 by the same group [38] which investigated a ball with a contact duration of 20ms and a maximum force input of 1400N. This paper concluded that the rubber ball with a contact duration of 20ms and maximum force input of 1400N was necessary based on the subjective evaluation due to the correlation between real impact sounds (e.g. children jumping) and the tyre source. The English version was published by Tachibana *et al.* [36] in 1998.

The rubber ball is a hollow spherical shell that is made from a temperature invariant silicone rubber (-40 to +50˚C) [39]. The maximum difference in the single event level was 0.5dB with the range between -30 to 30˚C with 10˚C increment. The rubber ball is fabricated from two hemispheres that are connected using glue [39]. On one side of the hemisphere, there is an embedded serial number plate and a 1mm diameter hole for keeping the internal pressure consistent over wide temperature range [39].

In 2000, the rubber ball source was added as an excitation source to JIS A 1418-2:2000 [14,40]. An additional study on the rubber ball was published by Inoue *et al*. in 2001 [41] and 2003 [39]. These papers summarised the measurement of restitution coefficient by video recording, the dynamic stiffness of the rubber ball with a compression test, and repeatability due to the influence of ball rotation, height, and temperature variance.

In 2010 and 2015, the rubber ball source was added to the ISO 10140:2010 and ISO 16283:2015 series as a standard heavy impact source for field and laboratory measurements respectively.

1.2.1.4 Measurement procedures for impact sound insulation using standard heavy impact source

For field measurements, the default measurement procedure in the International standard ISO 16283-2:2015 requires a minimum of four random excitation positions, and a minimum of four microphone positions that are uniformly distributed within the maximum permitted space throughout the room. There should be at least 0.7m between (a) microphone positions, (b) at least 0.5m between any microphone position and room boundaries, and (c) 1m between any microphone position and the floor being excited by the impact source. The low-frequency procedure for the 50, 63 and 80Hz one-third octave bands also measures the sound pressure level in corner positions and uses a weighted energy average to give an estimate of the room-average sound pressure level.

In Japan and Korea, field measurements are conducted according to JIS A 1418-2:2000 or KS 2810-2 respectively although there are additional national guidelines for excitation and measurement positions. In Japan, the sub-committee of the floor impact sound research group of I-INCE-JAPAN (I-INCE-J) have produced recommendations for excitation and measurement positions [42]. In South Korea, the Ministry of Construction Transportation (MOCT-K) issued a notice for the excitation and measurement positions [43]. Both I-INCE-J and MOCT-K procedures use corner measurements to give better estimates of the room-average level.

Figure 1-4 summarises the excitation and measurement positions used in I-INCE-J and MOCT-K. The I-INCE-J and MOCT-K procedures implement the requirements of JIS A 1418-2:2000 and KS F 2810-2 with at least 0.7m between microphone positions, and 0.5m from any room boundaries.

I-INCE-J requires five excitation positions: one central and four corner positions located one-quarter of the way along both room diagonals from the corner; these are referred to as JP ExP1 to ExP5 – see Figure 1-4 (upper). The five microphone positions are directly underneath the excitation positions, JP P1 to P5, where the central position (P1) is at 0.6m height and the four corner positions (P2 to P5) increase in height in a spiral pattern around the room by adding 0.3m height to each subsequent position - see Figure 1-4 (lower).

MOCT-K requires five excitation positions: one central and four corner positions that are 0.75m from each wall; these are referred to as KR ExP1 to ExP5 Figure 1-4 (lower). The five microphone positions (P1 to P5) are directly underneath the excitation position at the height of 1.2m from the ground.

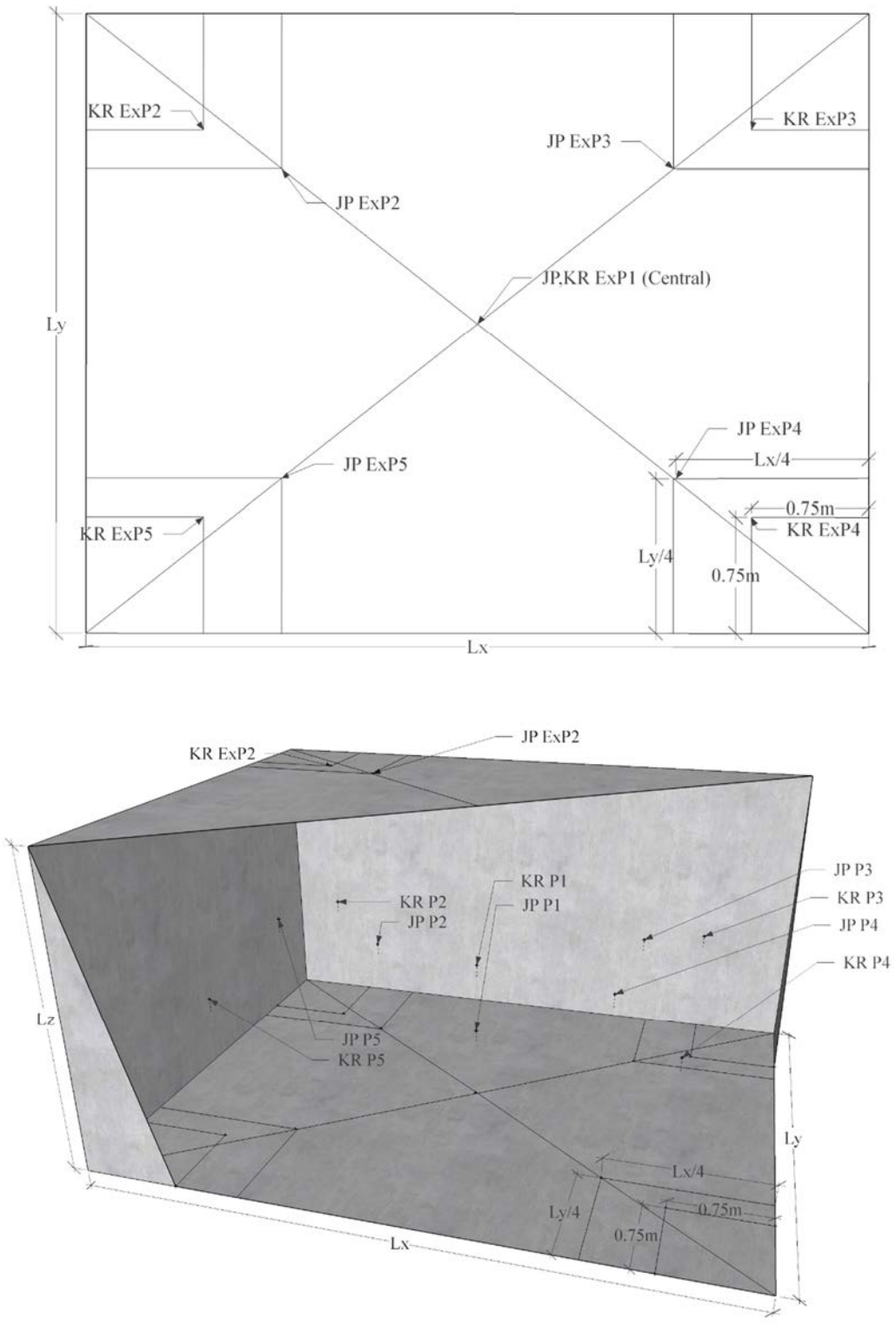

Figure 1-4. I-INCE-J and MOCK-K field measurement positions: (upper) excitation positions on the concrete slab and (lower) measurement positions in the room.

1.2.2 Prediction models for impact sound insulation from standard heavy impact sources

1.2.2.1 Impedance model

Yasuoka [29] considered input impedance and radiation impedance to predict the impact sound insulation of a homogeneous slab from the tapping machine and tyre source. Subsequently, Kimura and Inoue [35] developed an approach to predict the impact sound insulation from a heavyweight floor due to excitation with the tyre source called impedance model. This model assumes a blocked force and requires the floor slab impedance to calculate the sound pressure level. It uses empirical correction terms based on measurements in order to predict maximum levels with Fast time-weighting. Kimura and Inoue [35] indicate that the agreement between theory and measurement is ≈8 dB when using the evaluation curve (assumed to be in JIS A 1419:1978). Those prediction models assume a diffuse vibration field on the concrete slab and diffuse field conditions in the receiver room.

Koga *et al* [44] subsequently proposed that the terms relating to the effective radiating area of the floor and the absorption area in the room were not needed, although later work has shown that the effect of the reverberation time in the receiving room affects the Fast time-weighted maximum sound pressure level that is measured with heavy impact sources [45].

Koga [46] further developed the model to include decay constants of the floor vibration, sound field and the Fast time-weighting. Koga also incorporated impedance values that were predicted from finite element models to model different floor shapes and boundary conditions.

In 2009, Architectural Institute of Japan (AIJ) published a guide book [47] that described a new impedance model based on Kimura and Inoue's impedance model [35] with five new empirical correction terms.

$$L_{\mathrm{p}} = 10\log_{10}\left[\frac{F_{\mathrm{rms}}^2}{Z_{\mathrm{b,T}}^2} S_{\mathrm{eff}} \frac{4}{A}\right] + \Delta L_{\mathrm{d}} + \Delta L_{\mathrm{k}} + \Delta L_{\mathrm{C}} - \Delta L_{\mathrm{fin}} + 120 \qquad (1.1)$$

where F_{rms} is the input force from the rubber ball impact, $Z_{\mathrm{b,T}}$ is the impedance of the floor ($Z_{\mathrm{b,T}} = \Delta L_{\mathrm{b}} + \Delta L_{\mathrm{z}} + \Delta L_{\mathrm{R}}$, where ΔL_{b} is the impedance level of the floor slab,

ΔL_{z} is the boundary condition correction in relation determined by regression of accumulated data and ΔL_{R} floor is the floor resonance frequency correction), S_{eff} is effective area of the plate, A is the equivalent absorption area of the room, ΔL_{d} is the slab damping correction, ΔL_{k} is the sound radiation efficiency correction, ΔL_{C} is the time weighting correction, and ΔL_{fin} is the floor finishing correction. The correction factors ΔL_{z}, ΔL_{R}, and ΔL_{fin} are dependent on the accumulated measurement data and craftsmanship of Japanese buildings and the values given in the book have no theoretical validations. Hence, the use of the impedance model is currently limited to the Japanese floor plans which have been compared with measured data. Due to the weak theoretical background for this impedance method, the thesis did not consider its use.

The agreement between the measurement values in the architectural guidebook and the new impedance model agreed within 1dB for 63 to 500Hz for a typical concrete floor slab. However, the impedance model does not account for flanking transmission and is limited to direct transmission.

Okano and Koyanagi [48] noted that when using the impedance model for the tyre source on a concrete floor, there were often errors of 5 to 10dB in the 63Hz octave band. The accuracy of the prediction was improved by accounting for the rapid change in the force spectrum between the lower and upper band edge frequencies of the 63Hz band, and by using transfer impedances for the floor that were determined using finite element methods.

Masuda and Tanaka [49] further developed the impedance model by using a mode shape function for the low frequency range (25 to 315Hz in one-third octave band) including A-weighting to the $L_{\mathrm{p,Fmax}}$. The approach considers low-order vibration modes of the floor slabs and the sound pressure field due to zero or low order eigenmodes of the room which is important for dwellings where the room response is highly modal at low frequencies. The comparison between measured and predicted value showed close agreement in terms of the A-weighted maximum heavy impact sound pressure level, L_{iA}.

1.2.2.2 Transient Statistical Energy Analysis

Transient Statistical Energy Analysis (TSEA) is an application of the Statistical Energy Analysis (SEA) concept to transient excitation. SEA is a method for predicting

the sound and vibration transmission by using a statistical approach which does not require detailed geometrical information [50,51]. This is useful when the resonance frequency spacing within a frequency band becomes smaller and the average response is determined by many modes for which it is not possible to accurately predict the response due to any one mode because of uncertainties in the geometry and material properties. TSEA uses similar notation to SEA and considers the energy balance for each frequency band over a short time interval.

Manning and Lee [52] initiated the application of SEA to transient and time-dependent problems. This work assumed steady-state SEA coupling loss factors and determined the energy balance in the time domain with transient structure-borne excitation. Reasonable agreement between measured and predicted vibration response was obtained for a beam-plate system. This work essentially defined TSEA.

Lyon [53] investigated transient vibration in the frequency domain with mechanical shock excitation. It was reported that the maximum level occurs when most of the individual modes respond at the same time.

Powell and Quartararo [54] investigated a two subsystem SEA model in the time domain to predict structural decay curves from interrupted steady-state excitation. The work compared measured and predicted multiple-slope decay curves in structures. The study indicated that it is possible to predict the multiple-slope decay using a total loss factor that does not vary with time. It also showed that energy returning to a given subsystem is responsible for multiple decay slopes in the energy response of that subsystem.

Lai and Soom [55] investigated time-varying energy flow between two lightly damped oscillators and concluded that it required time-varying coupling loss factors to describe the modal interactions immediately following transient excitation when using a transient form of SEA. However, later work showed that the use of steady-state coupling loss factors is reasonable as discussed by Robinson and Hopkins [56,57].

In the second edition of the SEA book by Lyon and Dejong [50], a short chapter was added on TSEA. TSEA was used to assess an impulse response with three subsystems model, and the decay rate in $3.5m^3$ acoustic space. These examples showed close agreement between measured and predicted time-varying levels.

Pinnington and Lednik [58] studied the transient response of a two-degree-of-freedom system and compared the exact solution to the transient statistical energy response. They concluded that TSEA could correctly predict the peak value of energy and the decay, but not the correct rise time of the time-varying response.

Pinnington and Lednik [59] investigated the use of TSEA for predicting peak levels on a structure with low-mode count and low modal overlap factor for certain frequency bands at two coupled beams. Based on this work, Robinson and Hopkins [56] indicated the potential use of TSEA for the heavyweight buildings, which often have low mode count and low modal overlap factors in the low-frequency range.

Robinson and Hopkins [56] investigated the specification of appropriate time intervals for TSEA and the use of steady-state SEA coupling loss factors. The study showed that to ensure the steady-state coupling loss factors are valid for use in TSEA, the lower limit time interval needed to be chosen in order to allow a reverberant field in the source subsystem. Also, the concept of transient power input was defined, and practical examples given to allow its implementation.

Subsequently, experimental validation of TSEA was carried out [57] with two experiments. The close agreement between the measurement and TSEA predicted maximum level confirmed the validity of the time interval, steady-state radiation efficiencies and transient power input. Those two studies confirmed that TSEA can be used to predict maximum Fast time-weighted sound and vibration levels in buildings from the combination of direct and flanking paths with similar accuracy to steady-state SEA.

A subsequent study by Robinson and Hopkins [60] also showed that TSEA could be used to predict $L_{p,Fmax}$ due to excitation of a concrete base floor that is directly excited by the rubber ball or human footsteps. This thesis extends this work to realistic floors which always need a floating floor to provide impact sound insulation.

1.3 Thesis outline

Five main aspects are considered in this thesis

1. Structural dynamics of the rubber ball used as a heavy impact source.

2. A new methodology to allow floating floors on heavyweight base floors to be incorporated in TSEA models of heavyweight buildings; this uses an experimental approach in a laboratory facility with an inverse form of TSEA, which is referred to as ITSEA.

3. Validation of TSEA models to predict Fast time-weighted maximum levels from heavy impacts on a base floor with a floating floor.

4. Validation of FEM models to assess the accuracy of TSEA in small room volumes.

5. Comparison and assessment of field measurement procedures from Japan, South Korea and International standards that are used to determine impact sound insulation with heavy impact sources.

Chapter 2 introduces the theory that has been used in the thesis. It starts by introducing the SEA framework and parameters used in the SEA. In this chapter, the concept of TSEA and Finite Element Method (FEM) is also introduced with the signal processing used to process the transient sound pressure and vibration signals from measurements and prediction models. An inverse form of TSEA, called ITSEA is introduced to determine the structure-borne sound power input from a heavy impact source into a heavyweight base floor with a floating floor.

Chapter 3 investigates the structural dynamics of an isolated rubber ball. This involves measurements of driving-point mobility, Experimental Modal Analysis (EMA) and the blocked force using a force plate. A prediction model for the applied force by the rubber ball is developed with a single-degree-of-freedom mass-spring-damper system using MATLAB Simulink.

Chapter 4 investigates the structural dynamics of an isolated rubber ball when it impacts upon locally reacting mass-spring systems. Measurement of the blocked force is not possible when there is a floating floor on top of the base floor; hence it requires a new approach to measure or estimate the power input into a base floor when the impact is applied to the floating floor. For this investigation, locally reacting mass-spring systems (representing idealised floating floors) are introduced to measure the blocked force on the force plate. To try and predict the force applied by the rubber ball to the

base floor, two-degree-of-freedom mass-spring-damper systems are developed using MATLAB Simulink.

Chapter 5 validates the normalised transient power input from force plate measurement and ITSEA when incorporated in TSEA through comparison of measurement and the prediction using the two heavy impact excitation sources (i.e. rubber ball and tyre source) using different facilities, locally reacting mass-spring systems and floating floors.

Chapter 6 concerns numerical experiments to predict $L_{p,Fmax}$ from rubber ball impacts using FEM which are compared with measurements and TSEA. FEM is then used to model various room sizes and various room boundary impedances to assess the accurately of TSEA for predicting $L_{p,Fmax}$ in the low-frequency range. This chapter also assesses and compares the modal response of the room due to the rubber ball impact, and different field measurement procedures for the impact sound insulation with heavy impact sources.

Chapter 7 contains the conclusions and addresses the areas of research that could be developed in the future.

2. THEORY FOR PREDICTION OF IMPACT SOUND INSULATION FROM HEAVY IMPACT SOURCES

2.1 Introduction

In this chapter, Sections 2.2, 2.3 and 2.4 introduce the theory for SEA, TSEA and ITSEA. Sections 2.5 introduces FEM in terms of the time-marching solving technique. Section 2.6 gives the signal processing techniques used to process the TSEA and FEM output to give Fast time-weighted maximum sound pressure and velocity levels.

2.2 Statistical Energy Analysis (SEA)

2.2.1 Introduction

SEA is a framework of analysis for predicting sound and vibration transmission by using a statistical approach which does not require detailed geometrical information [50,51]. SEA was introduced in the 1960s for aerospace manufacturing [61,62] and it is now a well-established technique in building acoustics [24,51].

2.2.2 Fundamentals of SEA

In SEA, a system is defined that represents the structure of interest. This system is divided into subsystems which are defined by their ability to store modal energy. Using the SEA energy balance description, the distribution of energy among the subsystems can be calculated in frequency bands using the steady-state power input. These energy levels represent time and spatial average values.

Figure 2-1 shows an example of a two-subsystem SEA model for direct sound transmission from a floor to a room. The power is injected (W_i^{inj}) to the plate that represents a solid base floor (subsystem i). Power is dissipated in this plate as W_i^{dis}, and in the receiving room (subsystem j) as W_j^{dis}. Power is exchanged between these subsystems, as indicated by $W_{i\to j}$, and $W_{j\to i}$.

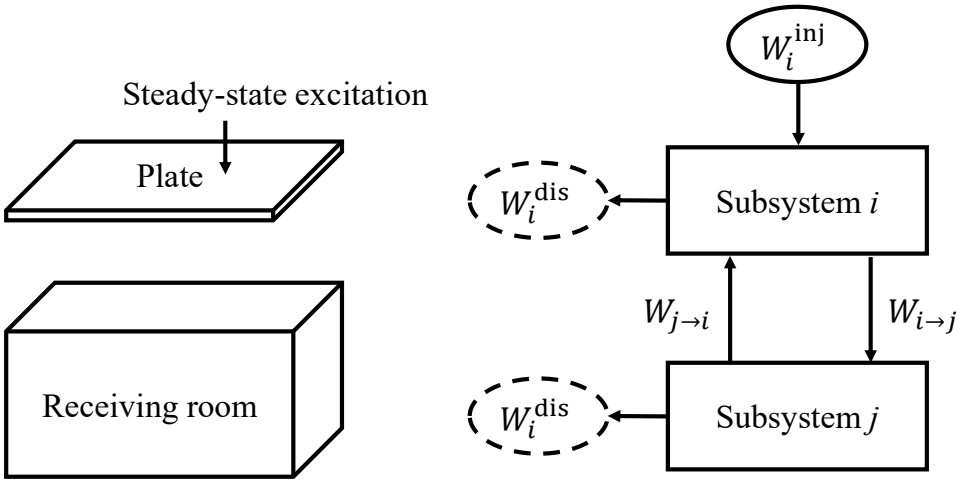

Figure 2-1. Two-subsystem SEA model for excitaion of a solid floor that radiates into a room.

The power balance equation for SEA considers the injected power W_i^{inj}, the transferred power W_{ij}, and the dissipated power W_i^{dis} where

$$W_i^{\mathrm{inj}} = \sum_{i \neq j} W_{ij} + W_i^{\mathrm{dis}} \tag{2.1}$$

The dissipated power is given by

$$W_i^{\mathrm{dis}} = \omega \eta_{ii} E_i \tag{2.2}$$

where ω is the angular frequency in radian, η_{ii} is the Internal Loss Factor (ILF) of the subsystem i, E_i is the energy in subsystem i.

The power flow between coupled subsystems i and j [61] is given by

$$W_{ij} = \omega \eta_{ij} E_i \tag{2.3}$$

where η_{ij} is the Coupling Loss Factor (CLF) between subsystems i and j, and E_i is the energy in subsystem i.

The power balance equations for subsystems 1 and 2 are given by

$$W_i^{\mathrm{inj}} + \omega \eta_{ji} E_j = \omega \eta_{ii} E_i + \omega \eta_{ij} E_i \tag{2.4}$$

$$\omega \eta_{ij} E_i = \omega \eta_{jj} E_j + \omega \eta_{ji} E_j \tag{2.5}$$

2.2.3 Loss Factor

This section describes the three loss factors used in the SEA equation; ILF, CLF and the Total Loss Factor (TLF).

2.2.3.1 Internal loss factor

The ILF describes the conversion of sound/vibration energy into heat. For a plate, the ILF is dependent on the material properties of the plate and is often measured or taken from textbooks [24]. For a room, if the heat conversion process is only due to the absorption within the space, the ILF is given by

$$\eta_{ii} = \frac{c_0 A_{\mathrm{T}}}{8 f \pi V} \tag{2.6}$$

where c_0 is the speed of sound in air, A_{T} is the total absorption area, f is the centre band frequency, and V is the volume of the room.

2.2.3.2 Coupling loss factor

The CLF is the fraction of energy transmitted between two subsystems per radian cycle.

To calculate the CLF from a plate to room, consider sound power radiated from bending waves on the plate in terms of the radiation efficiency, σ.

$$\sigma = \frac{W_{ij}}{S \rho_0 c_0 < v^2 >_{\mathrm{t,s}}} \tag{2.7}$$

where W_{ij} is the power transmitted from subsystem i to j, S is the surface area of the excited plate, c_0 the speed of sound, ρ_0 is the density of air, and $<v^2>_{\mathrm{t,s}}$ is the time and spatial average mean-square velocity.

Rewriting Eq. (2.7) in terms of the CLF from a plate to room using Eqs. (2.3) and (2.14) gives

$$\eta_{ij} = \frac{\rho_0 c_0 \sigma}{\omega \rho_{\mathrm{s}}} \tag{2.8}$$

where ρ_{s} is the mass per unit area of the plate.

From the Leppington [63–66], the frequency-average radiation efficiency can be estimated for a homogeneous and rectangular plate with dimensions of $L_1 \times L_2$.

Below the critical frequency

$$\sigma = \frac{U}{2\pi\mu k S\sqrt{\mu^2-1}}\left[\ln\left(\frac{\mu+1}{\mu-1}\right)+\frac{2\mu}{\mu^2-1}\right][C_{\mathrm{BC}}C_{\mathrm{OB}} - \mu^{-8}(C_{\mathrm{BC}}C_{\mathrm{OB}}-1)] \tag{2.9}$$

where U is the plate perimeter, S is the plate area, C_{BC} is a constant for the plate boundary conditions (C_{BC} =1 for simply supported boundaries, C_{BC} =2 for clamped boundaries), C_{OB} is a constant for the orientation of the baffle that surrounds the edges of the plate (C_{OB} =1 when the plate lies within the plane of an infinite rigid baffle, C_{OB} =2 when the rigid baffles along the plate perimeter are perpendicular to the plate surface) and, μ is calculated using

$$\mu = \sqrt{\frac{f_{\mathrm{c}}}{f}} \tag{2.10}$$

Above the critical frequency

$$\sigma = \frac{1}{\sqrt{1-\mu^2}} \tag{2.11}$$

At the critical frequency

$$\sigma \approx \left(0.5 - \frac{0.15L_1}{L_2}\right)\sqrt{k}\sqrt{L_1} \tag{2.12}$$

where $L_1 < L_2$.

The critical frequency of the plate can be calculated from

$$f_{\mathrm{c}} = \frac{kc_0}{2\pi} \tag{2.13}$$

where k is the wave number in the rectangular plate.

The power flow from subsystem *i* to *j* can be calculated from Eq. (2.3). for which the plate energy is calculated from mean-square velocity as

$$E_i = m < v^2 >_{\mathrm{t,s}} \tag{2.14}$$

where *m* is the mass of the plate

Similarly, the room energy is calculated from the mean-square pressure as

$$E_j = \frac{V < p^2 >_{t,s}}{\rho_0 c_0^2} \tag{2.15}$$

The CLF from the room (*j*) to the plate (*i*) can then be calculated using the consistency relationship [50]

$$\frac{\eta_{ij}}{N_j} = \frac{\eta_{ji}}{N_i} \tag{2.16}$$

where $N_{i,j}$ is the modal density.

2.2.3.3 Total loss factor

The TLF of a subsystem describes the damping of the subsystem due to all processes and is equal to the sum of all CLFs from a subsystem and the ILF [51].

$$\eta_i = \eta_{ii} + \sum_{i(i \neq j)} \eta_{ij} \tag{2.17}$$

The TLF is related to the reverberation time [24] by

$$\eta_i = \frac{6\ln 10}{2\pi f T} = \frac{2.2}{fT} \tag{2.18}$$

where *T* is the reverberation time of a room or the structural reverberation time of a plate.

For bending wave motion on masonry/concrete plates that are rigidly connected on all sides, estimates for the TLF can be calculated according to [24,51].

$$\eta_i = \eta_{ii} + \frac{X}{\sqrt{f}} \tag{2.19}$$

where f is frequency and, X is usually $0.3 \leq X \leq 1$ for masonry/concrete walls or floors in the field or the laboratory [24].

2.2.4 Assumptions in SEA

The main assumptions in SEA are as follows [24,51].

1. Statistically independent excitation forces

SEA assumes the modal vibrations must be uncorrelated hence a linear relationship can be used between power flow and modal energies (using local modes) for a coupled system.

For point excitation, statistically independent modal response does not necessarily occur [67]. However, Bies and Hamid [68] show that point excitation data that is averaged from randomly chosen points can approximate statistical independence between modes.

2. Equal probability of eigenfrequencies occurring in a frequency band

In heavyweight buildings, only estimates are available for the mode frequencies and mode shapes. There will be uncertainty in describing the modes of real spaces or buildings due to uncertainty in the dimensions, material properties and the quality of workmanship. Hence it is reasonable to assume that there is an equal probability of the mode frequencies falling within a certain frequency band.

3. Equipartition of modal energy in a subsystem and incoherent modal response between modes in the coupled system

   In building acoustics, it is reasonable to assume equipartition of modal energy in a subsystem and incoherent modal response between modes in the coupled system because of the uncertainty in describing the modes of real building structures and quality of workmanship. This uncertainty allows the use of the statistical modal density.

4. ‘Weak’ coupling between subsystems.

For predictive SEA, the weak coupling can (to some extent) be considered as occurring when the local mode behaviour of an uncoupled subsystem is hardly changed when it is coupled to the other subsystems such that energy flow can be related to the local modal energies [24]. More detail on the assumptions in SEA can be found in the literature [24,50,51,69].

2.3 Transient Statistical Energy Analysis (TSEA)

2.3.1 Introduction

TSEA is a method for predicting the transmission of transient sound and vibration using the basic principles of SEA and assumes steady-state net power flow between subsystems but in a short time interval. Using that assumption, the time-average net power flow can be calculated using steady-state CLFs from SEA. TSEA essentially concerns power balance as a stationary phenomenon over a short duration time interval. The following derivation of TSEA is based on the work of Powell and Quartararo [54] and Lyon and Dejong [50].

2.3.2 Overview of the theory

Based on the conservation of energy in the resonant modes of a subsystem, i, which falls within the frequency band, the rate of change of energy is

$$\frac{\mathrm{d}E_i(t)}{\mathrm{d}t} = W_{\mathrm{in},i}(t) - W_{\mathrm{out},i}(t) \tag{2.20}$$

where E_i is the energy of subsystem i, $W_{\mathrm{in},i}$ is the power input into subsystem i, and $W_{\mathrm{out},i}$ is the power flowing out of subsystem i.

Using the two subsystem SEA model shown in Figure 2-1 we can now consider a TSEA model

$$W_{\mathrm{in},i}(t) = W_{\mathrm{inj}}(t) + \sum_{j(i\neq j)} \omega\eta_{ji}E_j(t) \tag{2.21}$$

$$W_{\text{out},i}(t) = \omega\eta_{ii}E_i(t) + \sum_{i(i\neq j)} \omega\eta_{ij}E_i(t) \tag{2.22}$$

where W_{inj} is injected power from the transient source.

SEA considers the temporal average energies of oscillators where net power transfer takes place from the subsystem with higher energy to the subsystem with lower energy. Assuming this applies when considering temporal-average energies over a small-time interval, Eq. (2.20) can be re-written to give the TSEA equation as

$$\frac{\mathrm{d}E_i(t)}{\mathrm{d}t} = \left(W_{\text{inj}}(t) + \sum_{j(i\neq j)} \omega\eta_{ji}E_j(t)\right) - \left(\omega\eta_{ii}E_i(t) + \sum_{i(i\neq j)} \omega\eta_{ij}E_i(t)\right) \tag{2.23}$$

Assume the current time step is t_{n} and the next time step is $t_{\text{n+1}}$ and rearranging Eq. (2.23), the TSEA equation is

$$E(\mathrm{t}_{n+1}) = E(t_n) + \left[\left(W_{in}(t_n) + \sum_{j(j\neq i)} \omega\eta_{ji}E_j(t_n)\right) - \left(\omega\eta_{ii}E_i(t) + \sum_{i(i\neq j)} \omega\eta_{ij}E_i(t_n)\right)\right]\Delta t \tag{2.24}$$

The power loss term can be simplified by making it a function of the TLF, η_i, for subsystem i as

$$E_{\mathrm{i}}(t_{n+1}) = E_i(t_n) + \Delta t\left(W_{in}(t_n) + \sum_{j(j\neq i)} \omega\eta_{ji}E_j(t_n) - \omega\eta_i E_i(t_n)\right) \tag{2.25}$$

The accuracy of the solution depends on the size of time increment, Δt, for which the lower and upper limits can be estimated using the subsystem properties in the TSEA model as given by [56].

$$\frac{d_{\text{mfp}}}{2c_{\text{g(B)}}} \leq \Delta t \leq \frac{1}{b\omega\eta} \tag{2.26}$$

where d_{mfp} is the mean free path, and $c_{\text{g(B)}}$ is the group velocity of bending waves into which the power is injected, b is an integer constant for which the optimum value for the prediction of maximum time-weighted levels will typically fall in the range $3\leq b \leq 43$ [56].

Previous work on TSEA [56] also assessed the level difference in terms of $L_{v,Fmax}$ of the source subsystem and $L_{p,Fmax}$ in the receiver subsystem due to the value of b. Using b=3 instead of b=96 the maximum difference in $L_{v,Fmax}$ and $L_{p,Fmax}$ was approximately 0.03dB, and 0.025dB respectively. The authors therefore suggested that for heavyweight buildings, the value of b could be reduced to 6.

Solution of Eq. (2.25) gives the spatial and time average energy in each successive time step which can be converted to a mean-square pressure or velocity as follows

$$p_i^2(t_n) = \frac{E_i(t_n)\rho_0 c_0^2}{V_i} \tag{2.27}$$

$$v_i^2(t_n) = \frac{E_i(t_n)}{m_i} \tag{2.28}$$

2.3.2.1 Transient power input

TSEA models require a normalised transient power input for the excitation source. For heavyweight floors where the driving-point mobility is significantly lower than the source (this will be confirmed later in Chapter 4, Figure 4-6) a force plate can be used to measure the blocked force from the rubber ball, tyre source or human footsteps. With knowledge of the driving-point mobility of the receiver structure [24]. The power input is given by

$$W_{\text{in}} = F_{\text{rms}}^2 \text{Re}\{Y_{\text{dp}}\} \tag{2.29}$$

where F_{rms} is the root-mean-square force and $\text{Re}\{Y_{\text{dp}}\}$ is the real part of the driving-point mobility of the source subsystem.

For most excitation sources, F_{rms} can be measured or estimated, and an analytical model to determine F_{rms} for the rubber ball will be discussed in sections 3.3.3, 3.8.1 and 4.4.3.

The driving-point mobility can be estimated by assuming the plate is infinite or finite in extent [70].

The infinite plate version of the driving-point mobility can be calculated using [70]

$$Y_{\mathrm{dp},\infty} = \frac{1}{2.3\rho c_{\mathrm{L}} h^2} \tag{2.30}$$

where ρ is the density of the plate, c_{L} is the quasi-longitudinal wave speed of the plate, and h is the thickness of the plate.

The infinite plate mobility provides a reasonable representation of the measured driving-point mobility when the plate is highly damped and there are many modes in the frequency band of interest. This tends to occur in the mid and high frequency ranges for heavyweight walls and floors that are connected to other walls and floors [24].

In the low-frequency range, modes are widely spaced and the modal responses can be estimated using the finite plate driving-point mobility. This can be estimated from the summation of the local bending modes, $f_{p,q}$. The bending mode frequencies for a simply supported, isotropic, rectangular plate can be calculated by [70]

$$f_{p,q(\mathrm{B})} = \frac{\pi h c_L}{4\sqrt{3}} \left[\left(\frac{p}{L_x} \right)^2 + \left(\frac{q}{L_y} \right)^2 \right] \tag{2.31}$$

where p and q are positive integers defining the local mode $f_{p,q}$, and L_{x} and L_{y} are the dimensions of the rectangular plate.

The driving-point mobility of a finite plate can be described by Eqs. (2.31) and (2.33) [70]

$$Y_{\mathrm{dp,finite}} = \frac{i4\omega}{\rho_s S} \sum_{p=1}^{\infty} \sum_{q=1}^{\infty} \frac{\psi_{p,q}^2(x,y)}{\left[\omega_{p,q}(1+i\eta)\right] - \omega^2} \tag{2.32}$$

where η is the total loss factor of the plate and $\psi_{p,q}$ is the local mode shape of a thin isotropic rectangular plate with simply supported boundaries is described by

$$\psi_{p,q} = \sin\left(\frac{p\pi x}{L_x}\right) \sin\left(\frac{q\pi y}{L_y}\right) \tag{2.33}$$

In a building, the actual boundary condition of a plate is often unknown. This makes it difficult to gain an accurate estimate for their modal responses. However, the assumption of simply supported boundaries is often sufficient [24].

The TSEA model requires the losses per radian cycle to occur in every time step. Therefore, if the transient power input into a subsystem is applied over a longer duration than the force is applied to the subsystem, the energy in each time step will be incorrect [56]. The TSEA model also requires a power input in defined frequency bands. Hence, it is necessary to convert the transient power input from narrow-band FFT (defined later on section 2.6.2.3) lines to frequency bands by summing the power in the narrow bands that lie within the filter band limits.

The normalised transient power input, W'_{in}, can then be calculated using (a) FFT window length, t_{w}, that is long enough to ensure that the acceleration response decays to zero, and (b) the duration of the transient force, t_{F}. This normalised transient power input into the TSEA model must be over time duration of the transient force [56]. This requires a correction factor, *NF*, given by

$$NF = \frac{t_{\mathrm{w}}}{t_{\mathrm{F}}} \tag{2.34}$$

$$W'_{\mathrm{in}} = NF \times W_{\mathrm{in}} \tag{2.35}$$

The normalised transient power input is usually determined in one-third or octave bands. Whilst feeding this signal into the TSEA model, the normalised transient input will have the duration of t_{F} for each frequency bands; hence it has a step-function shape for the duration of t_{F}, and is then zero for the rest of the signal.

2.4 Inverse Transient Statistical Energy Analysis (ITSEA)

2.4.1 Introduction

In most buildings, there will usually be a floating floor on top of the base floor to provide insulation against light impacts such as footsteps from walkers in shoes, as well as heavy impacts such as from children running or jumping. For this reason, it is necessary to identify and experimentally validate a new approach to incorporate floating floors in TSEA models of heavyweight buildings.

TSEA models require a transient power input from the excitation source. This can be calculated by using a force plate to measure the blocked force from the standard impact sources or human footsteps along with knowledge of the driving-point mobility of the receiver structure (e.g. base floor). However, the size of the force plate means that this experimental approach is not feasible for a large floating floor with a rigid walking surface that is undergoing wave motion due to the excitation. Assuming the surface of the floating floor has low mobility relative to the mobility of the heavy impact source, one possibility could be to predict the dynamic behaviour of the floating floor to predict the improvement in impact sound insulation. However, it is difficult to accurately predict the performance of floating floors near the mass-spring resonance [24]

To facilitate the inclusion of floating floors in TSEA models, inverse form of TSEA is proposed to determine the transient power input into the base floor for the combination of the heavy impact source and floating floor.

It is possible to use laboratory measurements with ITSEA to experimentally determine the normalised transient power input into the base floor for the heavy impact source on the base floor ($W'_{\text{in,ITSEA,Base}}$) and on the combination of the floating floor and base floor ($W'_{\text{in,ITSEA,Base\_with\_floating\_floor}}$) indicated in Figure 2-2. The application of these laboratory measurements to the field requires that the thickness and material properties of the concrete base floor in the laboratory are the same or similar to the thickness of the base floor in the field that is being modelled with TSEA.

The laboratory measurements will allow calculation of the change in normalised transient power due to the floating floor, $\Delta L_{W'_{\text{in,ITSEA}}}$ as given by

$$\Delta L_{W'_{\text{in,ITSEA}}} = 10\log_{10}\left(\frac{W'_{\text{in,ITSEA,Base}}}{W'_{\text{in,ITSEA,Base\_with\_floating\_floor}}}\right) \quad (2.36)$$

where $W'_{\text{in,ITSEA,Base}}$ is the normalised transient power input for the heavy impact source directly exciting the base floor and $W'_{\text{in,ITSEA,Base\_with\_floating\_floor}}$ is the normalised transient power input for the heavy impact source exciting the floating floor.

There are two steps in creating a TSEA model for a heavyweight base floor with a floating floor. The first step is to calculate the normalised transient power,

$L_{W'_{\text{in},\infty\text{Base}}}$ referenced to 10^{-12}W, for a heavy impact source exciting the base floor when represented as an infinite plate according to

$$L_{W'_{\text{in},\infty\text{Base}}} = 10\log_{10}\left(\frac{F_{\text{rms}}^2 Y_\infty}{10^{-12}}\right) \tag{2.37}$$

where Y_∞ is the driving-point mobility of the base floor when assumed to act as an infinite plate. The second step is to modify the power input to the base floor using $\Delta L_{W'_{\text{in,ITSEA}}}$ to account for the floating floor using

$$L_{W'_{\text{in,Base\_with\_floating\_floor}}} = L_{W'_{\text{in},\infty\text{Base}}} - \Delta L_{W'_{\text{in,ITSEA}}} \tag{2.38}$$

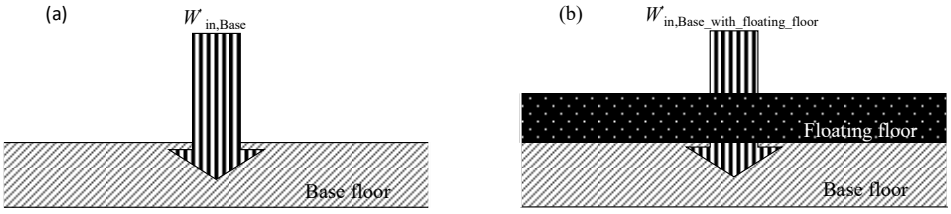

Figure 2-2. Power injection into (a) the base floor and (b) the base floor when there is a floating floor.

2.4.2 Theory

ITSEA is used to determine the transient power input into the source subsystem, *i*, in a system comprising of *X* subsystems by rewriting Eq. (2.25).

$$W_{\text{in,ITSEA},i} = \frac{1}{N}\sum_{n=1}^{N}\frac{\left(E_i(t_{n+1}) - E_i(t_n)\right)}{\Delta t} - \left(\sum_{j\neq i}^{X}\omega\eta_{ji}E_j(t_n) - \omega\eta_i E_i(t_n)\right) \tag{2.39}$$

where N is the integer number of time steps between 0ms and t_{peak}.

Use of Eq. (2.39) requires (a) the time-varying, mean-square energy on the source subsystem and all subsystems directly connected to the source subsystem, (b) all the CLFs that directly transfer energy from other subsystems to the source subsystem, and (c) the TLF of the source subsystem. In practice, it is possible to measure the CLFs and the TLF [24], but their inclusion in Eq. (2.39) is likely to increase the uncertainty. In addition, it is experimentally demanding to measure time-varying, mean-square energy on the source subsystem and all the subsystems that are directly connected to it.

Therefore, for practical purposes, it is simpler if ITSEA only considers the source subsystem. This allows Eq. (2.39) to be simplified to

$$W_{\text{in,ITSEA},i} \approx \frac{1}{N}\sum_{n=1}^{N}\left[\frac{\left(E_i(t_{n+1}) - E_i(t_n)\right)}{\Delta t} + \omega\eta_i E_i(t_n)\right] \qquad (2.40)$$

To quantify the transient power input which is to be injected into a TSEA model during the time that the force is applied, the values obtained from Eq. (2.40) need to be modified to give the normalised transient power input using

$$W'_{\text{in,ITSEA},i} = \frac{t_{\text{peak}}}{t_{\text{input\_duration}}} W_{\text{in,ITSEA},i} \qquad (2.41)$$

where t_{peak} is the time at which the first peak occurs in the mean-square velocity, and $t_{\text{input\_duration}}$ is the actual duration of the force pulse. For a heavy impact directly onto the base floor, $t_{\text{input\_duration}}$ can be determined from force plate measurements, but it is not possible to use the force plate to determine $t_{\text{input\_duration}}$ for a heavy impact on a full-size floating floor.

A full discussion and assessment of the signal processing required for implementation of ITSEA is given in section 5.3 as this uses the test facility descriptions in section 5.2.1.

2.5 Finite Element Methods (FEM)

2.5.1 Introduction

FEM is used to predict and determine the floor impact sound insulation due to a heavy impact. The FEM model includes the rubber ball, the concrete slab excited by the rubber ball, and the receiving room.

FEM is a deterministic approach which allows calculation of individual modal responses or simulation of the dynamics of complex structures by discretising the structure into a set of elements connected at nodal points [71]. For this reason, FEM can be computationally expensive compared to SEA and TSEA. In this thesis, FEM simulations are carried out using ABAQUS v6.14 [72].

2.5.2 Governing equation for the explicit time marching FEM

The response of each element is determined by a governing function. For a finite element system, a linear differential equation of second order consists of the mass, spring and damping matrices along with displacement, velocity, acceleration, and externally applied loads [73]

$$[\mathrm{M}]\{\ddot{U}_\mathrm{t}\} + [\mathrm{C}]\{\dot{U}_\mathrm{t}\} + [\mathrm{K}]\{U_\mathrm{t}\} = \{\mathrm{R}_\mathrm{t}\} \tag{2.42}$$

where [M], [C] and [K] are the mass, damping and stiffness matrices respectively of the associated finite element, $\{U_\mathrm{t}\}$, $\{\dot{U}_\mathrm{t}\}$, and $\{\ddot{U}_\mathrm{t}\}$ are the time dependent displacement, velocity, and acceleration vectors of the associated finite element, $\mathrm{R_t}$ is a vector of externally applied loads.

The solution for the equilibrium relation can be solved by a finite difference method to approximate the accelerations, velocities with regard to the displacements. The finite difference method with the central difference operator to solve this relation is called the explicit method, and is suitable for rapid dynamic events [74].

The displacement at time t, Δt, and $t+\Delta t$ can be related with Taylor expansion of the displacement limiting it to the order of Δt^2, where

$$\{U_{t+\Delta t}\} = \{U_t\} + \Delta t\{\dot{U}_t\} + \frac{\Delta t^2}{2!}\{\ddot{U}_t\} \tag{2.43}$$

$$\{U_{t-\Delta t}\} = \{U_t\} - \Delta t\{\dot{U}_t\} + \frac{\Delta t^2}{2!}\{\ddot{U}_t\} \tag{2.44}$$

Rearranging (2.43) and (2.44) gives the velocity and acceleration at time t [73]

$$\{\dot{U}_t\} = \frac{1}{2\Delta t}(\{U_{t+\Delta t}\} - \{U_{t-\Delta t}\}) \tag{2.45}$$

$$\{\ddot{U}_t\} = \frac{1}{\Delta t^2}(\{U_{t+\Delta t}\} - 2\{U_t\} + \{U_{t-\Delta t}\}) \tag{2.46}$$

Substituting those two equations into the equation of motion at time t, and rearranging it for $U_{t+\Delta t}$ gives

$$\left(\frac{1}{\Delta t^2}[\mathrm{M}]+\frac{1}{2\Delta t}[\mathrm{C}]\right)\{U_{t+\Delta t}\} = \mathrm{R_t}-\left([\mathrm{K}]-\frac{2}{\Delta t^2}[\mathrm{M}]\right)\{U_t\} - \left(\frac{1}{\Delta t^2}[\mathrm{M}]-\frac{1}{2\Delta t}[\mathrm{C}]\right)\{U_{t-\Delta t}\} \quad (2.47)$$

Eq. (2.47) requires $\{U_t\}$ and $\{U_{t-\Delta t}\}$ to calculate $\{U_{t+\Delta t}\}$.

The initial condition $\{U_{-\Delta t}\}$ can be determined from Eqs. (2.45) and (2.46)

$$U_{-\Delta t} = U_1 - \Delta t\dot{U}_1 + \frac{\Delta t^2}{2}\ddot{U}_1 \quad (2.48)$$

The advantage of the explicit method is that $\{U_{t+\Delta t}\}$ can be calculated from $\{U_t\}$ and $\{U_{t-\Delta t}\}$ without iterations or convergence check, hence, each increment is relatively inexpensive compared to an implicit method such as the direct-integration dynamic analysis procedure. Also, there is no matrix inversion required for [K] in the explicit method which can also reduce further computation time.

In the implicit solver, if the time step is arbitrarily large, the solution remains well behaved. However, for the explicit method, the stability of the result depends on the size of the time step. Therefore, it is conditionally stable when the time step size is smaller than the maximum size of Δt.

2.5.3 Time increment

The explicit approach is conditionally stable, and requires small time increments to obtain an accurate result. The stability limit for the time increment is estimated from the smallest transit time of a dilatational wave across any of the elements in the mesh [75,76].

$$\Delta t \leq \frac{L}{c_\mathrm{d}} \quad (2.49)$$

where L is the smallest element size of the global model, and the c_d is dilatational wave speed of the material [75]. Use of the dilatational wave speed is recommended in the ABAQUS manual, and this is reasonable because the dilatational wave speed is the fastest wave speed [76].

The dilatational wave speed is calculated using [76]

$$c_{\mathrm{d}} = \sqrt{\frac{\hat{\lambda} + 2\hat{\mu}}{\rho}} \tag{2.50}$$

where $\hat{\lambda}$ and $\hat{\mu}$ are Lame's constants given by

$$\hat{\lambda} = \frac{E\nu}{(1+\nu)(1-2\nu)} \tag{2.51}$$

$$\hat{\mu} = \frac{E}{2(1+\nu)} \tag{2.52}$$

where E is Young's modulus, and ν is Poisson's ratio in an isotropic elastic material.

The stable time increment size that ABAQUS chooses for the numerical computation is smaller than the estimated value in Eq. (2.49) by between $1/\sqrt{2}$ and 1 for the plate model, and $1/\sqrt{3}$ and 1 for the plate and room model [75].

2.5.3.1 Elements and suitable element size

For the concrete plate and the rubber ball, a general conventional shell element S3R [77] is used which allows transverse shear deformation. It uses thick shell theory as the shell thickness increases and becomes a discrete Kirchhoff thin shell element as the thickness decreases [77].

For the room, AC3D8R [77] is used which is a hexagonal eight-node linear acoustic brick element

The element size is determined by the type of element and the maximum frequency of interest to achieve the required accuracy. In building acoustics, it is common to use at least six elements per wavelength for structural and fluid domains [78]. In this thesis, the mesh element size is 0.1m for the room, 0.1m for the concrete floor, and 0.01m for the rubber ball at 708Hz (upper-frequency band of 500Hz octave band) which corresponds to $\lambda/5$, $\lambda_B/12$, and $\lambda_B/8$ for the room, the concrete floor and the rubber ball respectively.

The small stable time increment is estimated for the smallest element size with the fastest wave speed (i.e. dilatational waves for the concrete plate). The output file from ABAQUS is created at each node with requested vector (i.e. acceleration, velocity, force, sound pressure) for each time intervals for each direction. This could easily lead to a large output file that cannot be opened by the software.

The file size needs to be small enough to be openable and exportable after the completion of the analysis to allow post-processing to compute $L_{\mathrm{p,Fmax}}$. A pragmatic solution for this is to decimate the output signal while analysis is running in ABAQUS v6.14 [79]. This can be done by defining the output request option. This reduces the size of the output database by excluding high-frequency data before it is saved, and also reduces the aliasing problems.

For the decimation a 2nd order Butterworth filter with cut-off frequency of 2kHz was used, and the down-sampled signal was stored locally on the PC for further signal processing.

2.5.3.2 Specific acoustic impedance of room surfaces

Abaqus v6.14 requires boundary conditions for the room surfaces to be defined by a single number for the specific acoustic impedance. This is given by the following equation derived from consideration of plane waves

$$Z_{\mathrm{a,s}} = \frac{1}{\cos\theta}\frac{1+R}{1-R} \tag{2.53}$$

where θ is angle of incidence to the surface and R is the reflection coefficient.

For an individual room mode, the decay can be estimated by assuming: (1) the room is excited with a single frequency input that is the same frequency as the mode of interest, (2) the sinusoid only excites a single mode, (3) when the sound source is stopped at the time, the waves continue to travel along the path that is defined by this room mode and a fraction of the energy is reflected and dissipated [24].

The reverberant decay of an individual mode, m, in terms of energy can be described as [80]

$$E(t) = E_0 \mathrm{e}^{-2\delta_m c_0 t} \tag{2.54}$$

where $\delta_{\mathrm{m}} = \beta_{\mathrm{a,s}}\left(\varepsilon_{p,m}/L_x + \varepsilon_{q,m}/L_y + \varepsilon_{r,m}/L_z\right)$ in which $\beta_{\mathrm{a,s}}$ is the specific acoustic admittance (reciprocal of the specific acoustic impedance) and $\varepsilon_{p,m}$, $\varepsilon_{q,m}$ and $\varepsilon_{r,m}$ correspond to mode f_{pqr} (if p=0, then $\varepsilon_{p,m}$=1 else $\varepsilon_{p,m}$=2; q=0, then $\varepsilon_{q,m}$=1 else $\varepsilon_{q,m}$=2; if r=0, then $\varepsilon_{r,m}$=1 else $\varepsilon_{r,m}$=2).

$$T_m = \frac{3\ln 10}{c_0 \beta_{\mathrm{a,s}} \left(\frac{\varepsilon_{p,m}}{L_x} + \frac{\varepsilon_{q,m}}{L_y} + \frac{\varepsilon_{r,m}}{L_z}\right)} \tag{2.55}$$

The denominator of Eq. (2.55) is referred to as the damping constant of the mode from which it is possible to identify three different trends for the different mode types when the specific acoustic impedance or admittance is independent of frequency. A summary of these features is as follows [24,80]

(1) The axial modes associated with each room dimension have different reverberation times to each other when $L_{\mathrm{x}} \neq L_{\mathrm{y}} \neq L_{\mathrm{z}}$.

(2) When the tangential modes are considered in three groups defined by p=0, q=0 and r=0 each group will have the same reverberation time.

(3) All oblique modes have the same reverberation time.

At low frequencies the resulting decay curve is not usually straight across the entire 60dB decay range because the curve is determined by different combinations of axial, tangential and oblique modes. When the energetic sum of the decays for the individual mode is determined, the later part of the decay is strongly affected by the axial mode. For this reason, the initial 20dB of the approximately straight is often used to determine the reverberation times [24].

The numerical simulations using FEM in this thesis are primarily intended to assess the low-frequency range. In this range the room response is determined by small numbers of modes and the room response does not approximate a diffuse field. To carry out analysis in the time domain it is convenient to use a single value for the specific acoustic impedance and it is not feasible to use angle-dependent values. A pragmatic solution was adopted for the numerical simulations by taking Sabine reverberation times and then back calculating the specific acoustic impedance from Eq. (2.55) by

assuming all modes were oblique modes (i.e. $\varepsilon_{p,m}=\varepsilon_{q,m}=\varepsilon_{r,m}=2$) This has the advantage that values of acoustic impedance (which are not intuitive to interpret) can be related to the Sabine reverberation time.

2.5.3.3 Plate boundary conditions

In this thesis, the concrete base floors are assumed to have simply supported boundaries around the perimeter as this has been shown to be representative of real floors. simply supported boundaries have zero displacement but allow rotation.

2.6 Signal processing

2.6.1 Introduction

In order to calculate Fast time-weighted maximum sound pressure level it is necessary to process the time varying signal from measurements, TSEA and FEM.

Figure 2-3 shows the architecture of the MATLAB sound level meter used to process the time-varying signal output from measurements.

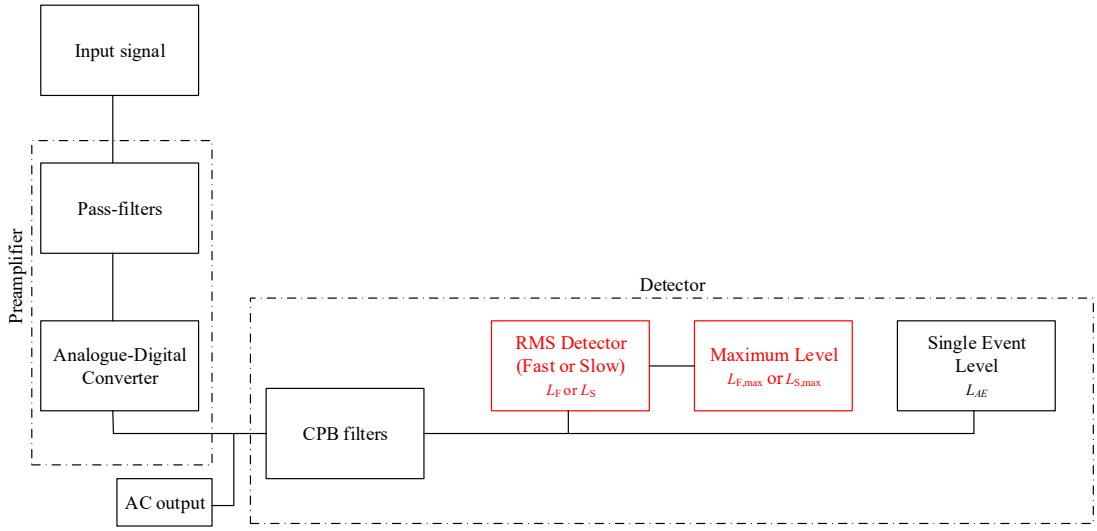

Figure 2-3. Architecture of the MATLAB sound level meter

2.6.2 Theory

2.6.2.1 Low-pass and high-pass filters

In the preamplifier, there are three different filters namely low-pass, band-pass and high-pass. These filters can be characterised by two parameters; the cutoff frequency

and slope of the filter above or below the cutoff frequency. The cutoff frequency normally describes where the gain is attenuated by 3dB.

In order to create a digital filter, it is common to create an analogue filter which satisfies filter characteristics. The frequency response of the simplest analogue filter is a first-order filter that is equivalent to the low-pass filter which has a gain of [81]

$$|G(\omega)| = \frac{1}{\sqrt{1 + (i\omega/\omega_c)^2}} \tag{2.56}$$

where G is the gain of the filter, i indicates an imaginary number, and ω_c is the cut-off frequency in radians.

The gain of the first-order high-pass filter is [81]

$$|G(\omega)| = \frac{(\omega/\omega_c)}{\sqrt{1 + (\omega/\omega_c)^2}} \tag{2.57}$$

To satisfy this, one of the most common general filter shapes is a Butterworth filter, and which has a gain of [81]

$$|G(\omega)| = \frac{1}{\sqrt{1 + (\omega/\omega_c)^{2n}}} \tag{2.58}$$

where n is the integer number corresponding to the filter order.

Eqs. (2.56) and (2.58) are identical when n=1. The Butterworth filter has maximum flat gain characteristics, and its phase characteristics are relatively linear, and for this reason, the low-pass, band-pass and high-pass filters are all created using Butterworth filters [81].

2.6.2.2 Constant Percentage Bandwidth (CPB) filter

For impact sound insulation, it is common to use octave band or one-third octave band filters. The design and specifications, of these filters are given in IEC 61260-1 [82].

2.6.2.3 Fast Fourier Transform

A Fast Fourier Transform (FFT) is implemented in MATLAB to process the force plate signals.

MATLAB '*fft*' command returns the double-side complex spectrum. Therefore, amplitude scaling is required. For a complex double-sided spectrum returned from MATLAB *fft* command, the energy is equally distributed to positive and negative frequencies. Hence the amplitude in the positive half above DC (f=0Hz) is multiplied by two to calculate peak values, $2/\sqrt{2}$ to calculate RMS values, and 4 to calculate peak-peak values. Figure 2-4 shows the difference in the scaling factors by using MATLAB '*fft*' function for 5Hz sinusoid input (df=0.004Hz). Figure 2-4 (upper) shows the amplitude of 2 for the peak-peak value, 1 is for the peak value, 0.707 is for the RMS value. This is equivalent to 6dB for the peak-peak value, 0dB for the peak value and -3dB for the RMS value in Figure 2-4 (lower).

For the transient signal, a rectangular window function used.

In order to convert the narrowband signal to one-third octave or octave bands, the narrowbands that fall in the frequency band are summed for absolute values or averaged for transfer functions.

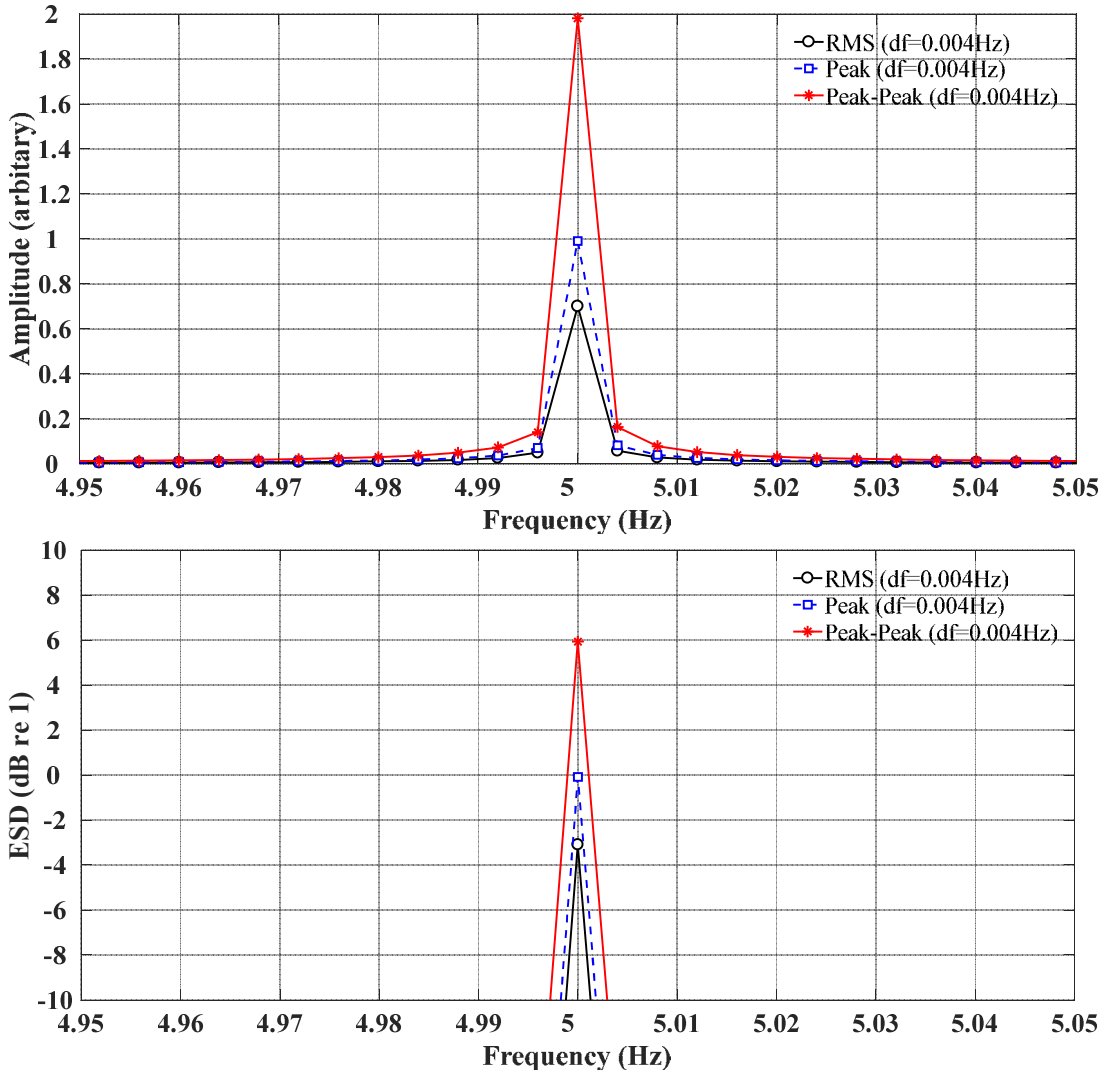

Figure 2-4. Amplitude of output fft function with different scaling factors

2.6.2.4 RMS detector

To determine time-weighting levels, IEC 61672-2:2013 [83] describes the specification for the time weighting as

$$L_{p\tau}(t) = 20\log_{10}\left[\frac{1}{\tau}\int_{-\infty}^{t}\left(p^2(\xi)e^{-\frac{t-\xi}{\tau}}d\xi\right)^{\frac{1}{2}}/p_0\right] \qquad (2.59)$$

where p is the instantaneous square sound pressure, ξ is a dummy variable of time integration from some time in the past, as indicated by $-\infty$ for the lower limit of the integral, to the time of observation t, and p_0 is the reference sound pressure.

This is implemented in MATLAB using an analogue integrator with a first-order Butterworth lowpass filter with the exponential time average constant equal to τ [81].

The relationship between cut-off frequency and integration time is [81]

$$f_{\text{cut}} = \frac{1}{2\pi\tau} \tag{2.60}$$

where f_{cut} is cut-off frequency and τ is the exponential time average constant for time weighting Fast (0.125s) or Slow (1s).

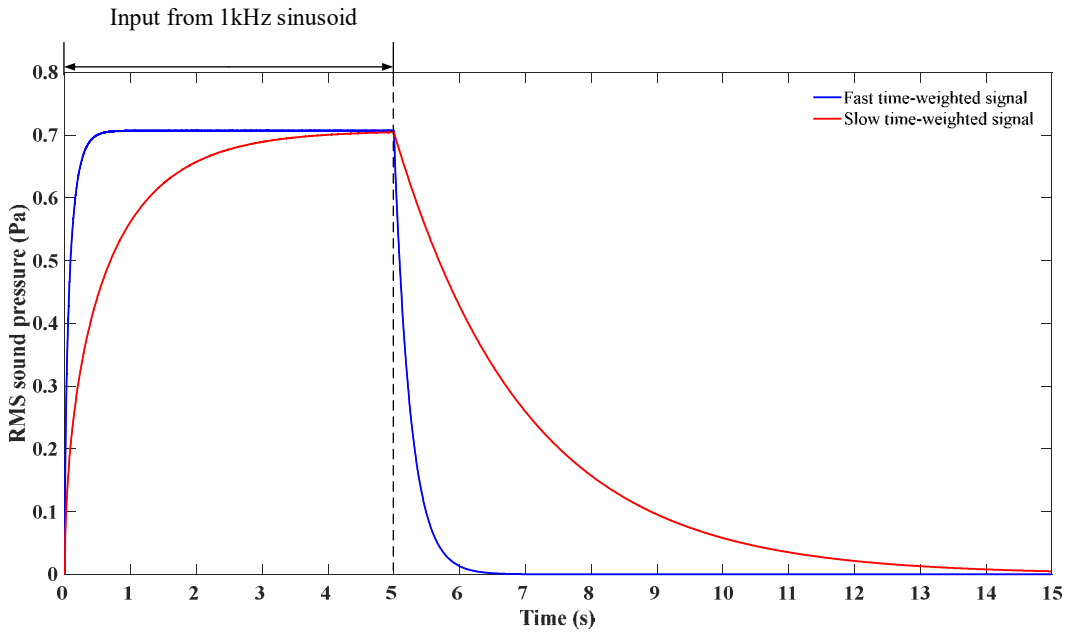

Figure 2-5. Filter response of the low-pass filter used to implement Fast- and Slow- time weightings to a 1kHz sinusoid.

Figure 2-5 shows the response of the time-weighting detector to a 1kHz sinusoidal input that has unity amplitude. Both Fast and Slow time-weighted curves show a maximum value of $1/\sqrt{2}$ of the input magnitude, but the rising curve has a different response speed. For this reason, if the input signal is a mean-square (i.e. from TSEA) then multiplication by $\sqrt{2}$ is required to give the RMS value [56].

2.6.2.5 Integration of acceleration signal to a velocity signal

The acceleration signal in the frequency domain is integrated to give velocity through division by $i\omega$ [24].

$$v = \frac{a}{i\omega} \tag{2.61}$$

where a is the acceleration in the frequency domain.

In the time domain, this can be done carried out using a first-order Butterworth high-pass filter which is equivalent to an analogue integrator found in a charge amplifier [81]. Figure 2-6 shows a sinusoidal input of 160Hz, along with the integrated signal that can be compared with a cosine. The difference in the peak value is 1.02%.

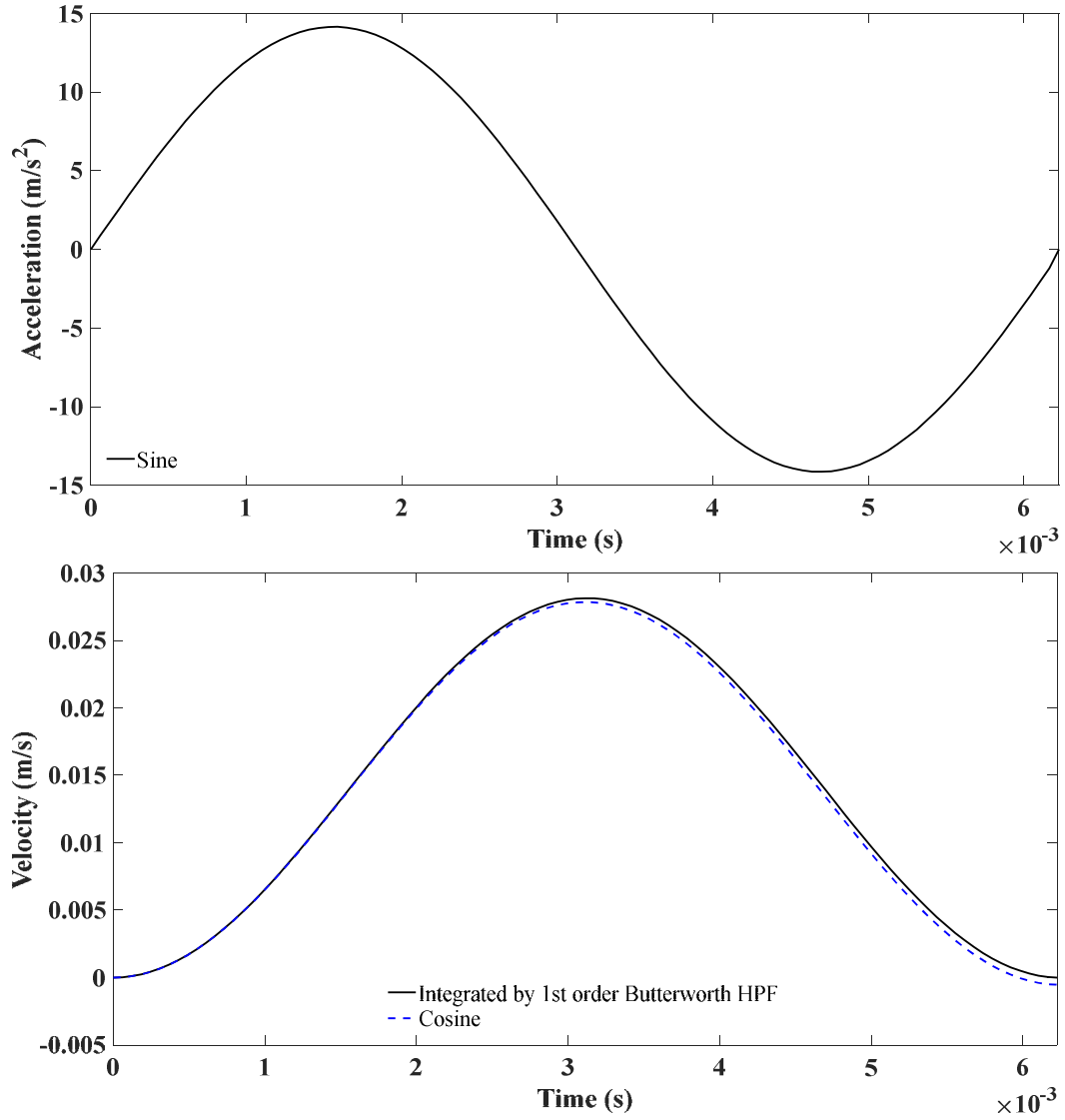

Figure 2-6. 160Hz sinusoid acceleration (upper). Integrated sinusoid acceleration (i.e. velocity) from a first-order Butterworth filter and the exact cosine function (lower).

2.7 Summary

This chapter introduced the theory needed to predict impact sound insulation with heavy impact sources in the thesis.

SEA provides a framework to predict sound transmission in buildings using steady-state conditions with statistical approach. The concept of TSEA is based on SEA to

incorporate transient excitation and response. TSEA concerns power balance as a stationary phenomenon over a short duration time interval by assuming the steady-state net power flow between subsystems occurs within a short interval. Hence, the time-averaged net power flow can be calculated using steady-state CLFs from SEA. TSEA assumes the net power transfer takes place from the subsystem with higher energy to the subsystem with lower energy over small time interval. Hence, the energy balance equation describes the net exchange of the subsystems in the time domain. TSEA requires the normalised transient power input; this can be determined by the transient power input (measured or estimated RMS force due to the excitation source, and the driving-point mobility of the receiver structure) and normalised to the input force duration.

This chapter introduced ITSEA to determine the normalised transient power input from the mean-square velocity of the source floor. It is based on TSEA and is introduced in order to use measurements to give the power input into a base floor when there is a floating floor. ITSEA does not require all the CLFs and energies from all subsystems which are directly connected to the source subsystems because it is too demanding to measure all subsystems directly connected to the source subsystems.

FEM with an explicit solver in the time domain was described to model a rubber ball impact on a base floor which radiates into a receiving room. The explicit solver is computationally efficient compared with the implicit solver as it does not require iteration for convergence of the result. As there are no iteration and convergence checks it requires a sufficiently small time increment to be smaller than the stability limit. Details were given on implementation of FEM in terms of elements for plates and rooms and boundary conditions.

The signal processing needed to process measurements, TSEA and FEM to give Fast time-weighted maximum levels were described in detail.

3. STRUCTURAL DYNAMICS OF THE RUBBER BALL

3.1 Introduction

This chapter focuses on the structural dynamics of the rubber ball both in isolation and when impacting a concrete base floor.

Section 3.2 describes the specification of the rubber ball from the manufacturers, JIS A 1418-2:2000 and ISO 10140-5:2010+A1 2014. Section 3.3 describes measurement of the blocked force of the rubber ball, and prediction of the blocked force by using a single-degree of freedom mass-spring-damper system. Section 3.4 and 3.5 contain experimental investigations into the modes of the rubber ball using the driving-point mobility and EMA. Section 3.6 describes an analytical model for a thin spherical elastic shell representing the rubber ball. Section 3.7 concerns estimation of Young's modulus of the rubber ball using the analytical model and the fundamental frequency of the rubber ball determined in sections 3.4 and 3.5. Section 3.8 simulates the blocked force of the rubber ball and the mode shapes of the rubber ball using FEM.

3.2 Rubber ball

3.2.1 Specification

There are different specifications for the rubber ball, and there are some differences in dimensions provided by the manufacturers, ISO 10140-5:2010+A1 2014 and JIS A 1418:2000 (NB: JIS A 1418:2000 is currently under review). For the rubber ball used in this thesis, the measured diameter and thickness correspond to ISO10140-5:2010+A1 2014/JIS A 1418-2:2000. The specifications of the rubber ball are given in Table 3.1.

Table 3.1. Specifications of the rubber ball.

	Diameter (m)	**Shell Thickness (m)**	**Mass (kg)**
Measured	0.178	Not possible to measure	2.486
NOK Ltd (RION) SN:010274B	0.178	0.032	2.5±0.1
ISO 10140-5:2010+A1 2014	0.180	0.03	2.5±0.1
JIS A 1418-2:2000	0.185	0.03	2.5±0.2

3.3 Blocked force measurement of the rubber ball using a force plate

3.3.1 Measurement equipment

A circular force plate was designed to measure the time-dependent force from a rubber ball (see Figure 3-1). It is constructed from a lower plate of 35mm thick steel with a 175mm radius (26.4kg) and an upper plate of 15.2mm thick aluminium with a 110mm radius (1.5kg). Three force transducers (Kistler 9041A, Serial numbers: 1667931, 643119, and 1667932) are bolted between the two plates.

In JIS A 1418-2:2000, there is a recommendation for the device that measures the blocked force (i.e. force plate) to have a measurable frequency range from at least 0.2 Hz to 1000Hz with flat frequency characteristics over this range. The measurable range of force shall be at least 0 to 5000N, and the linearity within the range shall be within ±2%.

Figure 3-1. Force plate.

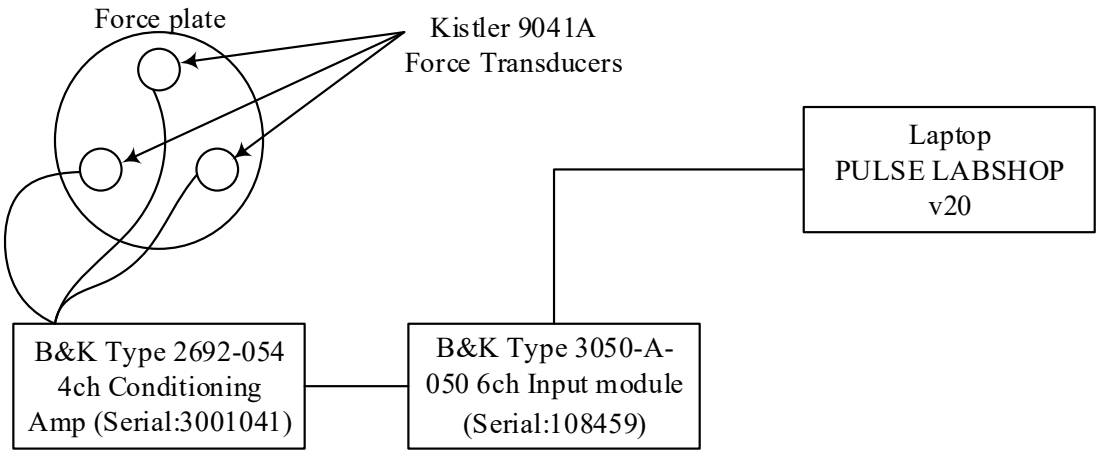

Figure 3-2. Force plate - schematic diagram of the associated equipment.

The force is measured by summing the output from the three force transducers in the time domain. The time-varying force was measured using the B&K PULSE Labshop system with a time resolution of 61.04μs and a frequency resolution of 1Hz. Experimental validation of the force plate was carried out by comparing the transient force from a force hammer impacting the centre of the force plate, with the summed output from the force plate.

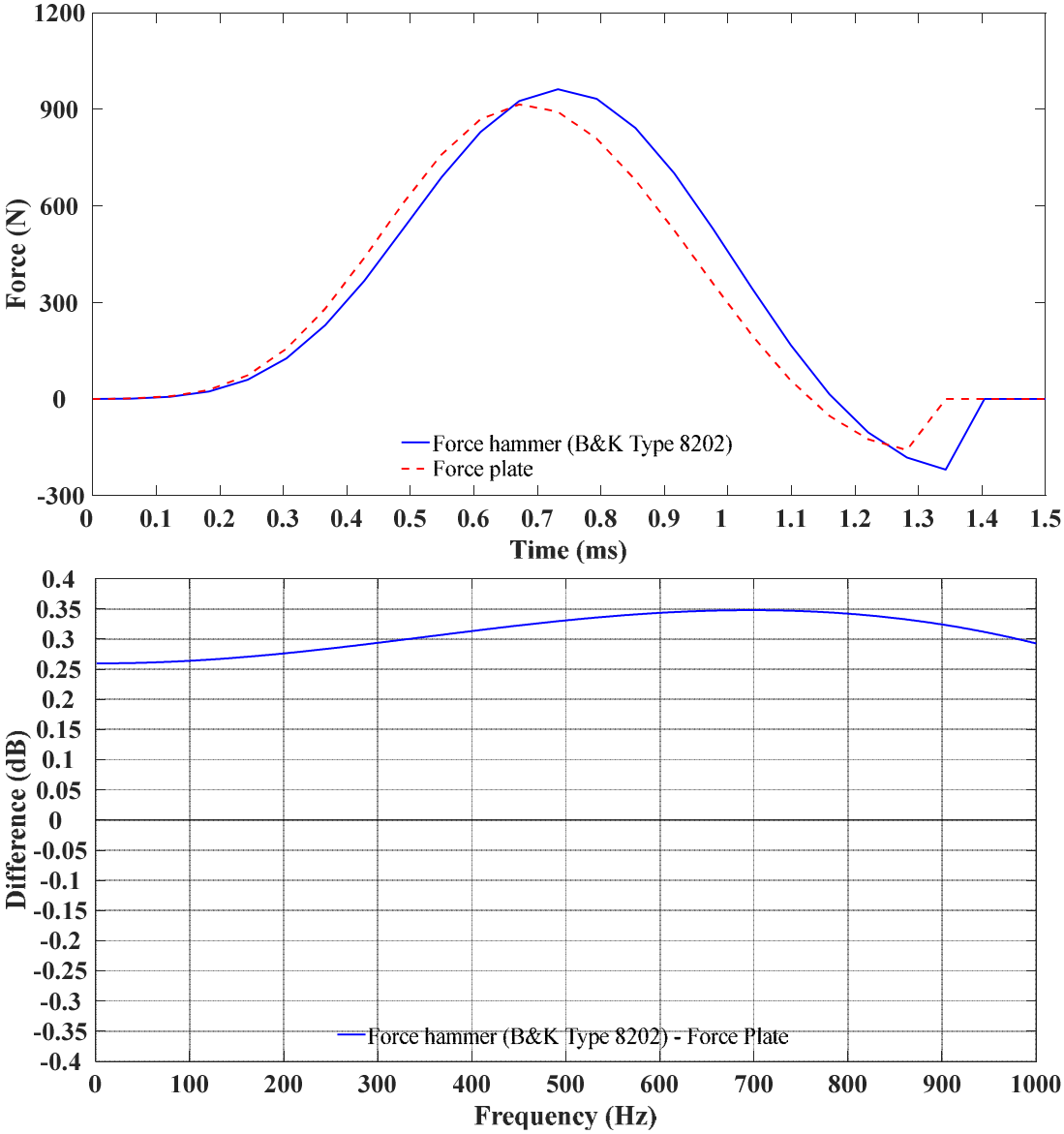

Figure 3-3. Comparison of the measured force in the time (upper) and frequency (lower) domains for a force hammer hit on the force plate.

Figure 3-3 shows the comparison between the input and output forces. A force hammer (B&K Type 8202) was used to input a peak force of approximately 1000N. At the peak, there is a time shift of 61.04μs, but the peak levels are within 5%. The frequency response from 0.7Hz to 1000Hz is shown in the lower graph indicating a difference up

to 0.35dB. The estimated fundamental frequency of the aluminium top plate is 1562Hz. This indicates that the force plate functions correctly and satisfies the requirements stated in JIS A 1418-2:2000.

3.3.2 Results

The blocked force of the rubber ball was measured by dropping a rubber ball from 1m height onto the force plate.

The definition of the blocked force is JIS A 1418-2:2000 associated to the starting time (F=0N and t=0s) to the completion of the first zero-crossing force point (F=0N and t=20ms) (see Figure 3-4 (upper)).

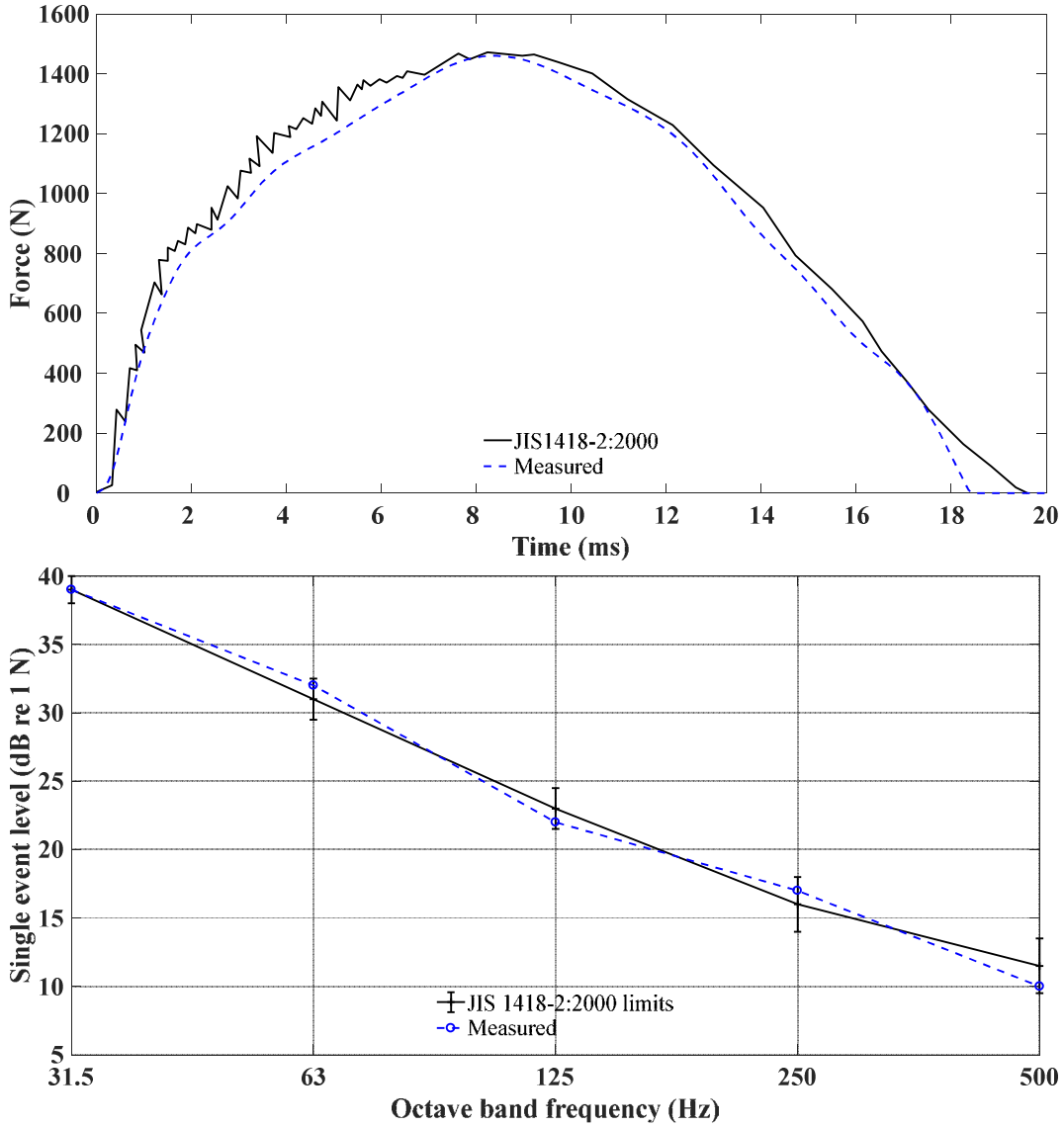

Figure 3-4. Comparison between JIS A 1418-2:2000 and the measured blocked force of the rubebr ball in the time domain (upper) and the single event level in octave bands (lower).

Figure 3-4 (upper) shows the force in the time domain. The post-processing was carried out in MATLAB using a fifth-order Butterworth low-pass filter at 1000Hz and a second-order Butterworth high-pass filter (1Hz). It is necessary to have the low-pass filter at this frequency because of the fundamental frequency of the aluminium top plate (1562Hz). The measurement of impact sound insulation with the rubber ball is usually only carried out up to the 500Hz octave band (upper band edge frequency of 708Hz) or one-third octave band (upper band edge frequency of 562 Hz). Comparing the force spectrum from JIS A 1418-2:2000 with measurements indicates that the duration is within the limit in the standard of 20ms±2ms, and the difference in the peak force between the measurement and JIS A 1418-2:2000 is within 1%.

Figure 3-4 (lower) shows the single event level in octave bands and in decibels using a reference value of 1N. The result shows that the measured force spectrum is within the lower and upper limits given in JIS A 1418-2:2000.

3.3.3 Single-degree-of-freedom mass-spring-damper system

Implementing excitation from the rubber ball in TSEA requires transient power input calculated from the blocked force. In this section, an attempt was made to predict this blocked force by assuming a single-degree-of-freedom (SDOF) mass-spring-damper system that represents the rubber ball.

A prediction model for the blocked force for a tyre source was investigated by Tanaka [84]. The model uses the SDOF mass-spring-damper model that predicts the shape of the force-time curve and single event level in octave bands. The results showed that it could not be used to predict the single event level in octave bands above 125Hz. This study indicates the force at t=0s is non-zero due to the constant spring stiffness and damping coefficients. The author also studied four different force-time curves that are (1) original, (2) modified to start at 0N at t=0s, (3) and (4) modified peak values to estimate the variance due to the force-time curves. The study showed that the variation due to the force-time curve could be up to an 11dB difference at 500Hz octave band for (1) and (2).

Subsequent studies by Schoenwald *et al.* [85–87] for the blocked force of the rubber ball predicted the force-time curve with a different approach. The model also derives

the SDOF equation of motion, but the force-time curve was estimated using momentum flux concept that was initially introduced by Percival [88] and applied to the table tennis ball by Hubbard and Stronge [89]. This model assumes the contact region on the spherical shell is deformed due to the contact velocity with time. Hence, the force due to the velocity part can be considered as a dissipation term at the compression phase. The force-time curve estimated from this model can obtain 0N at t=0s, but the difference in the single event level at 500Hz octave band is approximately 15dB.

To implement the rubber ball impact for the SDOF mass-spring-damper model, the damping coefficient, c_1, of the rubber ball can be determined from the period of the force duration and the restitution coefficient using [90]

$$c_1 = -\frac{2m_1}{\Delta T}\ln(e_1) \tag{3.1}$$

where m_1 is the mass of the rubber ball, ΔT is the contact duration of the rubber ball impact, and e_1 is the restitution coefficient of the rubber ball which is defined in JIS A 1418-2:2000, ISO 10140-2:2010 and KS F 2810-2 standards as 0.8±0.1.

The damped natural angular frequency of the rubber ball is [90]

$$\omega_{\mathrm{d1}} = \frac{\pi}{\Delta T} \tag{3.2}$$

Rearranging the Eq. (3.2) gives the spring stiffness [90]

$$k_1 = m_1\left(\frac{\pi}{\Delta T}\right)^2\left[1+\left(\frac{\ln(e_1)}{\pi}\right)^2\right] \tag{3.3}$$

The equilibrium equation for the blocked force is comprised of a stiffness and a damping component to give

$$F = m_1\ddot{y}_1 = k_1 y_1 - c_1\dot{y}_1 \tag{3.4}$$

where y_1 is the displacement, $\dot{y}_1$ is velocity and $\ddot{y}_1$ is the acceleration of the rubber ball (gravity). The initial condition of the rubber ball is y_1=1m, $\dot{y}_1 = -2\sqrt{2gh}$ m/s, and $\ddot{y}_1 = g$=9.81 m/s^2.

The SDOF mass-spring-damper model is modelled as follows (see Figure 3-5) using MATLAB Simulink.

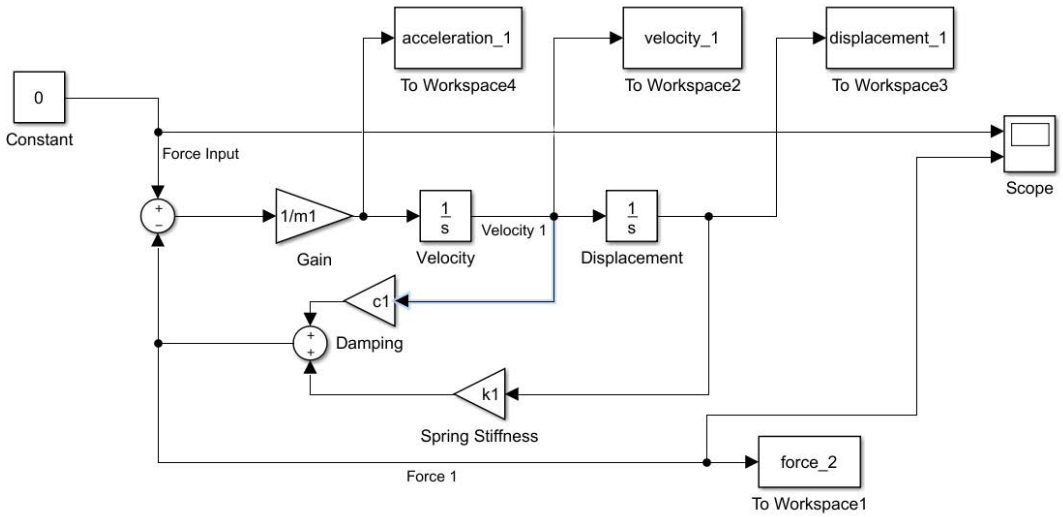

Figure 3-5. Schematic diagram of the SDOF mass-spring-damper model.

Figure 3-6 (upper) shows the blocked force calculated from Eq. (3.4) using $\dot{y}_1$ and y_1 outputs from Simulink with constant damping and stiffness values. Unlike the force spectrum that is shown in JIS A 1418-2:2000 (see Figure 3-4 (upper)), the simulated force has a total force that is a non-zero value at *t*=0s (see Figure 3-6 (upper)), and it is similar to the reported by Tanaka [84]. The contact duration defined from *t*=0s to the force where it crosses 0N at the end of the half-sine shape of the total force is within 1ms of the measurement result although the peak force is approximately 36N higher than the measurement result.

In Figure 3-6 (lower), the measured and simulated single event level in octave bands show agreement in the 31.5 and 63Hz octave bands but differ above this frequency by 2, 3 and 4.5dB at 125, 250 and 500Hz octave bands respectively. This suggests that even if the force does not start at 0N at *t*=0s, the agreement in the frequency band is better than the model derived by Schoenwald *et al*. which showed 15dB disagreement at 500Hz octave bands.

The rubber ball is deformed whilst it is in contact with a rigid surface due to the contact velocity and the structural elasticity like as assumed in the Schoenwald *et al.* model. This is the feature that cannot be simulated by the SDOF mass-spring-damper system as it assumes only one mass, spring and damper, and the stiffness and damping coef-

ficients are constant through the contact. The blocked force that involves the deformation of the rubber ball could be simulated with more than one mass-spring-damper components to approximate the deformation of the rubber ball (e.g. in a discretised model such as FEM).

Using the momentum flux approach for the SDOF mass-spring-damper system is not feasible for the current study as the aim of the thesis is to manipulate the blocked force of the rubber ball with and without a floating floor (see Figure 2-2).

In conclusion, the SDOF mass-spring-damper model can be used for the rubber ball to predict the force spectrum and maximum force level as the previous study on the tyre source [84] suggested. It can accurately predict the single event level in the first two octave bands (31.5 and 63Hz). It is worth noting that the underestimate in the prediction of single event level in the 125, 250 and 500Hz octave bands is closer to JIS A 1418-2:2000 limits than the prediction model used by Schoenwald *et al.* [87].

This shows that measurement rather than the SDOF prediction of the blocked force from the rubber ball is essential for use as input data in TSEA in order to give an accurate force spectrum from the 31.5 to the 500Hz octave bands.

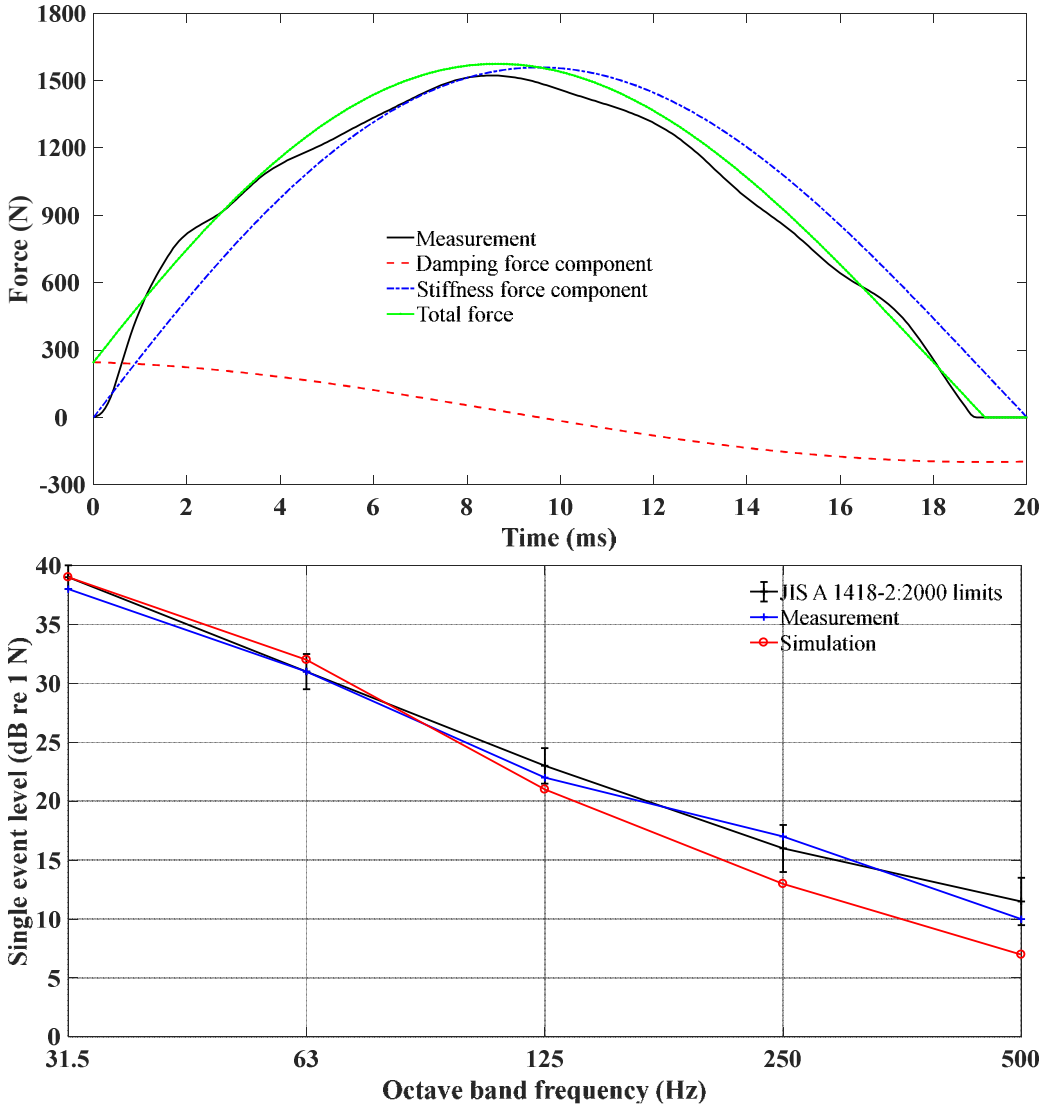

Figure 3-6. Simulink simulation of the blocked force in the time domain (upper) and the single event level in octave bands (lower) for the rubber ball impact.

3.4 Driving-point mobility of the rubber ball

The driving-point mobility of the rubber ball (RION Serial Number: 010274B) was measured using an impedance head (B&K Type 8001, Serial Number: 30171) attached to a dynamic shaker (B&K Type 406, Serial Number: 294948) with broadband excitation. The impedance head output the force and acceleration at the excitation point. The rubber ball was supported by elastic bands as shown in Figure 3-7

Figure 3-7. Experimental setup to measure driving-point mobility where the rubber ball is only supported by blue rubber bands.

Figure 3-8 shows the result of the impedance head measurement. At 20Hz there is an antinode in the magnitude of the driving-point mobility. This could be due to the supporting condition of the rubber ball. As the phase indicates (See Figure 3-8 (lower)), this is not the fundamental frequency of the rubber ball.

The zero-crossing in the phase indicates modes at 75 to 76Hz, 116 to 117Hz, 157 to 158Hz and 194 to 195Hz with associated driving-point mobility peaks at 74Hz, 115Hz, 158Hz and 197Hz.

Figure 3-8 (lower) shows the phase of the driving-point mobility. The phase below 20Hz is -90˚ which suggests it is mass-controlled region, and above this frequency where the phase is +90˚ this is indicative of a stiffness-controlled region up to the modal region which starts between 75 and 76Hz.

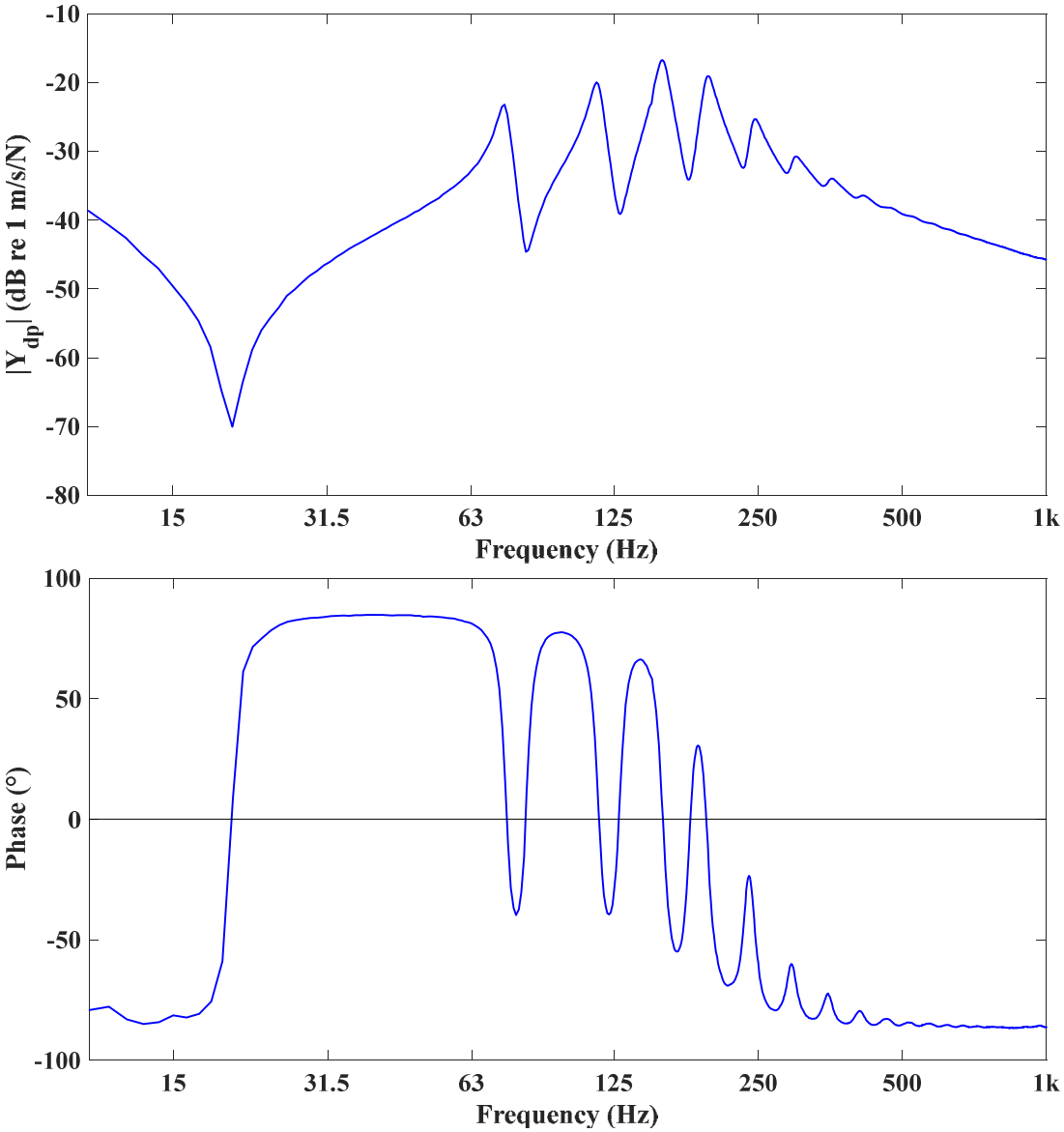

Figure 3-8. The magnitude of driving-point mobility of the rubber ball (upper), the phase of driving-point mobility of the rubber ball (lower).

3.5 Experimental modal analysis

3.5.1 Measurement procedure

To characterise the driving-point mobility of the rubber ball, it was measured with a 'free' support condition. However, under operating conditions the contact of the ball with the floor could change the modal response. Hence, Experimental Modal Analysis (EMA) of the rubber ball was carried out to characterise the modal behaviour of the rubber ball using two different supporting conditions: 'free' and 'a rigid surface contacting the ball. The main measurement equipment was a force hammer (B&K, Type

8202, Serial number: 1231918) and a laser vibrometer (Polytec, PDV1000, Serial number: 0218219). The EMA measurements used five hammer hits at each of the 146 points on the surface of the ball. The Pulse Labshop modal analysis package was used which required a CAD model of the test object surface to identify the excitation and measurement points.

The CAD geometry ignored the seam, hole and serial number plates. 146 points were defined as points including top and bottom crowns, and a point was created between the mid-point of two nodes node as a measurement point where the laser vibrometer measured the velocity normal to the surface. Hence, a total of 147 points were considered in the model. It was not possible to mark the positions on the surface of the ball. Therefore, fine thread with red marker points was used and wound around the ball.

The nodes are shown in Figure 3-9 (a), and (b) where the nodes are indicated by a thread and red points on the strings that indicate the node on the mesh.

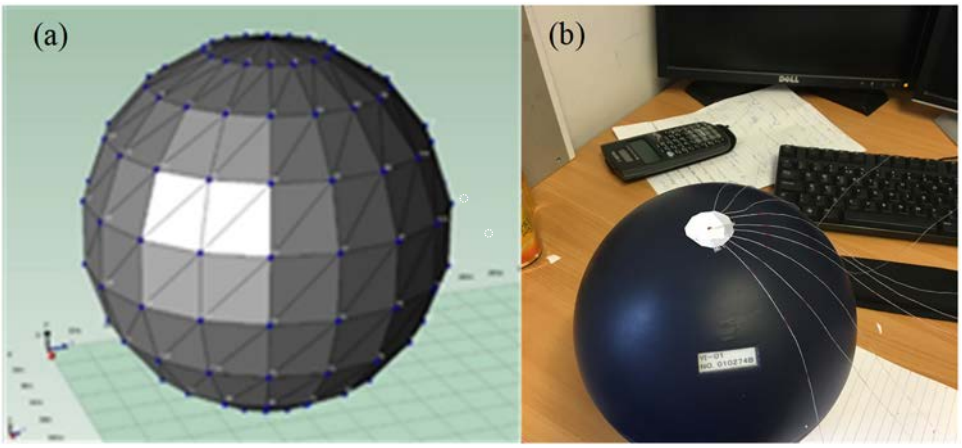

Figure 3-9. (a) CAD model of the rubber ball, (b) Thread used to mark the excitation positions.

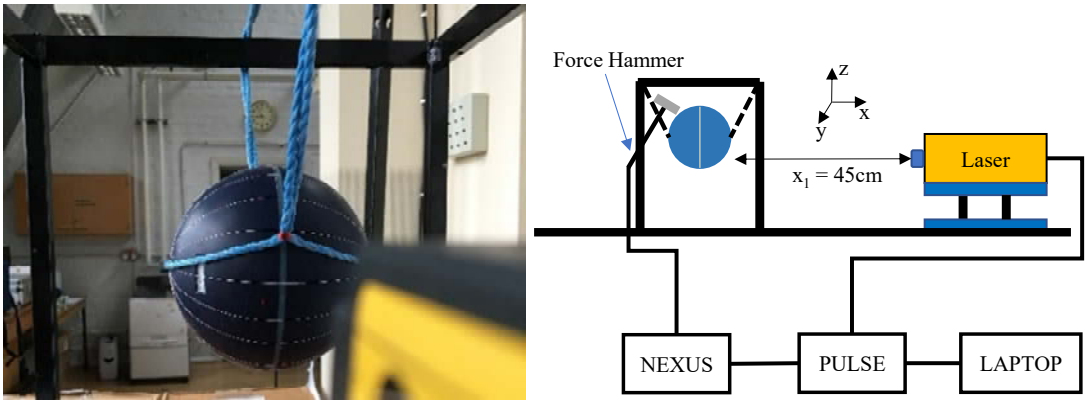

Figure 3-10. Schematic diagram for measurement setup A.

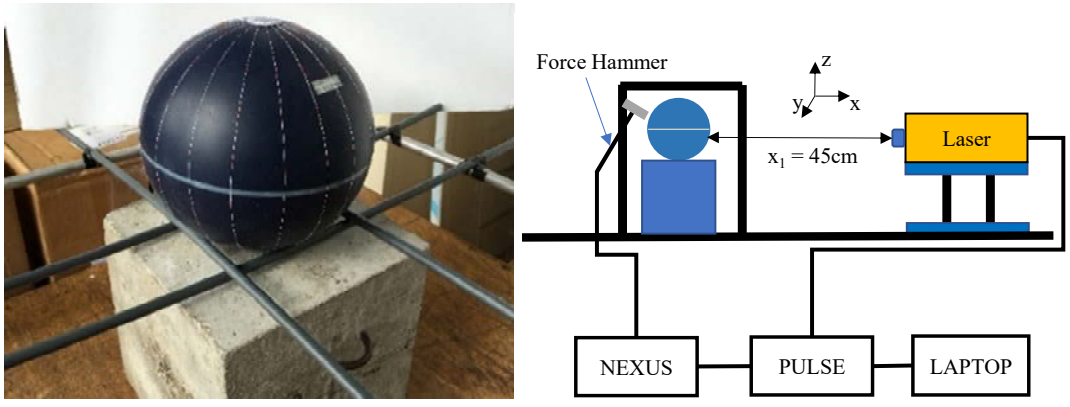

Figure 3-11. Schematic diagram for measurement setup B.

In setup A, the rubber ball is suspended in the air by using rope (see Figure 3-10). The background vibration on the frame was minimised by the green Sylomer underneath the feet of the frame. The laser vibrometer is located at a distance of 45cm from the measurement point on the surface of the rubber ball.

In setup B, the rubber ball is supported on a concrete block (200mm×200mm) (see Figure 3-11). Plastic rods are used to support the rubber ball on the concrete block so that it would not roll off the block.

Figure 3-12 shows the FFT window settings. The upper graph shows the transient window used to eliminate unwanted vibration response/movement of the rubber ball after the hammer hit. The window has a 100ms time shift setting because the trigger of the force hammer also has a delay of 100ms. The leading part of the window is 5ms with a tail edge of 200ms to allow sufficient decay to be captured. The middle graph shows the original input signal, and the lower graph shows the windowed signal.

Figure 3-13 shows an example of the modal parameter estimation using the B&K REFLEX Experimental Modal Analysis package. The curve fit uses the rational fraction polynomial-z method (RFP-Z). The x-axis shows frequencies between 1 to 400 Hz, left y-axis shows the magnitude of the driving-point mobility in log scale, and right y-axis shows the number of iterations. The solid red line shows a frequency response function of the measured node. It can be seen that the peaks and troughs are clear below 400Hz. For the curve fitting, the number of iterations was set as 100, and frequencies between 1 to 400Hz were considered. Stable modes are automatically selected by B&K REFLEX and shown in the figure with four different marks.

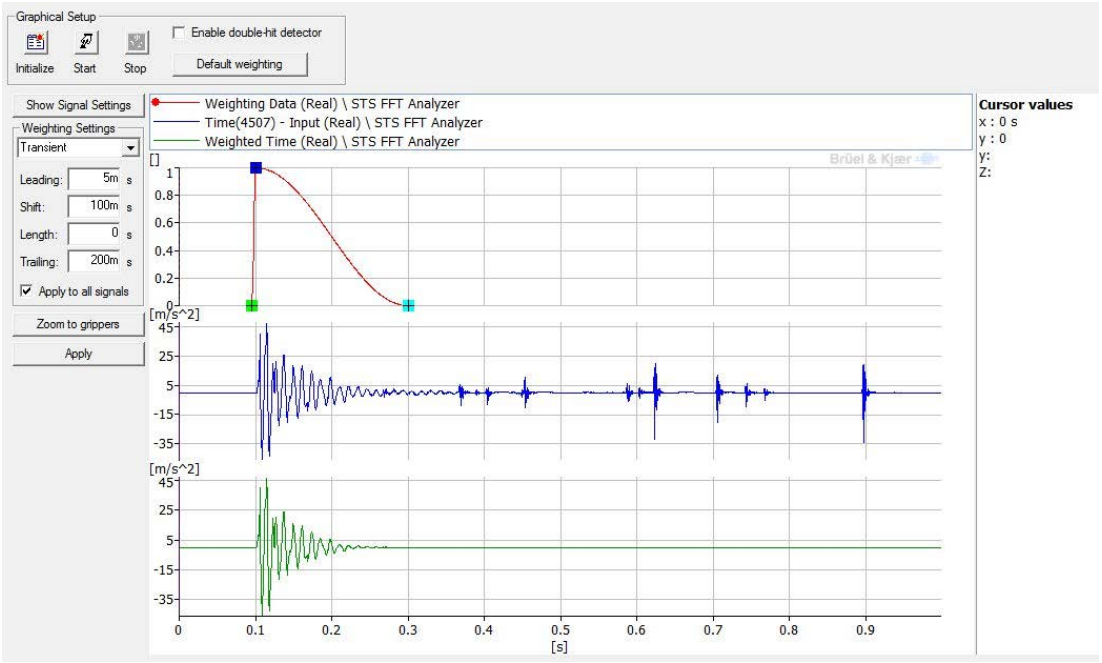

Figure 3-12. Analysis setup and windowing setup on Labshop.

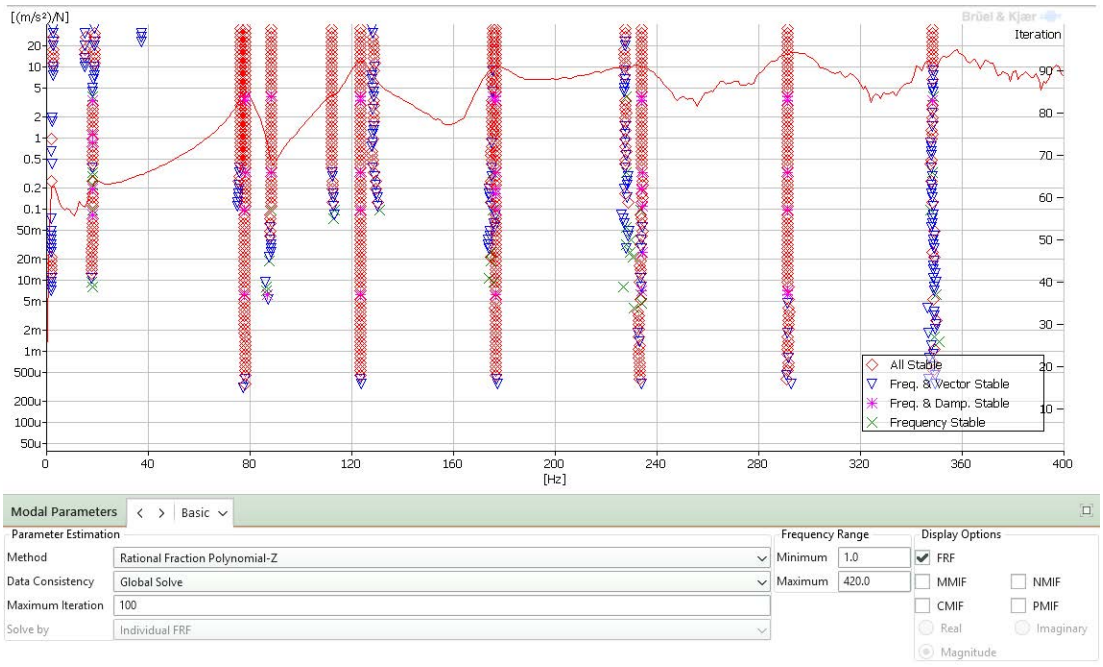

Figure 3-13. Example of the REFLEX analysis screen.

3.5.2 Result and discussion

Table 3.2 shows the measurement conditions during EMA in terms of room temperature, the surface temperature of the rubber ball, and the relative humidity of the room.

Table 3.2. The measured temperature just before the measurement started.

Setup A	**Room**	**Ball**
Temperature (°C)	24.7	25.0
RH (%)	56	----
Setup B	**Room**	**Ball**
Temperature(°C)	21.7	22.2
RH (%)	63	----

Table 3.3 and Table 3.4 show the results from EMA for measurement setups A and B.

Table 3.3. Modes from measurement setup A.

Mode number	**Frequency (Hz)**	**Damping ratio (%)**
1	77.8	3.90
2	123.5	3.54
3	176.5	3.28
4	176.5	3.38
5	232.9	2.78
6	233.7	2.73
7	291.2	2.79
8	291.4	2.76
9	348.7	1.37
10	348.9	1.24

For setup A, the mode numbers 3 and 4, 5 and 6, 7 and 8, and 9 and 10, are duplicate modes at the same frequency, and these modes are considered as degenerate modes (this will be discussed in the theory for spherical shell modes in section 3.6.2).

Table 3.4. Modes from measurement setup B.

Mode number	Frequency (Hz)	Damping ratio (%)
1	76.5	2.09
2	84.9	4.30
3	121.4	2.50
4	130.6	2.38
5	151.2	3.13
6	177.2	2.15
7	287.7	2.19

For Setup B, the mode numbers 1 and 3 are similar to mode numbers 1 and 2 from Setup A. Mode numbers 2 and 4 from Setup B were not observed in Setup A; this indicates that the support condition changes the modes as would occur during an actual impact of the ball on the base floor. The damping ratio for mode 1 is 3.9% and 2.1% in setups A and B respectively. The constraint on the lower surface of the ball in setup B could be the cause of this reduction.

The measured mode shapes are shown in Figure 3-14 and Figure 3-15. The mode shapes are exported from B&K Reflex using the "Analysis Validation" option. From EMA and driving-point mobility data, the lowest mode frequency of the rubber ball was identified as 78Hz which will be used to estimate the Young's modulus of the rubber in section 3.7.

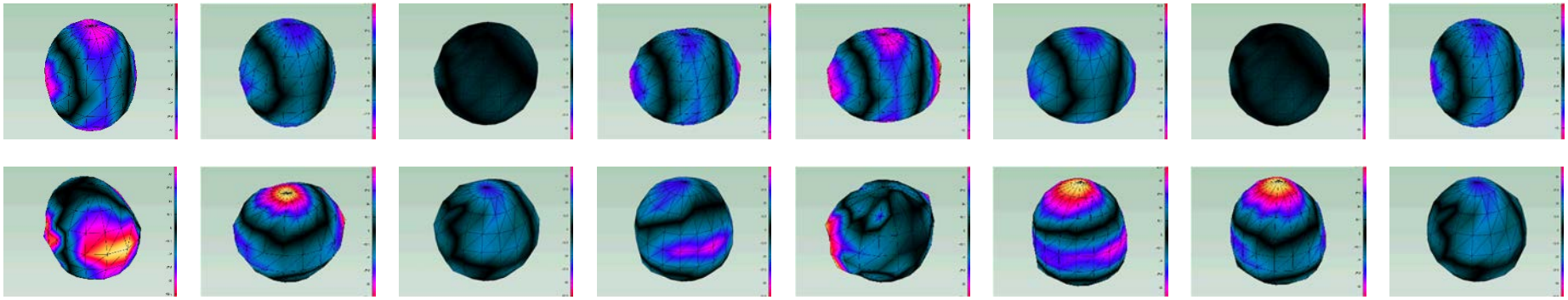

Figure 3-14. Mode shape of the first mode of the rubber ball from EMA (still images taken from the animation). Setup A (upper row) and Setup B (lower row).

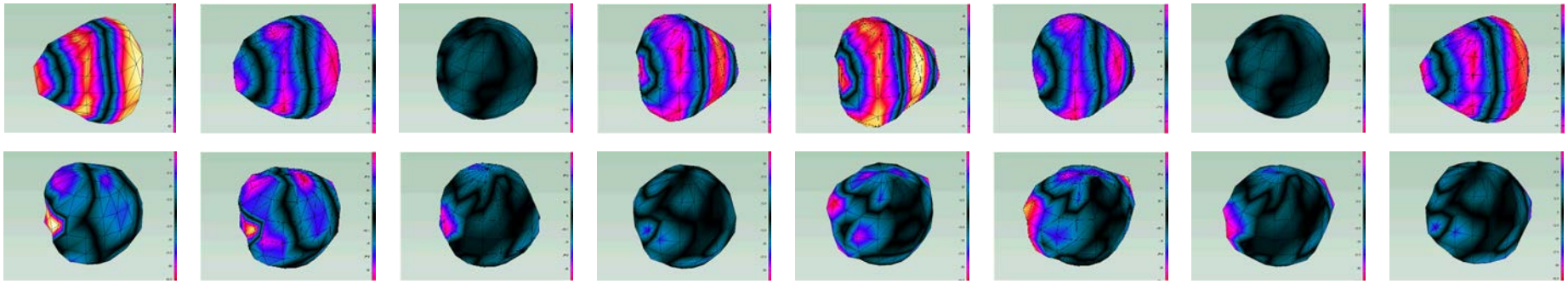

Figure 3-15. Mode shape of the second mode of the rubber ball from EMA (still images taken from the animation). Setup A (upper row) and Setup B (lower row).

3.6 Analytical model for the mode frequency of a thin spherical shell

3.6.1 Introduction

This section introduces the analytical model to estimate eigenfrequencies of the thin spherical shell which can be used to estimate Young's modulus of the rubber ball in conjunction with the experimentally determined result of the lowest mode frequency.

3.6.2 Analytical model for the mode frequencies of a thin spherical shell

The problem of free vibration of a spherical shell was first examined by Lamb [91] and subsequently studied by Baker [92]. Baker studied the behaviour of the axisymmetric spherical modes by deriving membrane theory. The radial-tangential modes of the spherical shell are derived in terms of Legendre polynomial of positive integer n with Laplace transform techniques. A consequence of the Legendre polynomial is that there are two distinct frequencies for each n. The branch b_n is the lower spectrum, and a_n is the higher spectrum. Figure 3-16 shows three lower spectrum modes that corresponds to the breathing mode (n=2), triangular mode (n=3), and rectangular mode (n =4). The first frequency (n =1) of the higher spectrum occurs well above other mode frequencies corresponds to the mode frequencies from b_n branch.

All natural frequencies of the spherical shell can be described as [92]

$$a_n = \sqrt{\frac{X_{a^2 n}}{A}} \tag{3.5}$$

$$b_n = \sqrt{\frac{X_{b^2 n}}{A}} \tag{3.6}$$

where a_n and b_n are higher and lower branch frequencies respectively, coefficient A is expressed in terms of the material properties of a spherical shell

$$A = \rho R^2 \left[\frac{(1-\nu^2)}{E}\right] \tag{3.7}$$

where R is the radius of the spherical shell from origin to mid-surface, ρ is density of spherical shell, and X_n are solutions of Legendre polynomial [92]

$$X_{a^2n} = \frac{1}{2}[n(n+1)+1+3\nu] + \{[n(n+1)+1+3\nu]^2 - 4(1-\nu^2)[n(n+1)-2]\}^{\frac{1}{2}} \tag{3.8}$$

$$X_{b^2n} = \frac{1}{2}[n(n+1)+1+3\nu] - \{[n(n+1)+1+3\nu]^2 - 4(1-\nu^2)[n(n+1)-2]\}^{\frac{1}{2}} \tag{3.9}$$

where n is an integer number $n = 0,1,2\ldots n+1$.

The higher branch Eq. (3.8) increases without limit as n increases, but the lower branch Eq. (3.9) rapidly reaches a limit which can be calculated using [92]

$$f_{\text{limit}} = \frac{1}{\sqrt{2}}\sqrt{\frac{E}{\rho R^2}} \tag{3.10}$$

Silbiger [93] noted that Baker did not consider non-axisymmetric modes which correspond to the axisymmetric mode at identical frequencies but are degenerate due to the spherical symmetry of the shell. Because of symmetry, the shell can vibrate in similar modes with similar or identical natural frequency independently with a different orientation of the axis. Because of degeneracy, Baker's notation can only extract one mode from $2n+1$ linearly independent modes.

Kalnin [94] claimed that membrane theory has limited applicability, and the theory is accurate only for very thin shells and for low mode numbers. Hence, a higher error can be expected if this theory is applied to a relatively higher thickness to radius ratio.

The analytical and the measured eigenfrequencies of a thin-steel spherical shell have been compared at Los Alamos National Laboratory by Robertson *et al.* [95]. These were within 1% difference up to the fourth mode. A comparison of the analytical approach and FEM simulation is published as a benchmark guide on the ABAQUS website [96] which were within a 5% difference up to the fourth mode.

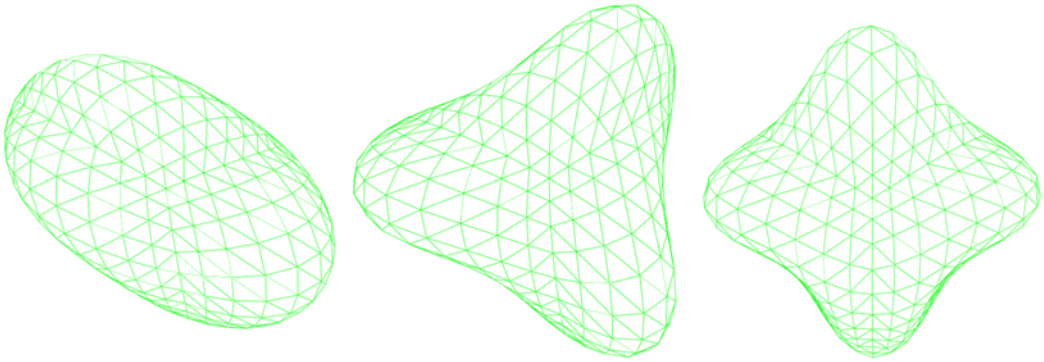

Figure 3-16. First (left), second (centre) and third (right) modes of a thin spherical shell.

3.7 Material properties of the rubber ball

3.7.1 Introduction

The parameters needed to model the rubber ball in FEM are not published by the manufacturer or stated in the standards. Hence this section aims to estimate the spring constant and Young's modulus from the experimentally determined lowest mode frequency of the rubber ball, 78Hz.

3.7.2 Poisson's ratio

The manufacturer or standards do not state the Poisson's ratio. Other researchers have assumed the Poisson's ratio is 0.5 based on literature [87]. According to the literature, the Poisson's ratio for silicone rubber is normally 0.48 to 0.49 [97]. In this thesis, the Poisson's ratio is assumed to be 0.48 for the calculations.

3.7.3 Young's modulus of the rubber ball

The Young's modulus of the rubber ball was reported in references as approximately 1.6×10^6 N/m^2 to 1.65×10^6 N/m^2 [85–87]. The Young's modulus can also be estimated from the experimental results (See sections 3.4, 3.5 and 3.7.3). The lowest mode frequency of the rubber ball is found by rearranging Eq. (3.6) to give

$$E = \rho R^2(1-\nu^2)\left(\frac{b_n^2}{X_{\mathrm{bn}}}\right) \tag{3.11}$$

where the density of the rubber ball is

$$\rho = \left(\frac{4}{3}\pi R^3\right) - \left(\frac{4}{3}\pi(R-h)^3\right) \tag{3.12}$$

The Young's modulus is estimated using (3.11) and (3.12) to be 3.2×10^6 N/m^2 which is almost twice the reported value from Schoenwald *et al.* [85–87]. This difference could be due to the general silicone rubber Young's modulus taken from the literature [98] and the estimation from the experiments. Hence, the estimated value from the experiments will be incorporated into the FEM model of the ball and compared with the experimental data.

3.8 Finite element model of the rubber ball

In this section, two FEM models were created for the rubber ball. Firstly, a model for the rubber ball falling from 1m height onto a concrete floor that is sufficiently low mobility to give the blocked force. Secondly, eigenfrequency analysis for the isolated rubber ball.

3.8.1 Blocked force

The first analysis determined the force spectrum using a FEM model of the concrete floor and rubber ball to obtain the time-domain contact force upon contact with the concrete floor.

Gravity was assigned as the initial condition on the rubber ball to simulate the free fall of the rubber ball from 1m height onto the concrete floor. The general 'Hard' contact relationship was used for the rubber ball and the concrete floor. The concrete floor has simply supported boundaries around its perimeter. The constraint between the concrete floor and the room below excitation was created using ABAQUS 'tie' constraints.

The total loss factor of the floor was modelled with Rayleigh damping to approximate a fully connected floor. The constant damping ratio of the concrete was estimated from the TLF [24]

$$\zeta = \frac{\eta_i}{2} \tag{3.13}$$

The Rayleigh damping that is required as input for the FEM model is determined by solving the simultaneous equation for α and β given by [99]

$$\zeta = \frac{\alpha}{2\omega} + \frac{\omega\beta}{2} \tag{3.14}$$

where α is mass proportional damping and β is stiffness proportional damping. And the relationship between η_i and η_{ii} for a fully connected concrete floor is given by Eq. (2.17)

The material properties for the FEM model are given in Table 3.5. The Young's modulus of concrete is taken from [100], Poisson's ratio of the concrete was set to 0.16 as the indicated range was 0.1-0.2 [101] and Rayleigh damping was calculated with Eq.(3.14) with TLF using Eq.(2.19) assuming ILF=0.005 and X=0.3.

Table 3.5. Material properties estimated from analytical sphere model.

	Young's Modulus (N/m^2)	**Poisson's Ratio**	**Density (kg/m^3)**	**Rayleigh Damping**
Rubber (Ball)	3.2×10^6	0.48	1188	N/A
Concrete (Floor)	31×10^9	0.16	2200	α=14.5489 $\beta=3.55\times10^{-6}$

Figure 3-17 allows comparison of measurement with two FEM simulations of the force spectra. The first simulation uses Young's modulus determined in section 3.7.3. The second simulation uses Young's modulus that is optimised to give closer agreement with the measurement and the values in JIS A 1418-2:2000.

The problem of the force starting at non-zero value at t=0s did not occur in the FEM simulation. This is because energy transfer during contact was correctly simulated with many mass-spring-damper systems in FEM.

Comparing the force-time curve with the measurement, the simulation with the original Young's modulus shows 15% smaller peak force and 5% shorter force duration. The simulation with optimised Young's modulus shows 10% smaller peak force and 7% shorter force duration.

For the single event level, the simulation with the estimated Young's modulus determined from the measurements is 1dB lower and 0.5dB lower than the limit shown in JIS A 1418-2:2000 at 31.5Hz and 125Hz respectively. However, the simulation with

optimised Young's modulus of 3.4×10^6 N/m^2 is within the lower and upper limit shown in JIS A 1418-2:2000. Hence, the optimised value gives a better estimate of Young's modulus and indicates that the value quoted by Schoenwald *et al.* [85–87]. is likely to be in error. Therefore, Young's modulus of 3.4×10^6 N/m^2 is used as input data for the FEM simulation.

Table 3.6. Optimised material properties of the rubber ball.

Optimised	**Young's Modulus (N/m^2)**	**Poisson's Ratio**	**Density (kg/m^3)**	**Rayleigh Damping**
Rubber	3.4×10^6	0.48	1188	N/A

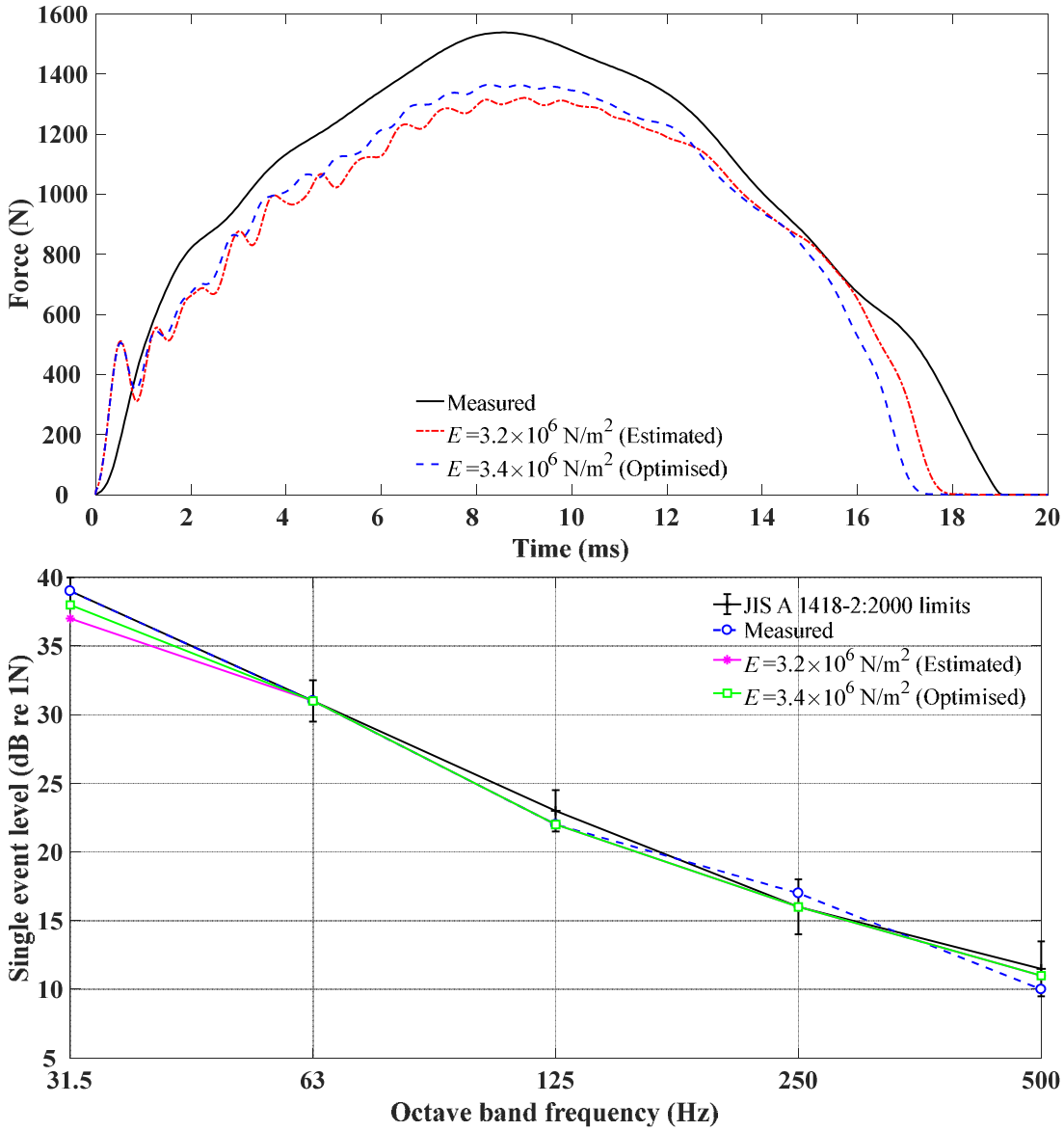

Figure 3-17. Comparison of the force spectra from measurement with two different FEM simulations in the time domain (upper) and the single event level in octave bands (lower).

3.8.2 Mode shape and eigenfrequency of the rubber ball

The second analysis carried out for validation of the eigenfrequency of the rubber ball uses estimated and optimised parameters shown in Table 3.5 and Table 3.6. The expected eigenfrequencies are compared with the analytical calculations using Eq. (3.6) and the mode shapes are compared with the EMA results. Table 3.7 summarises the eigenfrequency values estimated with the analytical model and extracted value from the ABAQUS. The eigenfrequency of the spherical shell has $2n+1$ modes for each value of n. This indicates that at least 16 eigenvalues are required to determine the modes up to n=3. It is not necessary to show every iteration as mode shapes are the same. Therefore, the eigenfrequency is rounded, and one mode shape is extracted.

Table 3.7. Eigenfrequency comparison between the analytical model and FEM result.

Analytical Eigenfrequency (Hz)	79	-	-	-
E=3.2×10^6 (N/m^2) Eigenfrequency (Hz)	89	131	138	195
E=3.2×10^6 (N/m^2) Mode shape	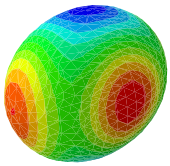	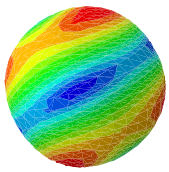	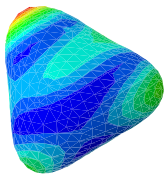	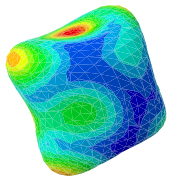
Analytical Eigenfrequency (Hz)	81	-	-	-
E=3.4×10^6 (N/m^2) Eigenfrequency (Hz)	91	135	144	201
E=3.4×10^6 (N/m^2) Mode shape	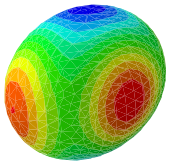	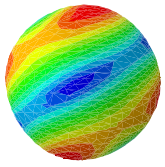	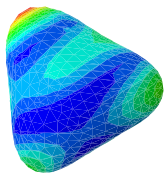	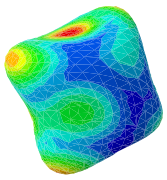

The lowest mode (breathing) frequency from EMA is at 78Hz (see Table 3.3), and the eigenfrequency estimated from the analytical model is at 81Hz. These are within a 5% difference in terms of frequency. However, the eigenfrequency using FEM eigenfrequency extraction is at 89Hz for Young's modulus of E=3.2×10^{6}N/m^2, and 91Hz for Young's modulus of E=3.4×10^{6}N/m^2. The difference between FEM and analytical or

EMA is approximately 10%. The breathing mode was evident in both EMA (see Figure 3-14) and FEM.

The second mode at 131Hz from the FEM eigenfrequency extraction was the torsional mode, and this was not observed in the EMA, and the analytical model does not give this eigenfrequency. The second mode (triangular mode) is at 123.5Hz from the EMA (see Figure 3-15). This mode is not to predicted by the analytical model since its limit frequency Eq. (3.10) is at 115Hz. The triangular shape was obtained at 138Hz from FEM eigenfrequency extraction. The difference between EMA and FEM is approximately 10%. The third mode (square mode) was not observed in the EMA and was not predicted by the analytical model.

For the first and second modes, the mode shapes obtained from the EMA matched with the eigenfrequency analysis from the FEM. However, the mode frequencies obtained from EMA do not match the analytical model or FEM eigenfrequency analysis. For this reason, the investigation for the use of ABAQUS eigenfrequency analysis for the thin-shell sphere has been carried out with 10 different thickness to radius ratios; 0.01, 0.02, 0.033, 0.05, 0.06, 0.1, 0.2, 0.33, 0.5, 1 to observe the change in eigenfrequency due to the change in the thickness. This test is based on the ABAQUS benchmark manual; their validation has been done with a hollow aluminium sphere of the ratio of the radius to shell thickness of 0.001. The parameter of the aluminium sphere is shown in Table 3.8, and the result of the analysis is summarised in Table 3.9. At h/R = 0.33, which is the closest ratio to the thickness to radius ratio of the rubber ball (rubber ball has h/R=0.34), the difference in the fundamental eigenfrequency from analytical solution and FEM was approximately 10%. This is close to the difference observed in the difference between EMA (and the analytical model) and FEM.

For the eigenfrequency analysis to estimate the lowest eigenfrequency, there was an approximately 10% difference between analytical and the measured results. Hence, ten case studies were used to investigate ten different thickness to radius ratios. The ten case studies suggest that FEM result vary depending on the thickness of the sphere shell to the radius ratio. For the h/R=0.333 (closest to the thickness to radius ratio of the rubber ball h/R=0.34), approximately 10% difference was shown. Hence, the 10% difference in the lowest eigenfrequency between the driving-point mobility, EMA and FEM can be considered to be reasonable.

Table 3.8. Material properties of the aluminium sphere.

	Young's Modulus (N/m^2)	**Poisson's ratio**	**Density (kg/m^3)**
Sphere	1.8×10^{11}	0.333	7670

Table 3.9. Eigenfrequency from the analytical model.

	Mode 1 (Hz)	**Mode 2 (Hz)**	**Mode 3 (Hz)**	**Mode 4 (Hz)**
Analytical	187	223	237	243
***h*/*R*=0.01**	190	230	233	250
***h*/*R*=0.02**	190	231	234	253
***h*/*R*=0.033**	191	233	235	256
***h*/*R*=0.05**	191	235	237	262
***h*/*R*=0.06**	191	237	240	269
***h*/*R*=0.1**	192	244	246	288
***h*/*R*=0.2**	197	271	273	319
***h*/*R*=0.33**	207	310	312	320
***h*/*R*=0.5**	219	321	348	351
***h*/*R*=1**	245	320	404	408

3.9 Summary

This chapter investigated the structural dynamics of the rubber ball and the rubber ball impact upon the concrete floor/block. The specification of the rubber ball from the manufacturer, JIS A 1418-2:2000 and ISO 10140-5:2010 were compared; this indicated minor differences in the diameter of the ball.

The blocked force due to the rubber ball drop from a 1m height was measured on the force plate and compared with a prediction based on the SDOF mass-spring-damper system using Simulink. The Simulink model could predict the peak force and duration of impact in the time domain within the limitations shown in the standard, but there was a positive force at t=0s. This was due to the SDOF system that only assume single mass, spring, damper, and constant spring stiffness, and damping coefficient. Hence, it cannot simulate the actual complexity of the actual contact. The predicted single event level only fell within the allowed limits given in JIS A 1418-2:2000 31.5 and 63Hz octave bands. This indicates that the rubber ball cannot be considered as a simple

mass-spring-damper system, and it is likely that the modal response of the ball needs to be considered to give better agreement up to the 500Hz band.

The driving-point mobility measurement was performed using an impedance head and electrodynamic shaker to estimate the eigenfrequencies of the rubber ball. This showed that the lowest eigenfrequency was 75 to 76Hz, and the second eigenfrequency occurred between 116 and 117Hz.

To validate the lowest predicted eigenfrequency of the rubber ball against mobility measurements, EMA was also performed to determine the eigenfrequency, and visualisation of the mode shape of the rubber ball with two conditions; (a) isolated, and (b) in contact with a concrete block. The measured fundamental frequency from EMA was 78Hz and 76.5Hz for (a) and (b) respectively, and the second mode was at 124Hz and 84.9Hz for (a) and (b) respectively. This indicates that the contact condition changed the eigenfrequencies above the lowest mode. EMA indicated breathing mode shape at the lowest eigenfrequency and a triangular shape at the second eigenfrequency.

The analytical model of the thin spherical shell was introduced and used to estimate Young's modulus from the lowest eigenfrequency. Young's modulus was obtained from the lowest eigenfrequency, but the value was twice as high as the reported value. The analytical model suggested that the eigenmode shapes of the thin spherical shell are breathing, triangle and square. This matched the EMA results. The analytical model has a limitation on the maximum eigenfrequency that can be calculated. For the rubber ball, this limit was 115Hz. Hence, according to the driving-point mobility and EMA results, only the fundamental mode can be obtained from the analytical model.

The rubber ball drop from 1m onto a rigid concrete block was simulated in FEM using the estimated Young's modulus determined from EMA. In comparison with the SDOF mass-spring-damper model, FEM successfully modelled the blocked force with the force-time curve starting from 0N at 0s. However, the single event level did not meet the limit values given in JIS A 1418-2:2000 for the 31.5Hz octave band when using Young's modulus estimated from EMA although it correctly obtained the single event level above the 31.5Hz octave band. For this reason, Young's modulus was optimised to E=3.4×10^6 N/m^2 to satisfy the limit values in JIS A 1418-2:2000 from 31.5 to 500Hz in octave bands.

After optimisation of Young's modulus, the single event level successfully met the requirement in JIS-1418-2:2000. This optimised Young's modulus will be used in FEM simulations later in this thesis.

4. STRUCTURAL DYNAMICS OF THE RUBBER BALL AND LOCALLY REACTING MASS-SPRING-SYSTEMS

4.1 Introduction

This chapter focuses on the structural dynamics of the rubber ball when impacting locally reacting mass-spring systems on a concrete floor/block.

Section 4.2 introduces the concept of the locally reacting mass-spring-damper system as a highly idealised version of the floating floor. Section 4.3 introduces the measurement of the dynamic stiffness of locally reacting mass-spring systems. Section 4.4 discusses measurement of the blocked force of the rubber ball with locally reacting mass-spring systems for comparison with a two degrees-of-freedom (TDOF) model of the mass-spring-damper system using MATLAB Simulink.

4.2 Locally reacting mass-spring systems

Locally reacting mass-spring systems are introduced in order to represent a highly idealised version of a floating floor. Their small size enables the blocked force due to the combination of the rubber ball and floating floor to be measured on the force plate described in section 3.3.1. Each mass-spring system comprises a 20mm thick steel plate (200mm × 200mm) on top of a different resilient material shown in Figure 4-1.

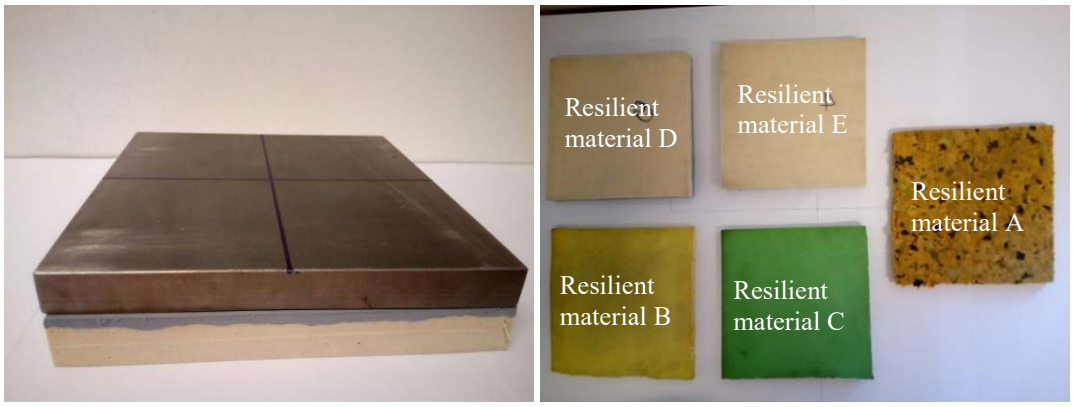

Figure 4-1. Resilient material and steel plate (locally reacting mass-spring systems) (left), and tested materials (A, B, C, D and E) (right).

The locally reacting mass-spring system was mounted on the top of the force plate to measure the blocked force as shown in Figure 4-2.

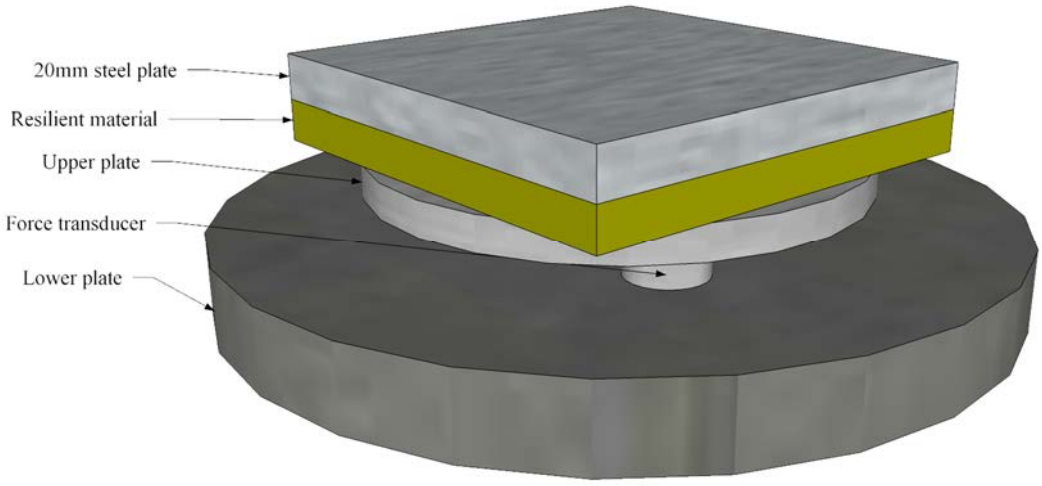

Figure 4-2. Force plate with a locally reacting mass-spring system.

4.3 Dynamic stiffness of the resilient materials used in the locally reacting mass-spring systems

The dynamic stiffness of the resilient materials is determined using the general approach described in BS EN 29052-1:1992 (ISO9052-1:1992) [102]. The standard recommends measuring the mass-spring resonance frequency of the load plate on a resilient material by using either sinusoidal, white noise or pulse signals and the resonance frequency determined by extrapolating to find the resonance frequency at 0N.

However, the maximum blocked force from the rubber ball is approximately 1500N. Due to this large force, it is possible that the dynamic stiffness at 0N would not be appropriate. In order to investigate the behaviour of the resilient material and its dynamic stiffness, two different approaches were used: (Approach 1) using a large force hammer to apply a peak force of 1500N±50N that is similar to the peak force applied by the rubber ball. (Approach 2) using a small and large force hammer to apply peak forces from 40N to 3000N.

The measurement requires a rectangular load plate with a dimension of (200±3) mm × (200±3) mm and total load weight of 8±0.5 kg. The specimen is placed between a base plate and the load plate. The inertia of the base plate is such that its velocity is negligible compared with that of the load plate. The schematic diagram is shown in Figure 4-3.

The square steel load plate is made for the inertial shaker measurement assuming extra mass from the inertial shaker (≈1.5kg). Therefore, the steel plate itself weighs 6.2kg.

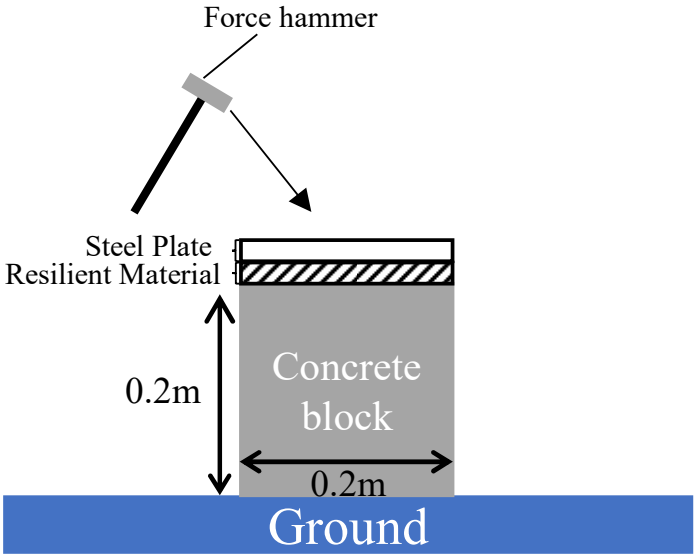

Figure 4-3. Schematic diagram of the dynamic stiffness measurement.

The driving-point mobility is measured to determine the mass-spring resonance frequency, f_r, and hence the dynamic stiffness [102].

$$s' = 4\pi^2 f_r^2 \rho_s \tag{4.1}$$

where ρ_s is the mass per unit area of the load plate

The estimation of ILF with 3dB down points tends to give a higher value when the driving-point magnitude peak has a wide peak and lower value with a sharp peak. If two peaks exist close to each other, there could potentially be an error in the estimation of ILF.

4.3.1 Result and discussion

Figure 4-4 shows the measured driving-point mobility magnitude using a large force hammer hit with 1500N (Approach 1). This has been used to estimate the ILF of the resilient materials. Table 4.1 summarises the detail of the resilient materials using a large force hammer hit with 1500N.

Table 4.1. Dynamic stiffness and loss factor of the mass-spring resonance frequency with a 1500N force from the large force hammer.

		Locally reacting mass-spring system			
	Name of locally reacting mass-spring systems	**Sample thickness (mm)**	**Dynamic stiffness per unit area (MN/m^3)**	**ILF (-)**	**Mass-spring frequency (Hz)**
A	Recycled foam	10	5.5	0.27	30
B	Yellow sylomer	15	23.5	0.37	62
C	Green sylomer	15	32.6	0.32	73
D	EPS (1)	20	41.1	0.62	82
E	EPS (2)	25	100.2	0.41	128

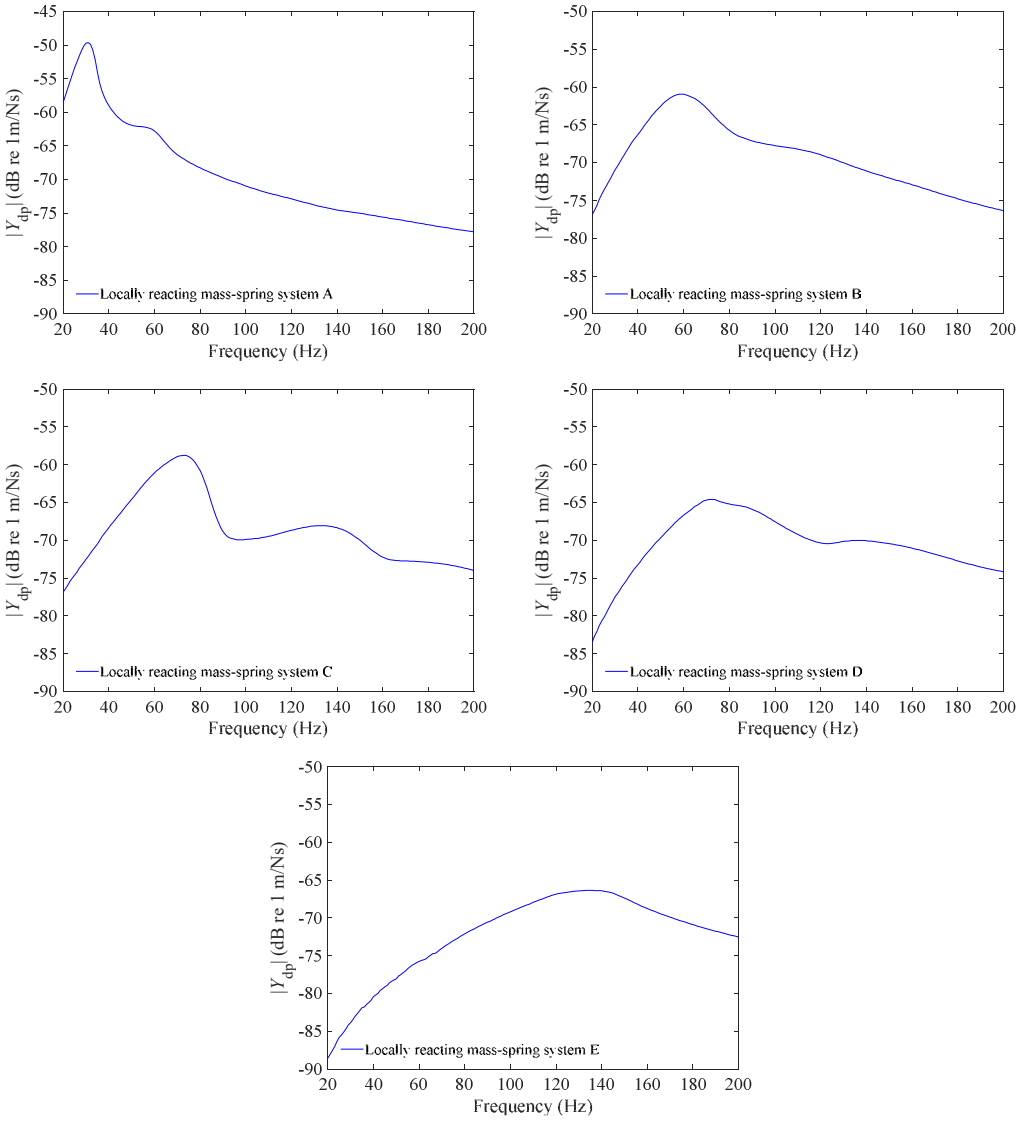

Figure 4-4. Measured magnitude of driving-point mobility for the locally reacting mass-spring systems with a 1500N force from the large force hammer.

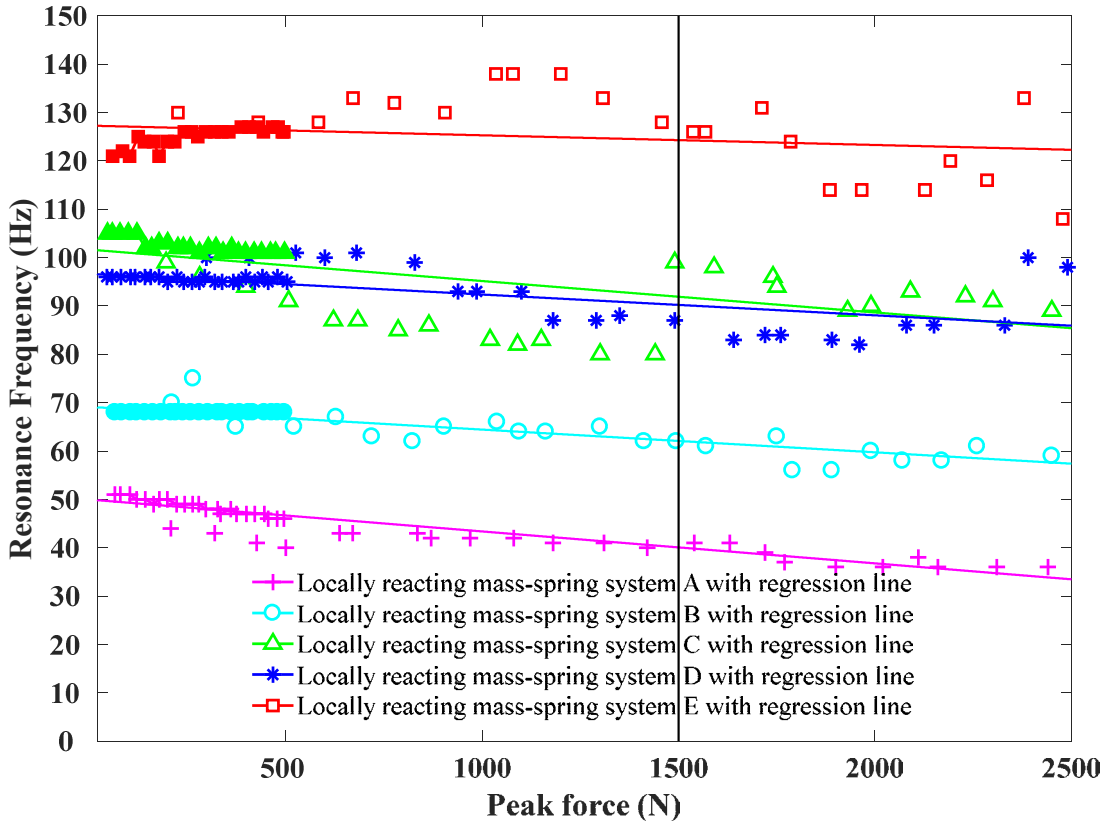

Figure 4-5. Mass-spring resonance frequencies with different applied force.

Figure 4-5 shows the resonance frequencies of the resilient materials using the small force and the large force hammer with different peak forces (Approach 2). The small force hammer was used to apply a force from 40N to 500N in 20N intervals, and the large force hammer was used to apply a force from 200N to 2500N in 100N intervals. For both cases, it is difficult to apply exactly the same force with different hammer hits. Hence, ±10N and ±50N were considered as a tolerance limit for the small force hammer and large force hammer respectively. Those values are obtained from Pulse Labshop using the FRF, H1, with $i\omega$ weighting on the acceleration signal to give velocity (see Eq.(2.61)). The regression line from 40N to 2500N is shown as a solid line for each mass-spring material. The results indicate that using a small hammer up to 500N gives similar results with differences within 5Hz for all resilient materials. However, use of the large hammer could cause a significant difference (resilient material C and D). The resonance frequency is similar for small and large force hammers for resilient materials B and E. However, there is an approximately 5Hz discontinuity between small and large force hammer results at 500N for the resilient materials A, C, and D. This suggests that there is some interaction between the hammer and the mass-spring system.

From this measurement, it is possible to rank order the resilient materials from relatively hard to relatively soft.

Table 4.2 shows the mass-spring frequency of the locally reacting mass-spring systems at 1500N determined from a regression line through all force data points up to 2500N of Figure 4-5.

Table 4.2. Mass-spring resonance frequency of the locally reacting mass-spring systems at 1500N.

Mass-spring frequency (Hz)	**A**	**B**	**C**	**D**	**E**
	40.1	62.1	90.2	111.4	124.3

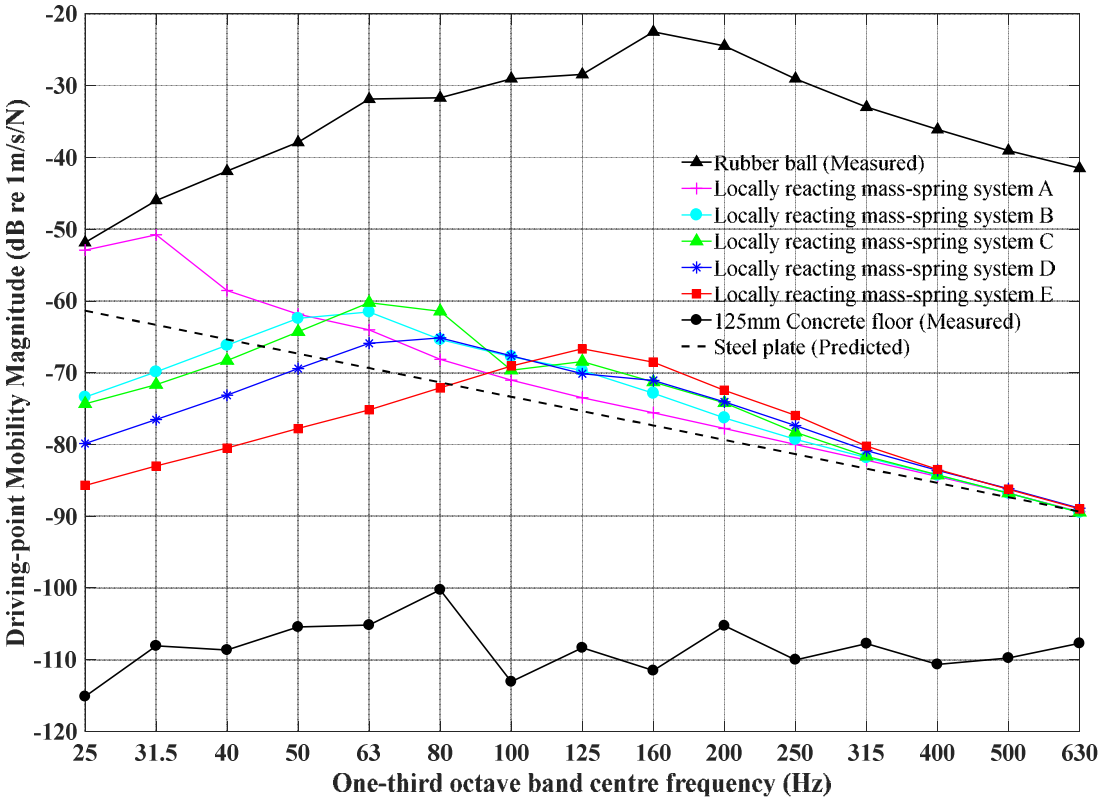

Figure 4-6. Driving-point mobility (magnitude) of the rubber ball, locally reacting mass-spring systems and 125mm concrete floor.

Figure 4-6 shows measured driving-point mobilities of the rubber ball, mass-spring systems (with excitation on the steel plate) and the 125 mm concrete floor. This confirms that the rubber ball has significantly higher mobility than the concrete floor and locally mass-spring systems; hence in this case considering a blocked force to determine the transient power is reasonable. For the mass-spring systems, the peaks in the

driving-point mobilities correspond to the mass-spring resonances calculated from the measured dynamic stiffness. As these mobilities tend to be at least 20dB higher than the concrete floor, it is also reasonable to consider blocked forces.

4.4 Blocked force measurement using a force plate

4.4.1 Introduction

For the measurement details on the force plate, refer to section 3.3.1.

4.4.2 Result and discussion

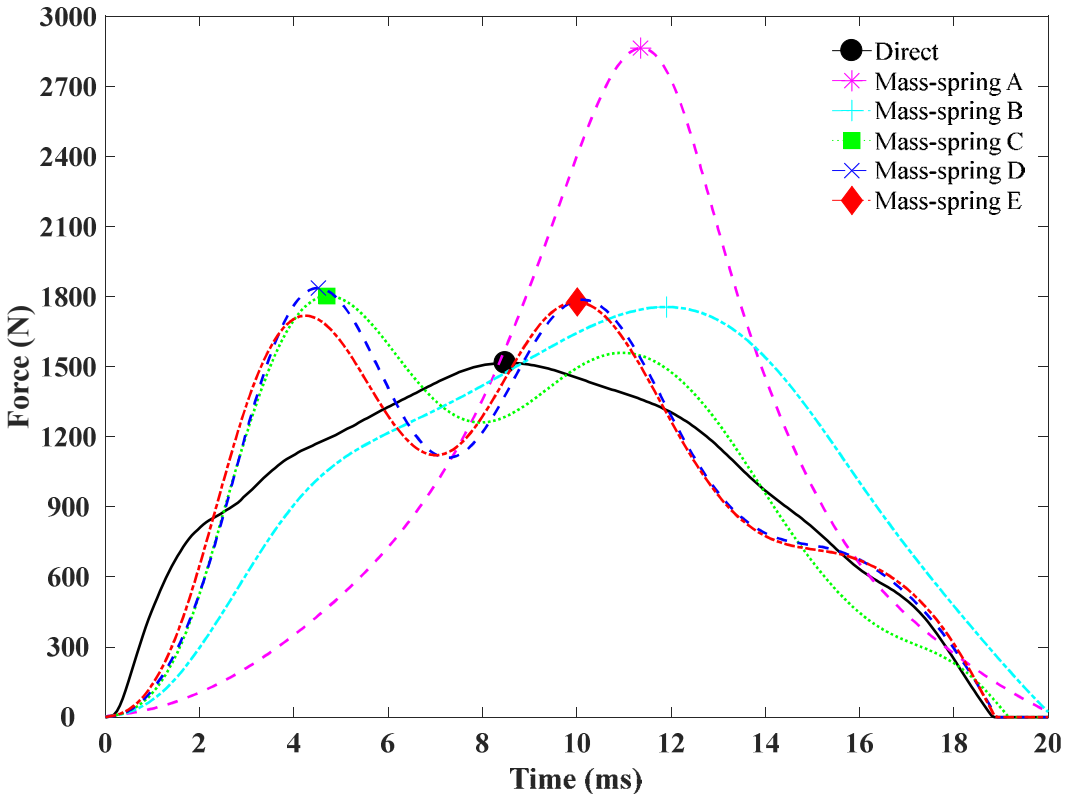

Figure 4-7. The force spectrum in the time domain from the locally reacting mass-spring systems. The marker indicates the peak force in the time domain force plate measurement for the rubber ball directly dropping onto the force plate and on different locally reacting mass-spring systems.

Figure 4-7 shows the measured force in the time domain with locally reacting mass-spring systems. This indicates that the dynamic stiffness of the locally reacting mass-spring systems does not significantly alter the duration, but the shape of the force-time curve is significantly altered. For the mass-spring systems with resilient materials A and B, the measured force had a single peak in the time domain but compared to the direct measurement the shape of the rising curve is significantly altered, the peak force

is significantly increased and the time at which the peak force occurs is increased. For the mass-spring systems with resilient materials C to E, the measured force has a double peak, and the peak force is higher (≈200 N) than the direct measurement but not as high as with material A.

For the locally reacting mass-spring systems which have a single peak, the peak occurred at 10.5ms and 2805N for mass-spring A, and 11.5ms and 1675N for mass-spring B. For the locally reacting mass-spring systems which have double peaks, the first peak occurs at 4.5ms and 1772N and the second peak occurs at 10.7ms and 1474N for mass-spring C, the first peak of 4.3ms and 1812N, and second peak of 9.9ms and 1711N for mass-spring D, and the first peak of 4.1ms and 1694N and the second peak of 9.8ms and 1703N for mass-spring E.

The force versus time curves shown in Figure 4-7 indicate that the resilient materials can be considered in two groups: Group 1 (resilient materials A and B) where there is a single peak, and mass-spring systems have a mass-spring resonance frequency below the fundamental mode frequency of the rubber ball, and Group 2 (resilient materials C, D and E) where there is a double peak and mass-spring systems have a mass-spring resonance frequency above the fundamental mode frequency of the rubber ball.

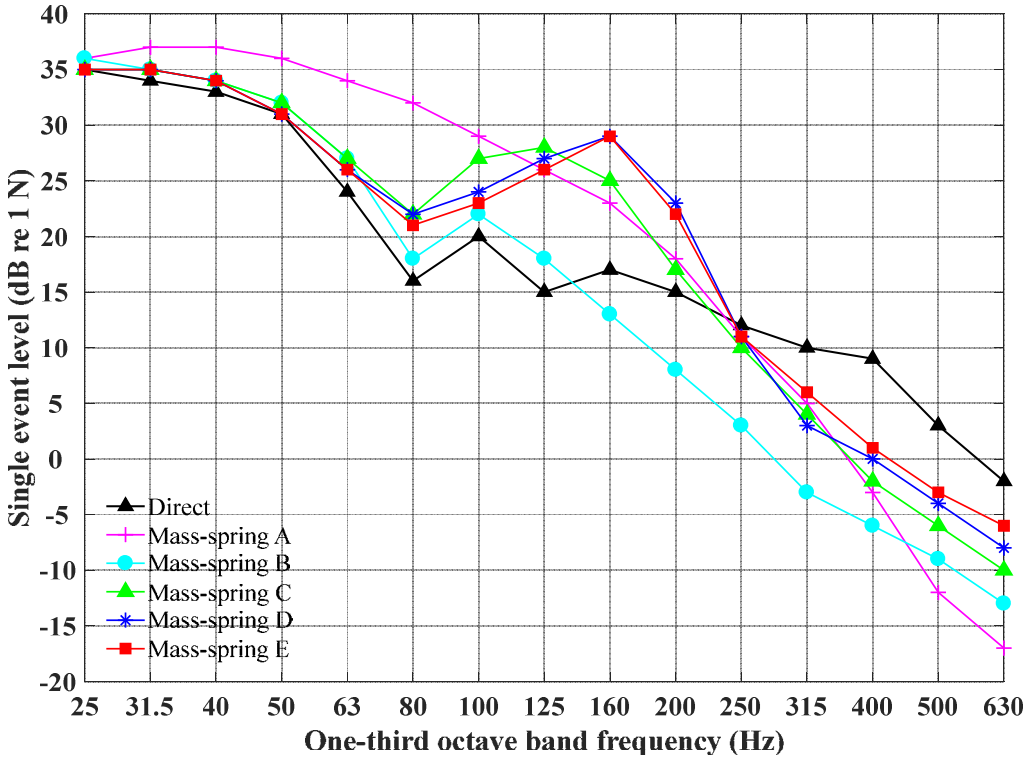

Figure 4-8. Comparison of the single event level with and without a locally reacting mass-spring system.

Figure 4-8 shows the single event level with and without the locally reacting mass-spring systems. Comparing force plate measurements in the frequency domain from the rubber ball directly onto the force plate and on different mass-spring systems in the vicinity of the locally reacting mass-spring system resonance frequency, the force for these systems tends to be higher than the direct force below 250Hz one-third octave band. For mass-spring systems B to E, the first dip of the single event level occurs in the 80Hz one-third octave band. The single event level is starting to rise at 100 to 160Hz one-third octave bands, then the single event level started to reduce significantly. This is possibly due to the effect of the mass-spring resonance frequency of the locally reacting mass-spring systems.

4.4.3 Two-degree-of-freedom mass-spring-damper system

This section introduces the two-degree-of-freedom (TDOF) mass-spring-damper system to model the force from the rubber ball falling on a mass-spring system.

The TDOF mass-spring-damper system can describe the rubber ball falling freely onto a locally reacting mass-spring.

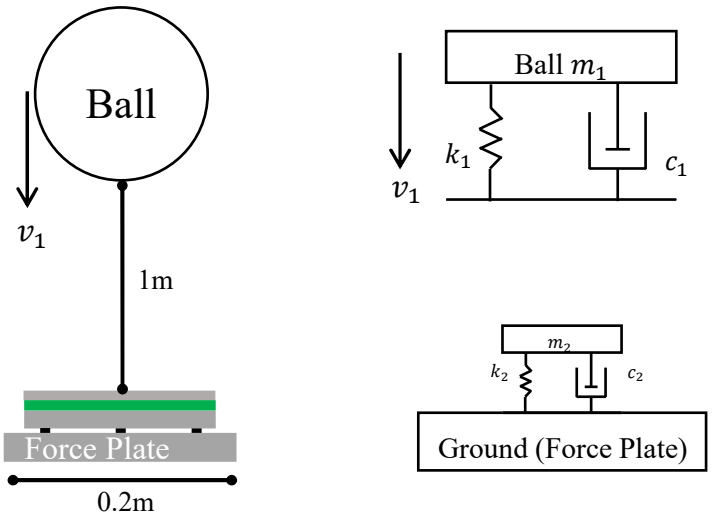

Figure 4-9. Schematic diagram of TDOF mass-spring system.

Two phases are considered: firstly, when the ball and the surface are independent, and secondly when they are coupled. For the coupled situation, the dynamics consider the elastic properties of the ball. This is the phase when the blocked force is determined.

The governing equation for the TDOF mass-spring-damper systems can be described with equations for (1) when the ball is not in contact, and (2) when the ball is in contact with a locally reacting mass-spring system [103]:

First, when the rubber ball is not in contact (i.e. it is still in the air), the governing equations are

$$\ddot{y}_1 = -g \tag{4.2}$$

$$m_2\ddot{y}_2 + c_2\dot{y}_2 + k_2(y_2 - a_2) = -m_2 g \tag{4.3}$$

where g is the acceleration due to gravity, m_2 is the mass of the steel plate, c_2 is the damping coefficient of the resilient material, k_2 is the stiffness of the resilient material in the mass-spring system for the model, h_1 is the height of the rubber ball (1m), and a_2 the thickness of the resilient material.

The initial condition is: $y_1 = h_1$, $\dot{y}_1=0$, $y_2=a_2$, $\dot{y}_2=0$

The variable c_2 describe the damping coefficient associated with the springs. For a mass-spring system, this can be calculated using

$$c_2 = \eta_2\sqrt{(k_2 m_2)} \tag{4.4}$$

where η_2 is the internal loss factor of the resilient material, and k_2 is given by

$$k_2 = 2\pi f_2 m_2 \tag{4.5}$$

where f_2 is the mass-spring frequency of the resilient materials.

Secondly, when the rubber ball is in contact with the locally reacting mass-spring system, the governing equations are

$$m_1\ddot{y}_1 + c_1(\dot{y}_1 - \dot{y}_2) + k_1(y_1 - y_2 - a_1) = -\mathrm{m}_1 g \tag{4.6}$$

$$\begin{aligned} m_2\ddot{y}_2 + c_2\dot{y}_2 + k_2(y_2 - a_2) - c_1(\dot{y}_1 - \dot{y}_2) \\ - k_1(y_1 - y_2 - a_1) = -m_2 g \end{aligned} \tag{4.7}$$

where m_1 is the mass of the rubber ball, k_1 is the stiffness of the rubber ball, and, a_1 is the diameter of a rubber ball.

The blocked force acting on the receiver is calculated according to

$$F = m_2\ddot{y}_2 - c_1(\dot{y}_1 - \dot{y}_2) - k_1(y_1 - y_2 - a_1) \tag{4.8}$$

In Simulink, the Linear Time-Variant (LPV) block was used to simulate the free fall of the rubber ball and interaction with the locally reacting mass-spring system on the force plate [103].

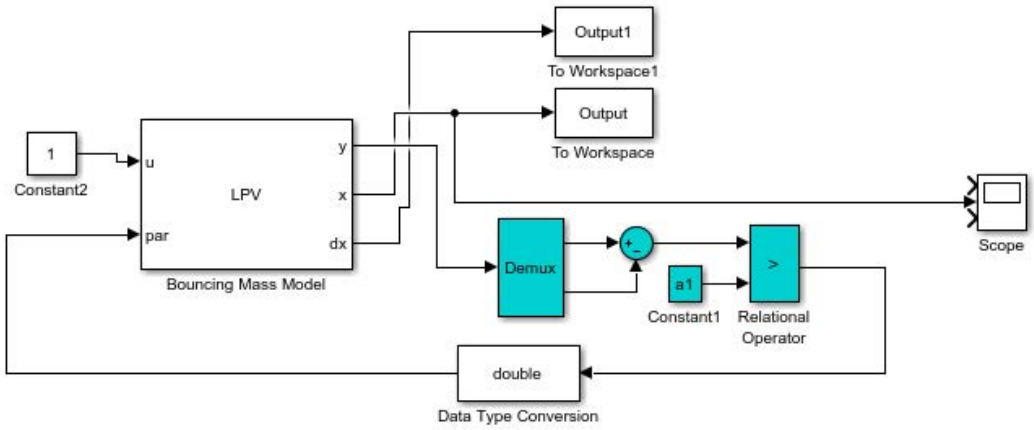

Figure 4-10. The LPV representation of the Simulink model for the TDOF mass-spring-damper model.

In the LPV block, the matrix according to the Eqs. (4.2), (4.3), (4.6), and (4.7) are defined as follows

When m_1 and m_2 are independent,

$$\mathrm{A}_1 = \begin{bmatrix} 0 & 1 & 0 & 0 \\ 0 & 0 & 0 & 0 \\ 0 & 0 & 0 & 1 \\ 0 & 0 & -k_2/m_2 & -c_2/m_2 \end{bmatrix}, B_1 = \begin{bmatrix} 0 \\ -g \\ 0 \\ -g + \left(k_2 \dfrac{a_2}{m_2}\right) \end{bmatrix}, \tag{4.9}$$

$$\mathrm{C}_1 = \begin{bmatrix} 1 & 0 & 0 & 0 \\ 0 & 0 & 1 & 0 \end{bmatrix}, \mathrm{D}_1 = \begin{bmatrix} 0 \\ 0 \end{bmatrix}$$

When m_1 and m_2 are coupled,

$$\mathrm{A}_2 = \begin{bmatrix} 0 & 1 & 0 & 0 \\ -\dfrac{k_1}{m_1} & -\dfrac{c_1}{m_1} & \dfrac{k_1}{m_1} & \dfrac{c_1}{m_1} \\ 0 & 0 & 0 & 1 \\ \dfrac{k_1}{m_2} & \dfrac{c_1}{m_2} & -(k_1 + k_2)/m_2 & -\dfrac{c_1 + c_2}{m_2} \end{bmatrix}, \tag{4.10}$$

$$B_2 = \begin{bmatrix} 0 \\ -g + \left(\frac{k_1 a_1}{m_1}\right) \\ 0 \\ -g + \left(\frac{k_2}{m_2 a_2}\right) - \left(\frac{k_1}{m_2 a_1}\right) \end{bmatrix},$$

$$\mathrm{C}_2 = \begin{bmatrix} 1 & 0 & 0 & 0 \\ 0 & 0 & 1 & 0 \end{bmatrix}, \mathrm{D}_2 = \begin{bmatrix} 0 \\ 0 \end{bmatrix}$$

Those matrices are stacked by using the "*stack*" function.

Table 4.3 summarises the parameters used to simulate the TDOF mass-spring systems for the locally reacting mass-spring systems A to E. Figure 4-11 to Figure 4-15 shows the measurement and simulation force-time curve.

Table 4.3. Estimated dynamic stiffness, damping of the rubber ball and the mass-spring systems for TDOF mass-spring-damper system.

	Original	***m*1 (kg)**	***k*1 (N/m)**	***c*1 (Ns/m)**	***m*2 (kg)**	***k*2 (N/m)**	***c*2 (Ns/m)**
Group 1	**A**	2.486	6.2e4	26	6.25	2e5	315
	B	2.486	6.2e4	26	6.25	1e6	1176
Group 2	**C**	2.486	6.2e4	26	6.25	1.3e6	917
	D	2.486	6.2e4	26	6.25	1.6e6	1965
	E	2.486	6.2e4	26	6.25	3.6e6	2600

Unlike SDOF mass-spring-damper system, the blocked force from TDOF mass-spring-damper system is 0N at *t*=0s. This is because the non-zero force at *t*=0s due to $c_1(\dot{y}_1 - \dot{y}_2)$ is cancelled out by the sum of $m_2\ddot{y}_2$ and $k_1(y_1 - y_2 - a_1)$.

In Figure 4-11 and Figure 4-12 (Group 1 materials), the simulation shows the same general features as the measurement, but it does not accurately predict the response. For example, the predicted peak force for locally reacting mass-spring system A is approximately 30% lower than the measurement, and 16% lower for locally reacting mass-spring B. In Figure 4-13 to Figure 4-15 (Group 2 materials) the simulation did not reproduce the double peak seen in the measurements. The simulated single event level for both Group 1 and Group 2 materials show that the agreement is within 5dB below 63Hz bands for both one-third octave and octave band except for mass-spring A.

The maximum difference in the single event level between measurement and simulation ranged from 8.1 to 19.5dB for one-third octave bands for the locally reacting mass-spring A to E, and 10.1 to 17.2dB for octave bands for locally reacting mass-spring systems A to E.

For Group 2 resilient materials, the simulation has the potential to emulate the double peak feature in the force-time curve that was observed in the measurements. This requires the stiffness and damping coefficients to be altered. It was found that changing in stiffness value of the resilient materials could lead to a double peak in the simulated force-time curve. The altered parameters are shown in Table 4.4, and results are shown in Figure 4-16 to Figure 4-18.

Table 4.4.Optimised dynamic stiffness, damping of the rubber ball and the mass-spring systems for TDOF mass-spring-damper system.

	Optimised	m_1 *(kg)*	k_1 **(N/m)**	c_1 **(Ns/m)**	m_2 *(kg)*	k_2 **(N/m)**	c_2 **(Ns/m)**
Group 2	**C**	2.486	6.4e4	110	7	5.4e6	1000
	D	2.486	6.4e4	110	7	6.5e6	600
	E	2.486	6.4e4	110	7	7e6	900

For the optimised simulation, the spring stiffness of the Group 2 resilient materials is increased by a factor of 1.9 to 4.1 times and the measured damping coefficient is increased by a factor of 0.3 to 1.1 times. The change to the stiffness of the rubber ball was negligible, but the damping coefficient increased by a factor of 4.2.

For the single event level calculated from optimised simulation, the maximum difference between measurement and simulation ranged from 1.4 to 2.9dB for one-third octave bands for the locally reacting mass-spring C, D and E respectively, and ranged from 0.8 to 1.8dB for octave bands for locally reacting mass-spring systems C, D and E respectively.

Therefore, the TDOF mass-spring-damper system can be used to predict the double-peak results with optimised spring stiffness.

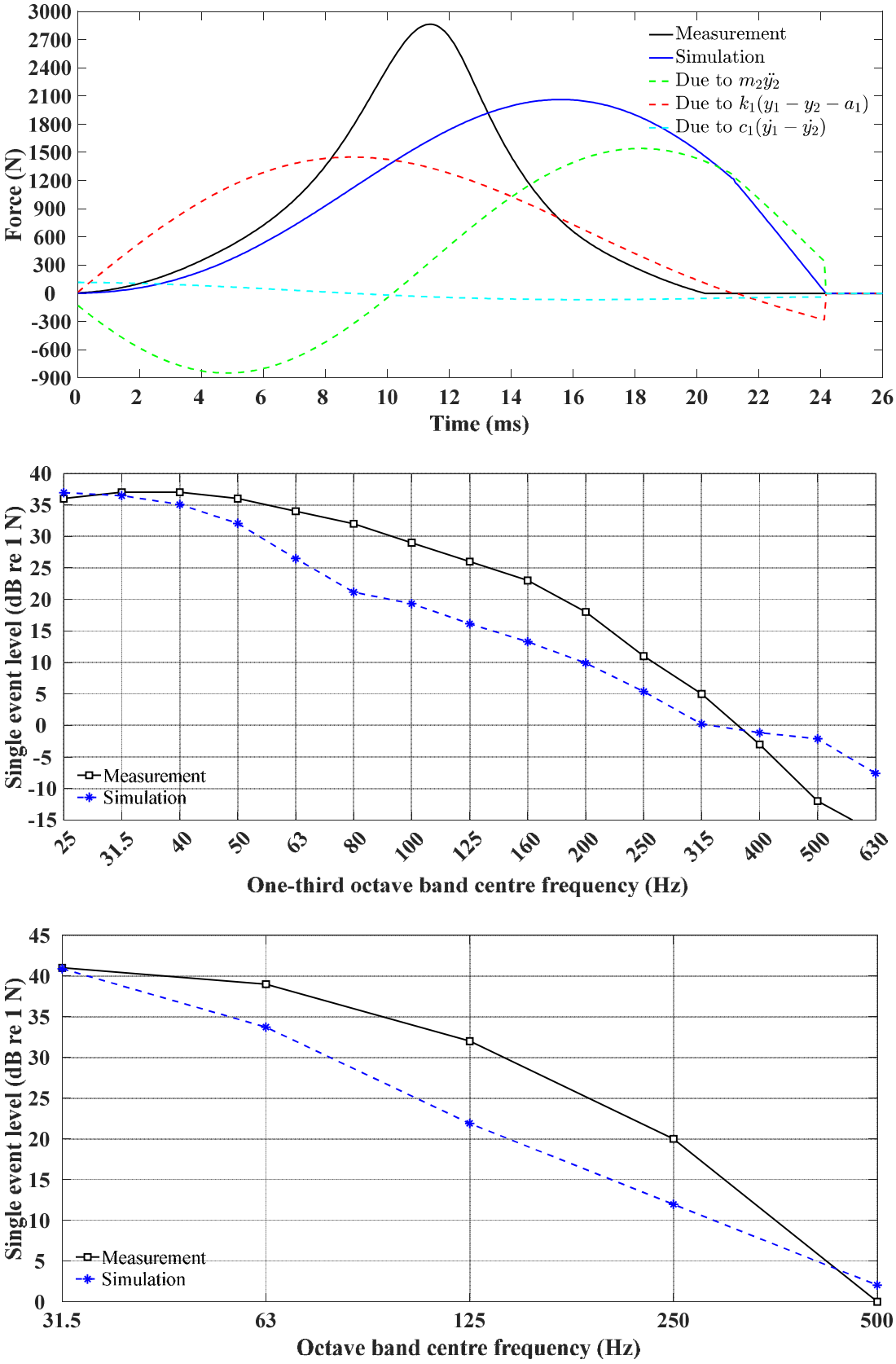

Figure 4-11. Simulink TDOF locally reacting mass-spring system A. Force-time (upper), single event level in one-third octave-bands (middle) and octave bands (lower).

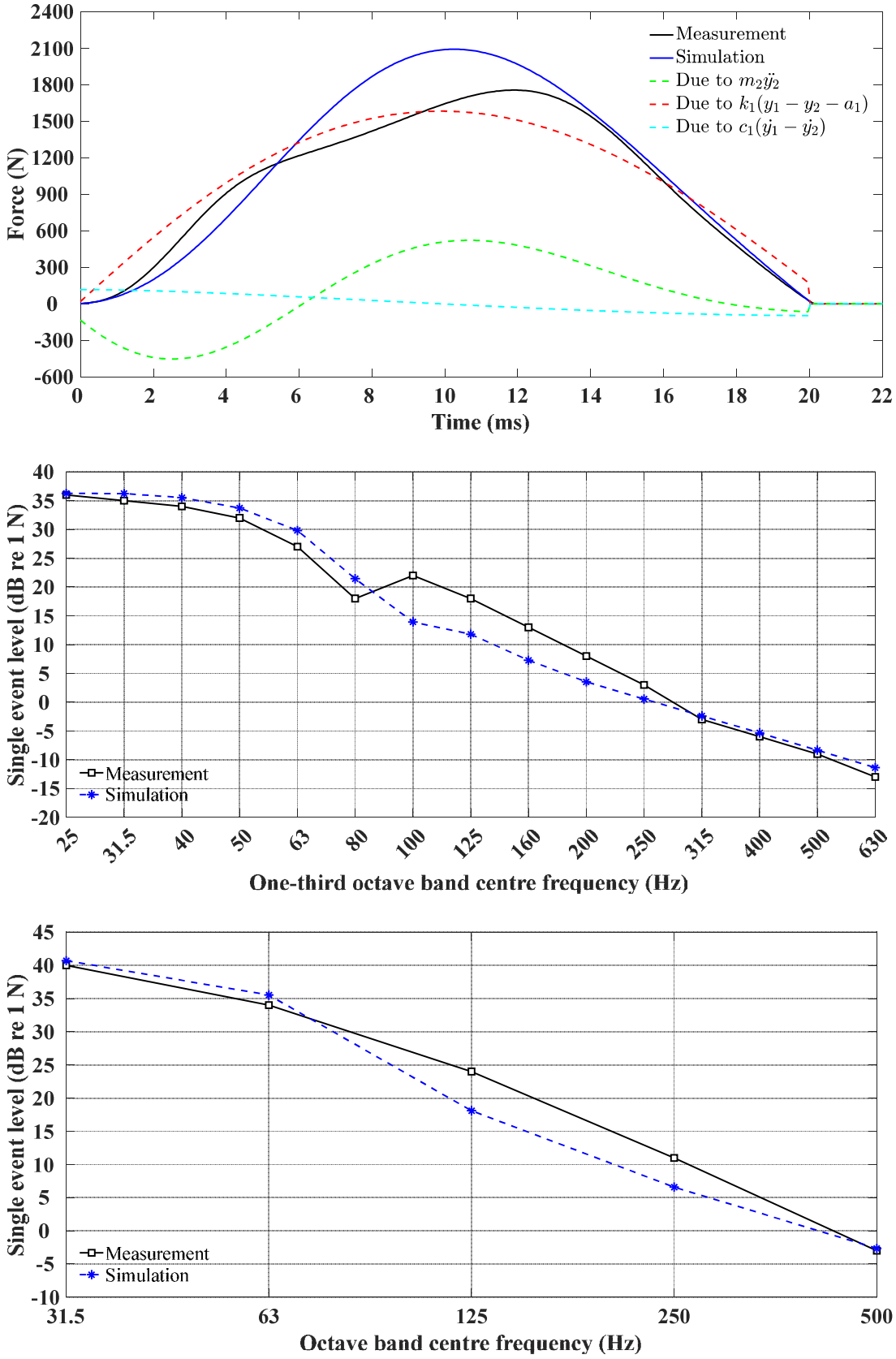

Figure 4-12. Simulink TDOF locally reacting mass-spring system B. Force-time (upper), single event level in one-third octave-bands (middle) and octave bands (lower).

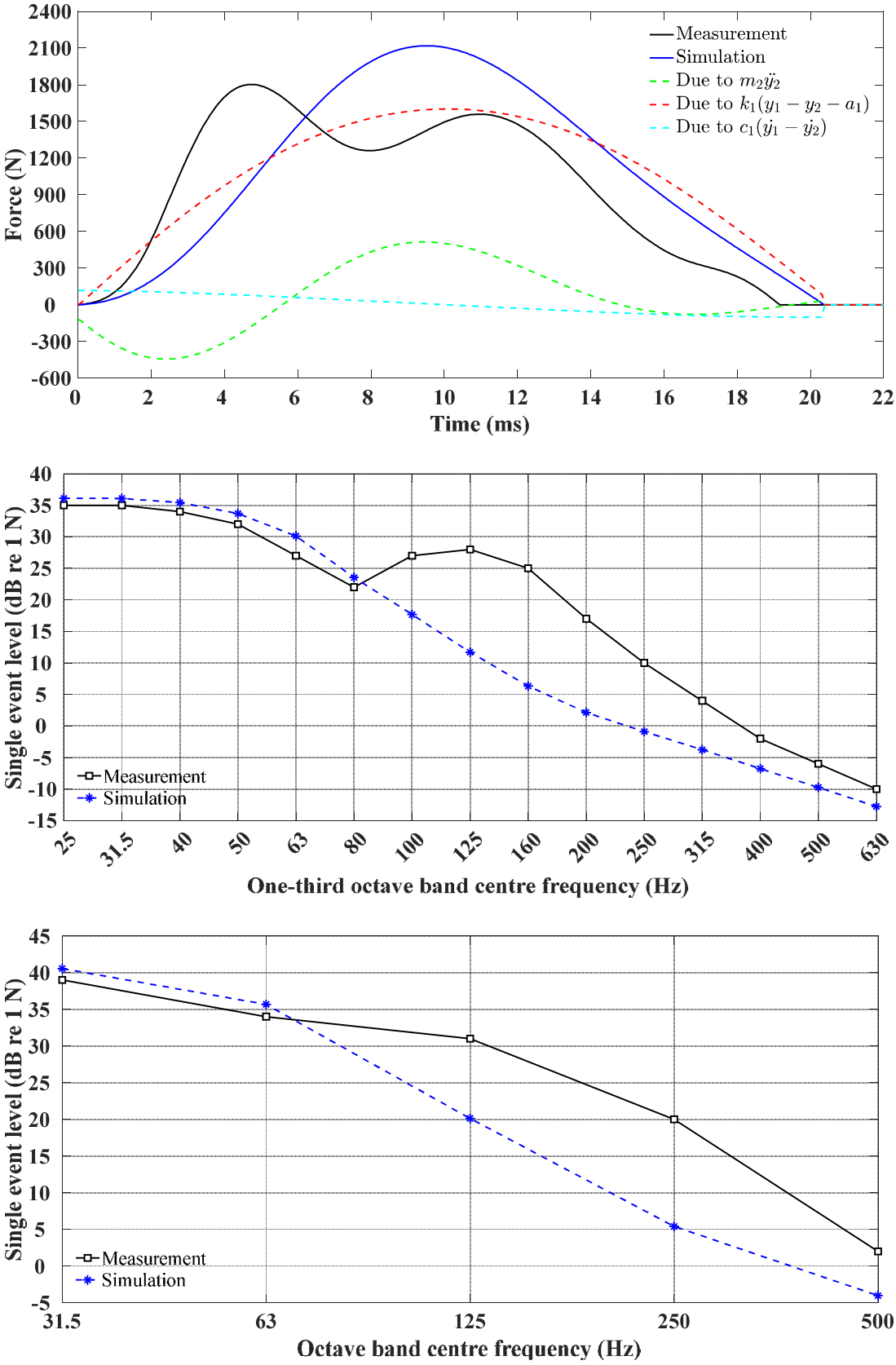

Figure 4-13. Simulink TDOF locally reacting mass-spring system C. Force-time (upper), single event level in one-third octave-bands (middle) and octave bands (lower).

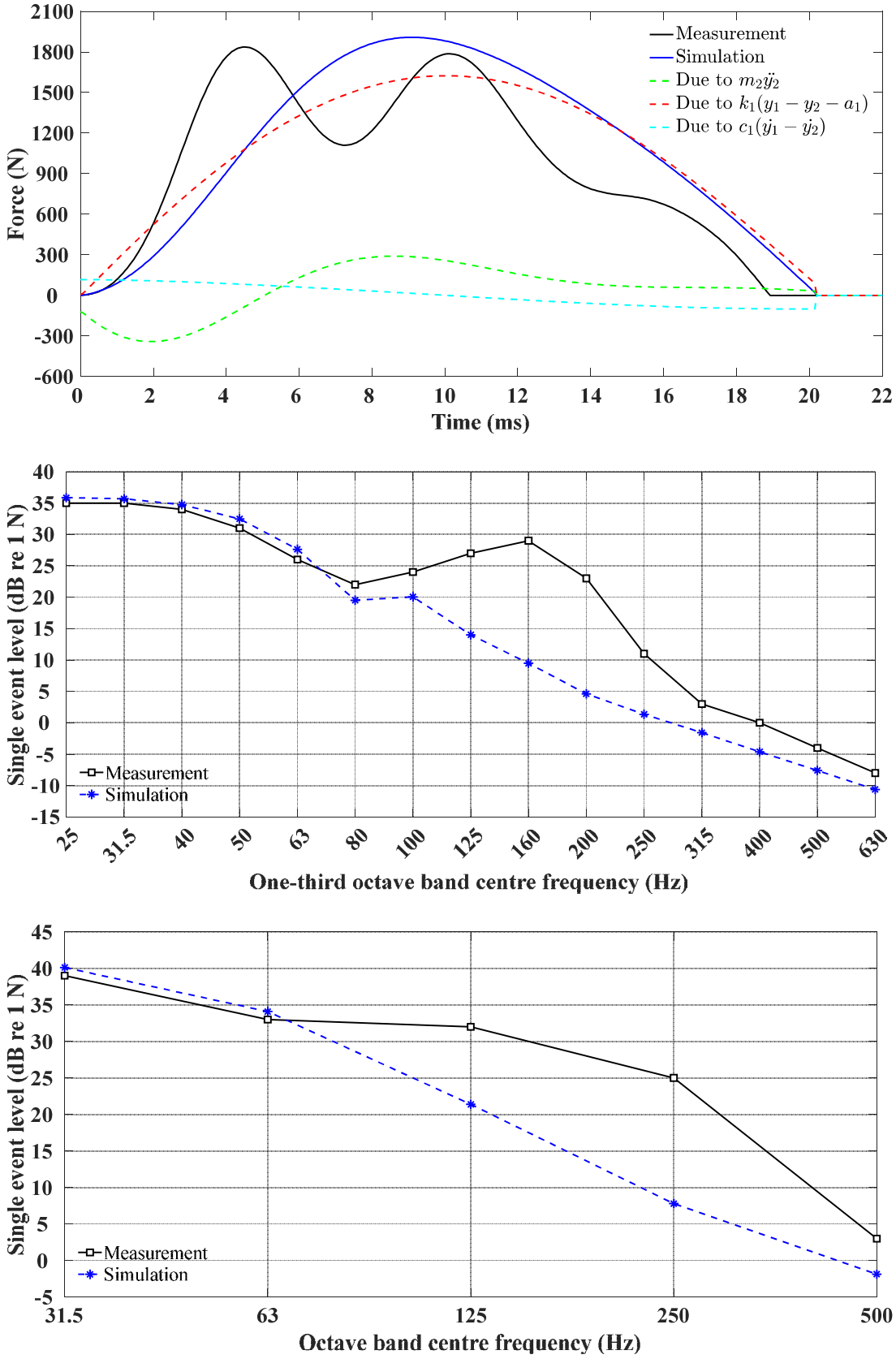

Figure 4-14. Simulink TDOF locally reacting mass-spring system D. Force-time (upper), single event level in one-third octave-bands (middle) and octave bands (lower).

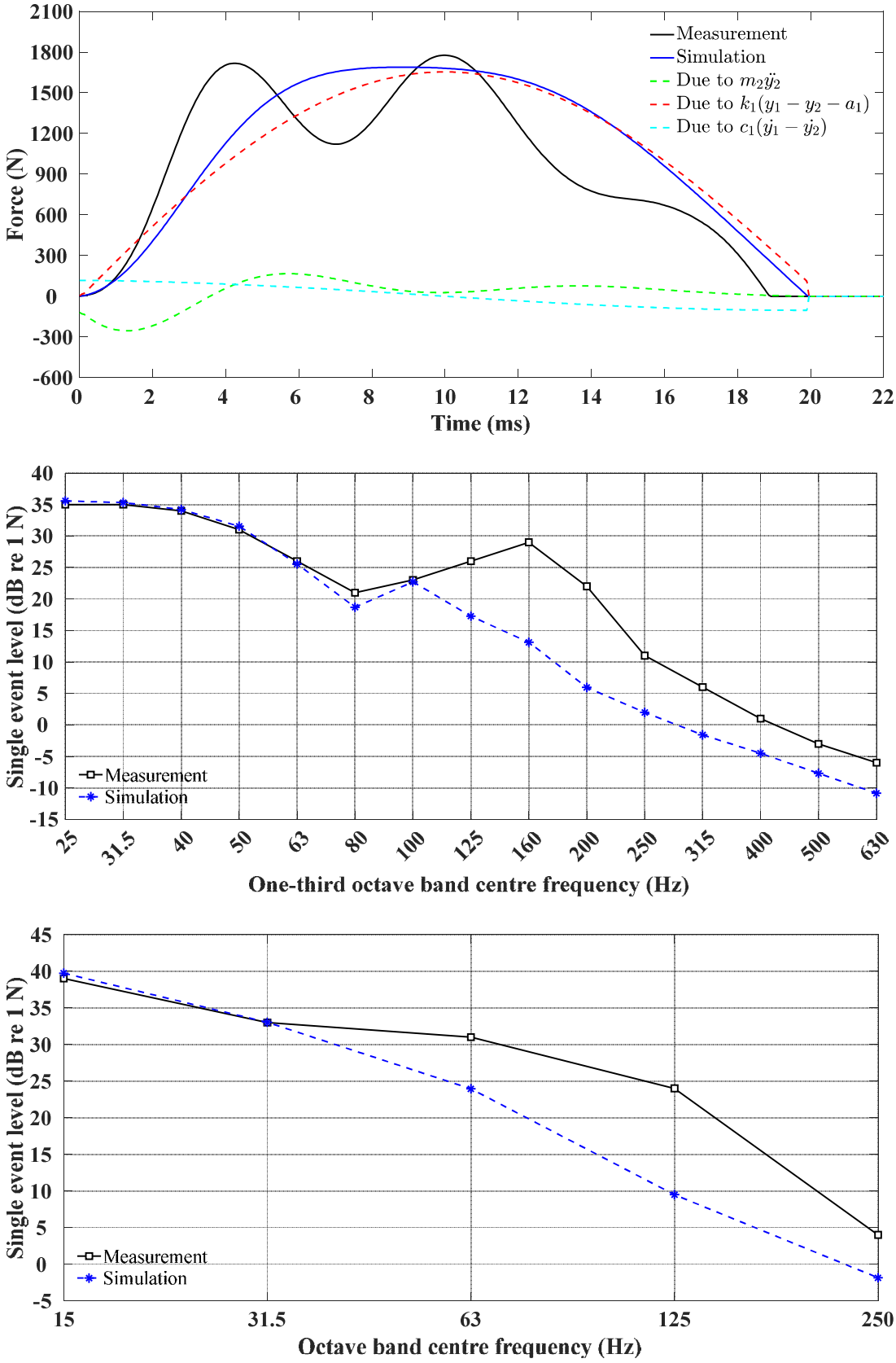

Figure 4-15. Simulink TDOF locally reacting mass-spring system E. Force-time (upper), single event level in one-third octave-bands (middle) and octave bands (lower).

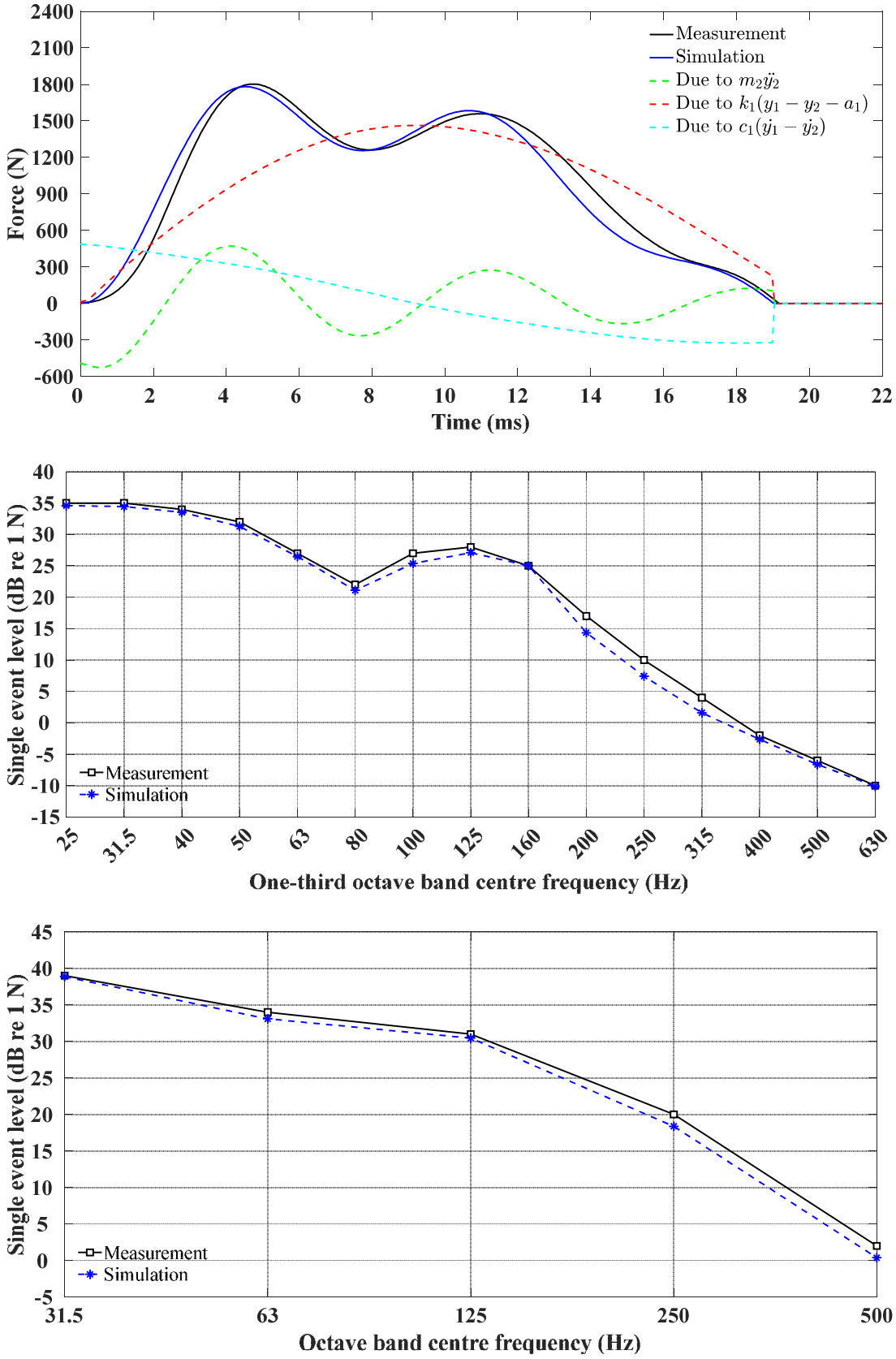

Figure 4-16. Simulink TDOF locally reacting mass-spring system C (Optimised). Force-time (upper), single event level in one-third octave-bands (middle) and octave bands (lower).

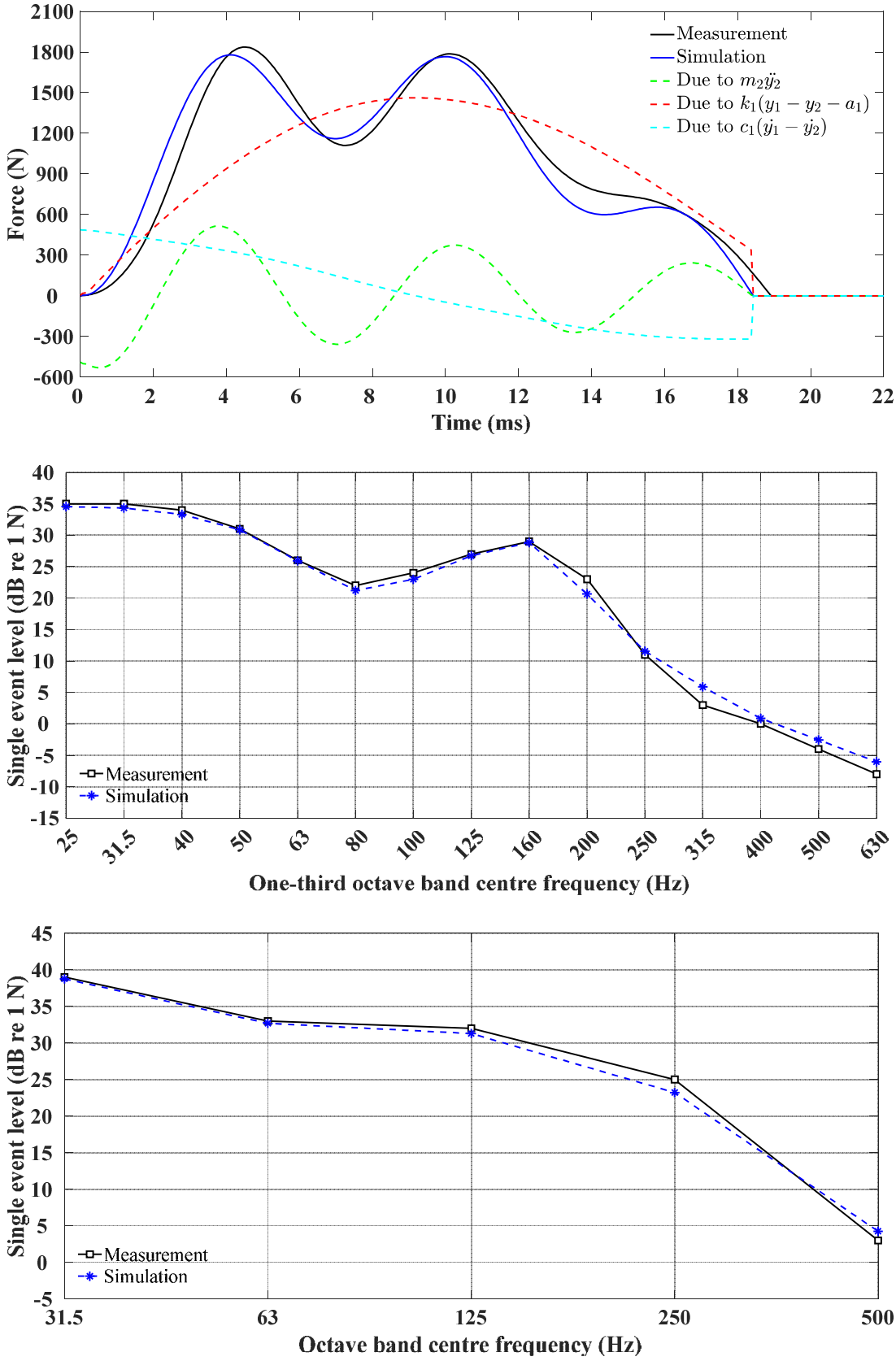

Figure 4-17. Simulink TDOF locally reacting mass-spring system D (Optimised). Force-time (upper), single event level in one-third octave-bands (middle) and octave bands (lower).

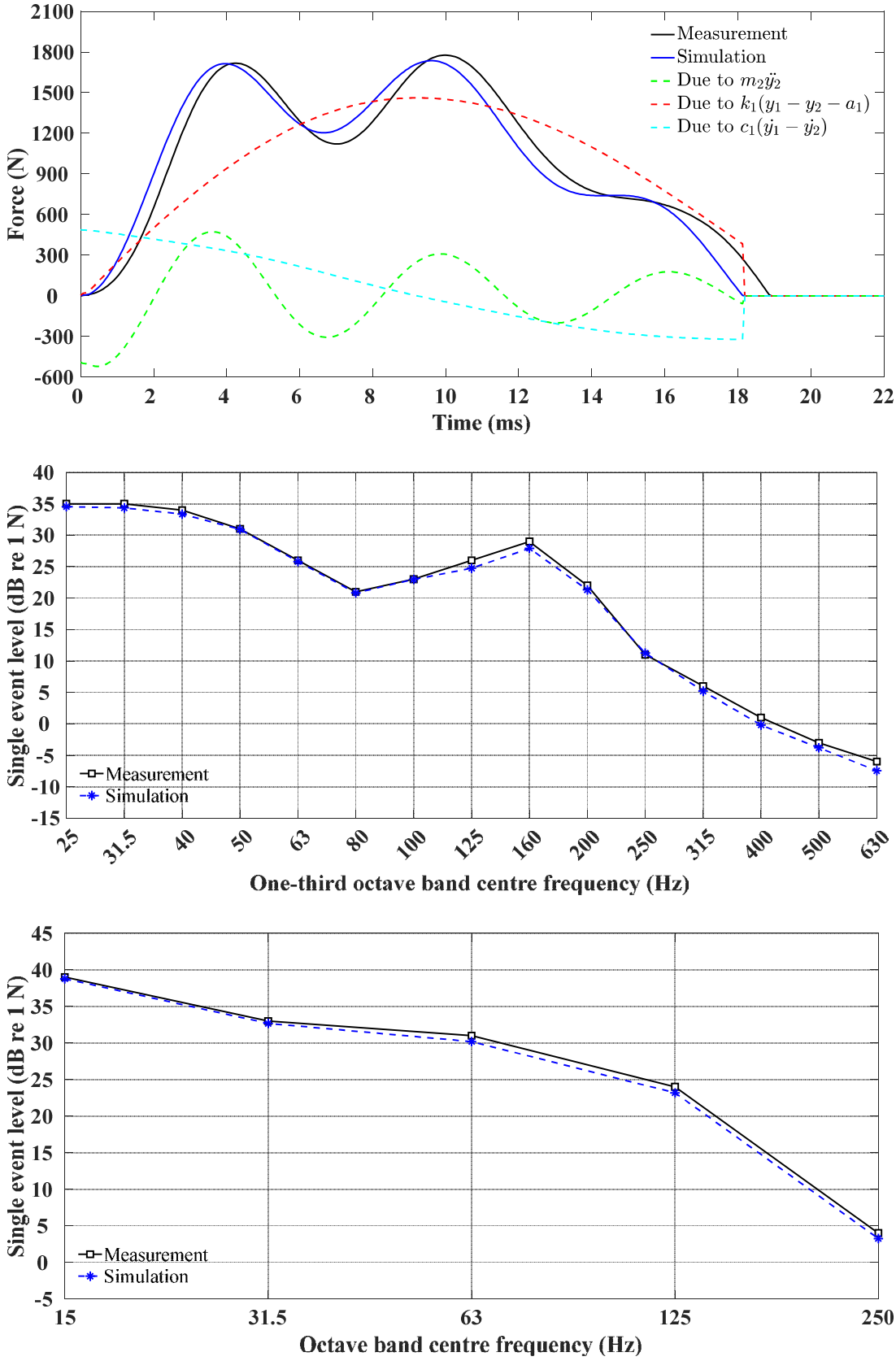

Figure 4-18. Simulink TDOF locally reacting mass-spring system E (Optimised). Force-time (upper), single event level in one-third octave-bands (middle) and octave bands (lower).

4.5 Summary

This chapter investigated the structural dynamics of the rubber ball when impacting upon locally reacting mass-spring systems. The locally reacting mass-spring system was introduced as an idealisation of a floating floor. This enables the blocked force due to the combination of the rubber ball and floating floor to be measured on the force plate.

The dynamic stiffness of the locally reacting mass-spring systems was measured by using a force hammer with peak force that is similar to the rubber ball. From this measurement, it is possible to rank order the resilient materials, but it is difficult to determine the exact dynamic stiffness from resonance frequency because it varies due to the applied force.

The blocked force of the rubber ball with locally reacting mass-spring systems was measured on the force plate. The blocked force measurement showed that the force versus time curve has a single or double peak when the resilient material is dynamically soft (Group 1) or stiff (Group 2) respectively. The finding suggested that there is negligible change in the ESD of the force below the 63Hz octave and one-third octave bands, and that the mass-spring resonance occurs between 100 and 250Hz, above which the force levels are significantly reduced.

MATLAB Simulink was used to predict the blocked force of the rubber ball with locally reacting mass-spring systems by TDOF mass-spring systems. With estimated spring stiffness and damping value, the single event level below 63Hz in one-third octave band and octave band could be predicted except for locally-reacting mass-spring system A. The duration and peak force were not reproduced by the model. The TDOF mass-spring systems could not predict the feature of double-peak unless using an optimised spring stiffness and damping coefficient. This indicates that the TDOF mass-spring system has potential to predict the injected force for the locally reacting mass-spring systems that has fundamental frequency above the rubber ball's fundamental frequency. However, the inability of the TDOF model to accurately describe the force means that measured data will be used to calculate the transient power input for the TSEA models in chapter 5.

5. VALIDATION OF ITSEA AND COMPARISON OF TSEA AND MEASUREMENTS

5.1 Introduction

This chapter focuses on the validation of the ITSEA approach to determine the transient power input and its inclusion in TSEA to predict $L_{p,Fmax}$ and $L_{v,Fmax}$ for comparison with measurements.

Section 5.2 desctibes two test facilities used in the heavy impact sound insulation measurements and the associated measurement procedures. Section 5.3 addresses the validation of the ITSEA using the two test facilities. Section 5.4 compares predictions using TSEA that incorporates transient power input from ITSEA with measurement in the two test facilities.

5.2 Heavy impact sound insulation

5.2.1 Laboratory and floor plans

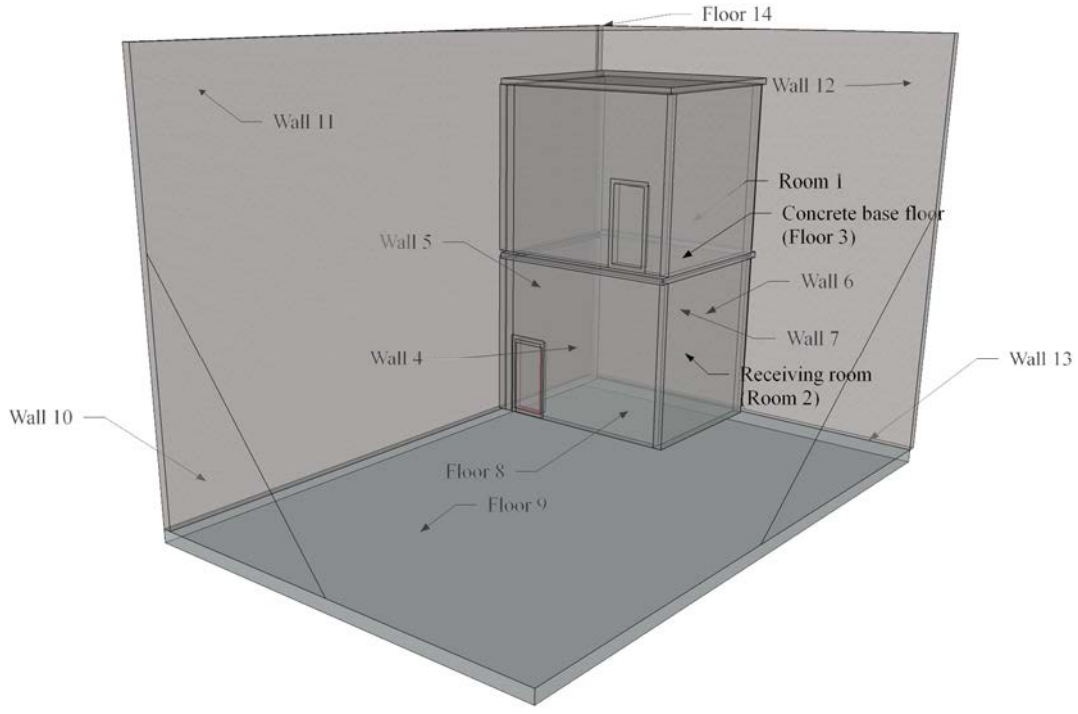

Figure 5-1. Test facility A.

Test facility A is a vertical transmission suite (BRE, UK) (see Figure 5-1) with suppressed flanking transmission. This has a 140mm solid concrete base floor (345kg/m^2) as prescribed in ISO 10140-5:2010+A1 2014 for the measurement of the

improvement of impact sound insulation from floor coverings. The base floor dimensions are 4.19m × 3.61m, and the lower and upper rooms each have a volume of ≈50m^3. The lower room is the receiving room which is formed by four 215mm solid masonry walls (430kg/m^2) that are built off a 300mm solid concrete ground floor (660kg/m^2). Flanking transmission is suppressed inside this lower room with independent plasterboard linings on the walls and a floating screed floor. The upper room is formed by lightweight plasterboard stud walls and a plasterboard ceiling. The dimensions of test facility A in terms of the subsystems used in the TSEA model are summarised in Table 5.1 where Room 2 is the receiving room and Floor 3 is the 140mm base floor (fundamental frequency is 32.3Hz).

Table 5.1. Test facility A: Specifications for the rooms, walls and floors.

Subsystem	L_x (m)	L_y (m)	L_z (m)	U (m)	S (m)	ρ_s (kg/m^2)	c_L (m)	η_{ii} (-)
Room 1	4.18	3.61	3.51	-	-	-	-	-
Room 2	**3.92**	**3.33**	**3.91**	**-**	**-**	**-**	**-**	**-**
Subsystem	L_x (m)	L_y (m)	h (m)	U (m)	S (m)	ρ_s (kg/m^2)	c_L (m)	η_{ii} (-)
Floor 3	**4.19**	**3.61**	**0.14**	**15.58**	**15.09**	**345.4**	**3856**	**0.005**
Wall 4	3.61	3.91	0.215	15.04	12.22	430	3200	0.01
Wall 5	4.19	3.91	0.215	16.18	16.34	430	3200	0.01
Wall 6	3.61	3.91	0.215	15.04	14.12	430	3200	0.01
Wall 7	4.19	3.91	0.3	16.18	16.34	430	3200	0.01
Floor 8	4.19	3.61	0.3	15.58	15.09	660	3680	0.005
Floor 9	14.03	9.15	0.2	46.00	113.28	660	3680	measured
Wall 10	9.76	9.15	0.2	37.82	89.4	440	3680	0.005
Wall 11	14.03	9.76	0.2	47.58	136.93	1088	3680	0.005
Wall 12	9.76	9.15	0.2	37.82	89.4	440	3680	0.005
Wall 13	14.03	9.76	0.2	47.58	136.93	440	3680	0.005
Floor 14	14.03	9.15	0.2	46.00	128.37	440	3680	0.005

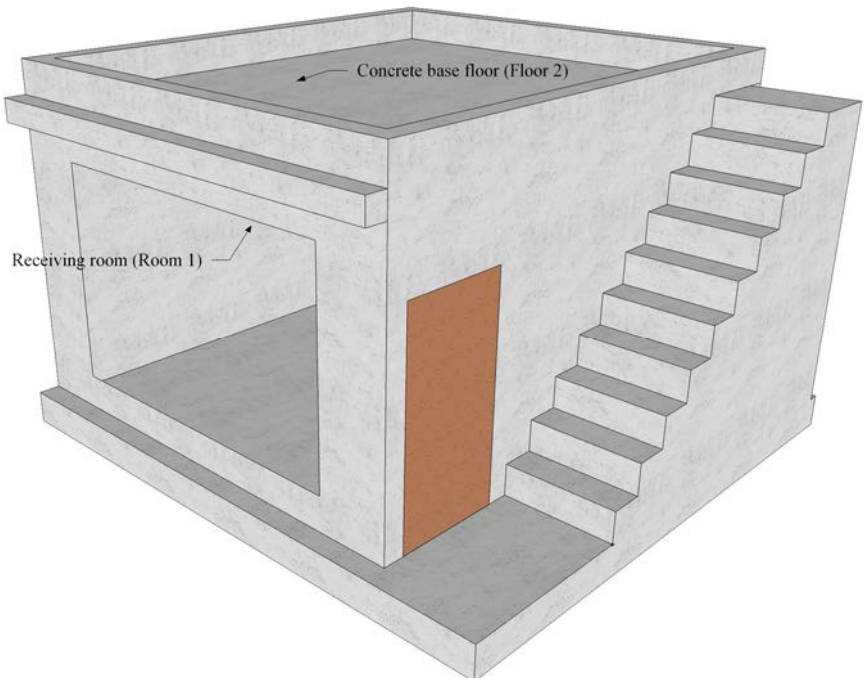

Figure 5-2. Test facility B.

Table 5.2. Test facility B: Specifications for the rooms, walls and floors.

Subsystem	L_x (m)	L_y (m)	L_z (m)	*U (m)*	*S (m)*	ρ_s *(kg/m²)*	c_L *(m)*	η_{ii} *(-)*
Room 1	4.78	4.10	2.59	-	-	-	-	-
Subsystem	L_x (m)	L_y (m)	*h* (m)	*U (m)*	*S (m)*	ρ_s *(kg/m²)*	c_L *(m)*	η_{ii} *(-)*
Floor 2	4.78	4.10	0.21	17.76	19.6	3200	3800	0.005

Test facility B (see Figure 5-2) is a stand-alone test room (LH, South Korea) with a 210mm solid concrete base floor (462kg/m^2) that is commonly used in Korean dwellings. The base floor dimensions are 4.76m × 4.10m (fundamental frequency is 37.4Hz). The receiving room has a volume of ≈50m^3. The facility has one glazed façade, three 200mm concrete walls without any wall linings, and a 300mm ground floor without a floating floor. The properties and dimensions of test facility B are given in Table 5.2 for the two subsystems used in the TSEA model. Due to the absence of information on the other walls and floors it was assumed that flanking transmission was negligible.

In test facility B, the floating floor is on top of the base floor the Ondol system that is commonly used in South Korea. The rigid walking surface is 40mm lightweight concrete (27.6kg/m^2) bonded directly to 40mm mortar (72kg/m^2) on a resilient material of

30mm EPS with dynamic stiffness per unit area of 20MN/m^3. The mass-spring resonance frequency is calculated to be 71Hz.

5.2.2 Measurement procedures

5.2.2.1 Structural reverberation time

The structural reverberation time was measured at multiple positions on the concrete floor with a single hit from a hammer. An accelerometer was used to measure the decaying plate response in terms of acceleration.

The spatial average structural reverberation time was determined from five excitation and two accelerometer positions per excitation position in test facility A, and four excitation and two accelerometer positions per excitation position in test facility B.

The integrated impulse response method was introduced by Schroeder [104] and uses impulsive excitation to measure the energy decay. This results in a decay curve that represents the characteristics of the acoustic system. This method is beneficial because a single measurement gives a decay curve without random fluctuations, which increases the accuracy of reverberation time calculation. This approach is carried out from the acceleration signal that is fed into the CPB filter and squared, and then the energy decay curve is determined from the time weighting averaging (either by linear or exponential). The exponential averaging requires the time constant that is *T*/20 in ISO 354:2003 [105], and *T*/30 in ISO 3382-1:2009 [106]. In this thesis, ISO 354:2003 was followed. The difference is discussed in [24]. The effect of the detector and filters on the decay curves are explained in [107,108].

5.2.2.2 Impact sound insulation

In test facility A, two measurements with rubber ball excitation were carried out with and without five different mass-spring systems on the base floor. Five different excitation positions were used on the base floor with three accelerometers (B&K, Type 4371) fixed to the floor at random positions for each excitation position. Two microphones (B&K, Type 4165) were used in the receiving room to measure the sound pressure at random positions for each excitation position. B&K Time Data Recorder was used with a time resolution of 61.04μs and an FFT frequency resolution of 1Hz.

In test facility B, two measurements on the floating floor were carried out in with excitation using (a) the rubber ball and (b) the tyre source. Four randomly chosen excitation positions were used on the floating floor with three accelerometers (B&K, Type 4371) fixed to the base floor at random positions for each excitation position, two microphones (B&K, Type 4165) were used in the receiving room to measure the sound pressure at random positions for each excitation position. B&K Pulse was used with a time resolution of 61.04μs and an FFT frequency resolution of 1Hz. In both measurements, the procedures for the rubber ball described in ISO 10140-3:2010 [12] were followed.

5.3 VALIDATION OF ITSEA

5.3.1 Introduction

To carry out ITSEA using Eq. (2.40) it is assumed that there is a single subsystem that ignores all other coupled subsystems that can return energy back to the source subsystem. Hence, a 14-subsystem model of the complete laboratory (see Figure 5-1) and a one-subsystem model of the concrete base floor were created to investigate the possible error. To validate the ITSEA model, measured normalised transient power input ($W'_{\text{in,Force\_Plate}}$) and ITSEA normalised transient power input ($W'_{\text{in,ITSEA}}$) were compared.

5.3.2 Effect of energy returning from other subsystems

Numerical experiments are used here to assess whether the errors in ITSEA are likely to be significant when energy returns to an excited subsystem.

Input data is taken from TSEA models of a 140mm concrete base floor, test facility A which has previously been validated [37, 43]. Firstly, the base floor is isolated so that there is a one-subsystem TSEA model. Secondly, the base floor is connected to masonry walls on all four sides in a test facility in a 14-subsystems TSEA model. $W'_{\text{in,Force\_Plate}}$ is injected to the source subsystem excited by the rubber ball. The time-varying, mean-square energy in the 50, 250 and 500Hz one-third octave bands for these two TSEA models is shown in Figure 5-3 where the transient excitation corresponds to an 18.8ms contact duration pulse applied by a rubber ball dropped from a height of 1m [60].

During the exponential growth in energy, the two TSEA models are nominally identical (i.e. the values are within 2.3% which corresponds to a 0.1dB difference) up to 18.8ms for 50Hz, up to 8.8ms for 250Hz and up to 6.3ms for 500Hz. The peak occurs at 18.8ms for both TSEA models, and this corresponds to the transient power duration. The peak value is higher with the 14-subsystem model than the one-subsystem model by a factor of 1.025 at 50Hz (corresponding to a 0.1dB difference), a factor of 1.1049 (corresponding to a 0.4dB difference) at 250Hz and a factor of 1.173 (corresponding to a 0.7dB difference) at 500Hz. This is because energy returns to the source subsystem from the other 13 subsystems that make up the 14-subsystem model. The subsequent decays from the two TSEA models also differ because energy returns to the source subsystem with the 14-subsystem model.

This assessment leads to the conclusion that if it is possible to identify the time, t_{peak}, at which the highest peak occurs in the time-varying mean-square energy, then it should be feasible to sum the mean-square energy between 0s and t_{peak} to estimate the transient power. However, when the base concrete floor is coupled to other walls and floors, there will be (relatively small) errors in the peak value. Note that the effect of energy returning from the room(s) to the excited floor can affect the decay curve in structural reverberation time measurements, but the peak tends to be unaffected [109].

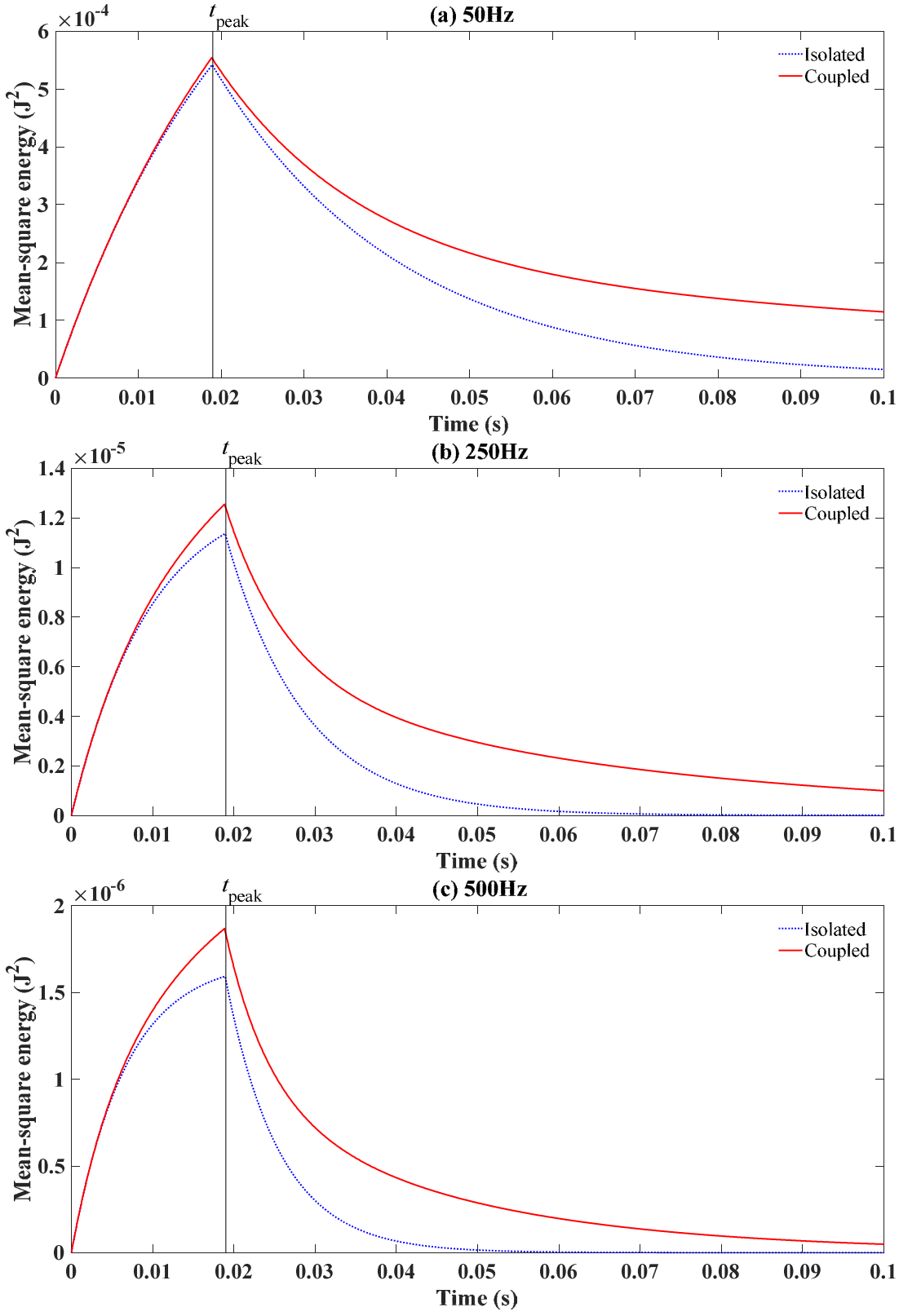

Figure 5-3. TSEA prediction of the time-varying, mean-square energy in the (a) 50Hz, (b) 250Hz and (c) 500Hz one-third octave bands for an isolated concrete base floor (one-subsystem model) and a coupled concrete base floor (14-subsystem model).

To assess the errors involved in using Eq. (2.40) the two TSEA models considered earlier in this section are used to determine the difference between the actual transient

power input used in TSEA and the transient power input determined using ITSEA with Eq. (2.41); see Figure 5-4.

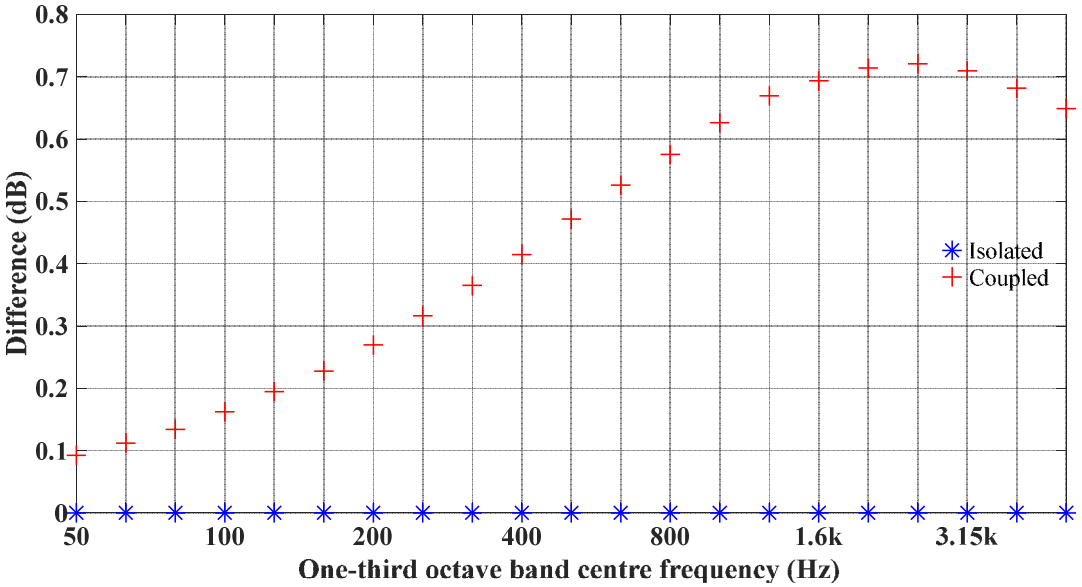

Figure 5-4. Difference between the normalised transient power input used in TSEA and the values calculated with ITSEA using the results from a TSEA model of the isolated and coupled concrete base floor as input data.

Figure 5-4 shows that the error is 0dB for a one subsystem model and <0.7dB for the 14-subsystem model. This indicates that if it was possible to have a laboratory with a suspended concrete floor base or one that rested upon resilient materials that isolated it from the rest of the structure, then that would effectively represent the one-subsystem model where errors should be negligible. In practice, concrete floors are usually rigidly connected to walls in order to provide structural stability and to provide TLFs that are representative of the field situation. Fortunately, below 500Hz the 14-subsystem model indicates that the error is <0.5dB and whilst this can be considered to be negligible, it will be assessed as the first part of the experimental validation in section 5.3.4.

5.3.3 Practical implementation of ITSEA

Unlike the smooth time-varying curve of energy from TSEA that was shown in Figure 5-3, the instantaneous mean-square velocity from an impact has many fluctuations with zero-value points; for example, see Figure 5-5 for the response in the 50Hz one-third octave band at a single accelerometer position. These fluctuations are problematic with Eq. (2.40) because the energy gradient with time needs to be positive. For this reason, the local maxima of the instantaneous mean-square velocity is identified.

and linear interpolation is carried out between them to give an envelope curve as shown in Figure 5-5.

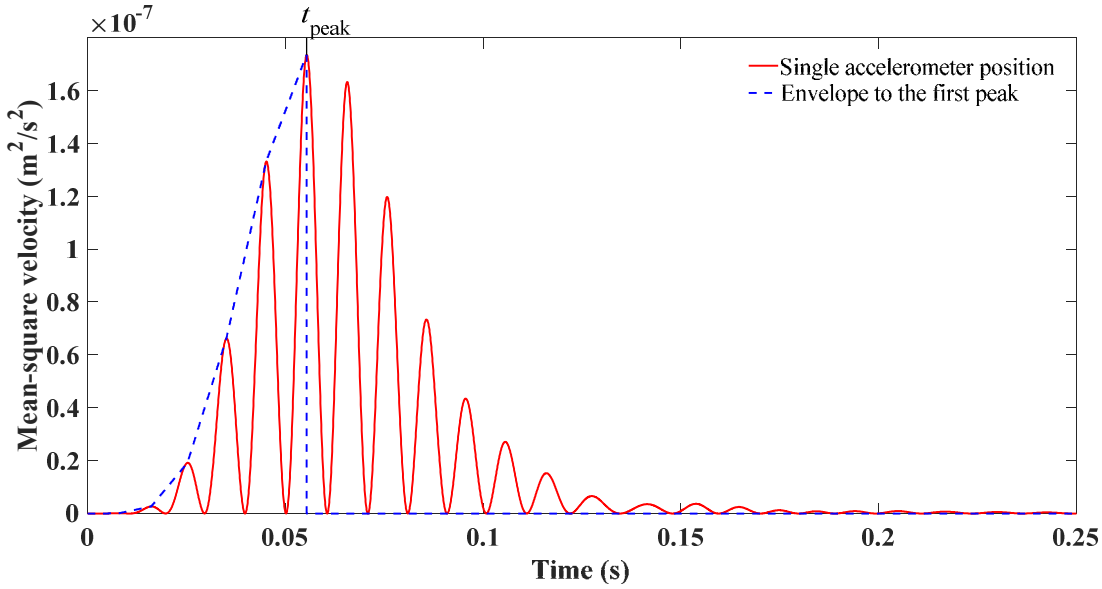

Figure 5-5. Instantaneous mean-square velocity due to a rubber ball impact from a single accelerometer position on a concrete floor (this example shows the 50Hz one-third octave band) and the corresponding envelope curve from linear interpolation up to the highest peak, t_{peak}, in the envelope.

This approach is reasonable because the real floor has a spatially-varying vibration field for which the response is specific to the floor geometry, excitation position and accelerometer position. However, the aim is to determine the spatial-average response of a plate subsystem with arbitrary geometry and arbitrary excitation position.

The zero values in the instantaneous mean-square velocity differ for different excitation and accelerometer positions. Therefore, if the boundaries of the floor were to be altered (but the floor area remained the same), then the peaks and troughs would shift. Hence, it is reasonable to use Eq. (2.40) on the envelope so that the results are applicable to a subsystem of arbitrary geometry but similar area. The process to choose the peak is discussed in 2.4.2. The normalised transient power input is calculated using Eq. (2.41) and outliers that are more than three standard deviations from the mean are removed before recalculating the mean normalised transient power input. The instantaneous mean-square velocity is converted to mean-square energy through multiplication by the mass of the base floor.

5.3.4 Predicting normalised transient power input

The total loss factor of each concrete base floor in one-third octave and octave bands was calculated from the measured structural reverberation times (see Figure 5-6). This loss factor was used in Eq. (2.40) to calculate the transient power input.

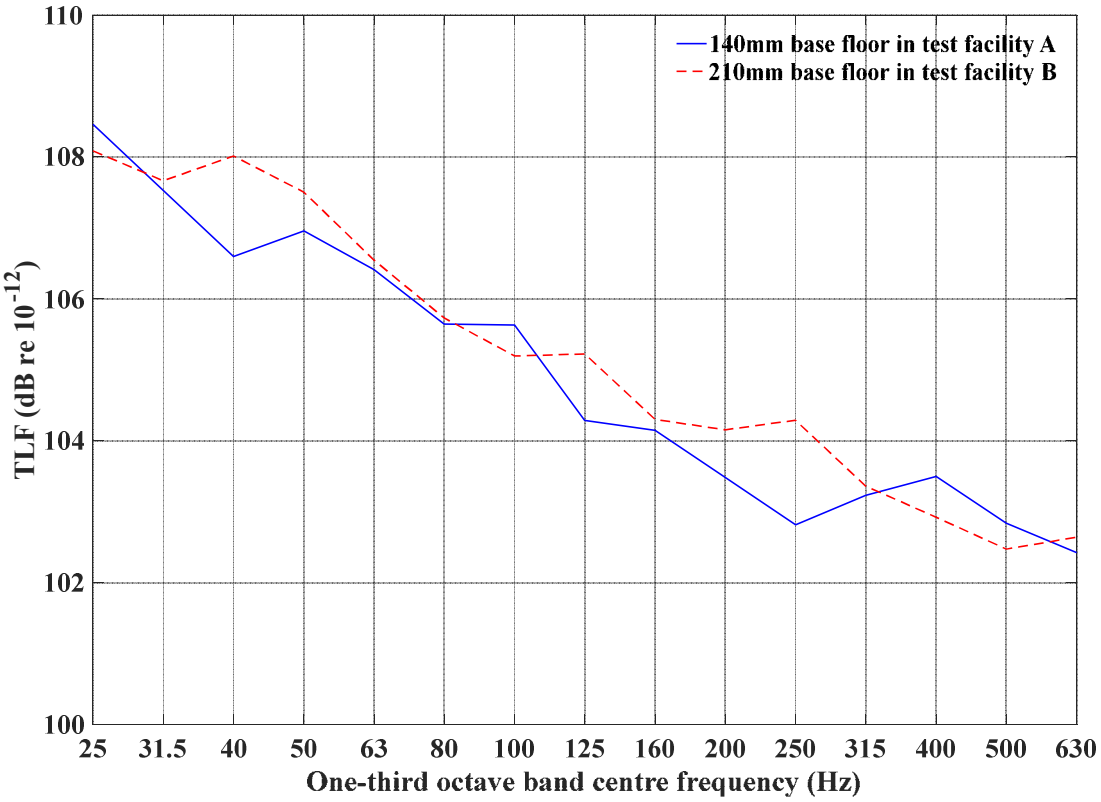

Figure 5-6. Measured TLF of the concrete base floors in test facilities A and B in one-third octave bands

The frequency range that is shown in the thesis depends on the effectiveness of each mass-spring system; hence results are only shown when there is a measurable signal that is at least 10dB above background noise.

In test facility A, the measured spatial averaged driving-point mobility at the excitation points was used to calculate $W'_{\text{in,Force\_Plate}}$ and the normalised transient power input from ITSEA, $W'_{\text{in,ITSEA}}$. In test facility B, $\text{Re}\{Y_{\text{dp}}\}$ was not measured; hence only $W'_{\text{in,ITSEA}}$ results are shown.

5.3.4.1 Test facility A

From the force plate measurements shown in the Fig 4-7, $t_{\text{input\_duration}}$ for the rubber ball is 18.8, and 20.3, 19.3, 18.9 and 18.8ms with the rubber ball on mass-spring systems

A, B, C, D and E respectively. These values are used to determine the normalised transient power input with Eq. (2.41). It is noteworthy that these $t_{\text{input\_duration}}$ values on the mass-spring systems are similar to the 18.8ms contact duration for a rubber ball directly impacting the force plate; hence these particular mass-spring systems do not significantly change $t_{\text{input\_duration}}$.

Figure 5-7 to Figure 5-12 allows comparison between $W'_{\text{in,Force\_Plate}}$ and $W'_{\text{in,ITSEA}}$ in one-third octave and octave bands. The second y-axis on the right-hand side shows difference estimated from $W'_{\text{in,Force\_Plate}} - W'_{\text{in,ITSEA}}$. For one-third octave bands, the absolute maximum difference between $W'_{\text{in,Force\_Plate}}$ and $W'_{\text{in,ITSEA}}$ ranged from 4.9 to 12.5dB for the direct and locally reacting mass-spring A to E. For octave bands, the absolute maximum difference between $W'_{\text{in,Force\_Plate}}$ and $W'_{\text{in,ITSEA}}$ ranged from 3.6 to 9.4dB for octave bands for the direct and locally reacting mass-spring A, B, C, D and E respectively.

Table 5.3 and Table 5.4 shows the frequency-average difference between $W'_{\text{in,Force\_Plate}}$ and $W'_{\text{in,ITSEA}}$ for one-third octave and octave band respectively. The difference (absolute value) ranged from 0 to 3.4dB and 1.3 to 3.9dB for one-third octave and octave band respectively. This is sufficiently accurate to justify the use of ITSEA.

Table 5.3. Frequency-average difference in W'_{in} between $W'_{\text{in,Force\_Plate}}$ and $W'_{\text{in,ITSEA}}$ in one-third octave bands.

		Locally reacting mass-spring systems				
	Direct	**A**	**B**	**C**	**D**	**E**
W′*in *(dB)	-0.9	-3.4	0.7	1.1	-2.3	0

Table 5.4. Frequency-average difference in W'_{in} between $W'_{\text{in,Force\_Plate}}$ and $W'_{\text{in,ITSEA}}$ in octave bands.

		Locally reacting mass-spring systems				
	Direct	**A**	**B**	**C**	**D**	**E**
W′*in *(dB)	2.1	-2.2	3.9	3.1	-1.3	2.1

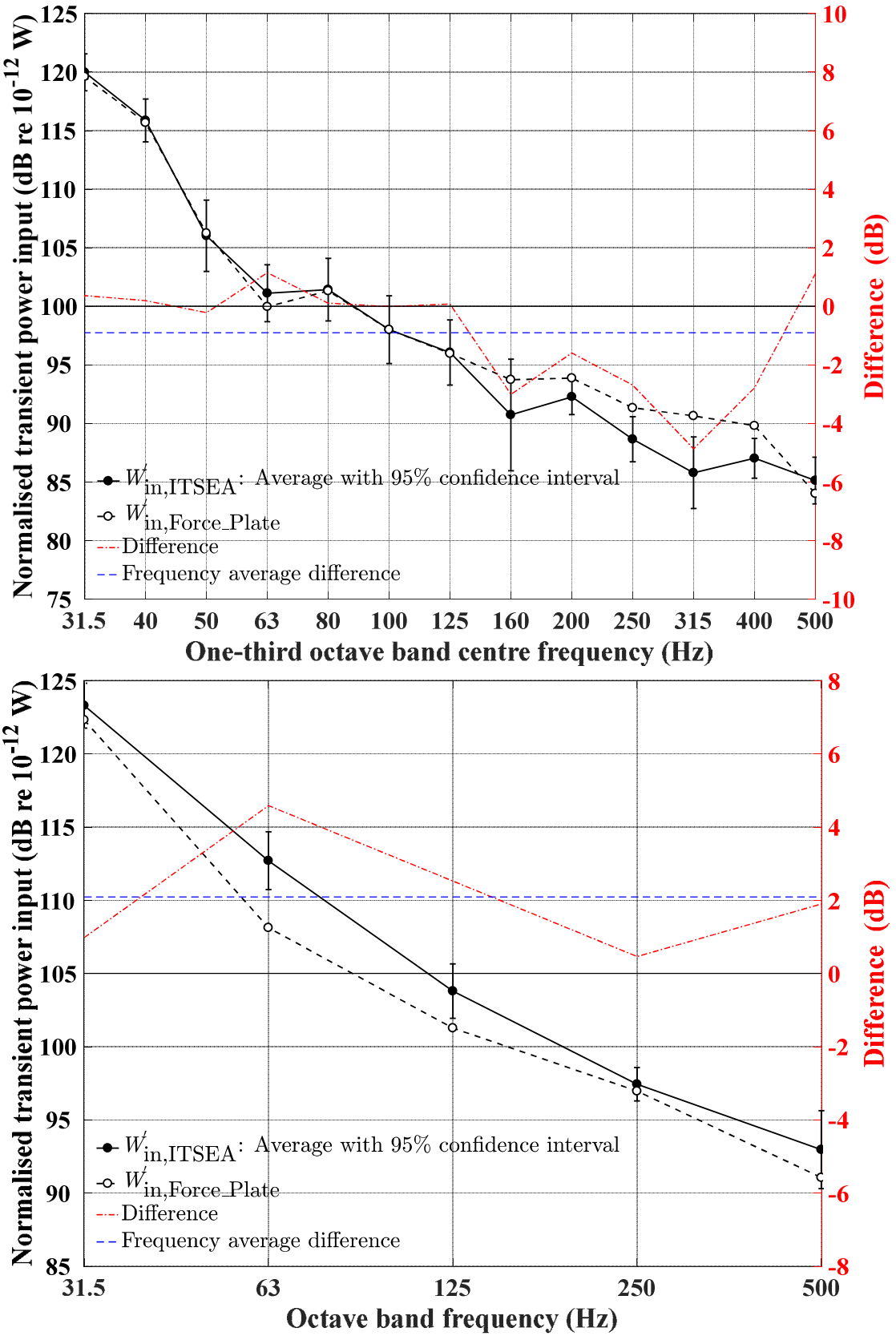

Figure 5-7. Comparison of the normalised transient power input for the rubber ball exciting a 140mm concrete base floor determined using ITSEA and the force plate in one-third octave bands (upper) and octave bands (lower).

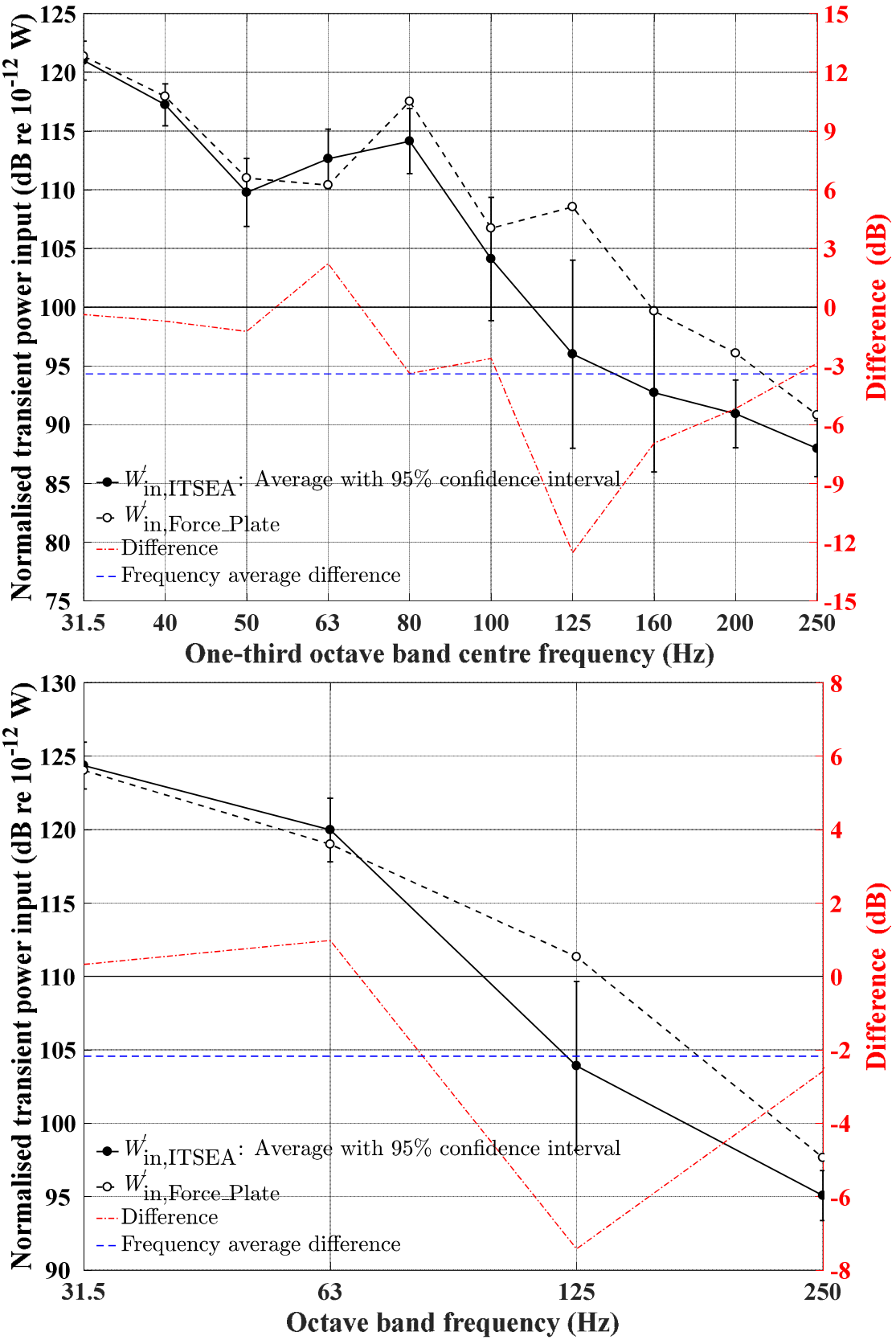

Figure 5-8. Comparison of the normalised transient power input for the rubber ball exciting locally reacting mass-spring system A on a 140mm concrete base floor determined using ITSEA and the force plate in one-third octave bands (upper) and octave bands (lower).

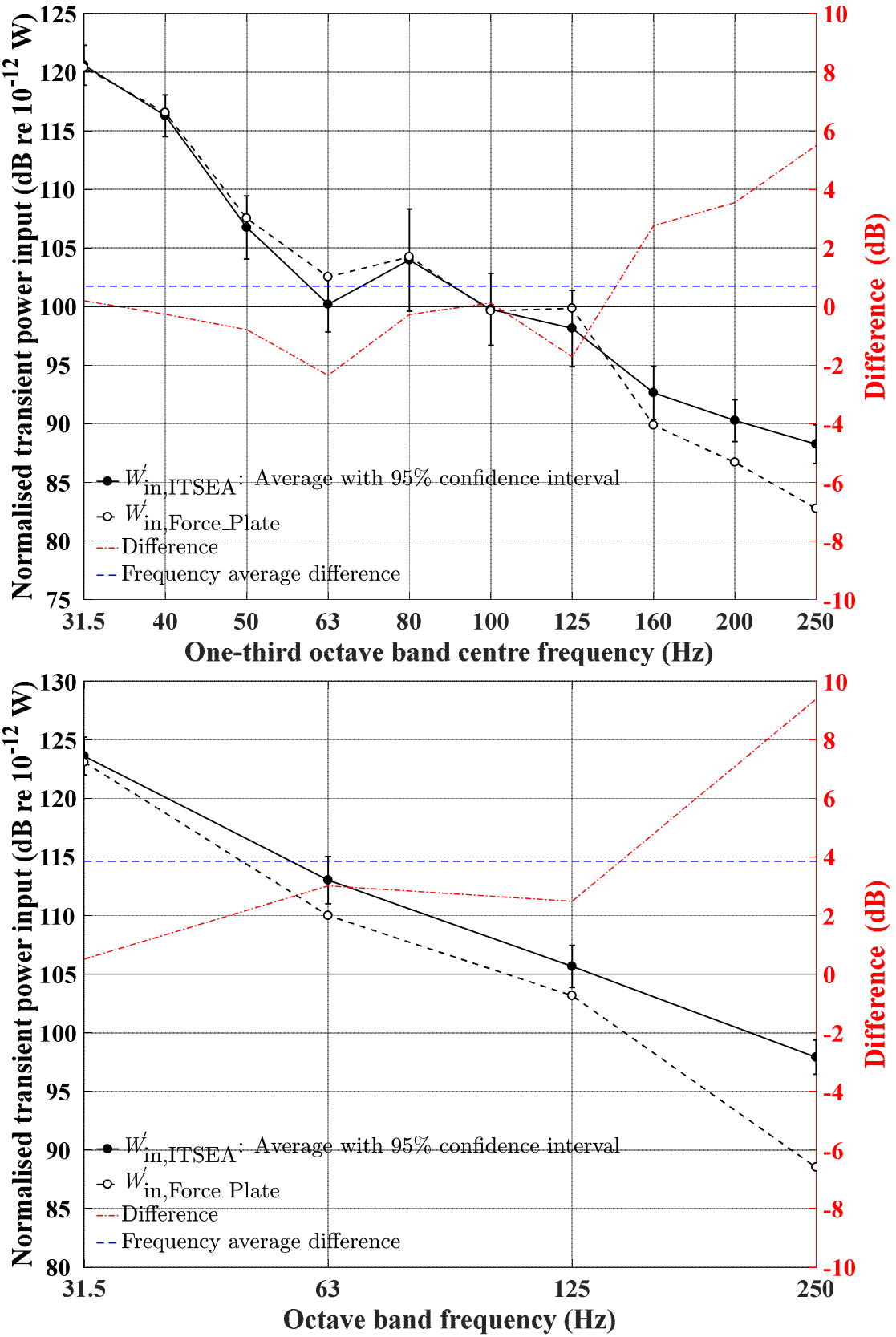

Figure 5-9. Comparison of the normalised transient power input for the rubber ball exciting locally reacting mass-spring system B on a 140mm concrete base floor determined using ITSEA and the force plate in one-third octave bands (upper) and octave bands (lower).

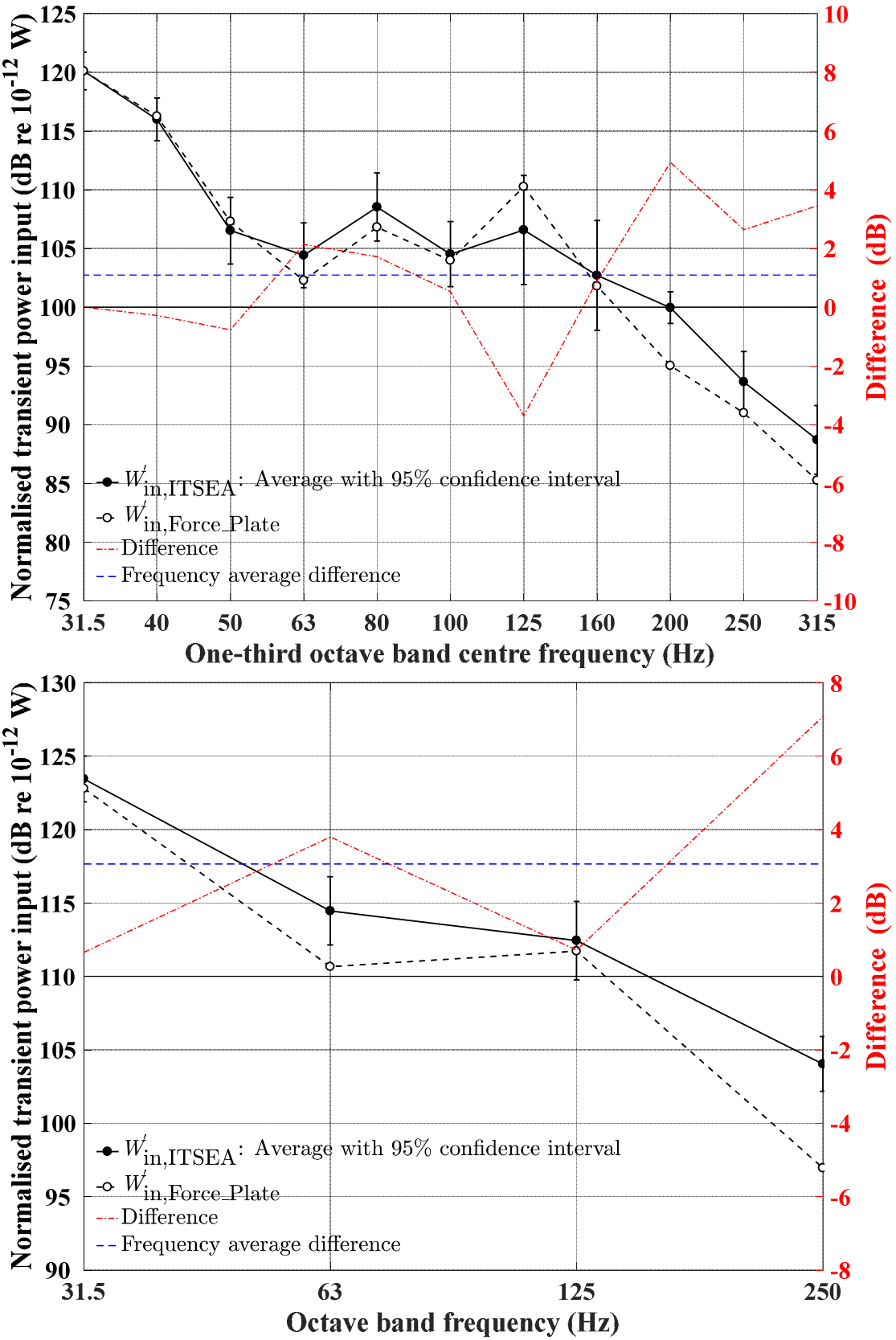

Figure 5-10. Comparison of the normalised transient power input for the rubber ball exciting locally reacting mass-spring system C on a 140mm concrete base floor determined using ITSEA and the force plate in one-third octave bands (upper) and octave bands (lower).

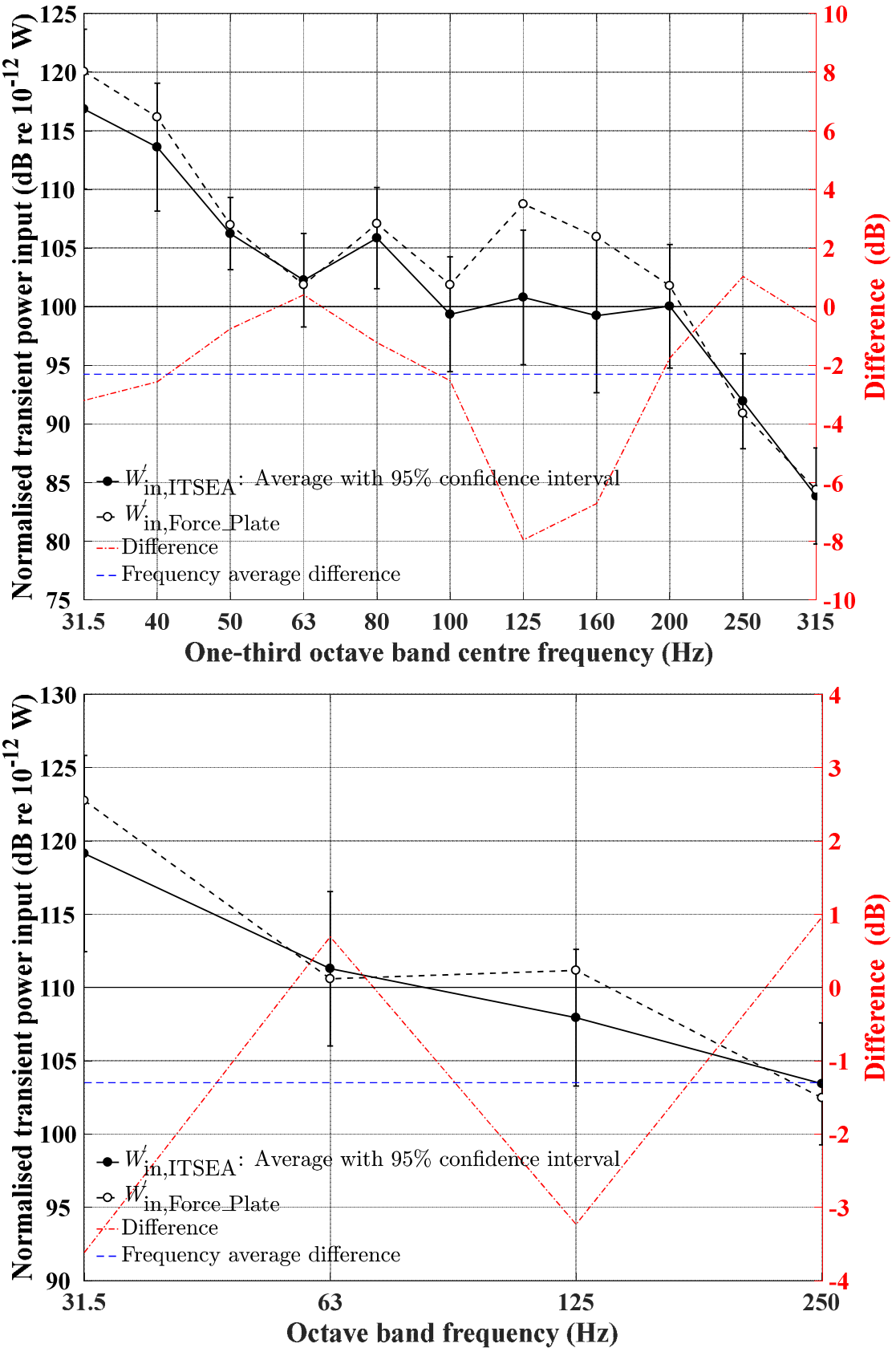

Figure 5-11. Comparison of the normalised transient power input for the rubber ball exciting locally reacting mass-spring system D on a 140mm concrete base floor determined using ITSEA and the force plate in one-third octave bands (upper) and octave bands (lower).

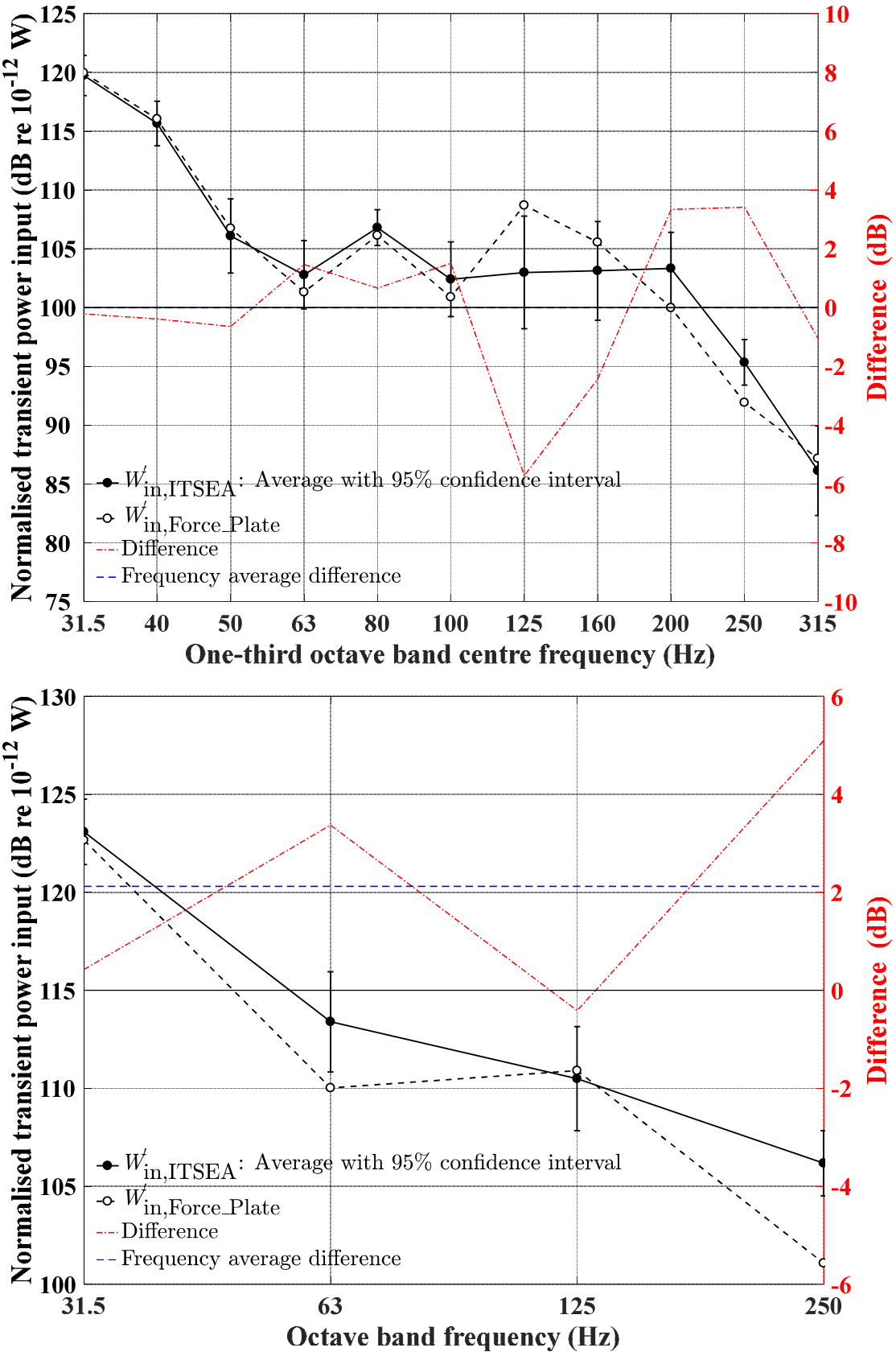

Figure 5-12. Comparison of the normalised transient power input for the rubber ball exciting locally reacting mass-spring system E on a 140mm concrete base floor determined using ITSEA and the force plate in one-third octave bands (upper) and octave bands (lower).

5.3.4.2 Test facility B

From the force plate measurements, $t_{\text{input\_duration}}$ is 18.8ms for the rubber ball and 20ms for the bang machine. These values are used to determine the normalised transient power input using Eq. (2.41).

Figure 5-13 allows comparison of the normalised transient power input from the rubber ball exciting the concrete base floor and the floating floor in octave bands. Due to the mass-spring resonance frequency of the floating floor, the power input for the floating floor at 125Hz band is higher than the power input to the bare slab for both the rubber ball and the tyre source.

Figure 5-14 allows comparison of the normalised transient power input from the tyre source exciting concrete floor and the floating floor in octave bands. Due to the mass-spring resonance frequency of the floating floor, the power input for the floating floor at 125Hz octave band is higher than the power input to the bare slab for both the rubber ball and the tyre source.

In both cases, the normalised transient power input into the base floor with the floating floor was slightly higher than the normalised transient power input for the concrete base floor in octave bands. This indicates that this particular floating floor is unlikely to be effective for heavy impacts.

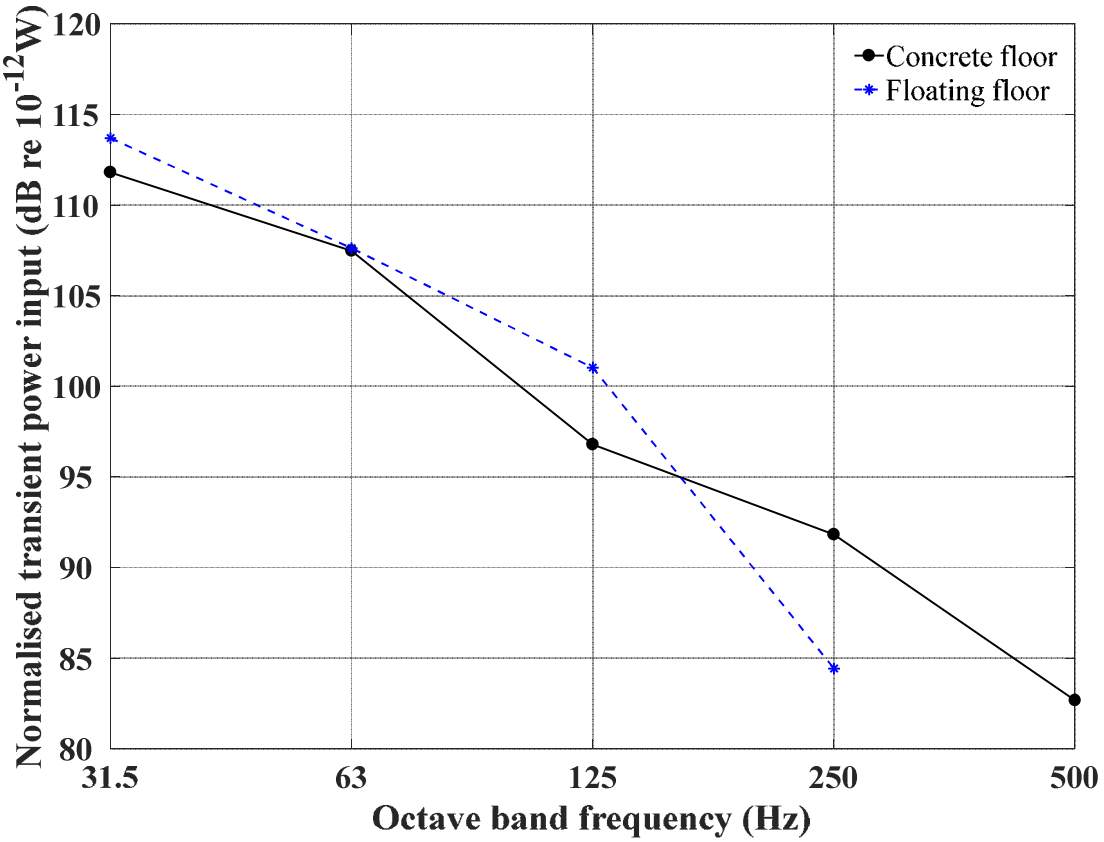

Figure 5-13.Comparison of the normalised transient power input for the rubber ball exciting different floor constructions in octave bands.

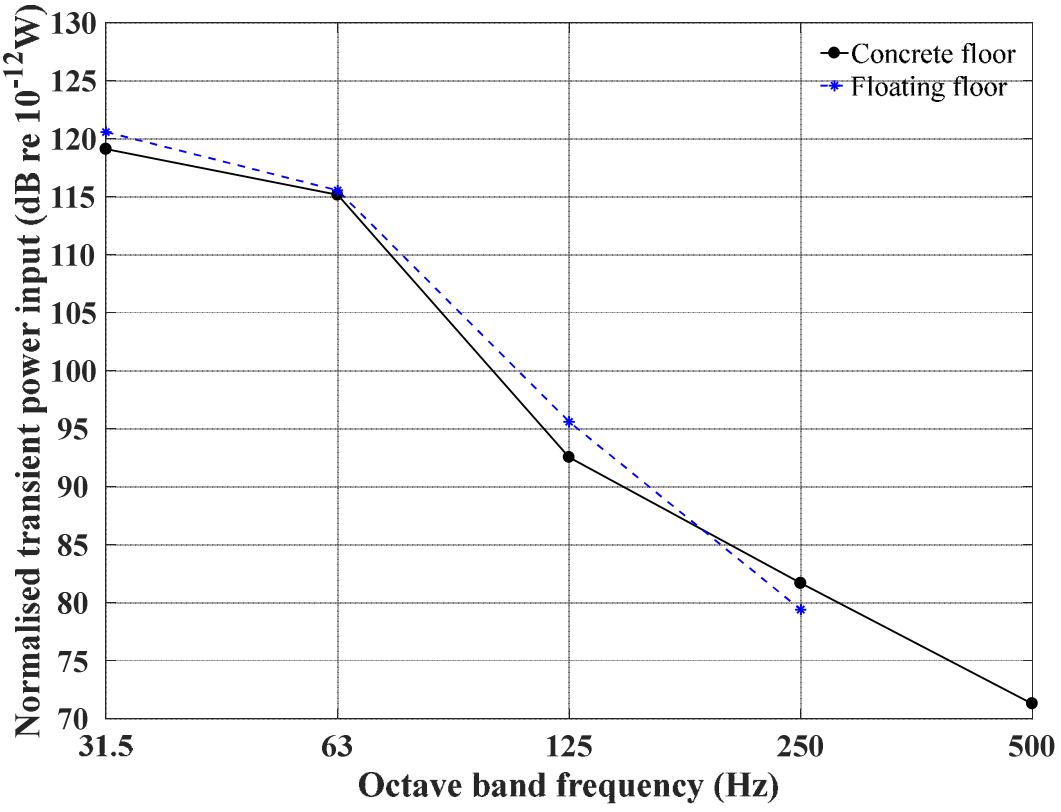

Figure 5-14. Comparison of the normalised transient power input for the tyre source exciting different floor constructions in octave bands.

5.4 Comparison of TSEA with measurements

5.4.1 Introduction

This section compares TSEA with measurements in test facility A with and without locally reacting mass-spring systems using the rubber ball and test facility B with and without a floating floor using the rubber ball and tyre source.

For the TSEA model of test facility A, the CLF from the floor to the room was calculated from the radiation efficiency that was estimated from a previous measurement [24] of the normalised impact sound pressure level with excitation from the ISO tapping machine measurement. The CLF in the reverse direction was determined using the consistency relationship. For test facility B, the CLF from the floor to the room was calculated from the frequency-average radiation efficiency using Eqs. (2.9) to (2.12) with Eq. (2.8). The CLF in the reverse direction was determined using the consistency relationship. For both facilities the TLF for the concrete base floor was estimated from the sum of all CLFs and the ILF in the TSEA model.

5.4.2 Predicting $L_{v,Fmax}$ and $L_{p,Fmax}$ in test facilities A and B

In all figures, the frequency range that is shown in the plot depends on the effectiveness of each mass-spring system or floating floor such that results are only shown when there is a measurable signal that is 10dB above background noise.

5.4.2.1 Test facility A – with and without a locally reacting mass-spring system

Figure 5-15 to Figure 5-26 allows comparison of the measurement with TSEA using from $W'_{in,Force\_Plate}$ and $W'_{in,ITSEA}$. The results are shown for the rubber ball exciting a 140mm concrete base floor and locally reacting mass-spring systems on the 140mm concrete base floor in one-third octave and octave bands. $L_{p,Fmax}$ is not shown for TSEA in the 31.5Hz in octave band because an estimate of the radiation efficiency was not available below the 50Hz one-third octave band [14].

For one-third octave bands, the maximum difference in $L_{v,Fmax}$ between measurement and TSEA (absolute value) ranged from 3.8 to 5dB, and 1.6 to 10.1dB when using $W'_{in,Force\_Plate}$ and $W'_{in,ITSEA}$ respectively. The maximum difference in $L_{p,Fmax}$ between

measurement and TSEA ranged from 5.3 to 8.3dB, and 6 to 7dB when using $W'_{\text{in,Force\_Plate}}$ and $W'_{\text{in,ITSEA}}$ respectively.

For octave bands, the maximum difference in $L_{\text{v,Fmax}}$ between measurement and TSEA (absolute value) ranged from 2.2 to 7.1dB, and 0.8 to 9.6dB for using $W'_{\text{in,Force\_Plate}}$ and $W'_{\text{in,ITSEA}}$ respectively. The maximum difference in $L_{\text{p,Fmax}}$ between measurement and TSEA ranged from 2.1 to 7.5dB, and 2 to 7dB when using $W'_{\text{in,Force\_Plate}}$ and $W'_{\text{in,ITSEA}}$ respectively.

It is noteworthy that measured and $L_{\text{v,Fmax}}$ predicted with TSEA using $W'_{\text{in,ITSEA}}$ is within the 95% confidence intervals of measurements in most of the time, except for locally reacting mass-spring A. For the mass-spring A, there is more than 6dB under-estimation in between 125 and 160Hz one-third octave bands, and 125Hz octave band. In general, the measurement and $L_{\text{p,Fmax}}$ predicted with TSEA using $W'_{\text{in,ITSEA}}$, the peaks and troughs occur at same frequency bands.

Table 5.5 and Table 5.6 summarises the frequency-average difference between measurement and TSEA using $W'_{\text{in,Force\_Plate}}$ or $W'_{\text{in,ITSEA}}$. in terms of $L_{\text{p,Fmax}}$ and $L_{\text{v,Fmax}}$ The average difference is considered to be acceptable because (1) the general trend of the measurement and TSEA values are similar; they overlap and cross over each other, and (2) the 95% confidence intervals in the measurement overalap the predicted curves. Therefore, the frequency-average difference in $L_{\text{p,Fmax}}$ between measurement and TSEA using $W'_{\text{in,ITSEA}}$ of 3.7dB in one-third octave bands and 2.7dB in octave bands is considered as an acceptable difference. This confirms that ITSEA can be used to predict the normalised transient power input with and without locally reacting mass-spring system, and can be used in the TSEA model to incorporate the locally reacting mass-spring systems.

Table 5.5. Frequency-average difference between measurement and TSEA for $L_{p,Fmax}$ and $L_{v,Fmax}$ in one-third octave band for test facility A.

	Transient power input		Locally reacting mass-spring systems				
		Direct	A	B	C	D	E
$L_{p,Fmax}$ (dB)	Force Plate	-2.6	-4.1	-1.8	-0.5	-1	-1.1
	ITSEA	-2	-1.3	-3.7	-2.4	-0.7	-2.1
$L_{v,Fmax}$ (dB)	Force Plate	-1.3	-1.3	1.8	2	1.2	1
	ITSEA	-0.7	1.5	-0.1	-0.3	1.3	0.1

Table 5.6. Frequency-average difference between measurement and TSEA for $L_{p,Fmax}$ and $L_{v,Fmax}$ in octave bands for test facility A.

	Transient power input		Locally reacting mass-spring systems				
		Direct	A	B	C	D	E
$L_{p,Fmax}$ (dB)	Force Plate	2.3	-1.2	2.6	3.5	2.9	3.3
	ITSEA	-0.7	1.2	-2.7	-1	0.6	0.1
$L_{v,Fmax}$ (dB)	Force Plate	1.7	1.4	5.4	4.7	3.1	3.7
	ITSEA	-1.2	3.8	0.1	0.3	0.8	0.3

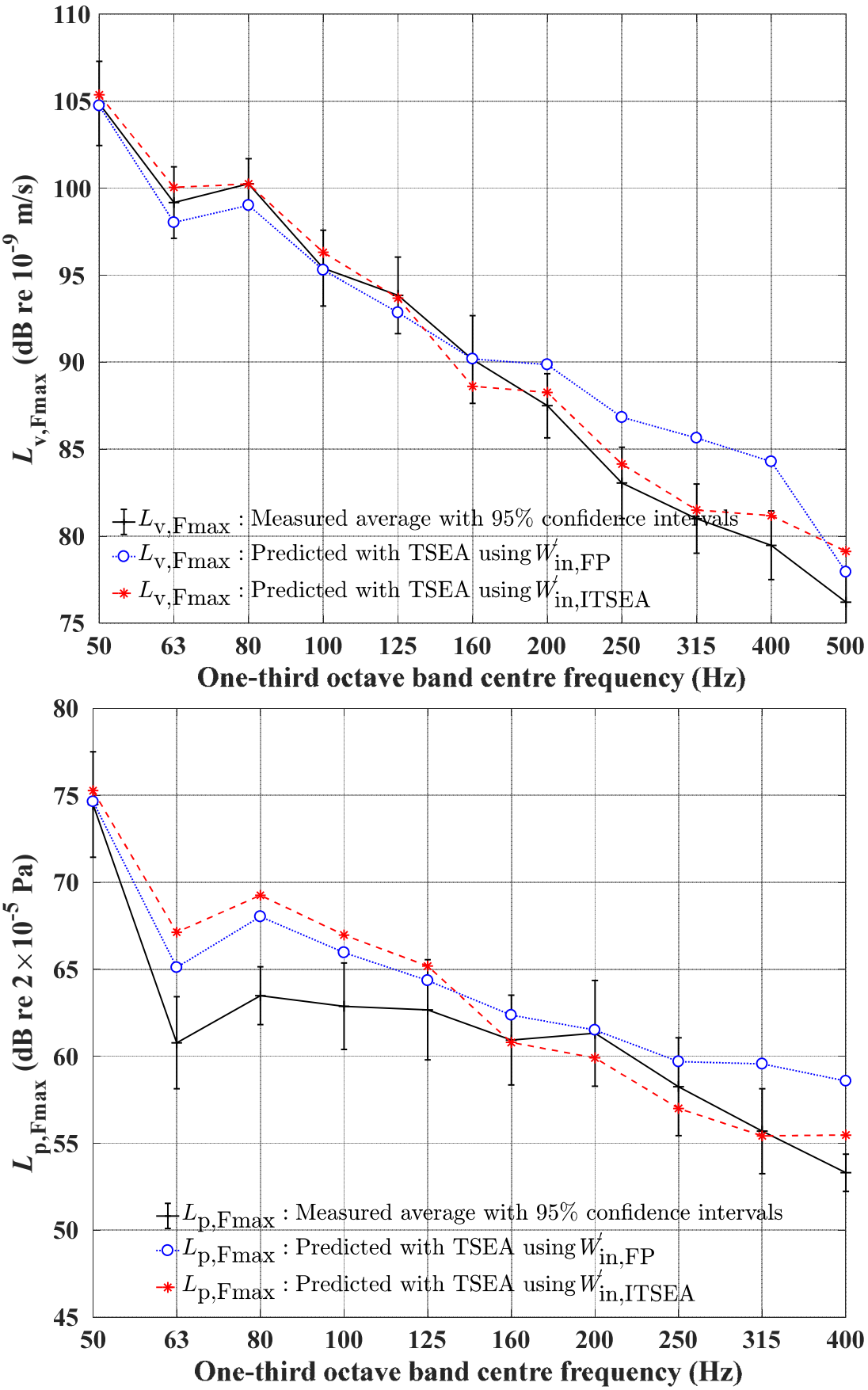

Figure 5-15. Comparison of measured and predicted $L_{v,Fmax}$ (upper) and $L_{p,Fmax}$ (lower) for the rubber ball exciting a 140mm concrete base floor in one-third octave bands.

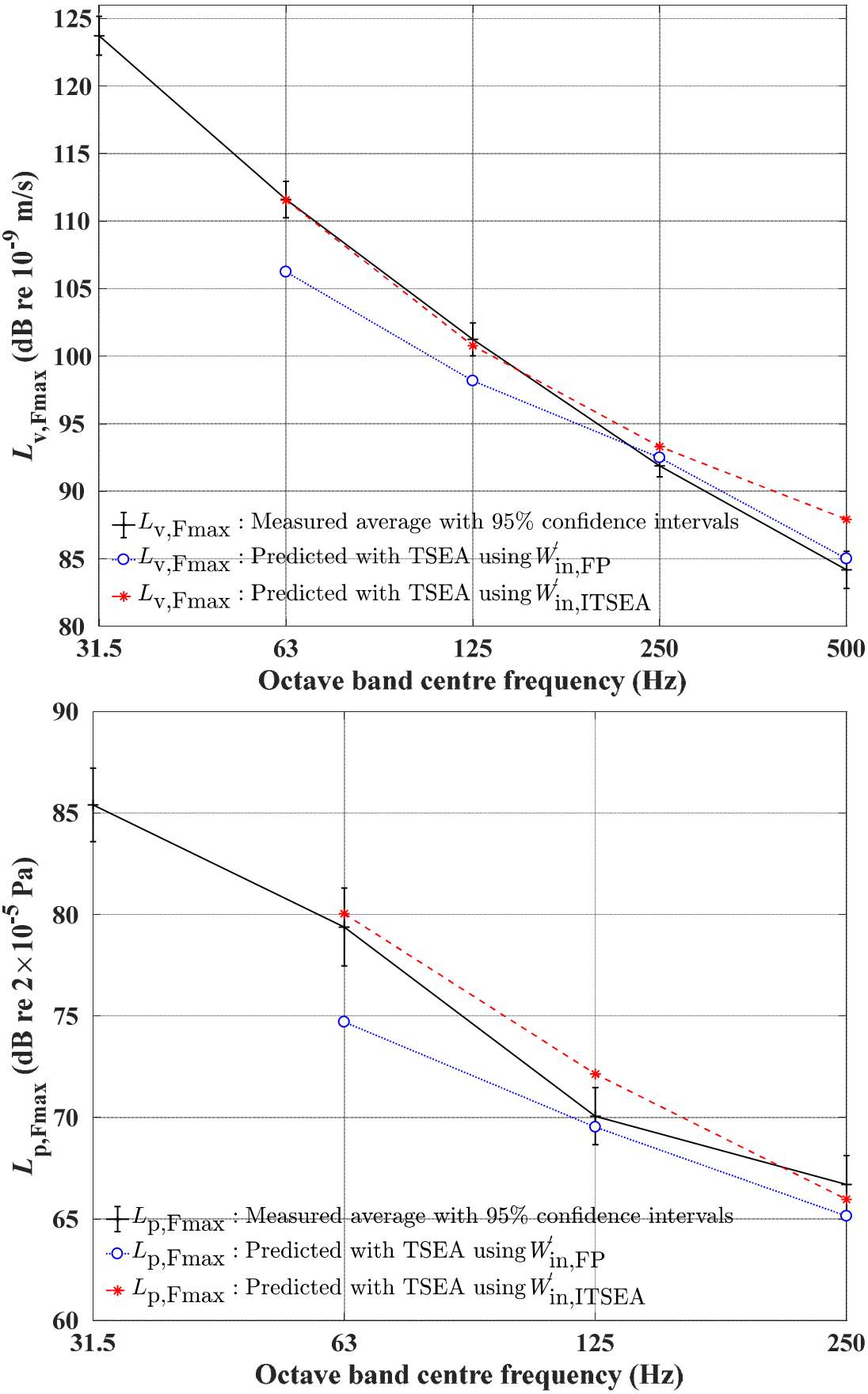

Figure 5-16. Comparison of measured and predicted $L_{v,Fmax}$ (upper) and $L_{p,Fmax}$ (lower) for the rubber ball exciting a 140mm concrete base floor in octave bands.

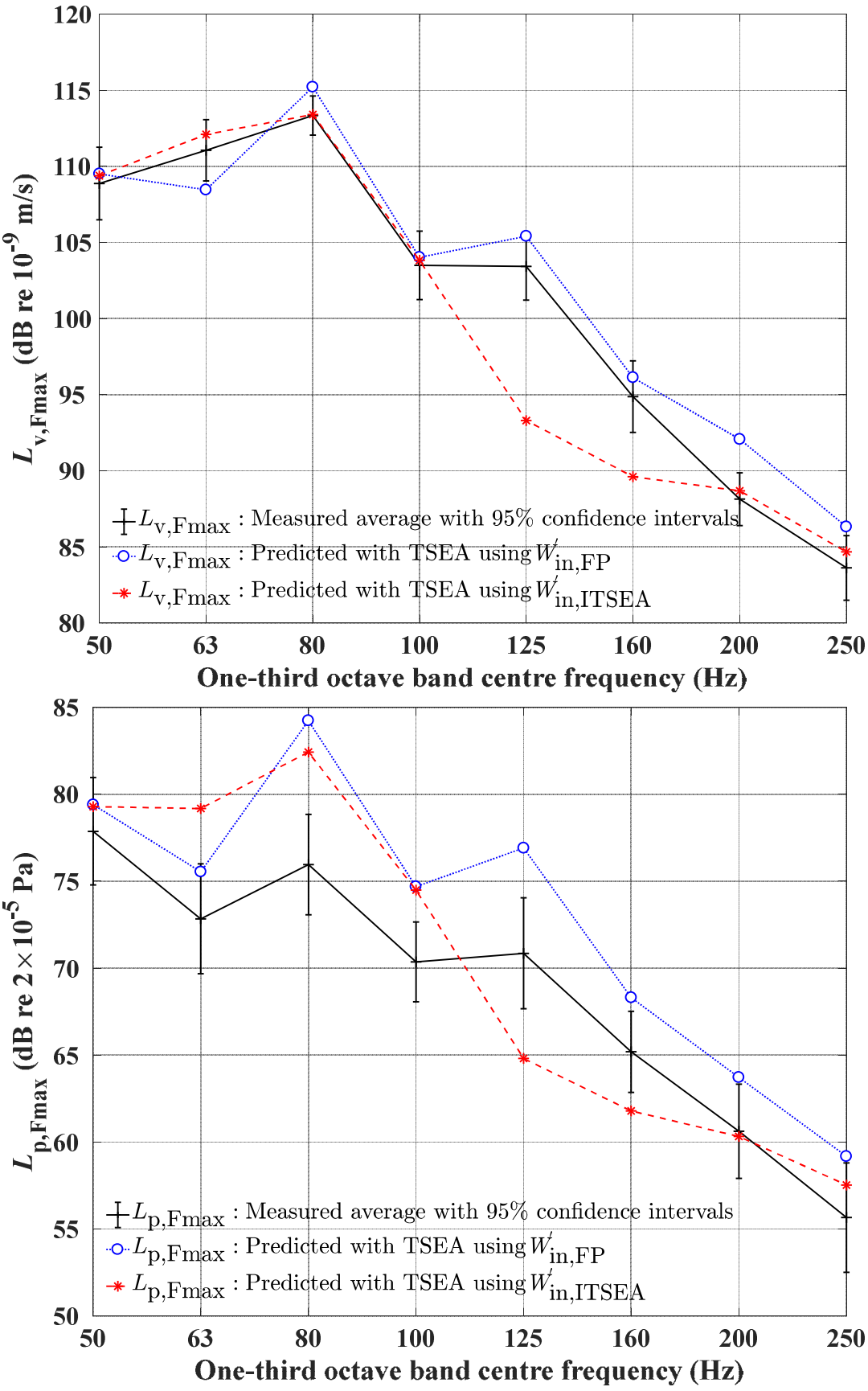

Figure 5-17. Comparison of measured and predicted $L_{v,Fmax}$ (upper) and $L_{p,Fmax}$ (lower) for the rubber ball exciting locally reacting mass-spring system A on the 140mm concrete base floor in one-third octave bands.

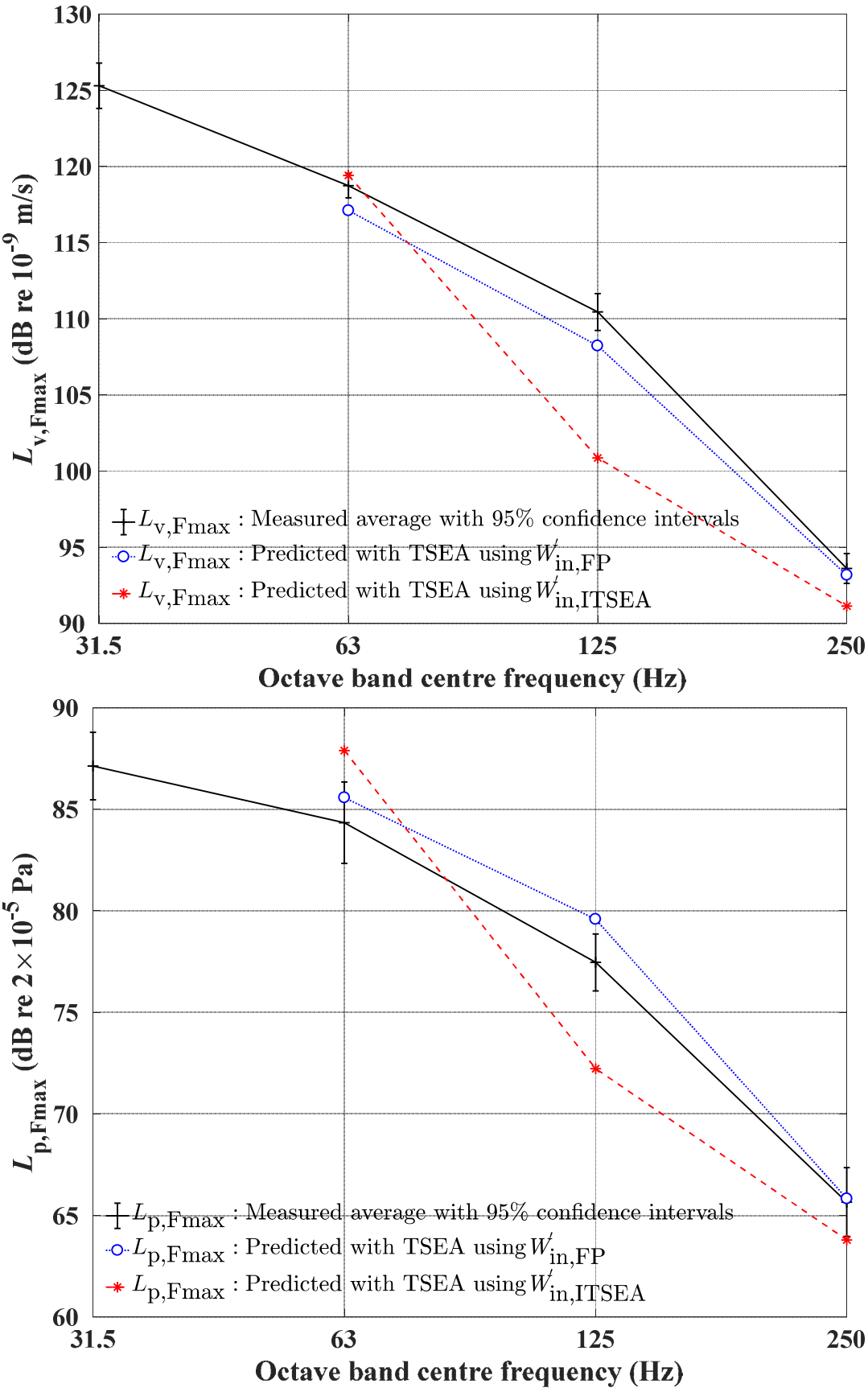

Figure 5-18. Comparison of measured and predicted $L_{v,Fmax}$ (upper) and $L_{p,Fmax}$ (lower) for the rubber ball exciting locally reacting mass-spring system A on the 140mm concrete base floor in octave bands.

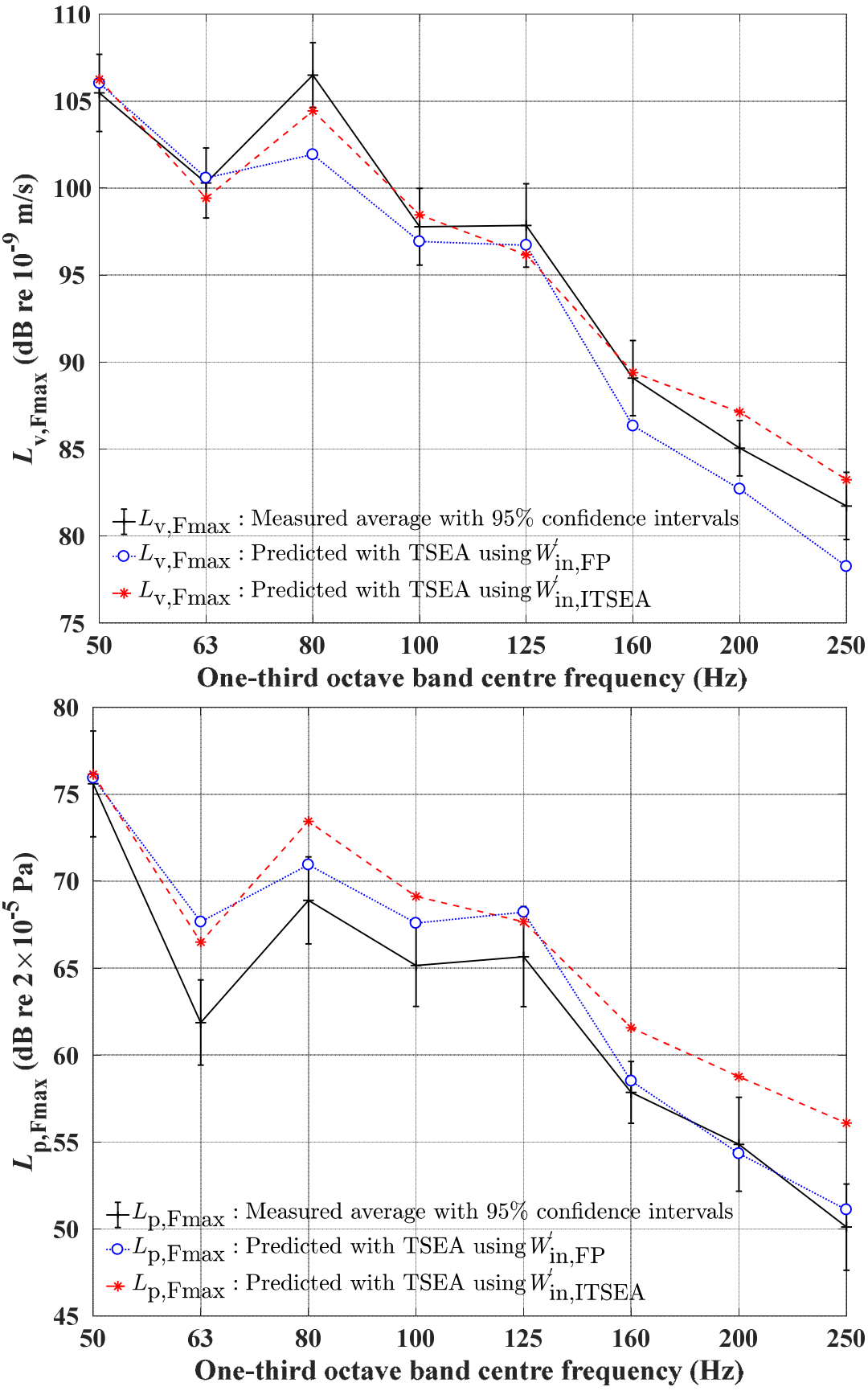

Figure 5-19. Comparison of measured and predicted $L_{v,Fmax}$ (upper) and $L_{p,Fmax}$ (lower) for the rubber ball exciting locally reacting mass-spring system B on the 140mm concrete base floor in one-third octave bands.

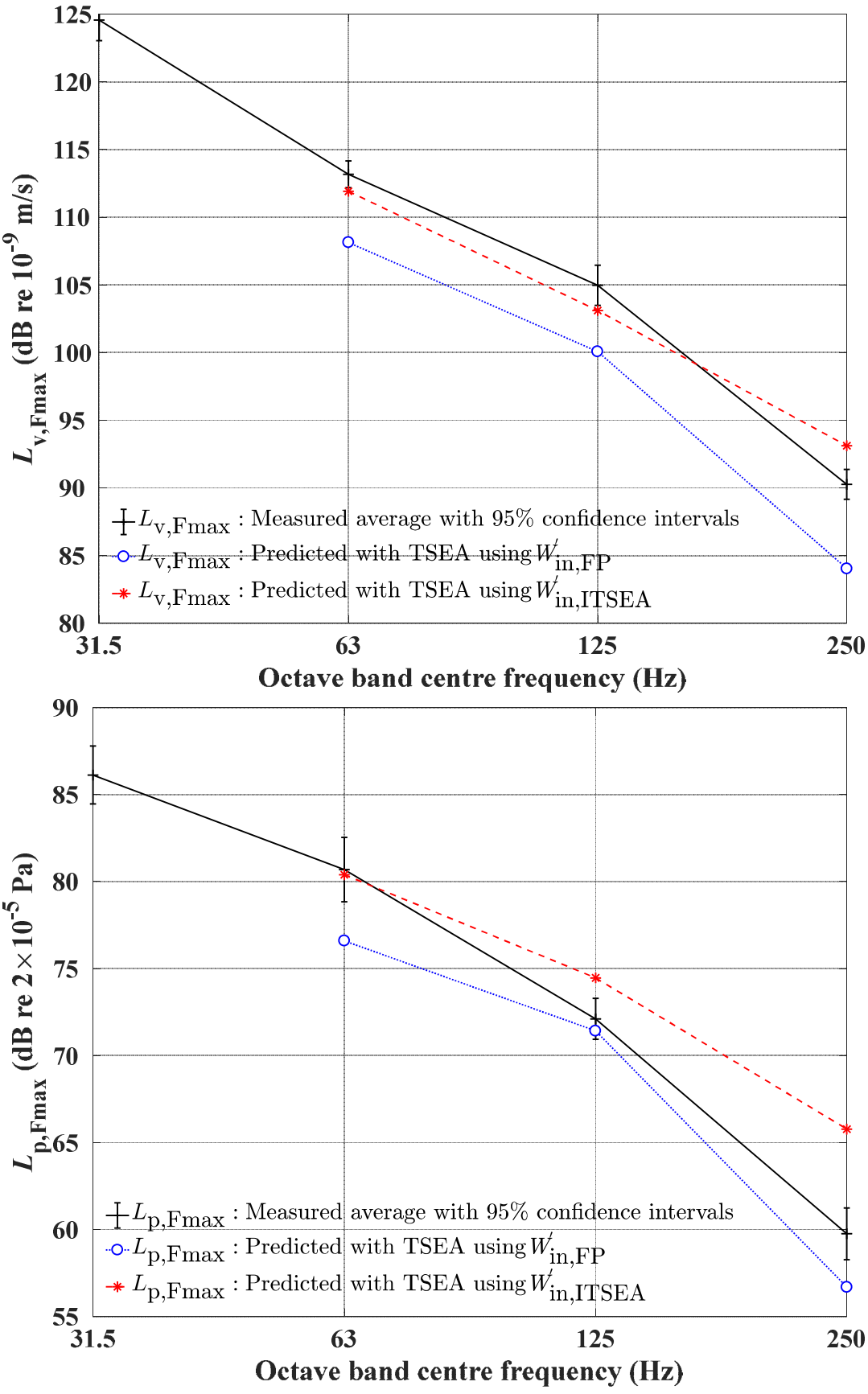

Figure 5-20. Comparison of measured and predicted $L_{v,Fmax}$ (upper) and $L_{p,Fmax}$ (lower) for the rubber ball exciting locally reacting mass-spring system B on the 140mm concrete base floor in octave bands.

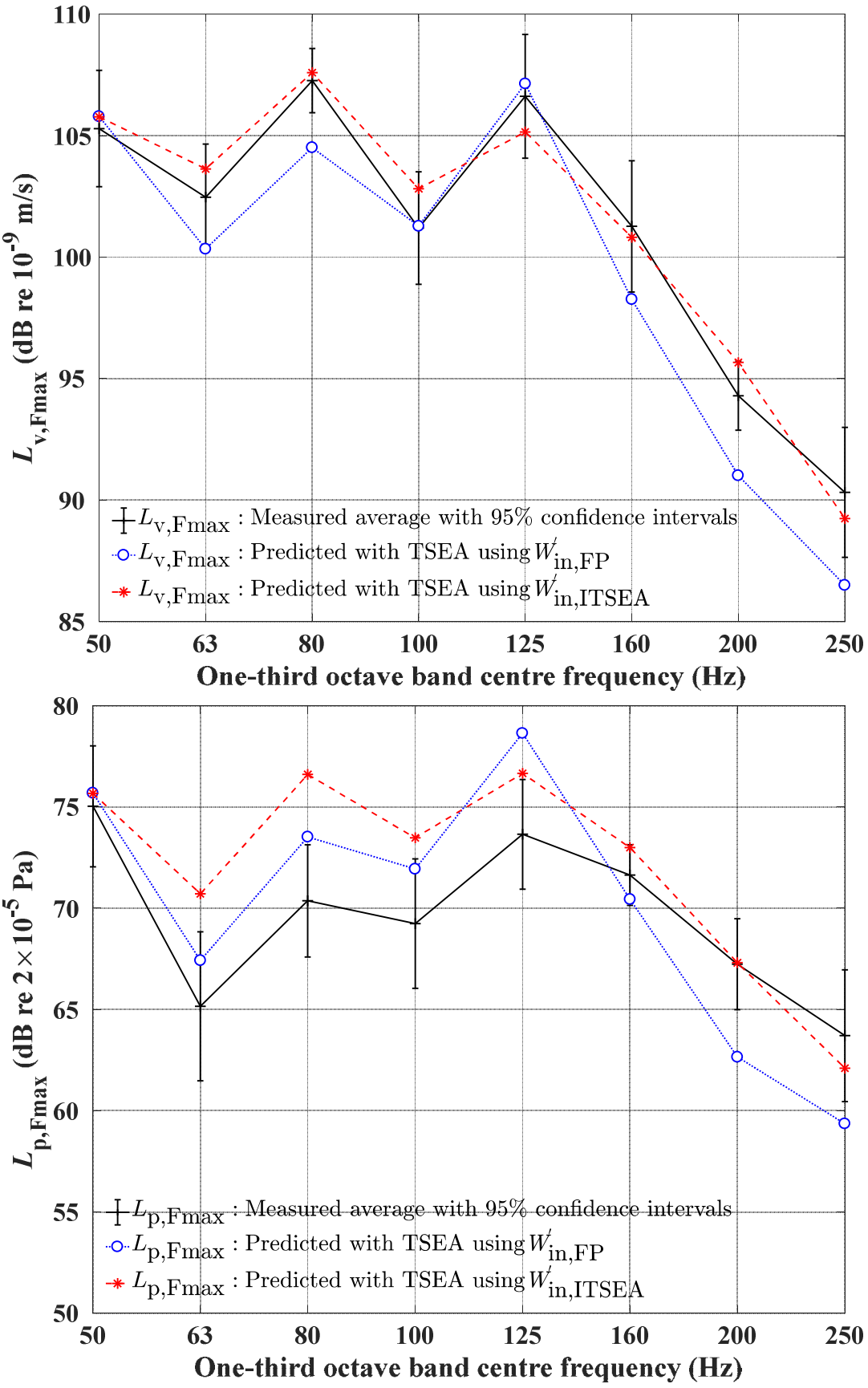

Figure 5-21. Comparison of measured and predicted $L_{v,Fmax}$ (upper) and $L_{p,Fmax}$ (lower) for the rubber ball exciting locally reacting mass-spring system C on the 140mm concrete base floor in one-third octave bands.

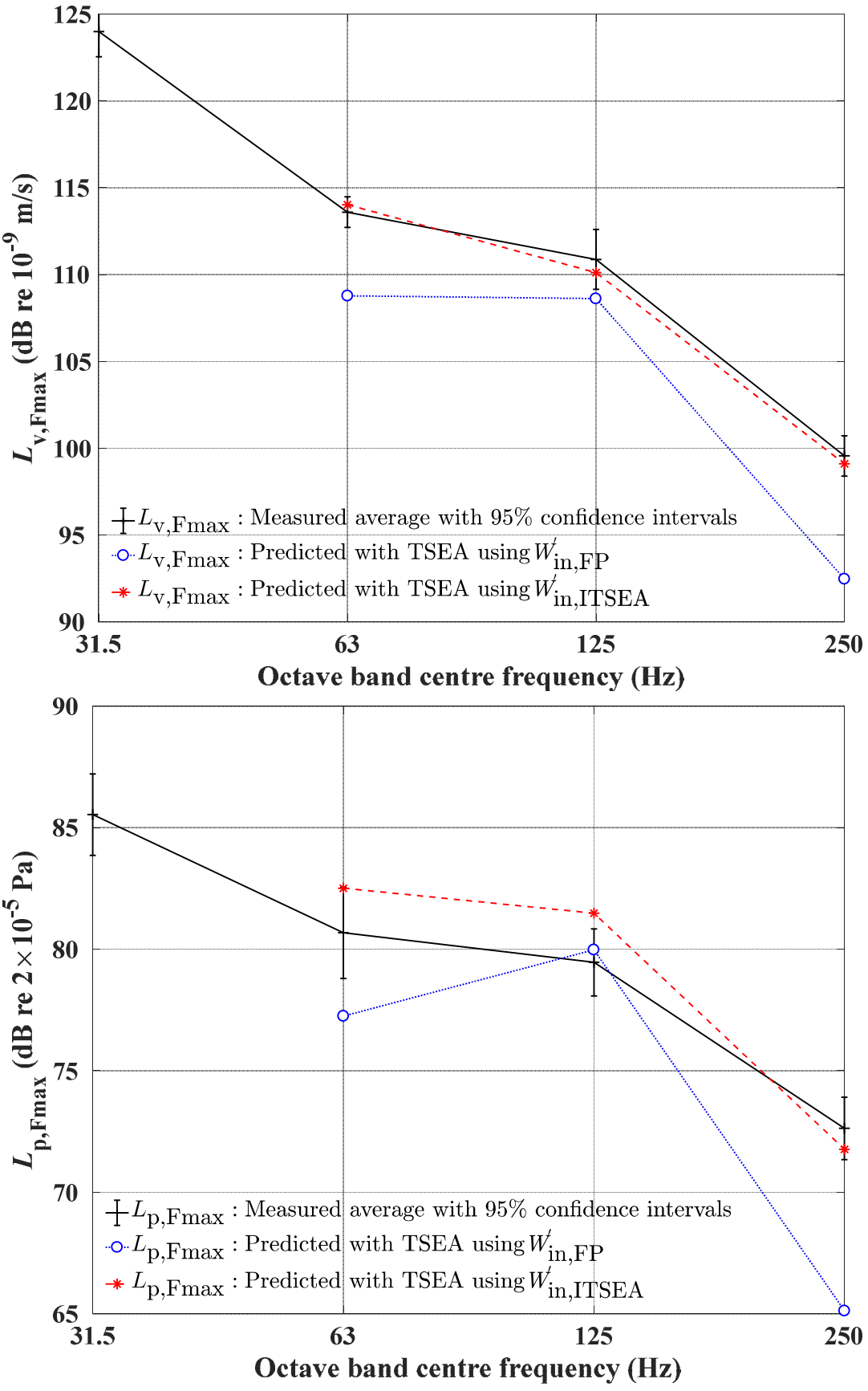

Figure 5-22. Comparison of measured and predicted $L_{v,Fmax}$ (upper) and $L_{p,Fmax}$ (lower) for the rubber ball exciting locally reacting mass-spring system C on the 140mm concrete base floor in octave bands.

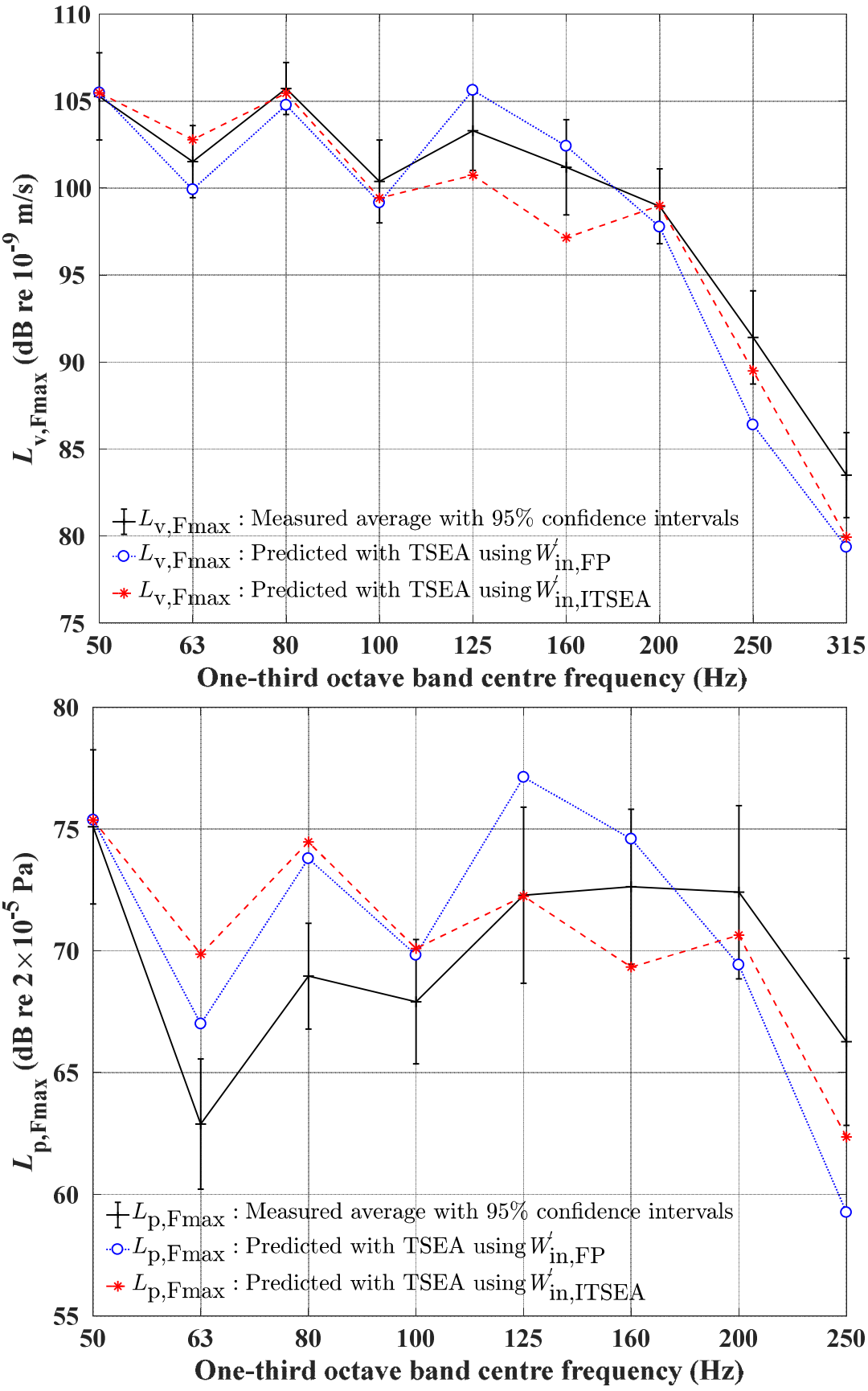

Figure 5-23. Comparison of measured and predicted $L_{v,Fmax}$ (upper) and $L_{p,Fmax}$ (lower) for the rubber ball exciting locally reacting mass-spring system D on the 140mm concrete base floor in one-third octave bands.

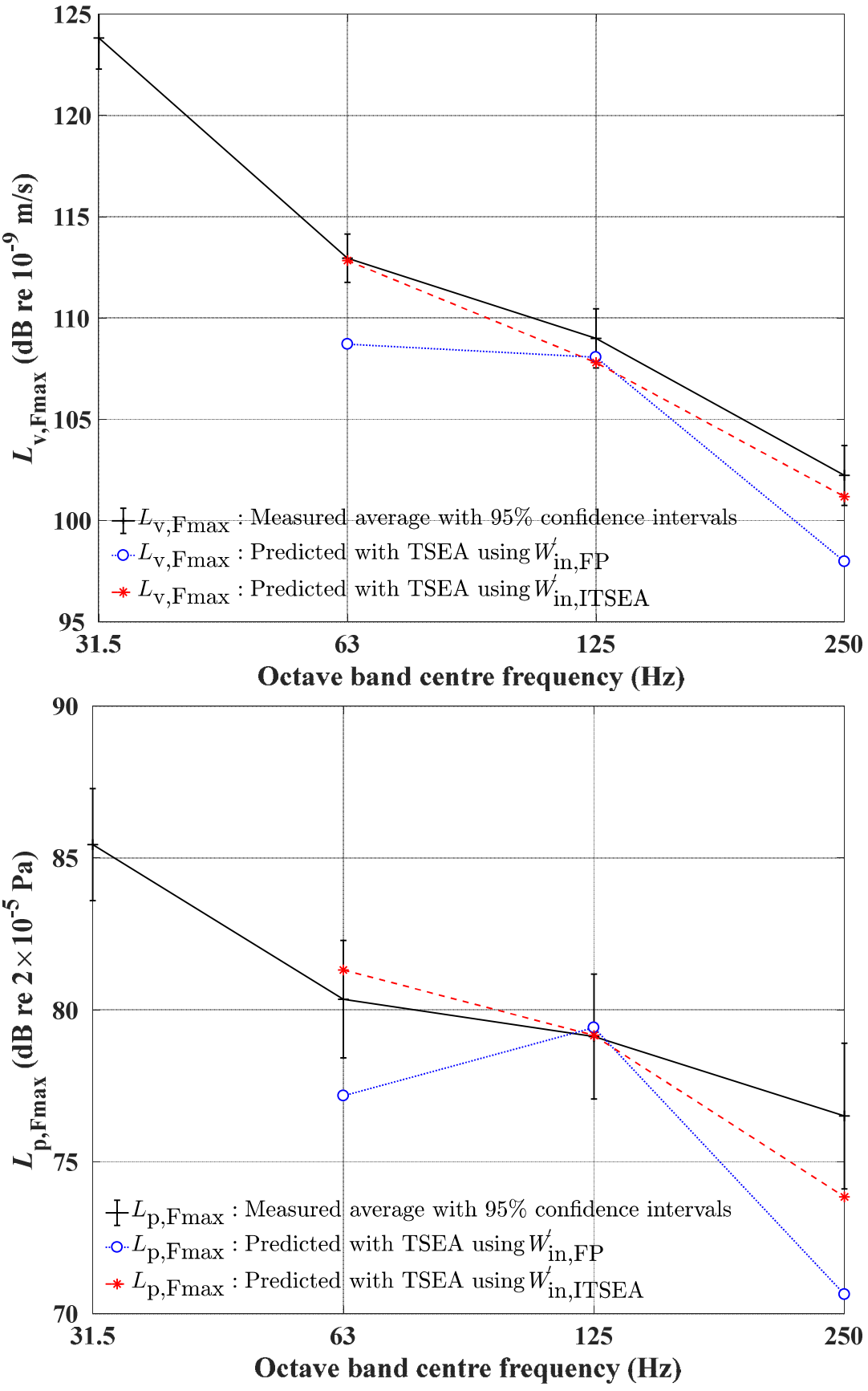

Figure 5-24. Comparison of measured and predicted $L_{v,Fmax}$ (upper) and $L_{p,Fmax}$ (lower) for the rubber ball exciting locally reacting mass-spring system D on the 140mm concrete base floor in octave bands.

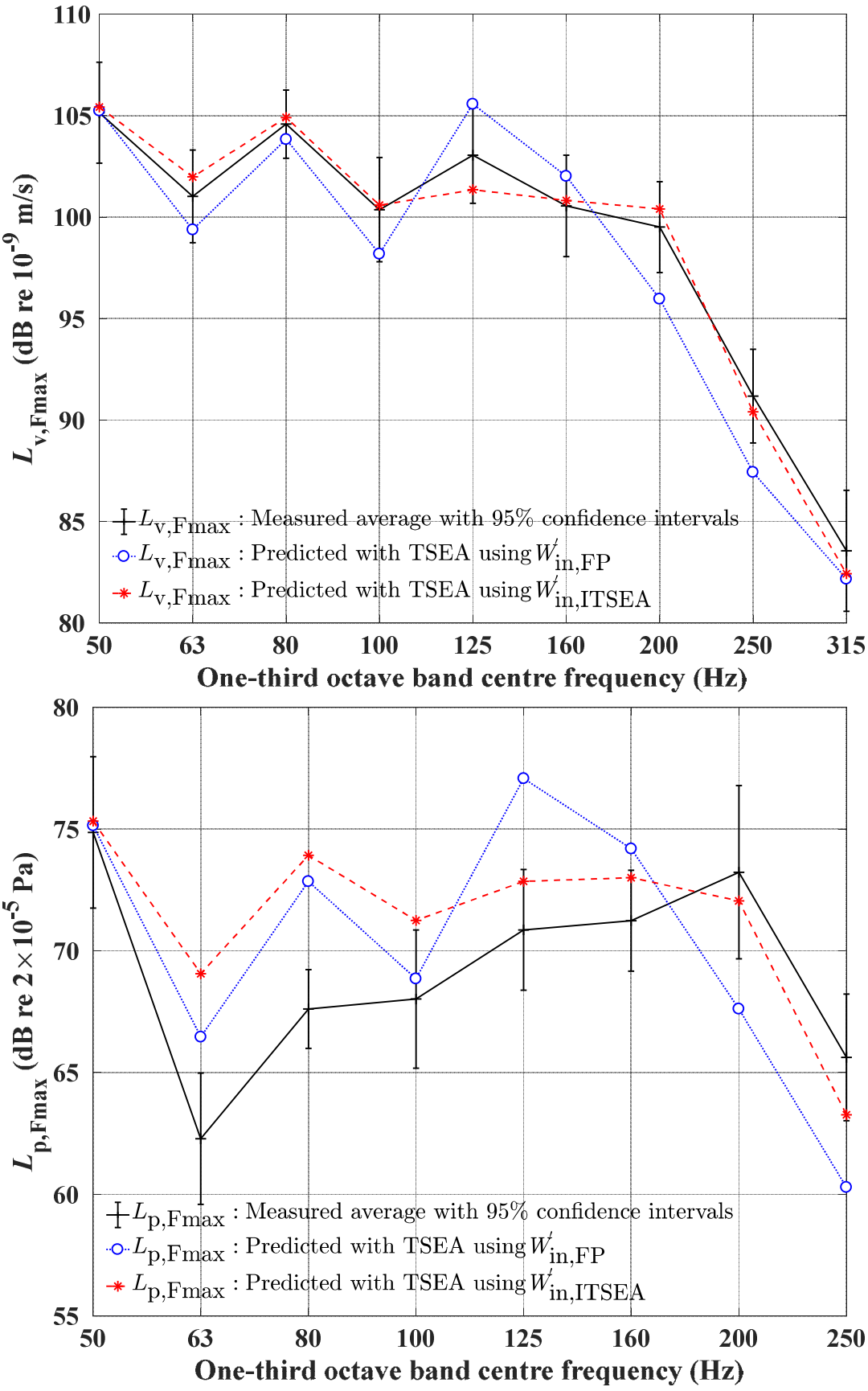

Figure 5-25. Comparison of measured and predicted $L_{v,Fmax}$ (upper) and $L_{p,Fmax}$ (lower) for the rubber ball exciting locally reacting mass-spring system E on the 140mm concrete base floor in one-third octave bands.

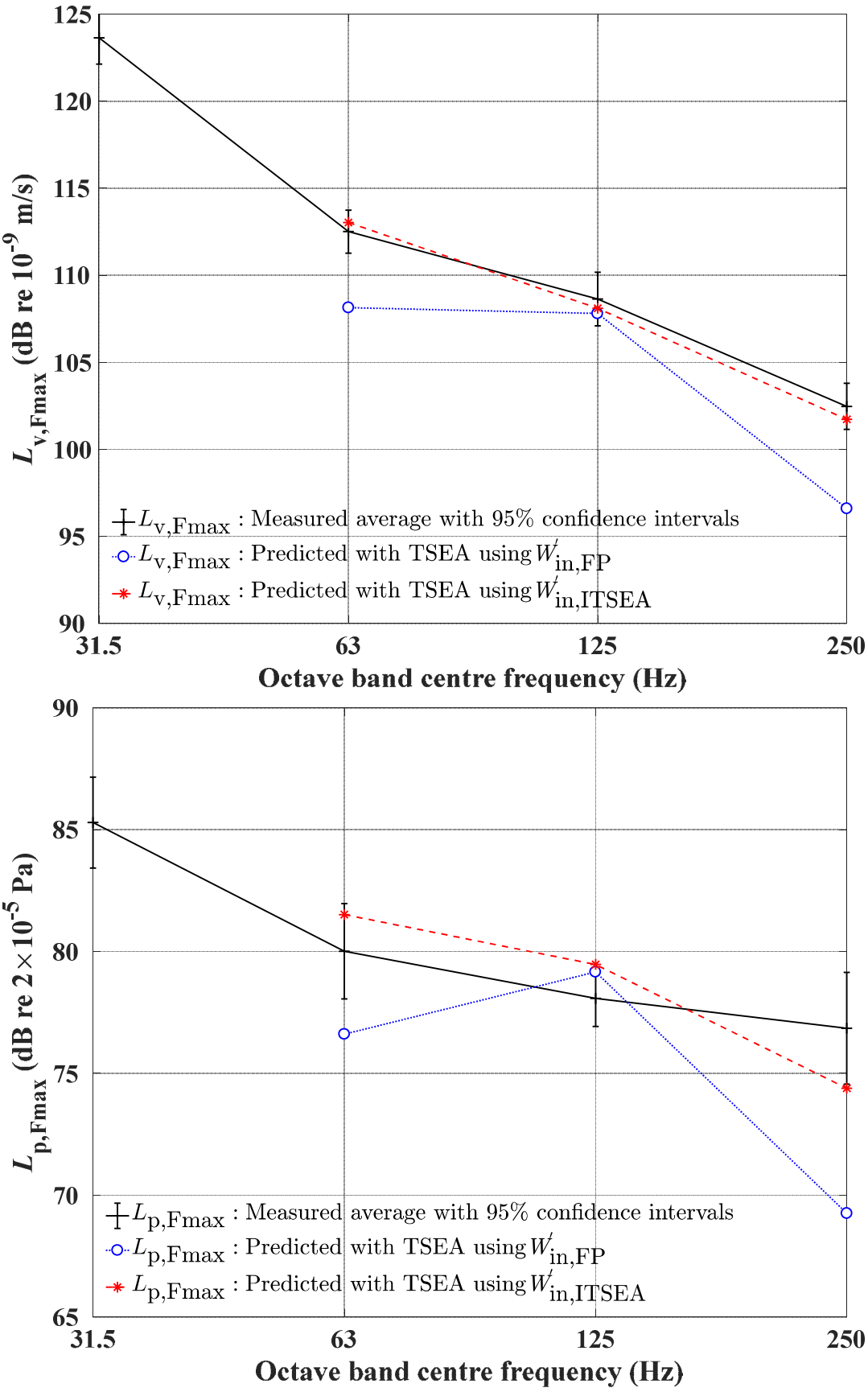

Figure 5-26. Comparison of measured and predicted $L_{v,Fmax}$ (upper) and $L_{p,Fmax}$ (lower) for the rubber ball exciting an locally reacting mass-spring system E on the 140mm concrete base floor in octave bands.

5.4.2.2 Test facility B – with and without floating floor

Figure 5-27 and Figure 5-28 allow comparison of $L_{v,Fmax}$ and $L_{p,Fmax}$ for the rubber ball and tyre source dropping on the 210mm base floor.

Figure 5-29 to Figure 5-30 shows the comparison of the $L_{v,Fmax}$ and $L_{p,Fmax}$ for the rubber ball and tyre source dropping on the floating floor on the 210mm base floor.

In octave bands there is a difference of over 10dB in $L_{p,Fmax}$ in the 31.5 and 63Hz octave bands. This is likely to be due to an overestimation of the CLF between the concrete slab and the room. An underestimation of $L_{p,Fmax}$ occurs with both excitation sources in the 500Hz octave bands. This may be due to the underestimation of W'_{in}.

Table 5.7 shows the frequency-average difference between measurement and TSEA over all octave bands. This shows that there is reasonable agreement(i.e. <5dB) between measurement and TSEA because the aforementioned overestimation and underestimation partly cancel each other out.

The general trend of the measurement and TSEA $L_{v,Fmax}$ and $L_{p,Fmax}$ above 125Hz octave bands are similar; they overlap and cross over each other. This confirms that ITSEA can be used with two different excitation sources, (rubber ball and tyre source) to predict the normalised transient power input with and without the Ondol floating floor. It also confirms that ITSEA can be used in the TSEA model to incorporate the floating floor and different excitation sources.

Table 5.7. Frequency-average difference in $L_{p,Fmax}$ and L_{vFmax} between measurement and TSEA in octave bands for test facility B.

	Rubber Ball	**Tyre source**	**Rubber ball (Floating floor)**	**Tyre source (Floating floor)**
$L_{p,Fmax}$ **(dB)**	-3.7	-2.5	-3.2	-2.6
$L_{v,Fmax}$ **(dB)**	-2.7	-1.5	-0.9	-0.7

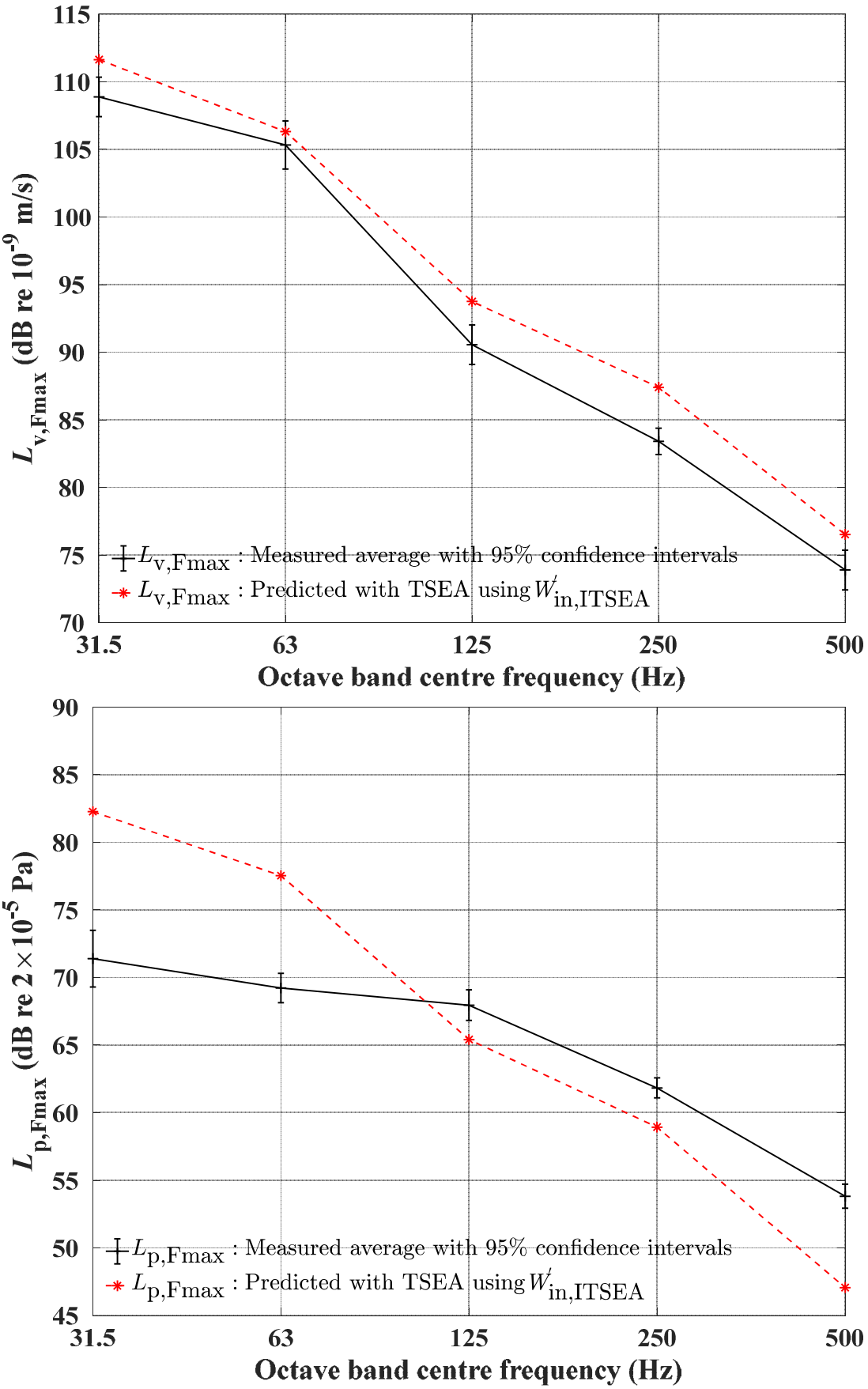

Figure 5-27. Comparison of $L_{v,Fmax}$ (upper) and $L_{p,Fmax}$ (lower) for the rubber ball exciting a 210mm concrete base floor in octave bands.

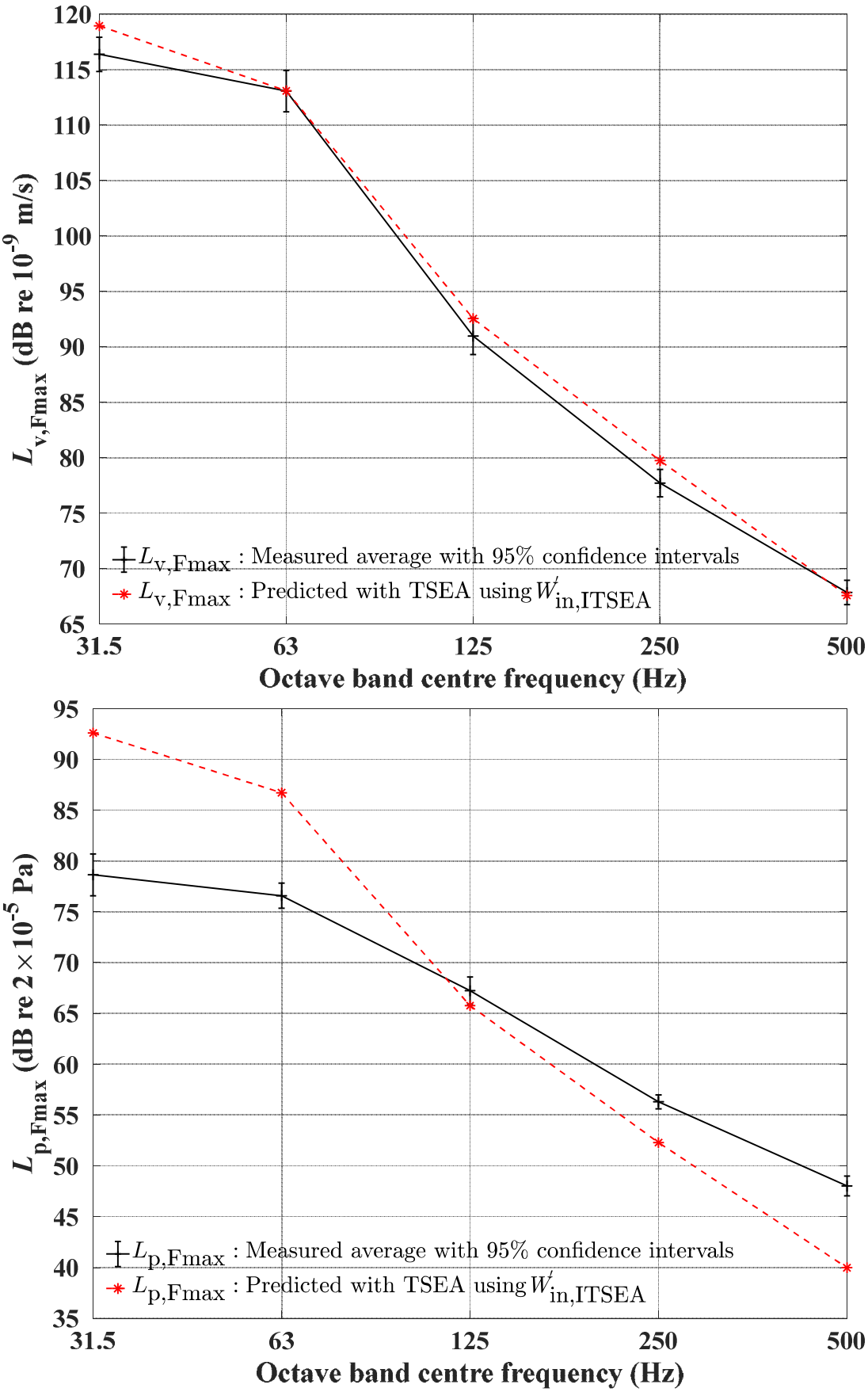

Figure 5-28. Comparison of $L_{v,Fmax}$ (upper) and $L_{p,Fmax}$ (lower) for the tyre source exciting a 210mm concrete base floor in octave bands.

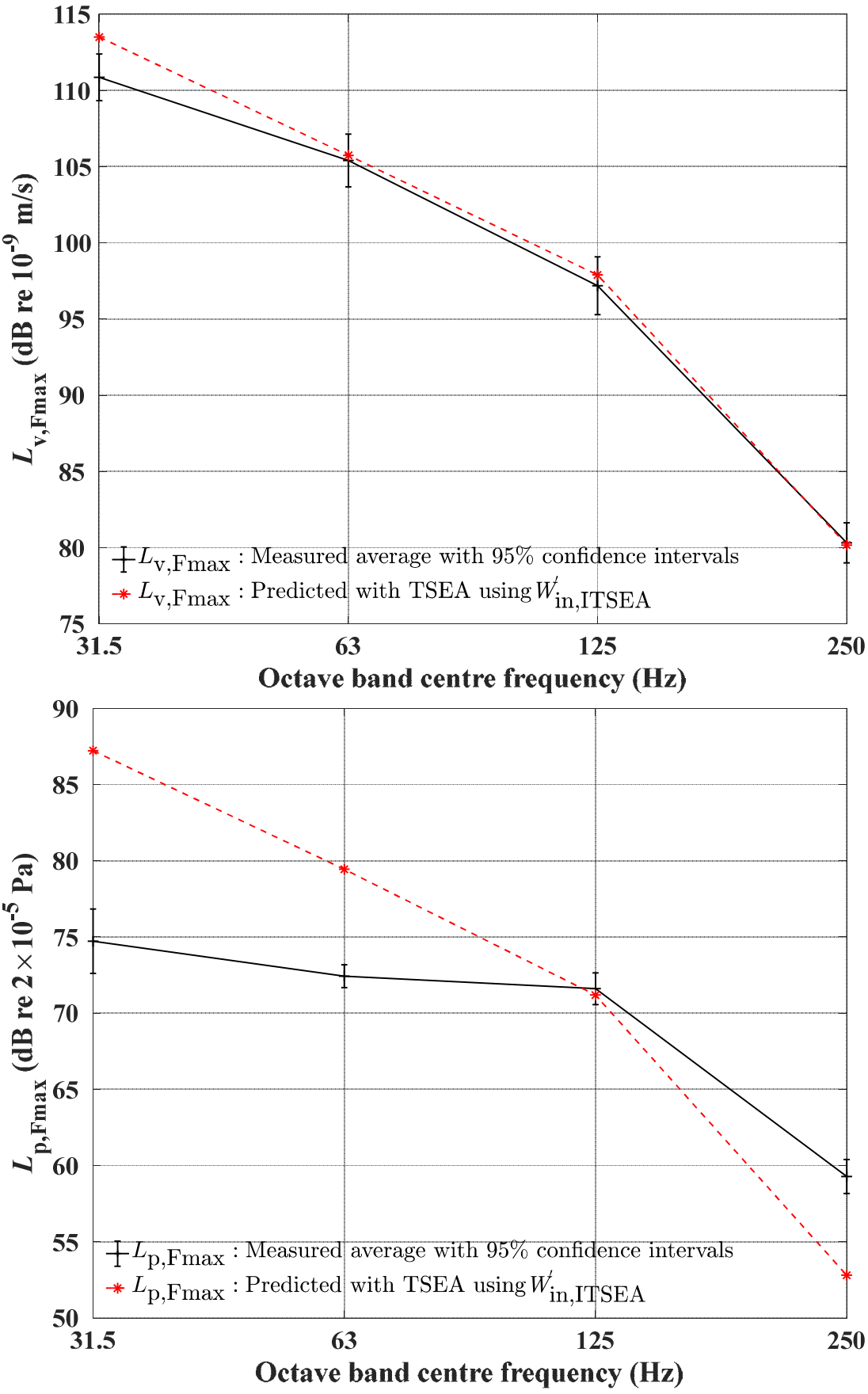

Figure 5-29. Comparison of $L_{v,Fmax}$ (upper) and $L_{p,Fmax}$ (lower) for the rubber ball exciting a floating floor on a 210mm concrete base floor excitation in octave bands.

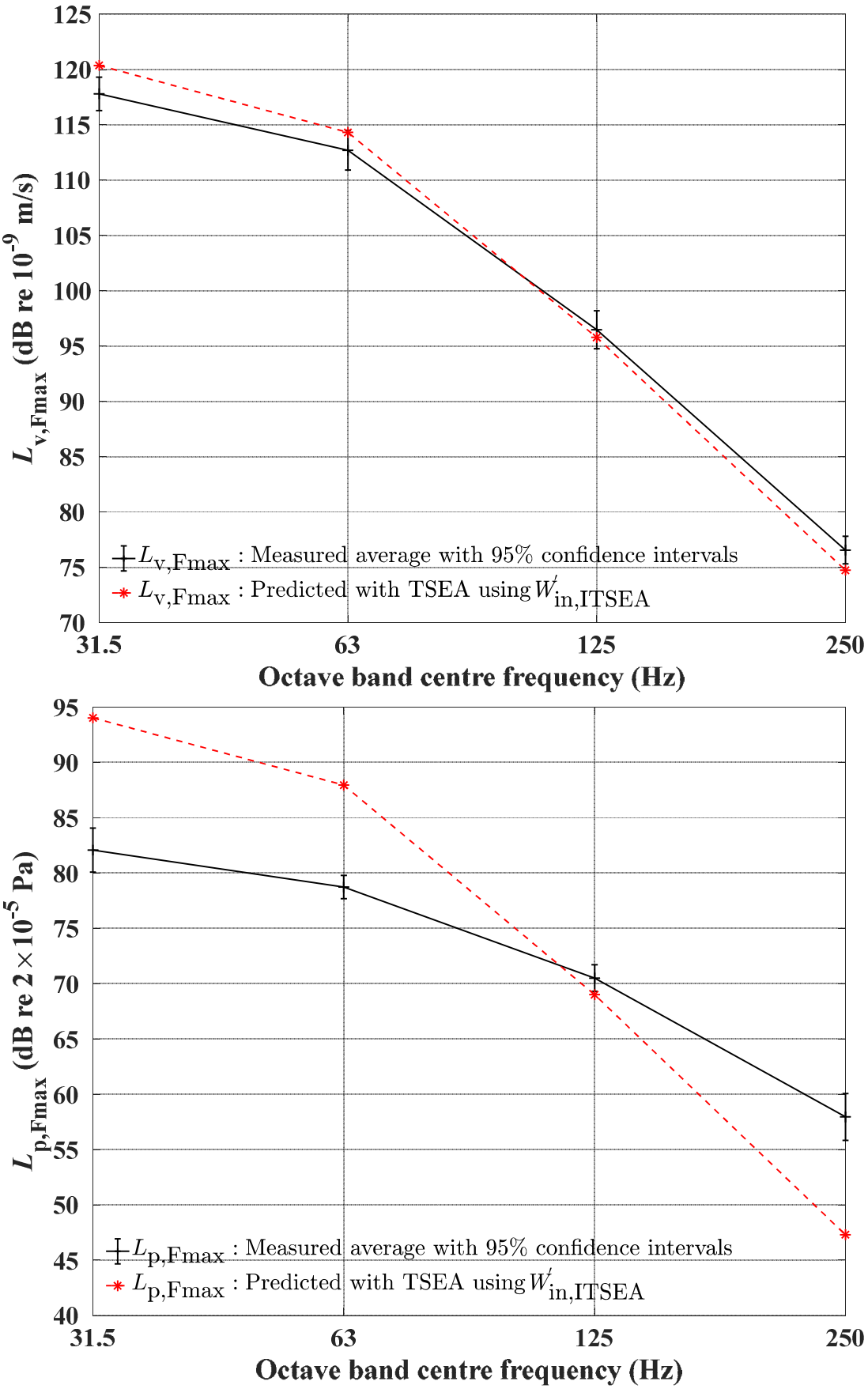

Figure 5-30. Comparison of $L_{v,Fmax}$ (upper) and $L_{p,Fmax}$ (lower) for the tyre source exciting a floating floor on a 210mm concrete base floor in octave bands.

5.4.3 Comparison of change in measured $L_{p,Fmax}$, predicted $L_{p,Fmax}$ and $W'_{in,ITSEA}$

5.4.3.1 Test facility A

Figure 5-31 to Figure 5-35 allow comparison of measured and predicted $\Delta L_{p,Fmax}$ in one-third octave and octave bands. In most cases, there is agreement within the 95% confidence interval of the measurement. Hence, this confirms that the values of $W'_{in,ITSEA}$ used in the TSEA model are correct. It is noteworthy that $\Delta L_{W'_{in,ITSEA}}$ is similar to both the measured and predicted $\Delta L_{p,Fmax}$; hence the change in the transient power input can be used estimate the change in the impact sound insulation. There is a 0.4dB and 0.3dB difference between $\Delta L_{W'_{in,ITSEA}}$ and $\Delta L_{p,Fmax}$ for locally reacting mass-spring systems A and B respectively that is predicted with TSEA using $W'_{in,ITSEA}$ in the one-third octave band results, but the values are identical in octave bands (although the reason is not known).

For Group 1 materials, the overlap can be seen at 50 to 100Hz and 31.5 to 63Hz for one-third octave and octave band respectively for mass-spring A, and 50 to 125Hz and 31.5 to 125Hz for one-third octave and octave band for mass-spring B. For Group 2 materials, the 95% confidence interval of the measured $\Delta L_{p,Fmax}$ overlaps with $\Delta L_{W'_{in,ITSEA}}$.

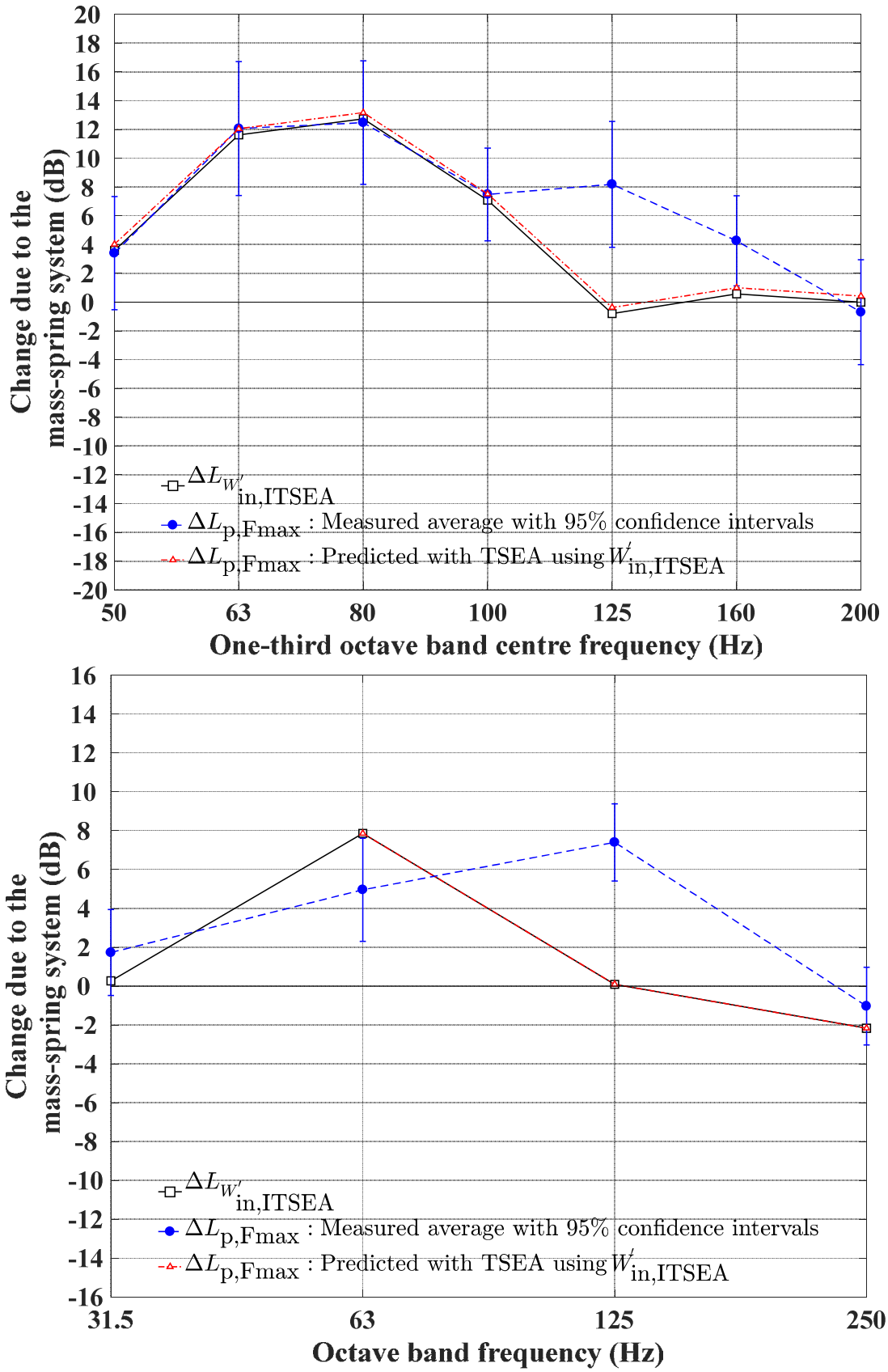

Figure 5-31. Comparison of the change in measured, predicted $L_{p,Fmax}$ and $W'_{in,ITSEA}$ for locally reacting mass-spring system A.

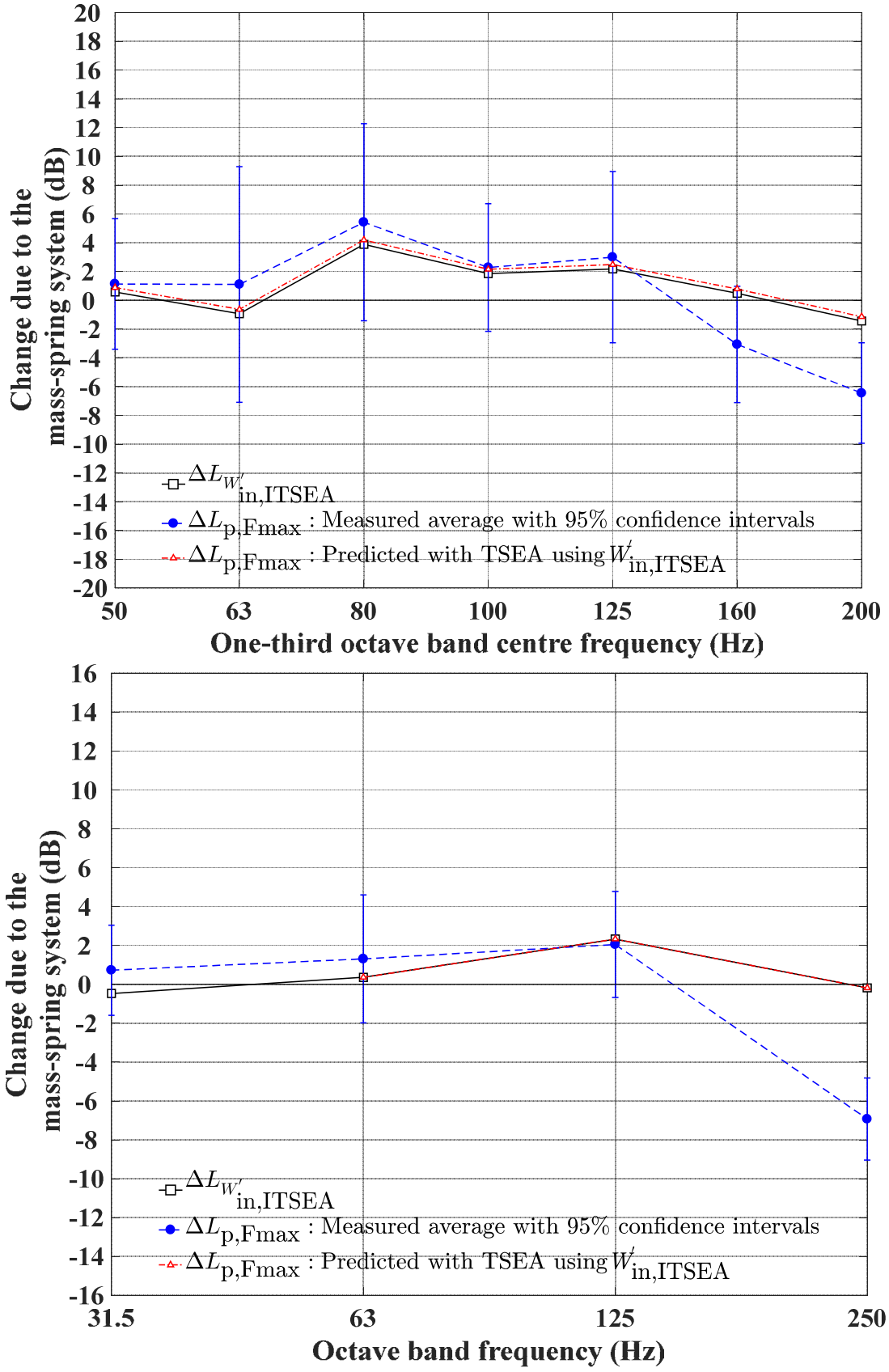

Figure 5-32. Comparison of the change in measured, predicted $L_{p,Fmax}$ and $W'_{in,ITSEA}$ for locally reacting mass-spring system B.

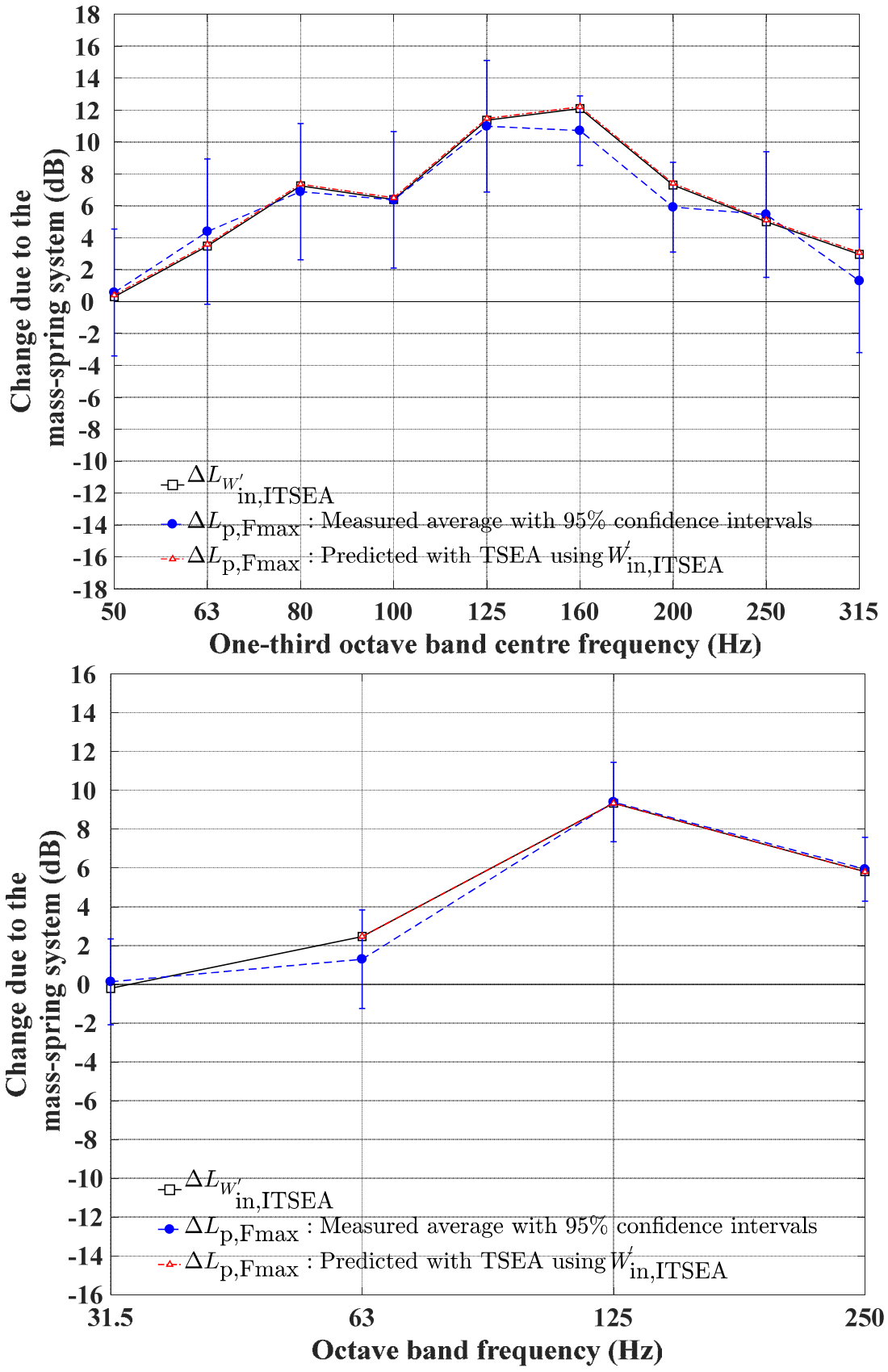

Figure 5-33. Comparison of the change in measured, predicted $L_{p,Fmax}$ and $W'_{in,ITSEA}$ for locally reacting mass-spring system C.

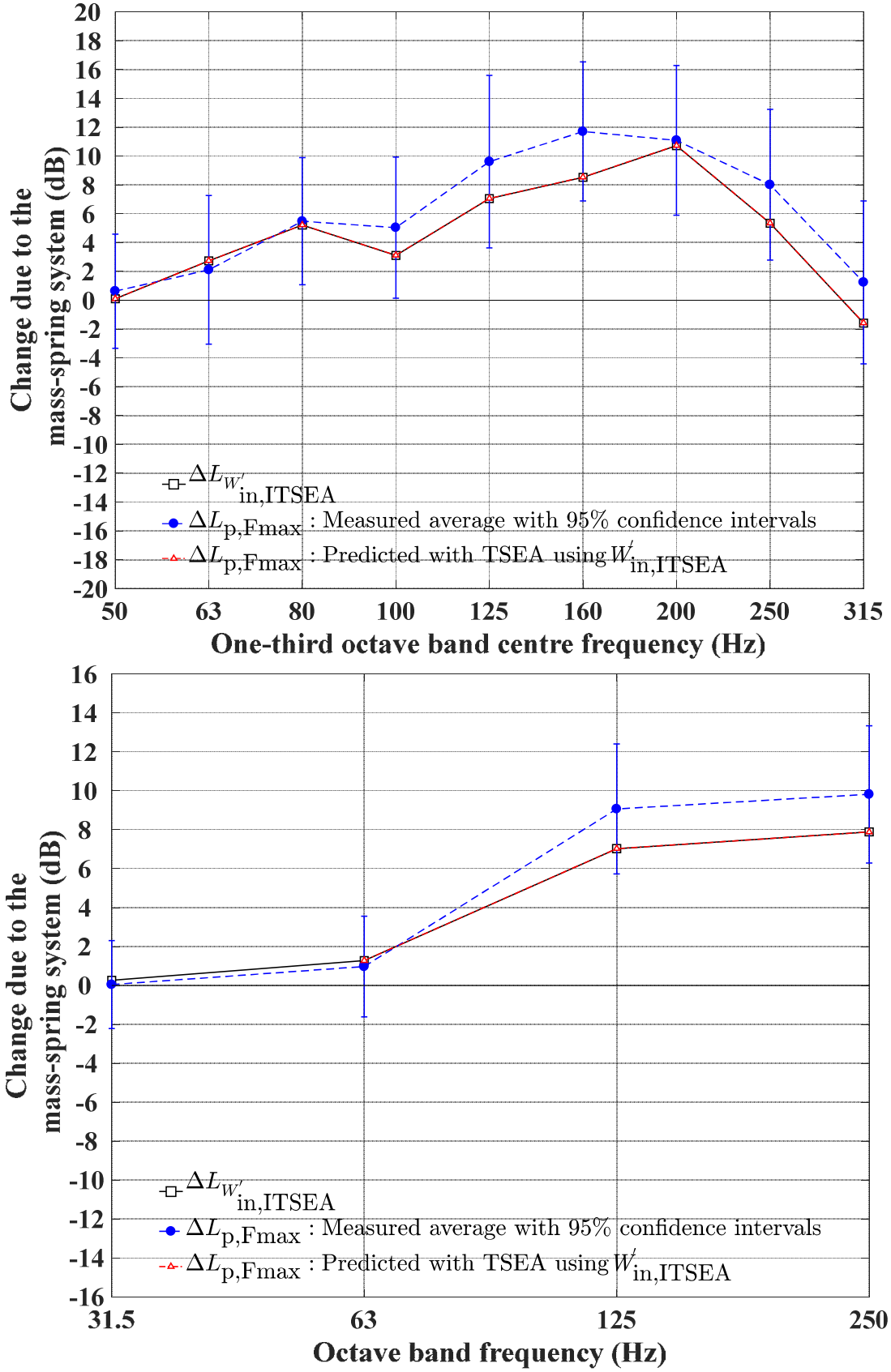

Figure 5-34. Comparison of the change in measured, predicted $L_{p,Fmax}$ and $W'_{in,ITSEA}$ for locally reacting mass-spring system D.

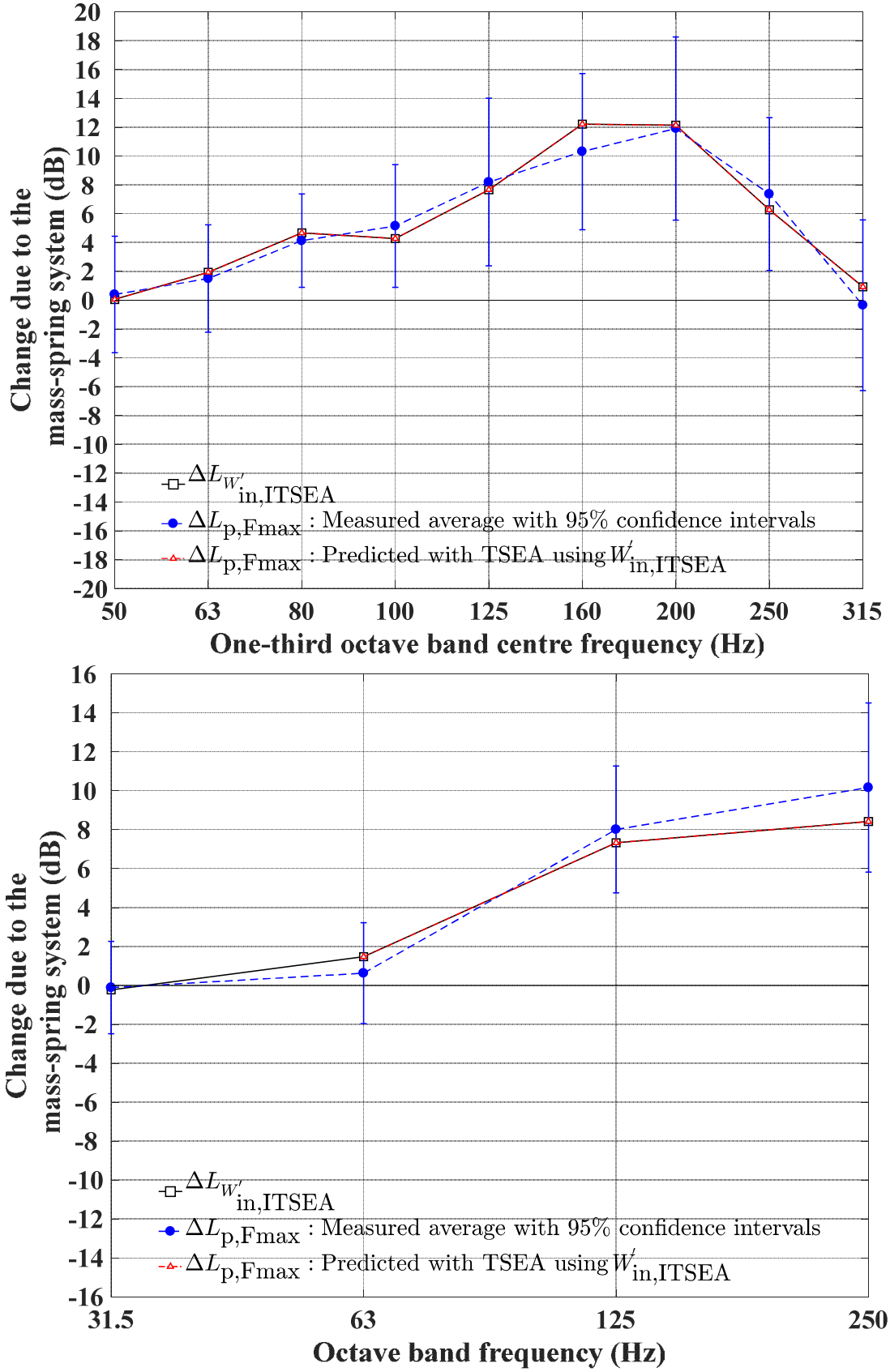

Figure 5-35. Comparison of the change in the measured, predicted $L_{p,Fmax}$ and $W'_{in,ITSEA}$ for locally reacting mass-spring system E.

5.4.3.2 Test facility B

Figure 5-36 and Figure 5-37 allows a comparison of the change in $L_{W'_{\text{in,ITSEA}}}$ and $L_{\text{p,Fmax}}$ due to the Ondol floating floor (see section 5.2.1) for excitation with the rubber ball and tyre source. For the octave band results, the 95% confidence intervals overlap below 125Hz. This indicates that ITSEA is appropriate when used on a floating floor with a walking surface that has a relatively high mass per unit area.

Although $\Delta L_{W'_{\text{in,ITSEA}}}$ from the rubber ball and the tyre source are slightly different as rubber ball shows a dip at 63Hz octave band whereas tyre source shows similar values at 31.5 and 63Hz octave bands. For the rubber ball and the tyre source this is unlikely to be significant due to the relatively large confidence intervals. However, it is possible that the performance of a floating floor could sometimes be specific to the heavy impact source. When the individual values of $\Delta L_{W'_{\text{in,ITSEA}}}$ are incorporated in a TSEA model there is also reasonable agreement (i.e. <5dB) between the measured and predicted $\Delta L_{\text{p,Fmax}}$. The differences between measured and predicted $\Delta L_{\text{p,Fmax}}$ are sufficiently low to indicate that the assumption of $t_{\text{input\_duration}}$=18.8ms in Eq. (2.41) for excitation of the floating floor is reasonable when using ITSEA to determine $\Delta L_{W'_{\text{in,ITSEA}}}$.

When the change in impact sound insulation due to a floating floor is measured using a tapping machine, it is common to observe a reduction near the mass-spring resonance frequency followed by a clear improvement in the impact sound insulation at higher frequencies [24].

In Figure 5-36 and Figure 5-37, there is a peak in $\Delta L_{W'_{\text{in,ITSEA}}}$ normalised transient power input of ≈3.5dB in the 125Hz octave band which is likely to be caused by the mass-spring resonance (although it is actually estimated to occur at 71Hz). This peak could potentially be reduced by using a double floating floor design [93].

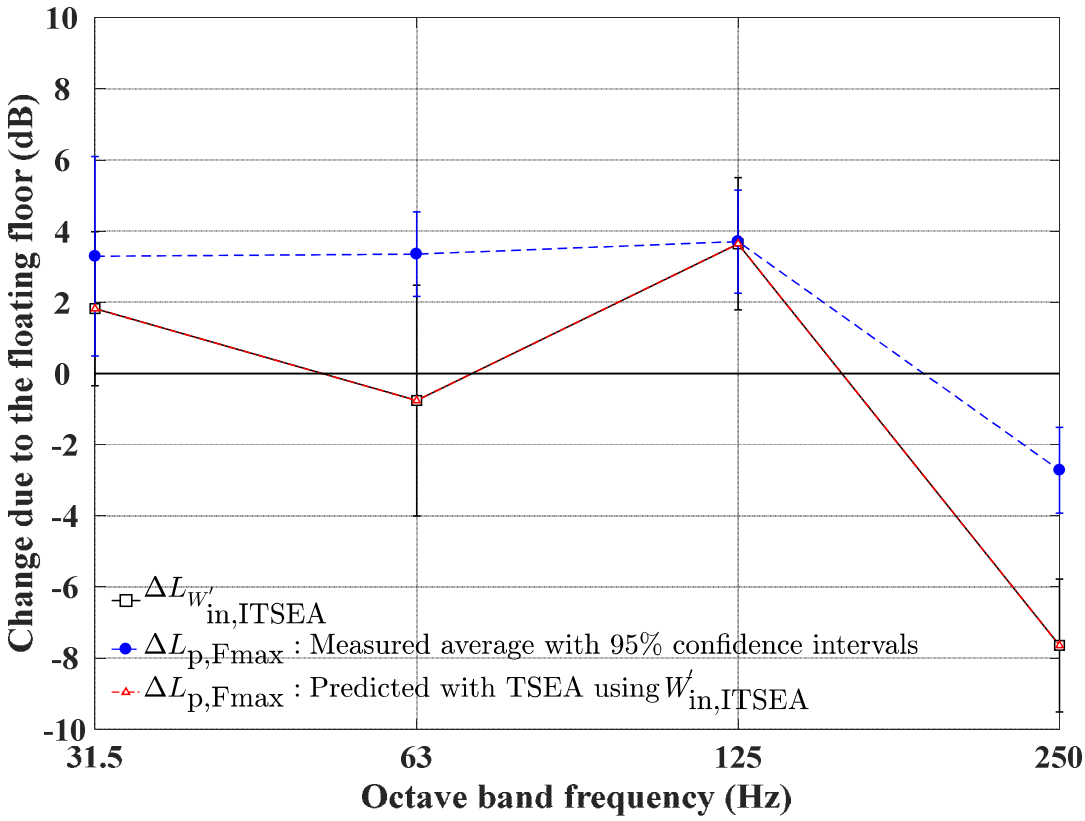

Figure 5-36. Comparison of the change in measured and predicted $L_{p,Fmax}$ with $W'_{in,ITSEA}$ using the rubber ball.

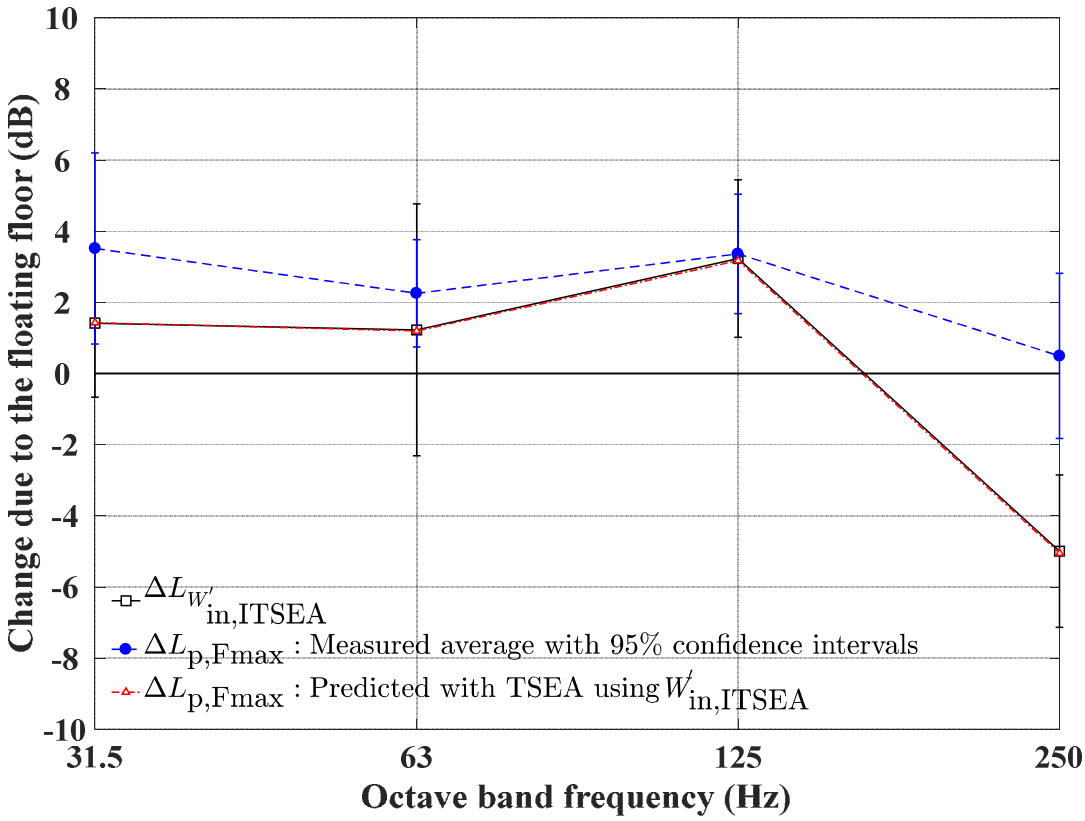

Figure 5-37. Comparison of the change in measured and predicted $L_{p,Fmax}$ with $W'_{in,ITSEA}$ using the tyre source.

5.5 Summary

In this chapter, ITSEA has been used to quantify the transient structure-borne sound power input from a heavy impact source into a heavyweight base floor with and without a locally reacting mass-spring system (test facility A), and with and without the Ondol floating floor (test facility B).

The first step was to assess the validity of the assumption that ITSEA can be based on a single subsystem by ignoring all other coupled subsystems that can return energy back to the source subsystem. Based on the output of a 14-subsystem SEA model representing the heavyweight base floor in test facility A the error in estimating the transient power input was found to be <0.7dB which is acceptable.

The next step was to use the rubber ball as a heavy impact source directly on a concrete base floor, and with locally reacting mass-spring systems in test facility A. This showed that the frequency-average difference between $W'_{\text{in,Force\_Plate}}$ and $W'_{\text{in,ITSEA}}$ (absolute values) ranged from 0 to 3.4dB for one-third octave bands and from 1.3 to 3.9dB for octave bands. It is concluded that this is sufficiently accurate to justify use of the ITSEA approach.

In test facility A, comparison of $L_{\text{v,Fmax}}$ and $L_{\text{p,Fmax}}$ from measurements and TSEA (predicted using $W'_{\text{in,ITSEA}}$ or $W'_{\text{in,ForcePlate}}$) showed frequency-average differences (absolute values) up to 4.1dB in one-third octave bands and up to 5.4dB in octave bands. In test facility B, the comparison in $L_{\text{v,Fmax}}$ and $L_{\text{p,Fmax}}$ between TSEA using $W'_{\text{in,ITSEA}}$ and measurement also showed frequency-averaged differences up to 3.7dB. As the 95% confidence intervals of the measurements overlapped the TSEA predictions this indicates that the use of $W'_{\text{in,ITSEA}}$ in TSEA model was reasonable for locally reacting mass-spring systems, and two different standard impact sources (rubber ball and tyre source) excited on the Ondol floating floor.

In terms of the predicted change due to the locally reacting mass-spring system for the test facility A, the 95% confidence interval of the measured $\Delta L_{\text{p,Fmax}}$ overlaps with $\Delta L_{W'_{\text{in,ITSEA}}}$ for the Group 2 materials. For Group 1 materials, the overlap can be seen at 50 to 100Hz and 31.5 to 63Hz for one-third octave and octave band respectively for mass-spring A, and 50 to 125Hz and 31.5 to 125Hz for one-third octave and octave band for mass-spring B.

Results from ITSEA on a full-size Ondol floating floor also showed that it could be used to calculate $\Delta L_{W'\text{in,ITSEA}}$ due to the Ondol floating floor that can be incorporated in a TSEA model. This indicated that the change in the transient power input provides a reasonable estimate of the change in the impact sound insulation. The 95% confidence interval from the measurement and the predicted $\Delta L_{\text{p,Fmax}}$ overlap each other from 31.5 to 125Hz octave band for rubber ball and tyre source. At 250Hz, the difference is within 2dB.

The results in this chapter indicates that the transient structure-borne sound power input from heavy impact sources into a heavyweight base floor with and without a locally reacting mass-system, two heavy impact sources (rubber ball and tyre source) on the full-size Ondol floating floors can be determined using ITSEA and incorporated in TSEA to predict the impact sound insulation with heavy impact sources.

6. NUMERICAL EXPERIMENTS WITH FEM AND TSEA

6.1 Introduction

This chapter uses FEM to carry out numerical experiments to assess a wider range of room volumes and reverberation times could be assessed in test facilities with a focus on the low-frequency performance

Section 6.2 validates laboratory measurement of impact sound insulation with a rubber ball drop in test facility A (see section 5.2.1) through a comparison of measurements, FEM and TSEA. Section 6.3 describes the numerical experiments with FEM. Section 6.4 compares $L_{p,Fmax}$ from FEM and TSEA in the low-frequency range for different room volumes and different reverberation times. Section 6.5.2 visualises and assesses the modal response of the four different box shape room with different volumes from the rubber ball impacting a 140mm concrete floor. Section 6.5.3 and 6.5.4 also investigates the difference in the spatial-average $L_{p,Fmax}$ from the three different measurement procedures (Japanese, Korean and International) using FEM and attempts to identify an improved measurement procedure.

6.2 Validation of FEM model using facility A

The first step is to validate the FEM model against the laboratory measurement of impact sound insulation with a rubber ball in test facility A as well as with TSEA.

For FEM, the measured TLFs of the concrete base floor (see Figure 5-6) were used to calculate Rayleigh damping using Eq. (3.14). The acoustic impedance associated with the Sabine reverberation time (T=1.7s) as described in section 2.5.3.2 was assigned as the boundary condition for all six room surfaces. The parameters of the concrete base floor and the room are described in Table 6.1.

For TSEA, The CLF from the floor to the room was calculated from the radiation efficiency that was estimated from previous measurements [24] of the normalised impact sound pressure level with excitation from the ISO tapping machine measurement. The CLF in the reverse direction was determined using the consistency relationship. The normalised transient power input for the rubber ball was calculated

from the RMS force measured with a force plate, and the real part of the measured spatial-average driving-point mobility.

Table 6.1. Material properties for test facility A.

	Young's Modulus (N/m^2)	Poisson's Ratio	Density (kg/m^3)	Rayleigh Damping
Rubber (Ball)	3.4×10^6	0.48	1188	N/A
Concrete (Floor)	31×10^9	0.16	2200	α=20.89 $\beta=5.30\times10^{-6}$
	Density (kg/m^3)		**Bulk Modulus (N/m^2)**	
Air (Room)	1.21		142355	

The spatial-average $L_{p,Fmax}$ in the receiving room was determined using results from four (randomly chosen) excitation positions for the rubber ball on the floor. The sound pressure sampling positions in the FEM simulation were created on a regular grid of 0.5m spacing in the room excluding nodes on the room surfaces.

Figure 6-1 compares measurements, TSEA and FEM in terms of the spatial-average $L_{p,Fmax}$ in the room. (NB No $L_{p,Fmax}$ result is shown for TSEA in the 31.5Hz band for octave band, and below 50Hz in one-third octave band because an estimate of the radiation efficiency was not available below the 50Hz one-third octave band.

For the octave band result, the maximum difference between measurements and FEM was 2.1dB and between measurements and TSEA was 3.9dB. The confidence intervals overlap between measurements and FEM over all the frequency range of interest, but only overlapped with TSEA at 125Hz. The frequency-average difference between the prediction models and measured $L_{p,Fmax}$ was 0.4dB for TSEA and 0.3dB for FEM.

For the one-third octave band results, the maximum difference between measurements and FEM was 9.4dB and between measurements, and TSEA was 7.2dB. This was due to the dip at 63Hz which was not predicted at all by FEM but was evident in TSEA. The confidence intervals overlapped between measurements and FEM except at 63, 125, 315 and 630Hz but TSEA only overlapped at 125Hz and 200Hz. The frequency-average difference between the prediction models and measured $L_{p,Fmax}$ was 3.5dB for TSEA and 1.8dB for FEM. FEM show closest agreement in octave bands.

The agreement between FEM and measurements is sufficient to validate the use of FEM for the numerical experiments in this chapter as 95% confidence intervals from measurement and FEM overlap in most frequency bands.

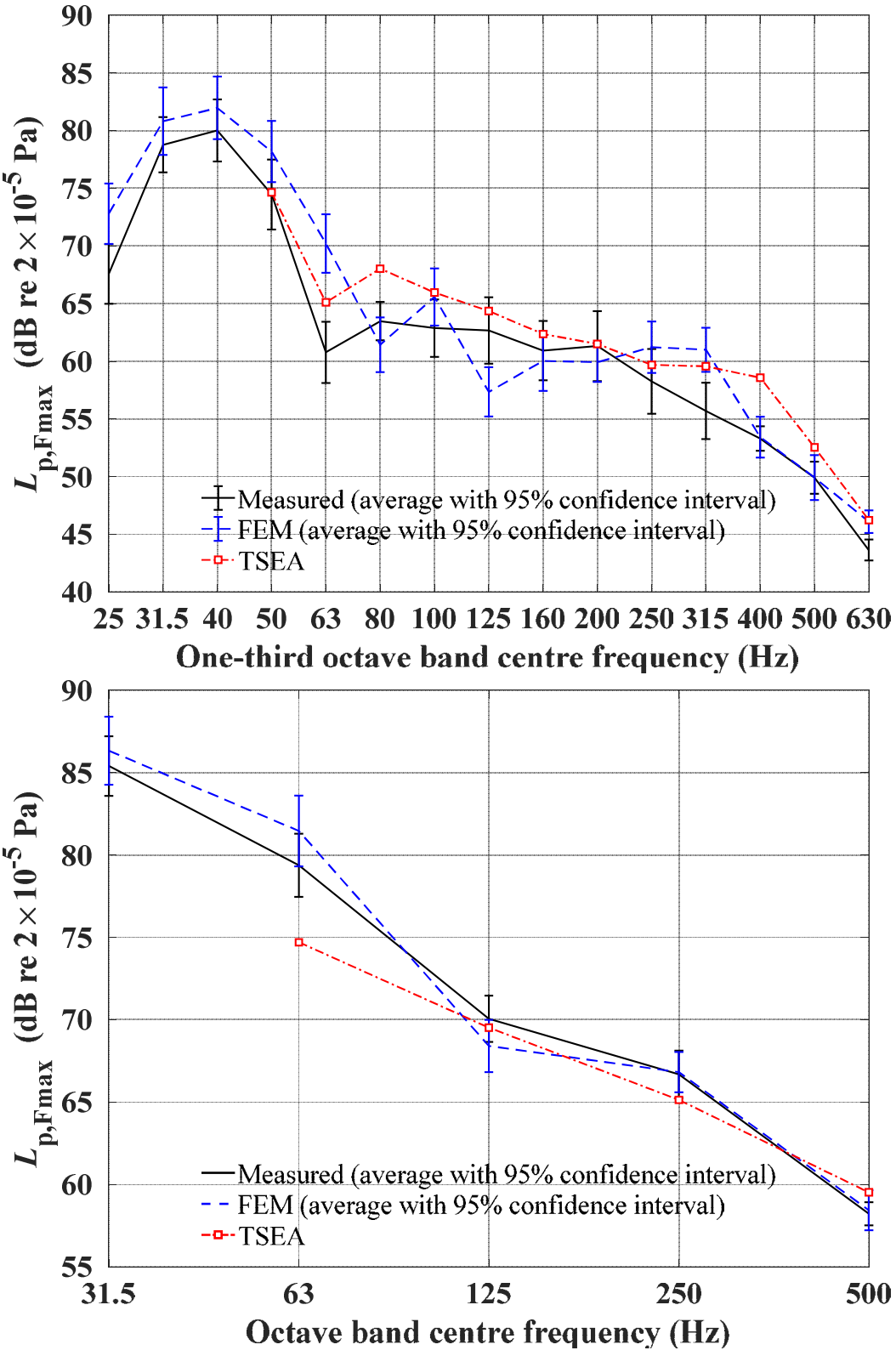

Figure 6-1. Comparison between measurements, FEM and TSEA in one-third octave bands (upper) and octave bands (lower) for test facility A.

6.3 Numerical experiments

Numerical experiments using FEM were created in order to (1) compare FEM and TSEA in different room volumes at low frequencies, (2) visualise the modal response of the room, (3) characterise the variation in the sound pressure level in the vertical direction which affects the positions chosen in different measurement procedures and (4) assess different measurement procedures.

The simulations in FEM involve a rubber ball impacting a 140mm concrete base floor with four box-shape rooms with different volumes (50, 37.5 25 and 15m^3) and six different Sabine reverberation times (1.5, 0.75 0.375, 0.1875, 0.0938, 0.0468s). FEM simulation details were given in section 3.8.1 and section 6.2.

To calculate the CLF from the floor to the room, a FEM simulation used rain-on-the-roof excitation (i.e. uniform amplitude with random phase) on the concrete base floor to ensure the modal vibration is uncorrelated and a linear relationship can be used between power flow and modal energies (see section 2.2.3.2). The sound pressure sampling positions in the were created on a regular grid of 0.5m in the room excluding nodes on the room surfaces. The acceleration sampling and excitation positions were created on a regular grid of 0.2m on the concrete slab excluding nodes on the boundary conditions. The CLF was calculated using

$$\eta_{ij} = \eta_j \frac{E_j}{E_i} \tag{6.1}$$

where the energies are given by Eqs. (2.14) and (2.15). The CLF in the reverse direction was calculated using consistency relationship.

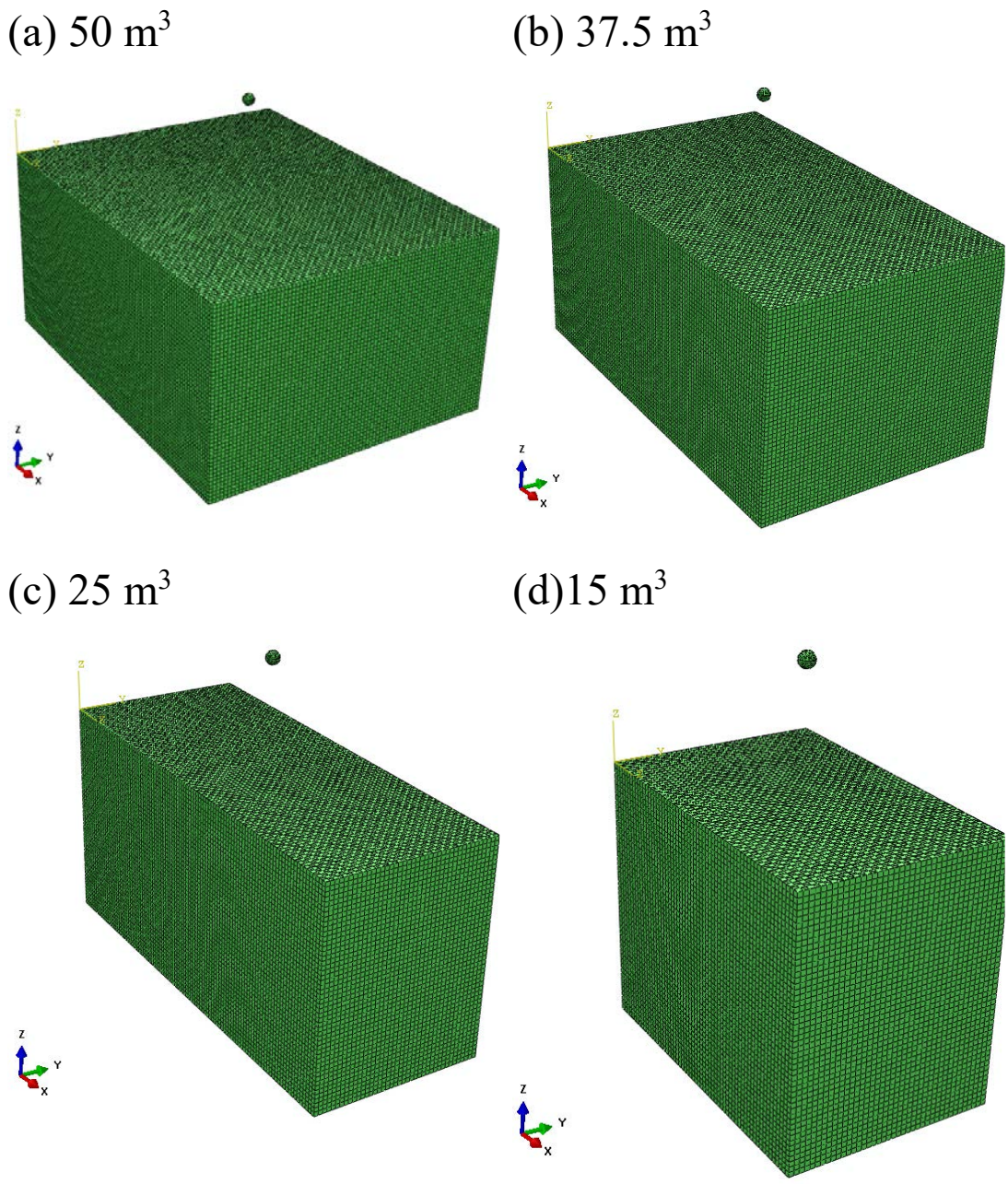

Figure 6-2. FEM models of the base floor and receiving room with the following volume: (a) A: 50m^3, (b) B: 37.5m^3, (c) C: 25m^3 and (d)15 m^3.

Table 6.2. Material properties for models A to D.

	Young's Modulus (N/m^2)	Poisson's Ratio	Density (kg/m^3)	Rayleigh Damping
Rubber (Ball)	3.4×10^6	0.48	1188	N/A
Concrete (Floor)	31×10^9	0.16	2200	α=14.5489 $\beta=3.55\times10^{-6}$
	Density (kg/m^3)	**Bulk Modulus (N/m^2)**		
Air (Room)	1.21	142355		

Table 6.3. Dimensions of the concrete base floor and the room, critical and fundamental frequencies for models A to D.

Model	**V (m^3)**	**L_x (m)**	**L_y (m)**	**L_z (m)**	**h (m)**	**Plate critical frequency (Hz)**	**Fundamental plate mode, f_{11} (Hz)**	**Vertical axial room mode, f_{001} (Hz)**
A	**50**	5	4	2.5	0.14	121.8	24.7	68.6
B	**37.5**	5	3	2.5	0.14		36.5	
C	**25**	5	2	2.5	0.14		70	
D	**15**	3	2	2.5	0.14		87.18	

Table 6.4: Acoustic impedances used for all room surfaces to simulate different reverberation times for models A to D.

Corresponding Sabine reverberation time (s)	**Acoustic impedance (Ns/m^3)**			
	Model A	**Model B**	**Model C**	**Model D**
1.5	52550	57703	68006.5	76249.7
0.75	26275	28851	34003.3	38124.9
0.375	13137.5	14425.6	17001.6	19062.4
0.1875	6568.8	7212.8	8500.8	9531.2
0.0938	3484.4	3606.4	4250.4	4765.6
0.0469	1642.2	1803.2	2125.2	2382.8

6.4 Assessment of low-frequency predictions from TSEA using FEM

6.4.1 Introduction

Due to the emphasis on low-frequency impact sound insulation with heavy impact sources there remains a need to investigate the accuracy of TSEA in the low-frequency range. With this aim, this section compares $L_{p,Fmax}$ from FEM with TSEA.

The numerical experiments with FEM and TSEA are defined using nine different situations. These involve the rubber ball impacting a 140mm concrete base floor with three box-shape rooms with volumes (50, 37.5 and 25 m^3) and six reverberation times (1.5, 0.75, 0.375, 0.1875, 0.0938, 0.0468s). These allow a comparison of FEM and TSEA in the low-frequency range. The model parameters are summarised in Table 6.2 to Table 6.4.

For Table 6.2, the parameters for air and the density of concrete is taken from the literature [24]. The parameters for concrete were given in Table 3.5, and the parameters for the rubber ball were determined in section 3.8.1 and shown in Table 3.6.

For Table 6.3, the standard laboratory measurement chamber is at least 50m^3, and smaller volume rooms were created to reflect flats in Japan and Korea where the room size is sometimes small. The critical frequency of plate is determined from Eq.(2.13), and Fundamental plate mode frequency is determined from Eq.(2.31).

For Table 6.4, acoustic impedance was estimated from the Sabine reverberation time and Eq.(2.55).

6.4.2 Comparison between TSEA and FEM

The numerical experiments are used to compare the spatial-average $L_{p,Fmax}$ predicted by FEM and TSEA using $W'_{in,\infty}$ and $W'_{in,Finite}$ in the low-frequency range as indicated in Figure 6-4 to Figure 6-9 for Model A, Figure 6-10 to Figure 6-15 for Model B, and Figure 6-16 to Figure 6-21 for Model C. This allows an assessment of the effect of room surface damping, the effect of the volume size, and the difference in using the infinite or finite plate driving-point mobility.

In all figures, results are only shown above the fundamental frequency of the concrete base floor. Note that for Model B and Model C, the fundamental frequency of this base floor is 24.7Hz and 36.5Hz; hence there is no TSEA prediction at lower frequencies.

In all three models, a 3dB change in $L_{p,Fmax}$ was expected due to halving the acoustic impedance. However, this did not occur in FEM and TSEA where the change in $L_{p,Fmax}$ was not uniform. This indicates that the transient signal is affected by both the Fast time-weighting and the room absorption. Also, there is a tendency for surfaces with higher damping to give better agreement between TSEA and FEM above the 125Hz one-third octave and octave band for all four models.

Figure 6-3 shows the difference between $Y_{dp,Infinite}$ and $\mathrm{Re}\{Y_{dp,finite}\}$ of the concrete base floors in the Models A, B and C. In octave bands, all three models show the largest differences between $Y_{dp,Infinite}$ and $\mathrm{Re}\{Y_{dp,finite}\}$ at the lowest frequency band which are -5.3dB at 31.5Hz band, -12.6dB at 31.5Hz band, and -13.7dB at 63Hz band for model A, B and C respectively. This is due to a single modal response within the frequency band. Above the lowest frequency band, the difference between $Y_{dp,Infinite}$ and $\mathrm{Re}\{Y_{dp,finite}\}$ are minimised and within 2dB. In one-third octave bands, the largest difference of Model A is 9.3dB at 40Hz, Model B is at -7.7dB at 50Hz, and Model C is at 5.9dB at 125Hz. All those maximum differences occur at troughs of the driving-point mobility. The fluctuations of $\mathrm{Re}\{Y_{dp,finite}\}$ become smoother and approximately within 2.2dB above 160Hz one-third octave band for all three models.

For octave band results, the maximum difference between $L_{p,Fmax}$ from TSEA and FEM was 5.8dB at 500Hz from Model B, T=1.5s. TSEA overestimates FEM. In comparison to the one-third octave band result, the effect of peak and troughs are insignificant.

For one-third octave band results, the accuracy of TSEA using $W'_{in,\infty}$ and $W'_{in,Finite}$ are similar above the 160Hz band. This is possibly due to the difference between $Y_{dp,Infinite}$ and $\mathrm{Re}\{Y_{dp,finite}\}$ is minimised to approximately 2dB. For the Models B and C, the use of $W'_{in,Finite}$ can be considered as an advantage in predicting $L_{p,Fmax}$ in frequency below the 160Hz band where it can capture peaks/troughs due to low-frequency plate modes where the modes are widely spaced.

For Model A, both TSEA using $W'_{\text{in},\infty}$ or $W'_{\text{in,Finite}}$ has a similar degree of difference to FEM. This is because $L_{\text{p,Fmax}}$ from FEM is in between $L_{\text{p,Fmax}}$ predicted from TSEA using $W'_{\text{in},\infty}$ and $W'_{\text{in,Finite}}$.

Table 6.5 to Table 6.7 summarises the average difference between FEM and TSEA for models A, B, and C, for six different reverberation times. The maximum frequency-averaged difference of -2.4dB was obtained from Model C, T=1.5s using $W'_{\text{in,Finite}}$ (octave band).

Table 6.5 to Table 6.7 also indicates that the use of $W'_{\text{in},\infty}$ could achieve similar accuracy to $W'_{\text{in,Finite}}$ as the difference in the frequency-average difference in $L_{\text{p,Fmax}}$ between $W'_{\text{in,Finite}}$ and $W'_{\text{in},\infty}$ fall in 1.2, 0.5 and 0.6dB for models A, B and C respectively.

These comparisons indicate that TSEA using $W'_{\text{in},\infty}$ and $W'_{\text{in,Finite}}$ could be used to predict $L_{\text{p,Fmax}}$ with similar accuracy to FEM. Compared to FEM, the advantage of TSEA is that it is quicker to create and run the model. As FEM it could take at least a week to create the model to post-process the data, whereas TSEA could be completed within 12 hours.

Table 6.5. Frequency-average difference in $L_{p,Fmax}$ between TSEA and FEM in one-third octave bands and octave bands for model A

Model A		***T* (s)**					
		1.5	**0.75**	**0.375**	**0.1875**	**0.0938**	**0.0369**
Frequency average difference in $L_{p,Fmax}$ (dB)	$W'_{in,Finite}$ (one-third octave band)	0.2	0.3	1.3	1.7	2.0	2.5
	$W'_{in,\infty}$ (one-third octave band)	-1	-0.8	0.1	0.5	0.8	1.3
	$W'_{in,Finite}$ (octave band)	-0.1	-1.2	-0.3	0.2	0.7	1.1
	$W'_{in,\infty}$ (octave band)	-0.9	-0.5	0.5	0.9	1.4	1.8

Table 6.6. Frequency-average difference in $L_{p,Fmax}$ between TSEA and FEM in one-third octave bands and octave bands for model B

Model B		***T* (s)**					
		1.5	**0.75**	**0.375**	**0.1875**	**0.0938**	**0.0369**
Frequency average difference in $L_{p,Fmax}$ (dB)	$W'_{in,Finite}$ (one-third octave band)	0.5	0.8	2.2	1.3	1.5	2.0
	$W'_{in,\infty}$ (one-third octave band)	0	0.3	1.7	0.8	1.0	1.4
	$W'_{in,Finite}$ (octave band)	-0.3	0	0.4	0.9	1.3	1.8
	$W'_{in,\infty}$ (octave band)	-0.7	-0.3	0.1	0.6	1.0	1.5

Table 6.7. Frequency-average difference in $L_{p,Fmax}$ between TSEA and FEM in one-third octave bands and octave bands for model C

Model C		***T* (s)**					
		1.5	**0.75**	**0.375**	**0.1875**	**0.0938**	**0.0369**
Frequency average difference in $L_{p,Fmax}$ (dB)	$W'_{in,Finite}$ (one-third octave band)	-1.0	-0.3	0.7	0.7	0.9	1.4
	$W'_{in,\infty}$ (one-third octave band)	-1.1	-0.4	0.7	0.6	0.8	1.4
	$W'_{in,Finite}$ (octave band)	-1.9	-1.3	-1.0	-0.5	0	0.7
	$W'_{in,\infty}$ (octave band)	-2.4	-1.8	-1.5	-1.1	-0.6	0.1

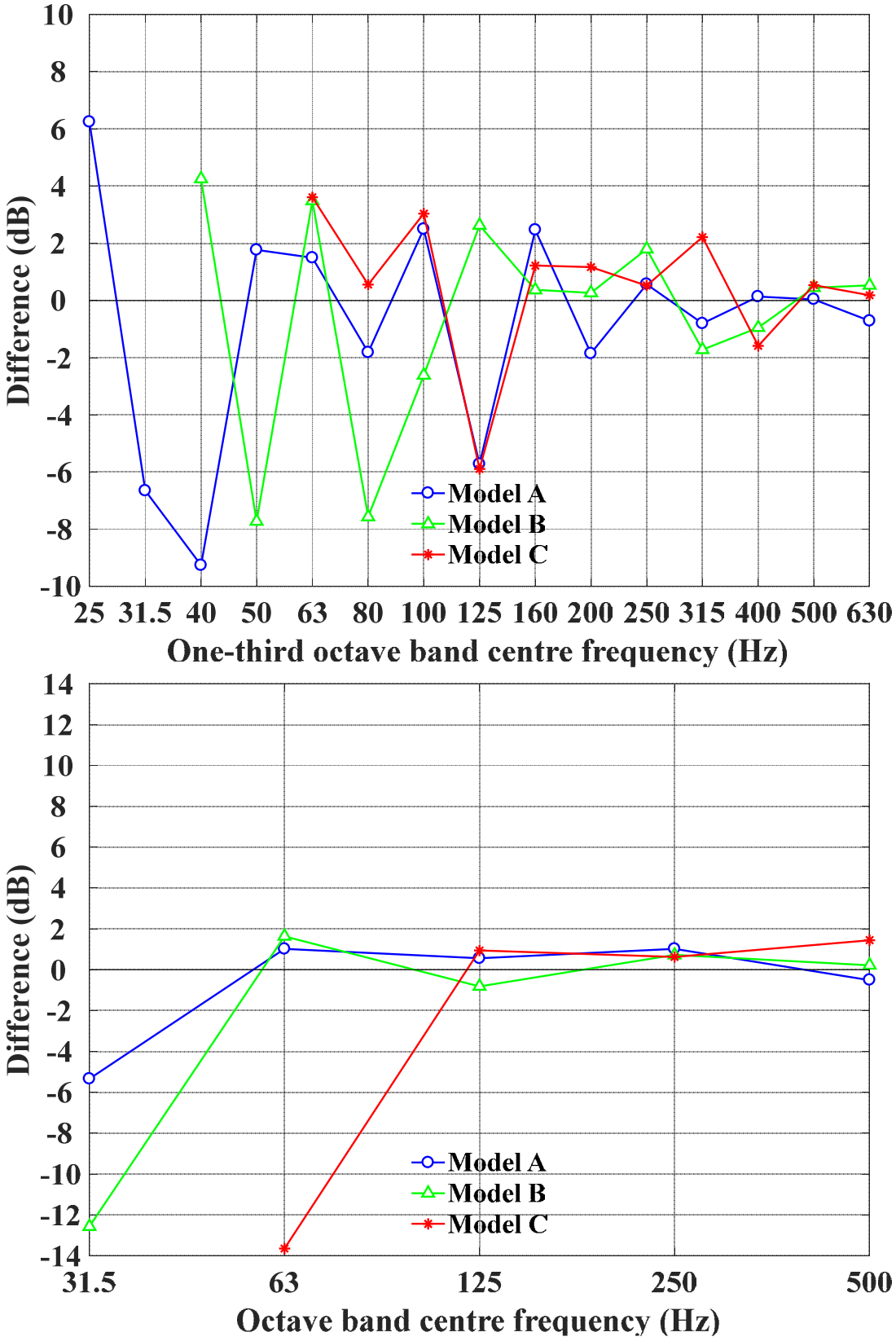

Figure 6-3. Difference in the mobilities ($Re\{Y_{dp,finite}\}$-$Y_{dp,infinite}$) of the 140mm concrete base floor for the models A, B and C in one-third octave bands (upper) and octave bands (lower). The spatial average $Re\{Y_{dp,finite}\}$ was obtained from the excitation positions associated to the numerical experiments.

6.4.2.1 Model A ($50m^3$)

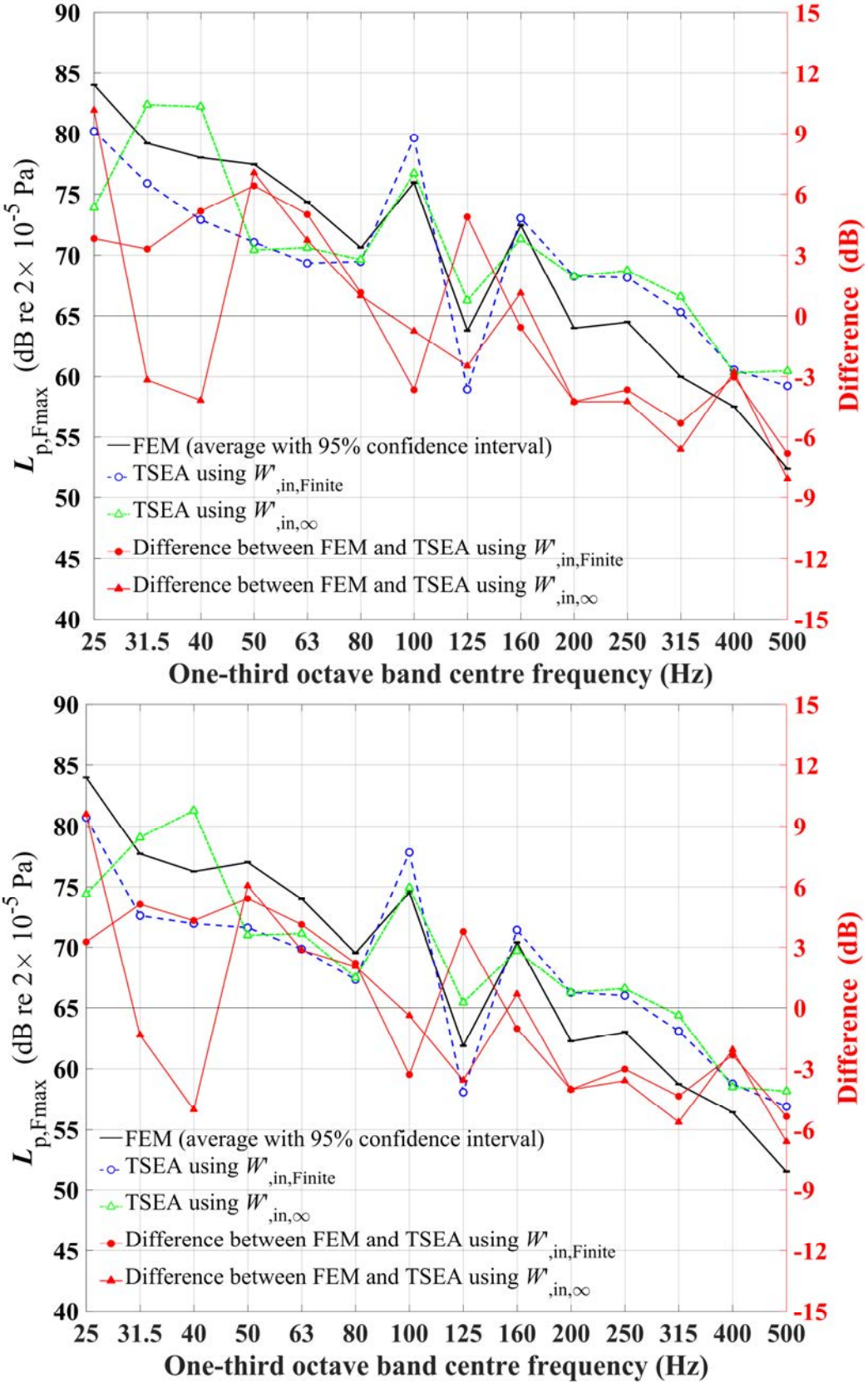

Figure 6-4. Comparison of $L_{p,Fmax}$ predicted using TSEA and FEM for model A for different room reverberation times. Room T=1.5s (upper), Room T=0.75s (lower) in one-third octave bands.

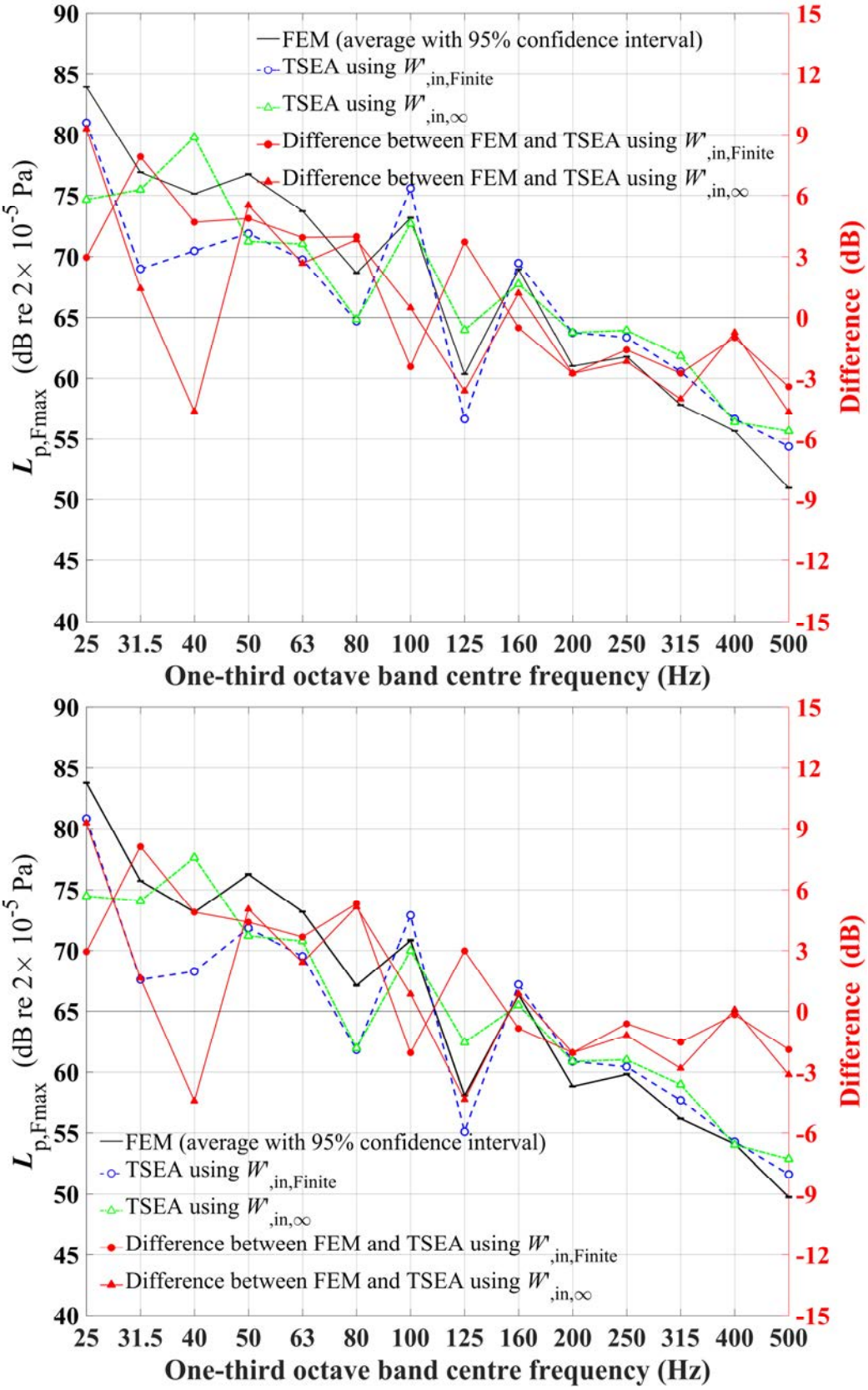

Figure 6-5. Comparison of $L_{p,Fmax}$ predicted using TSEA and FEM for model A for different room reverberation times. Room T=0.375s (upper), Room T=0.1875s (lower) in one-third octave bands.

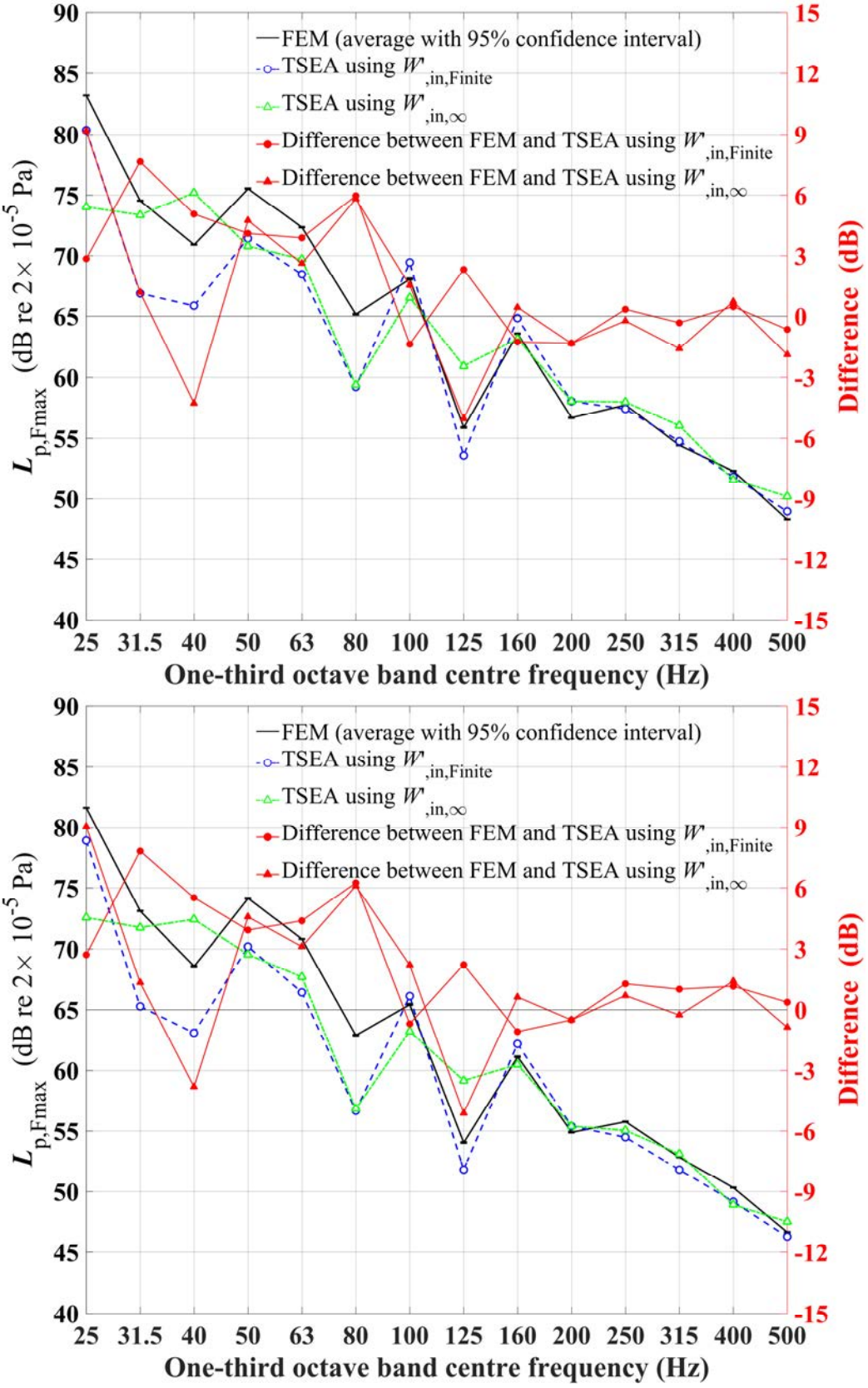

Figure 6-6. Comparison of $L_{p,Fmax}$ predicted using TSEA and FEM for model A for different room reverberation times. Room T=0.0938s (upper), Room T=0.0469s (lower) in one-third octave bands.

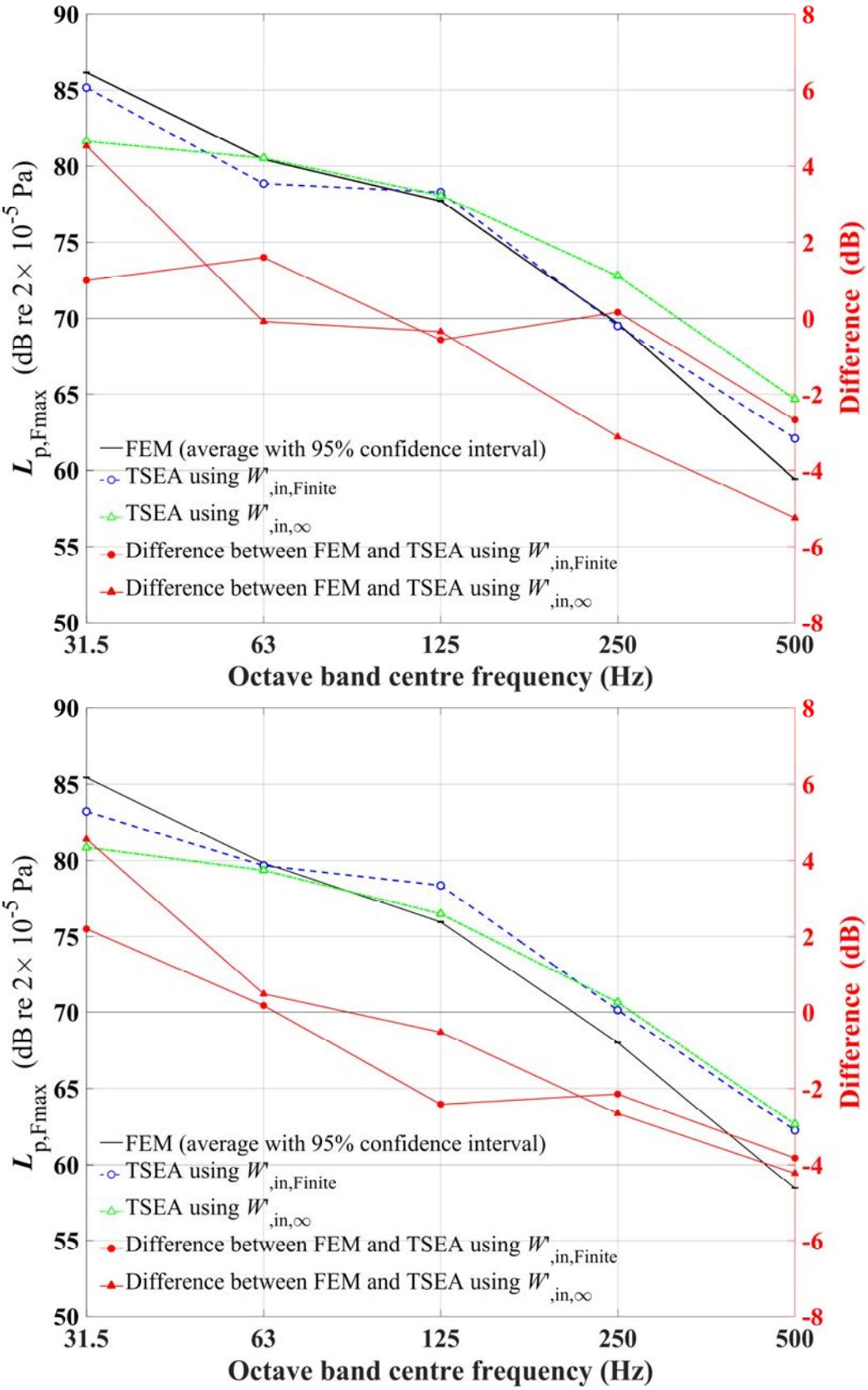

Figure 6-7. Comparison of $L_{p,Fmax}$ predicted using TSEA and FEM for model A for different room reverberation times. Room T=1.5s (upper), Room T=0.75s (lower) in octave bands.

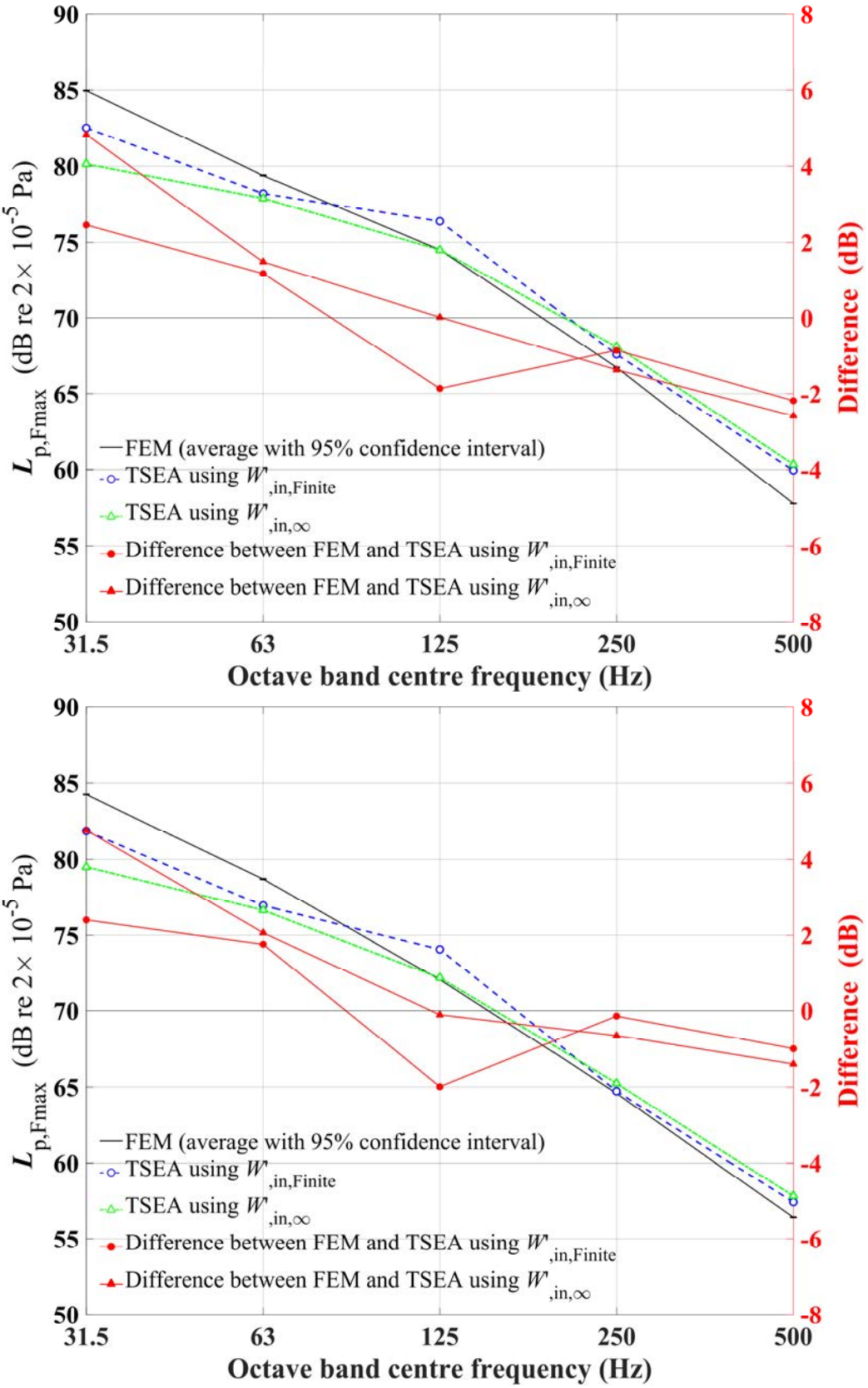

Figure 6-8. Comparison of $L_{p,Fmax}$ predicted using TSEA and FEM for model A for different room reverberation times. Room T=0.375s (upper), Room T=0.1875s (lower) in octave bands.

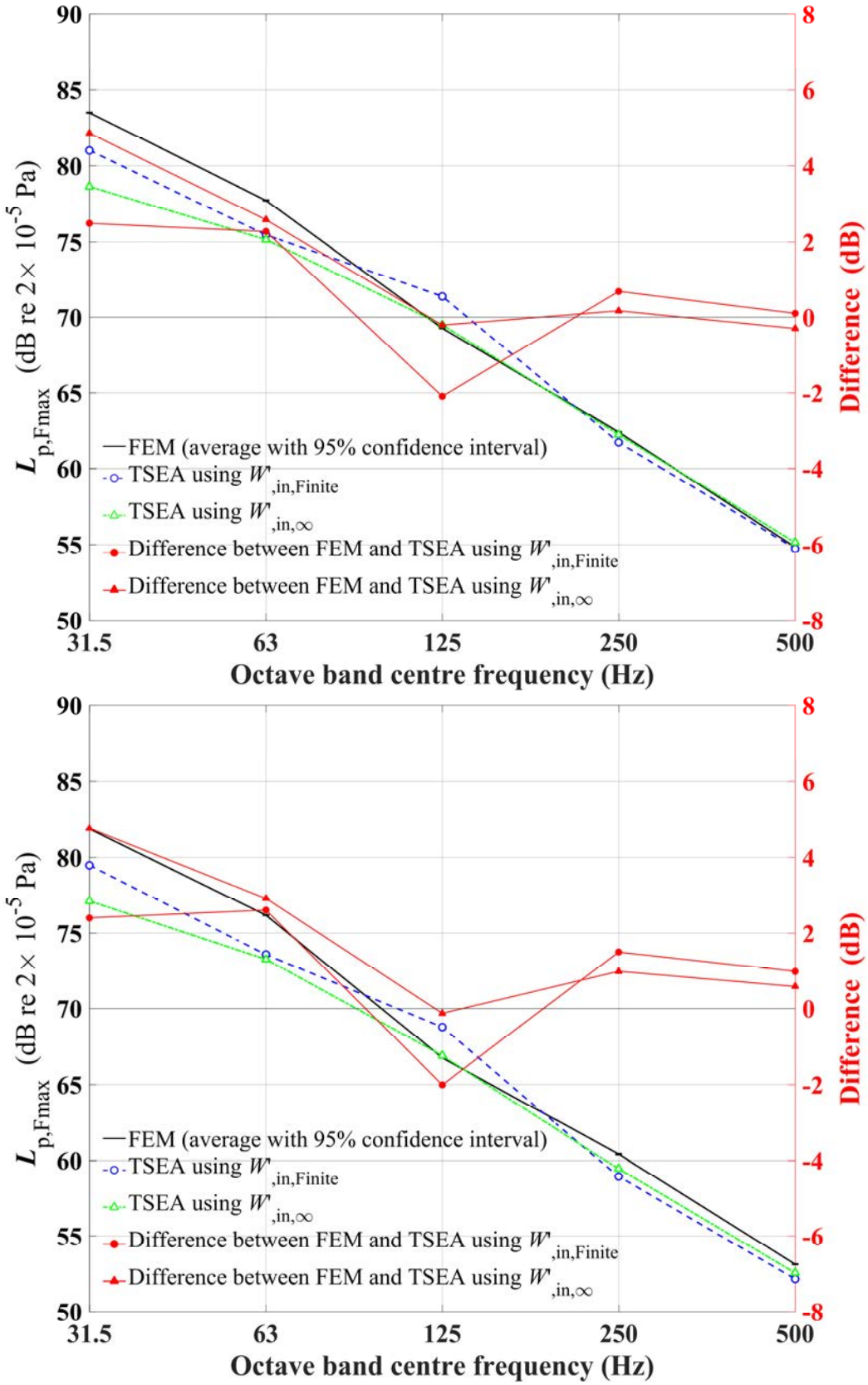

Figure 6-9. Comparison of $L_{p,Fmax}$ predicted using TSEA and FEM for model A for different room reverberation times. Room T=0.0938s (upper), Room T=0.0469s (lower) in octave bands.

6.4.2.2 Model B (37.5 m^3)

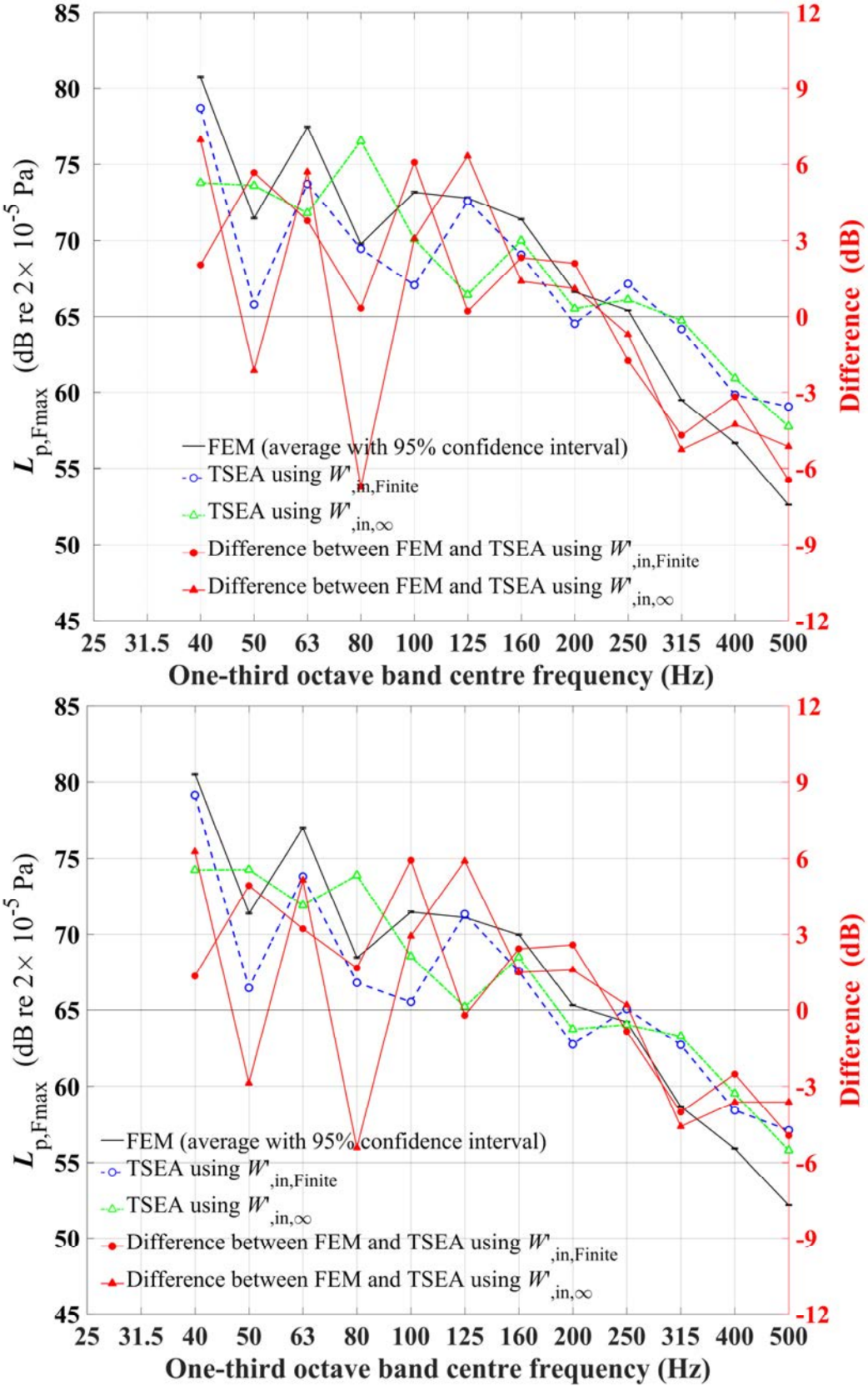

Figure 6-10. Comparison of $L_{p,Fmax}$ predicted using TSEA and FEM for model B for different room reverberation times. Room T=1.5s (upper), Room T=0.75s (lower) in one-third octave bands.

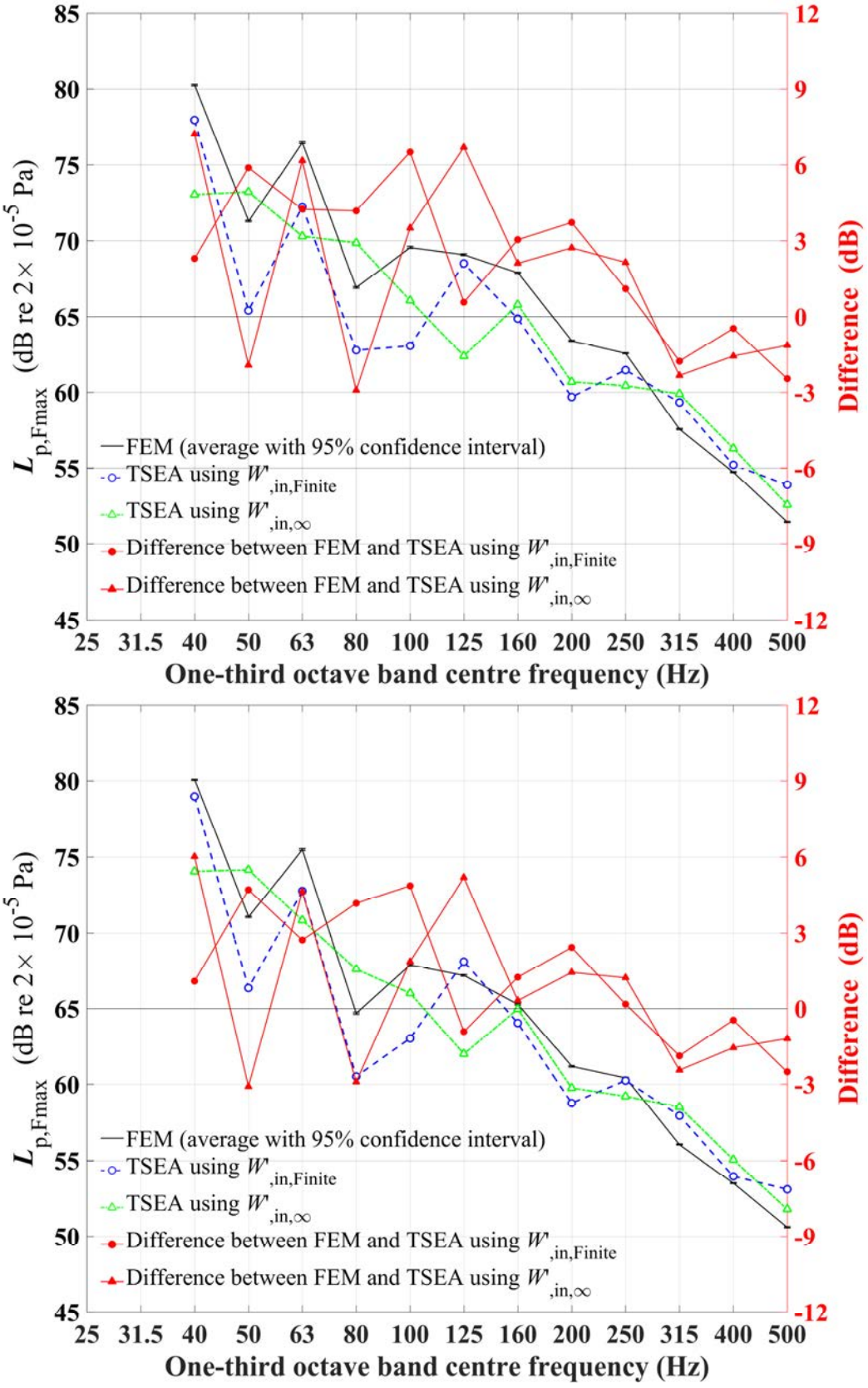

Figure 6-11. Comparison of $L_{p,Fmax}$ predicted using TSEA and FEM for model B for different room reverberation times. Room T=0.375s (upper), T=0.1875s (lower) in one-third octave bands.

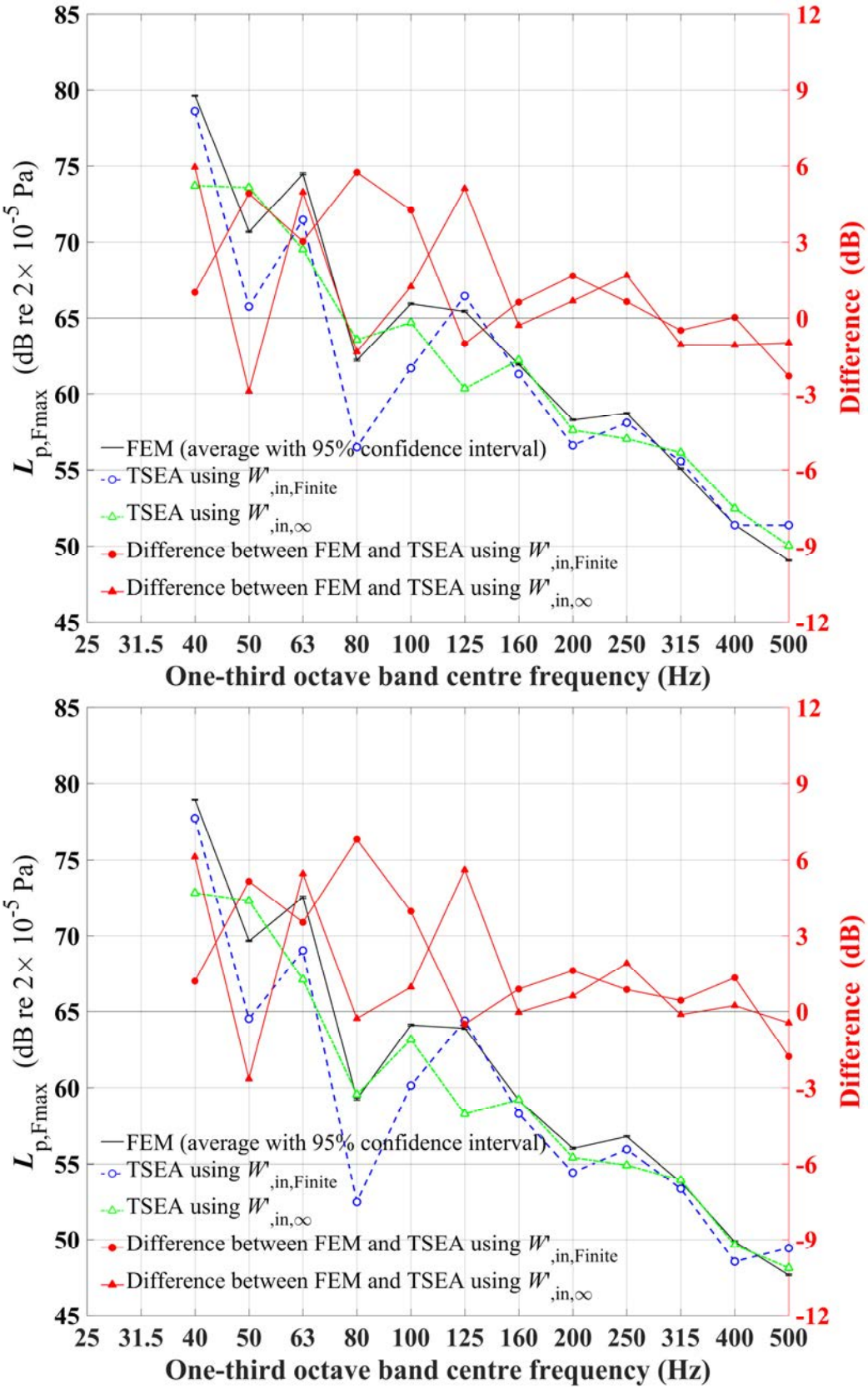

Figure 6-12. Comparison of $L_{p,Fmax}$ predicted using TSEA and FEM for model B for different room reverberation times. Room T=0.0938s (upper), T=0.0469s (lower) in one-third octave bands.

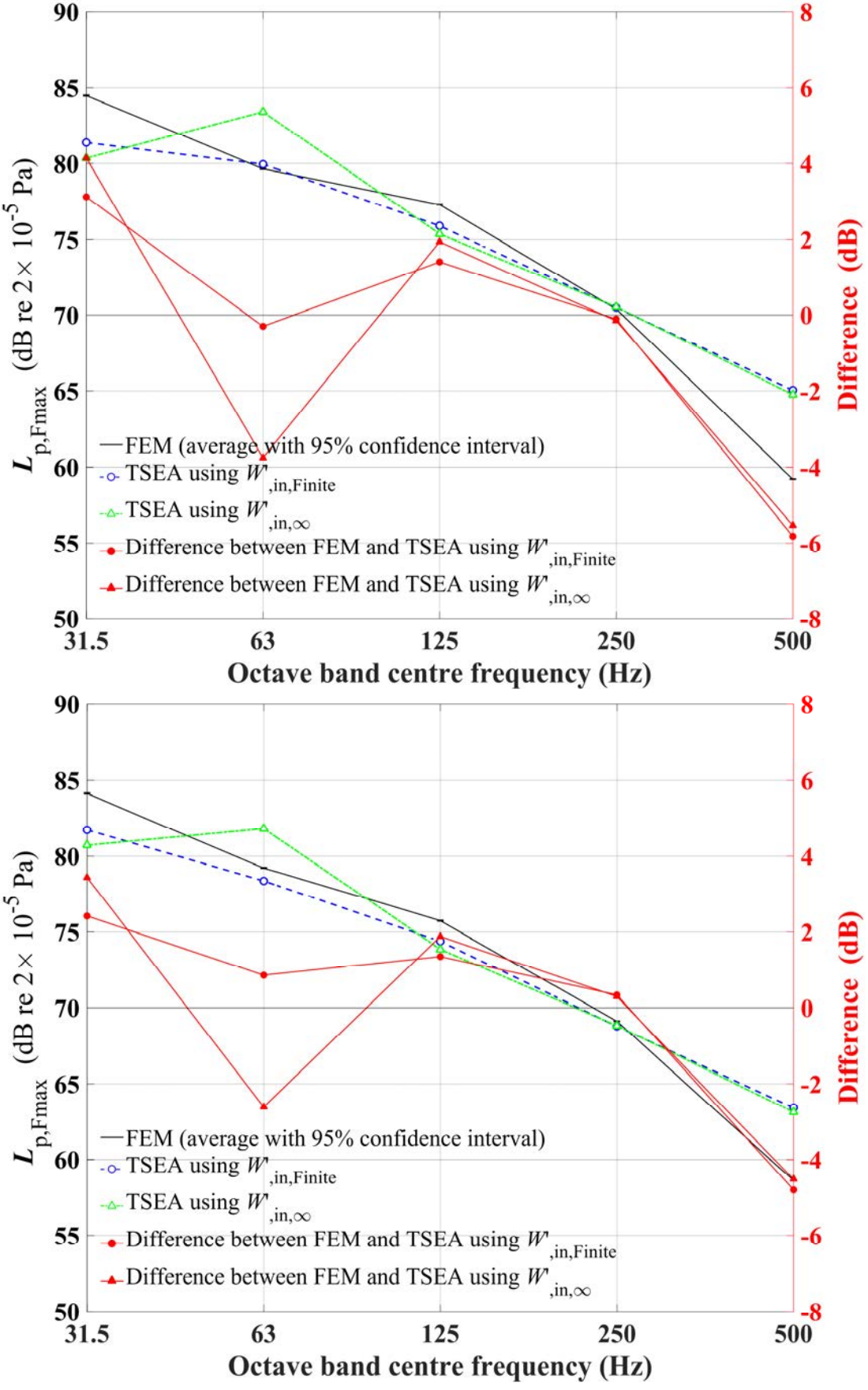

Figure 6-13. Comparison of $L_{p,Fmax}$ predicted using TSEA and FEM for model B for different room reverberation times. Room T=1.5s (upper), Room T=0.75s (lower) in octave bands.

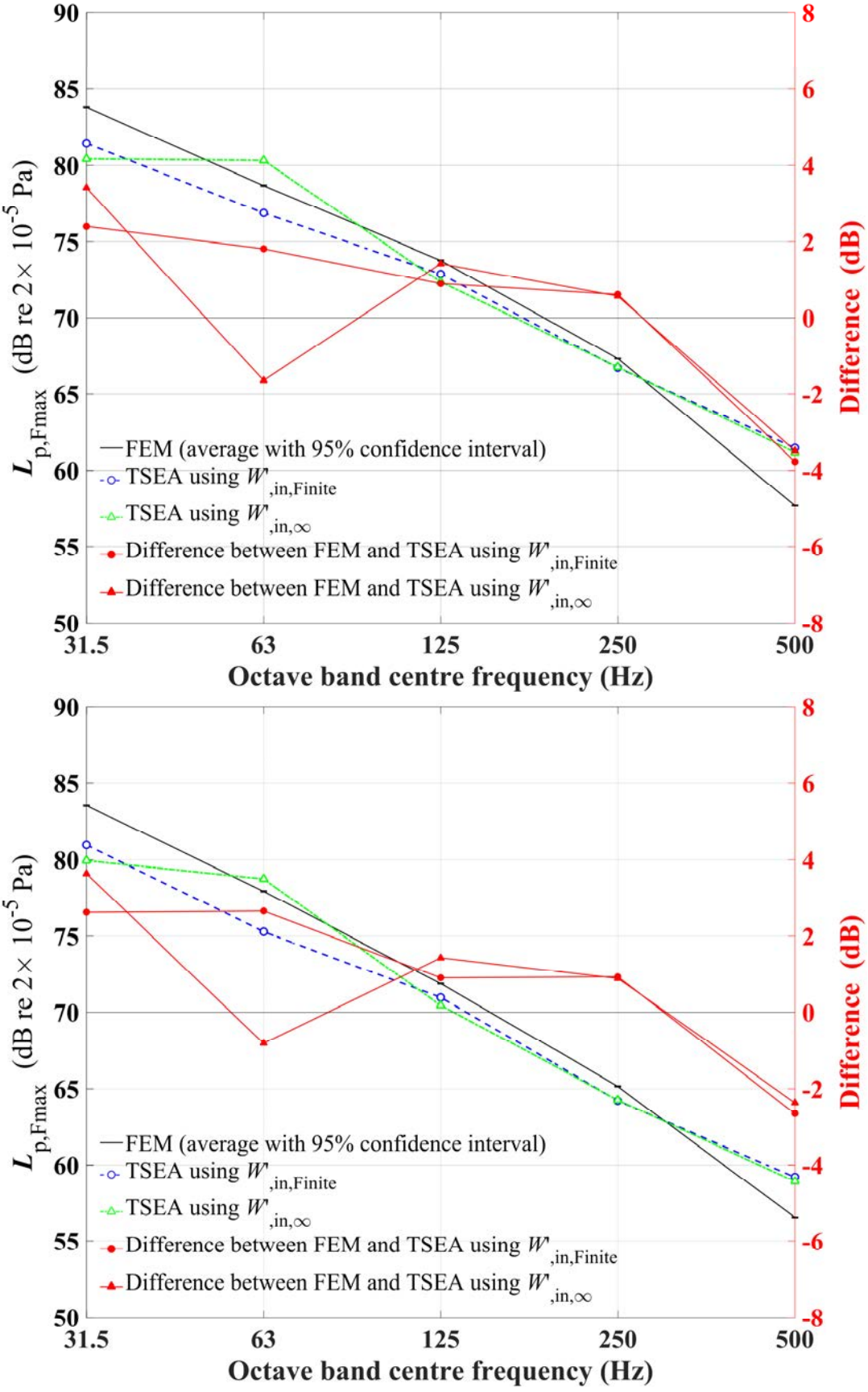

Figure 6-14. Comparison of $L_{p,Fmax}$ predicted using TSEA and FEM for model B for different room reverberation times. Room T=0.375s (upper), Room T=0.1875s (lower) in octave bands.

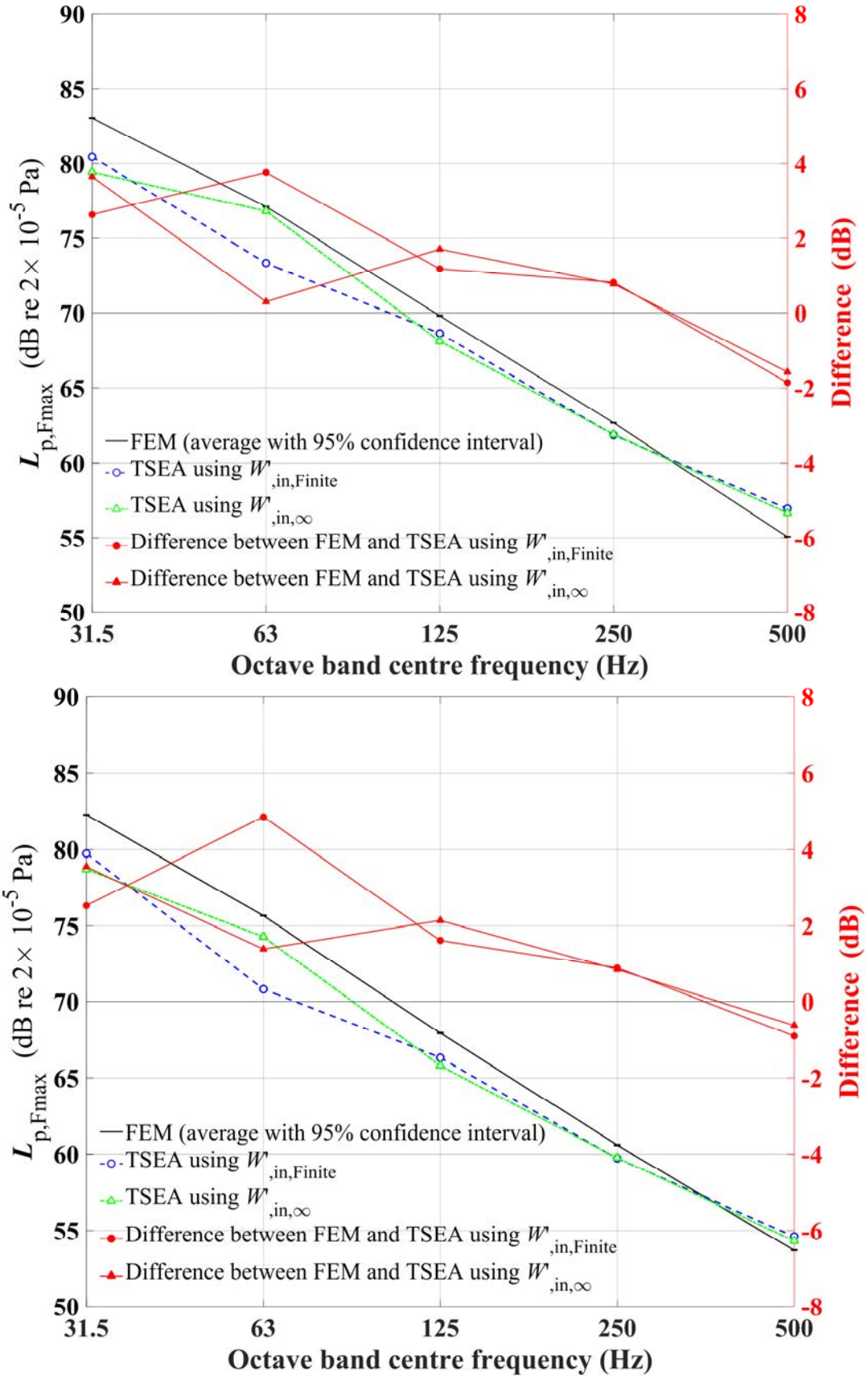

Figure 6-15. Comparison of $L_{p,Fmax}$ predicted using TSEA and FEM for model B for different room reverberation times. Room T=0.0938s (upper), Room T=0.0469s (lower) in octave bands.

6.4.2.3 Model C

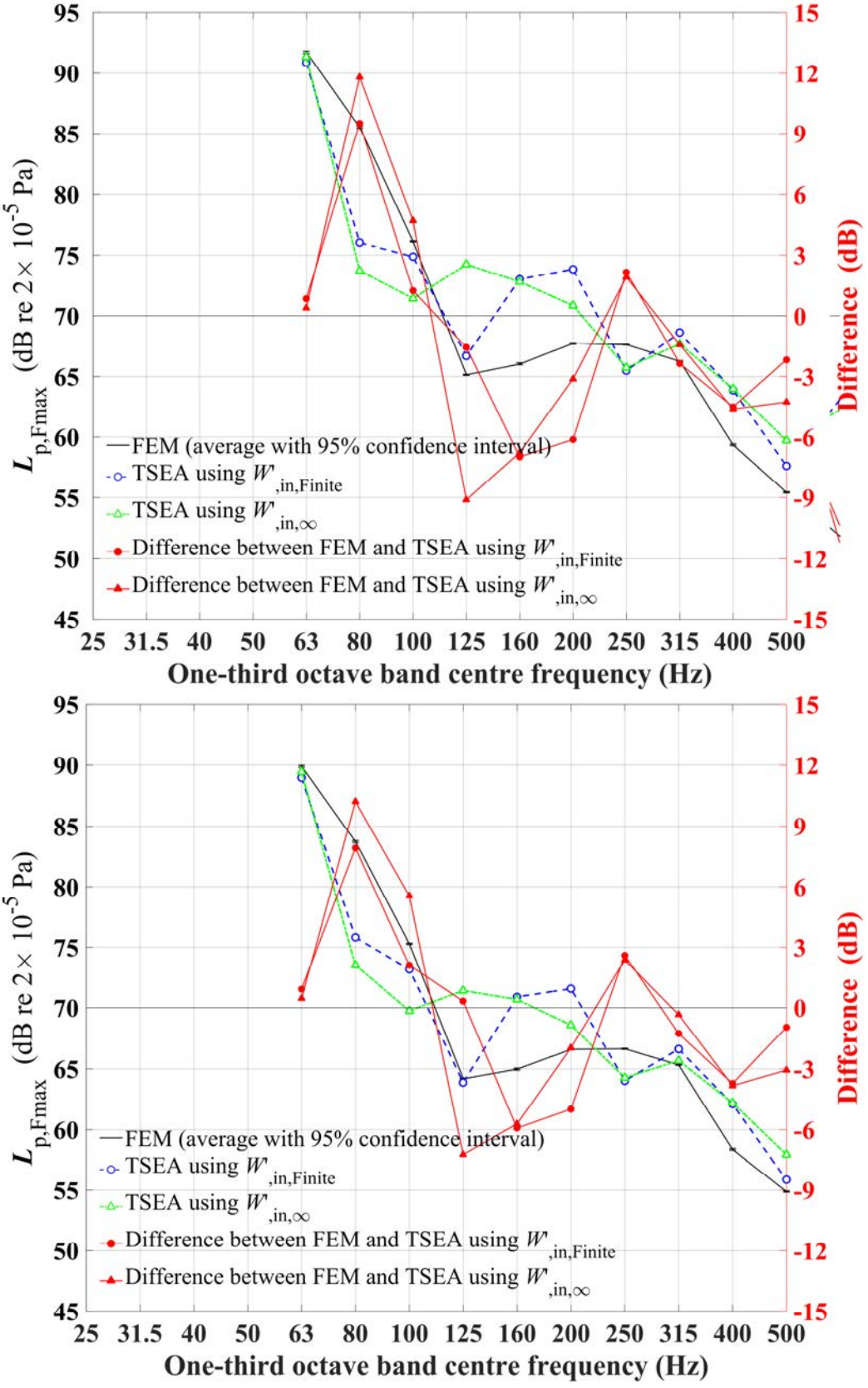

Figure 6-16. Comparison of $L_{p,Fmax}$ predicted using TSEA and FEM for model C for different room reverberation times. Room T=1.5s (upper), Room T=0.75s (lower) in one-third octave bands.

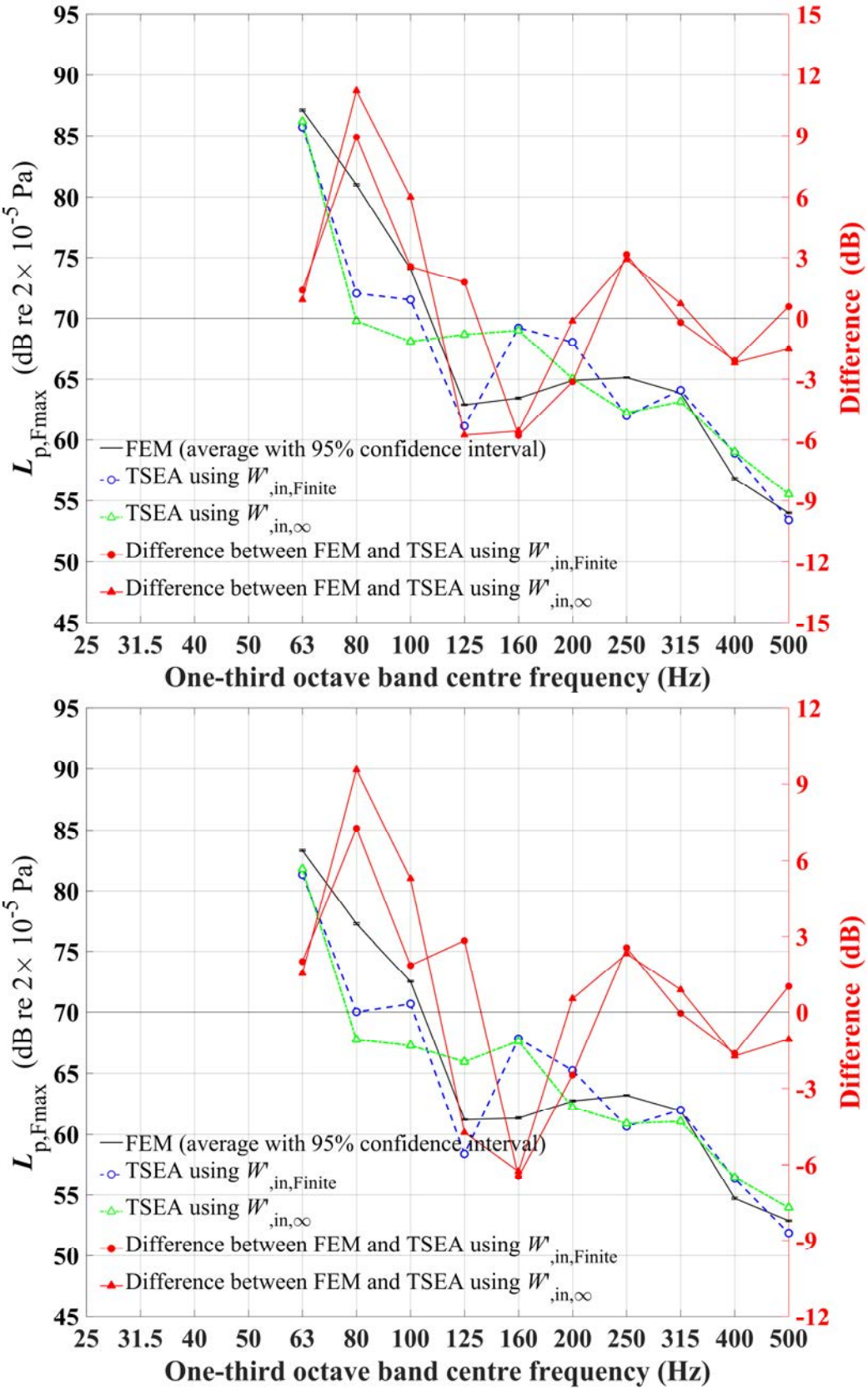

Figure 6-17. Comparison of $L_{p,Fmax}$ predicted using TSEA and FEM for model C for different room reverberation times. Room T=0.375s (upper), Room T=0.1875s (lower) in one-third octave bands.

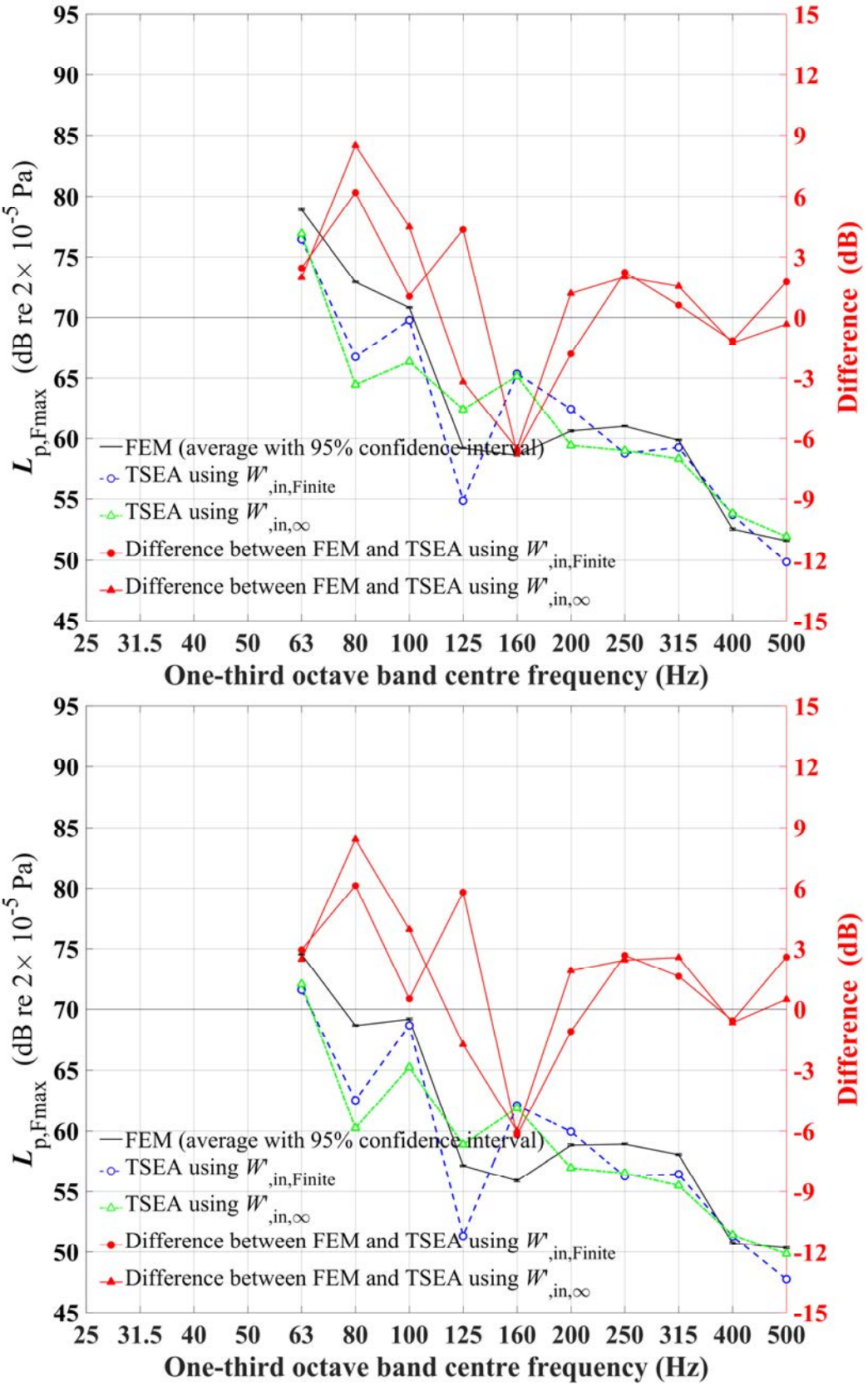

Figure 6-18. Comparison of $L_{p,Fmax}$ predicted using TSEA and FEM for model C for different room reverberation times. Room T=0.0938s (upper), Room T=0.0469s (lower) in one-third octave bands.

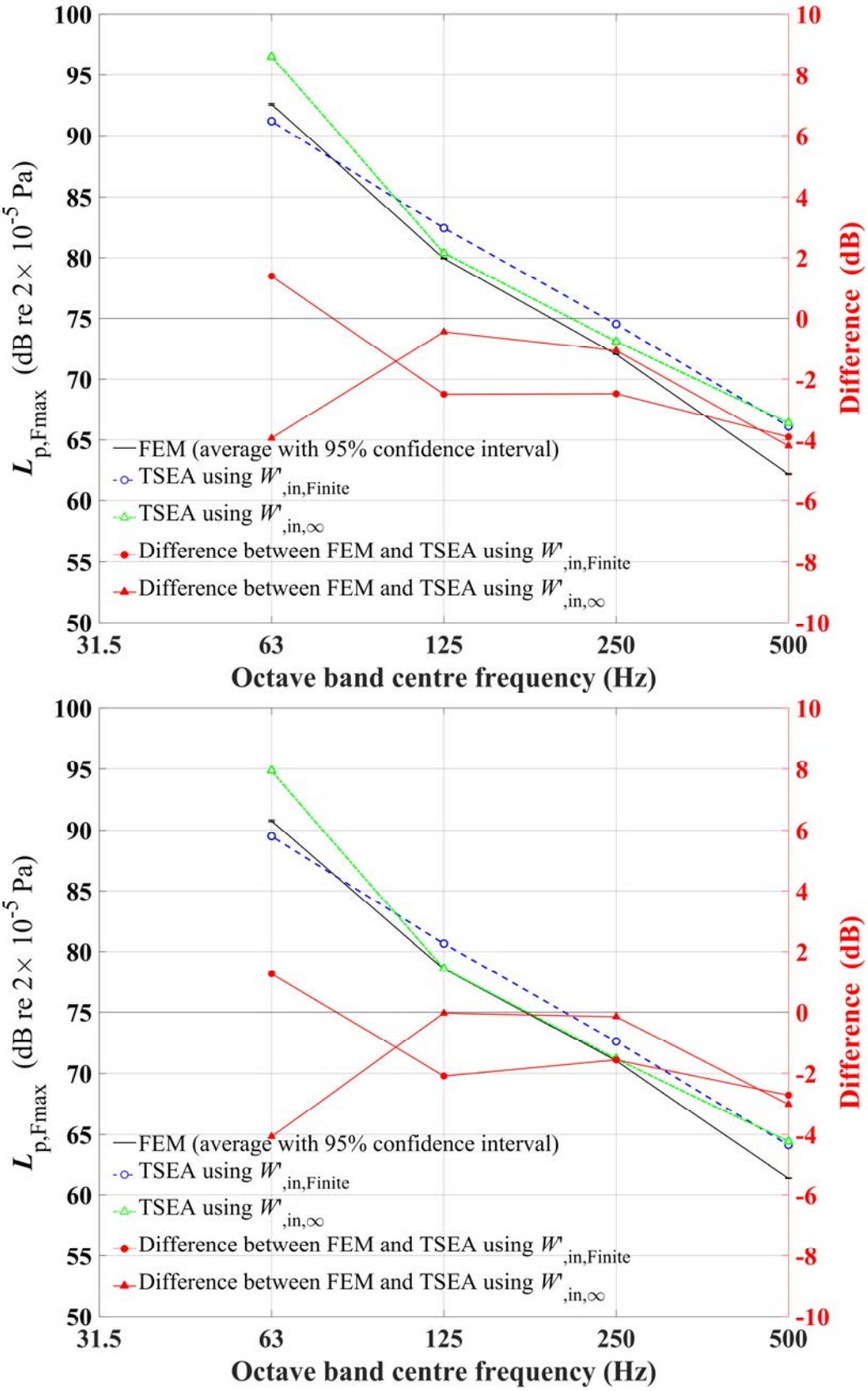

Figure 6-19. Comparison of $L_{p,Fmax}$ predicted using TSEA and FEM for model C for different room reverberation times. Room T=1.5s (upper), Room T=0.75s (lower) in octave bands.

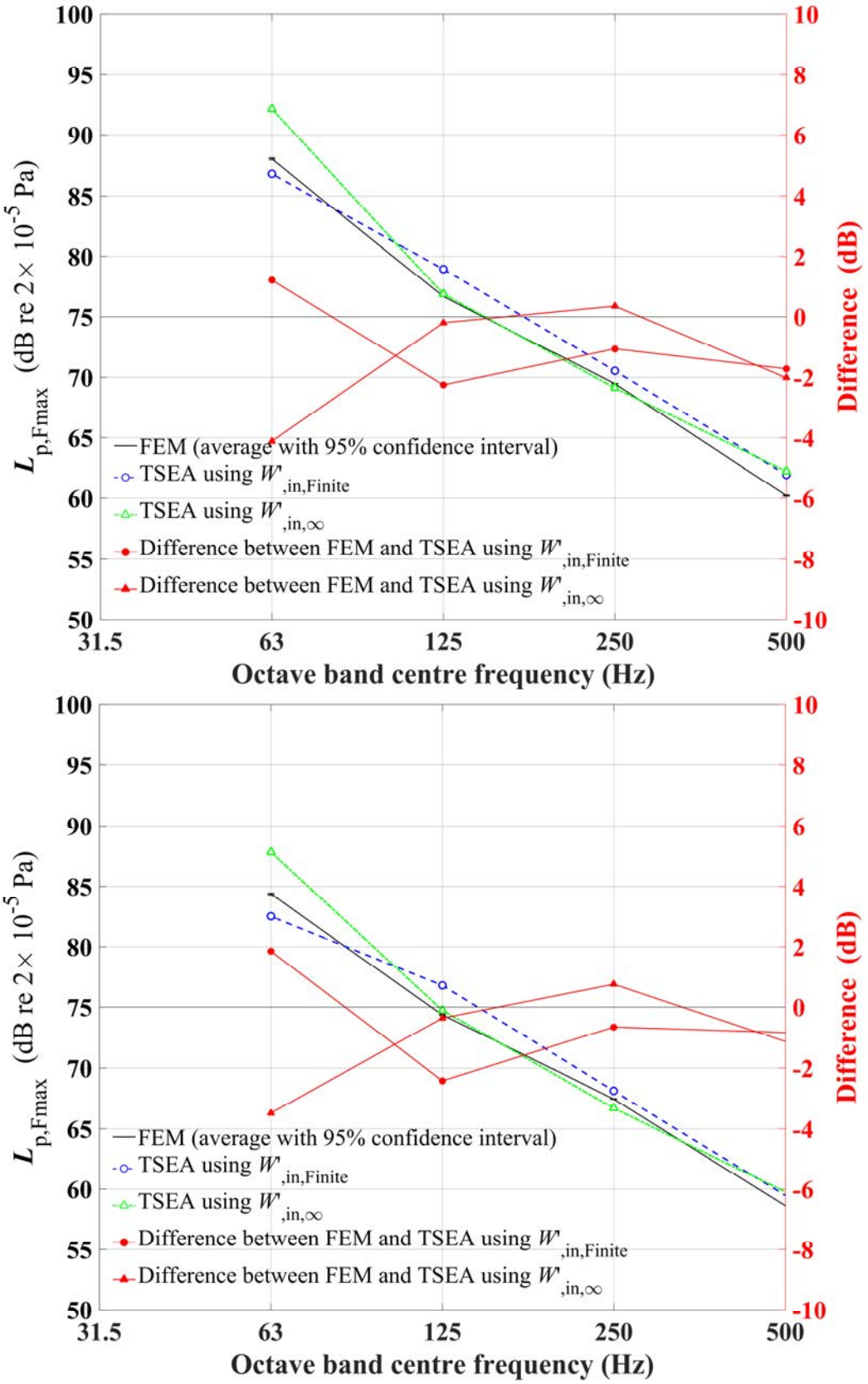

Figure 6-20. Comparison of $L_{p,Fmax}$ predicted using TSEA and FEM for model C for different room reverberation times. Room T=0.375s (upper), Room T=0.1875s (lower) in octave bands.

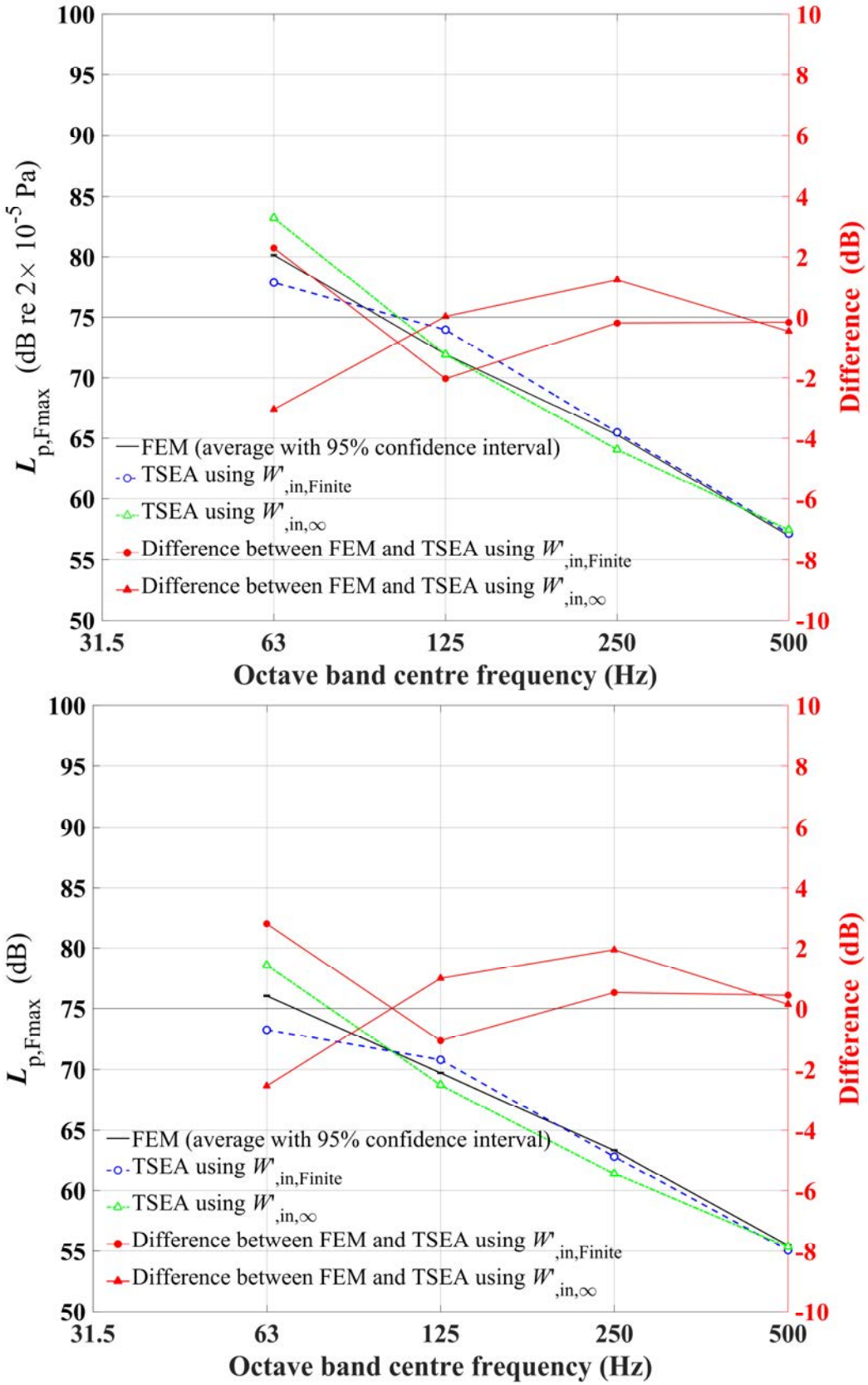

Figure 6-21. Comparison of $L_{p,Fmax}$ predicted using TSEA and FEM for model C for different room reverberation times. Room T=0.0938s (upper), Room T=0.0469s (lower) in octave bands.

6.5 Assessment of the modal response of the room using FEM

6.5.1 Introduction

With heavy impact sources, it tends to be the low-frequency range that is of particular interest. For field measurements in typical residential rooms, the diffuse field condition assumption used in laboratory measurements does not occur at low frequencies where individual room modes tend to dominate the response. This issue has been addressed for field measurements of airborne sound insulation and impact sound insulation (using the ISO tapping machine) by using corner measurements to give an estimate of the room-average level in order to improve the repeatability and reproducibility [77, 78]. There have also been studies on the spatial variation in the sound pressure level with the impact ball and tyre source [76, 79, 80].

In these numerical experiments with FEM, four models are created that consider the ISO rubber ball impacting a 140mm concrete base floor with four box-shape rooms with different volumes (50, 37.5, 25 and 15m^3) and a reverberation time of 1.5s. The model parameters are summarised in Table 6.2 to Table 6.4.

Firstly, the sound field in terms of $L_{p,Fmax}$ is visualised in order to give insights into the room response with different room dimensions. Secondly, a grid with finer detail is used to assess the variation of $L_{p,Fmax}$ in the vertical direction at the measurement positions according to Japanese and Korean guidelines. Thirdly, the spatial average $L_{p,Fmax}$ obtained from three measurement procedures is compared against the room-average $L_{p,Fmax}$ for four different rooms.

6.5.2 Modal response in the room

For models A, B, C and D, Figure 6-22 to Figure 6-25 show the sound pressure field in terms of $L_{p,Fmax}$ with rubber ball excitation at the central position of the concrete slab for the four different FEM models in the 31.5, 63 and 125Hz octave bands. The plots are normalised to the highest $L_{p,Fmax}$ values and show these normalised values on the room surfaces and three intersecting planes.

For Models A, B and C which all have the longest room dimension being 5m, the lowest room mode is f_{100} (34.3Hz), but this is not excited by the fundamental plate

mode; hence in the 31.5Hz octave band the sound field appears to be determined by the direct field radiated by the fundamental plate mode. In the 63Hz octave band, the f_{001} vertical axial mode (68.6Hz) and the f_{200} horizontal axial mode (68.6Hz) occur at the same frequency in the 63Hz band and are both excited by the fundamental plate mode. For Model A, the response appears to be a combination of f_{001} and f_{200}. For Models B and C, the f_{001} mode is evident. For Model D, f_{001} (68.6Hz) occurs in the 63Hz band and f_{200} (114.3Hz), f_{201} (133.3Hz) and f_{002} (137.2Hz) occur in the 125Hz band; this results in the spatial variation in the 63Hz band being clearly attributed to the f_{001} mode. In the 125Hz band, there is evidence of the f_{201} tangential room mode (97Hz) in Model A. For Models B, C and D it is difficult to identify this mode.

The highest spatial variation of $L_{p,Fmax}$ is between 6 and 30dB; the former occurs with the Model D room at 31.5Hz, and the latter occurs with the Model C room at 63Hz. Measurements in a 62m^3 room by Yoo *et al.* [112] indicate a maximum difference of ≈16dB at 31.5Hz and 63Hz.[112] indicate a maximum difference of ≈16dB at 31.5Hz and 63Hz. Note that for airborne sound insulation measurements with broadband noise sources using L_{eq}; measured data suggest this difference will be between 17 and 28 dB for typical rooms in the low-frequency range [24].

This indicates there is a risk of underestimating the room average $L_{p,Fmax}$ if the measurement positions are not randomised or chosen with a well-defined procedure.

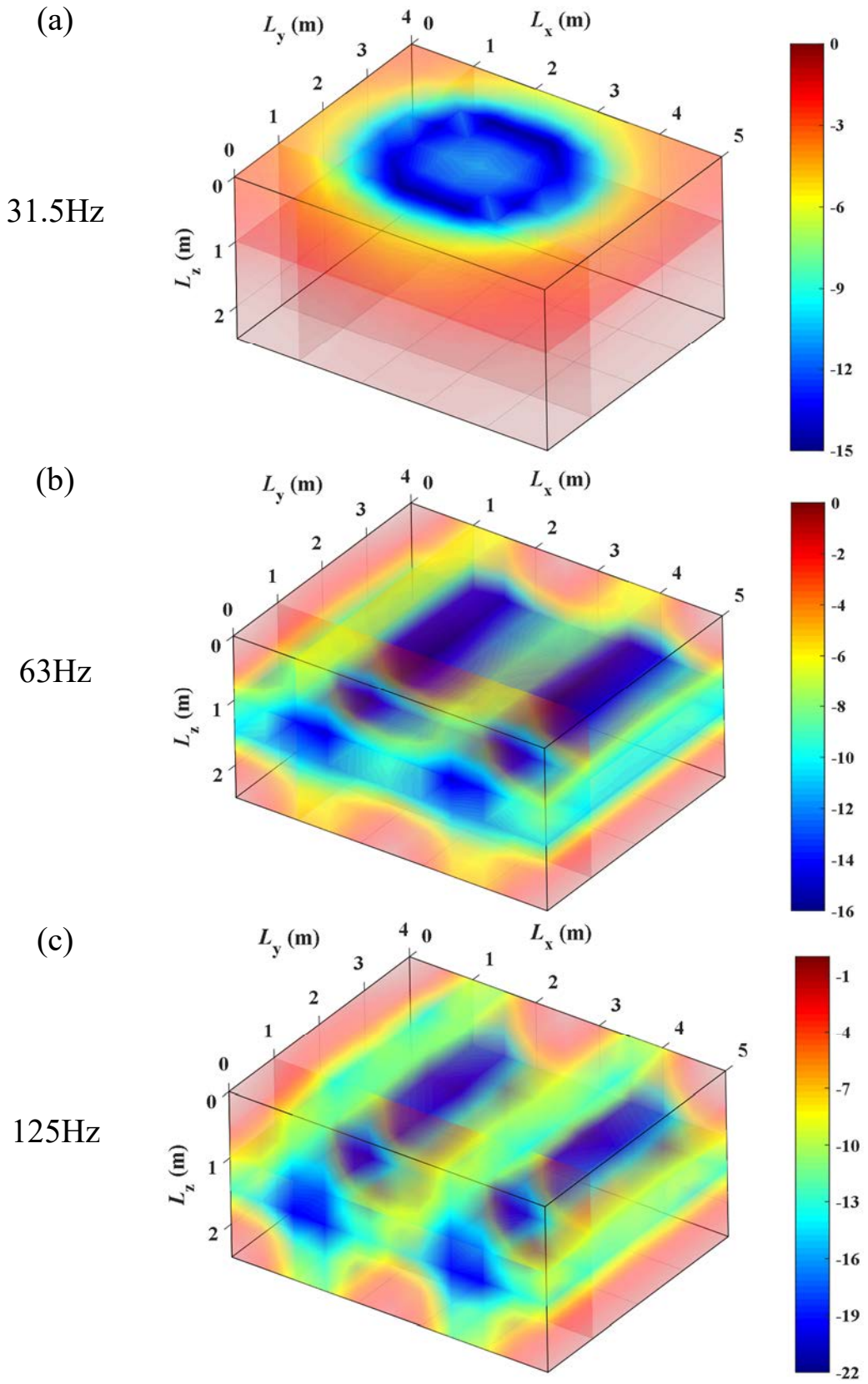

Figure 6-22. Sound pressure field in terms of $L_{p,Fmax}$ for model A (dB re the highest level in the room) for model A in the 31.5Hz (upper), 63Hz (middle) and 125Hz (lower) octave bands.

Model B (37.5m^3)

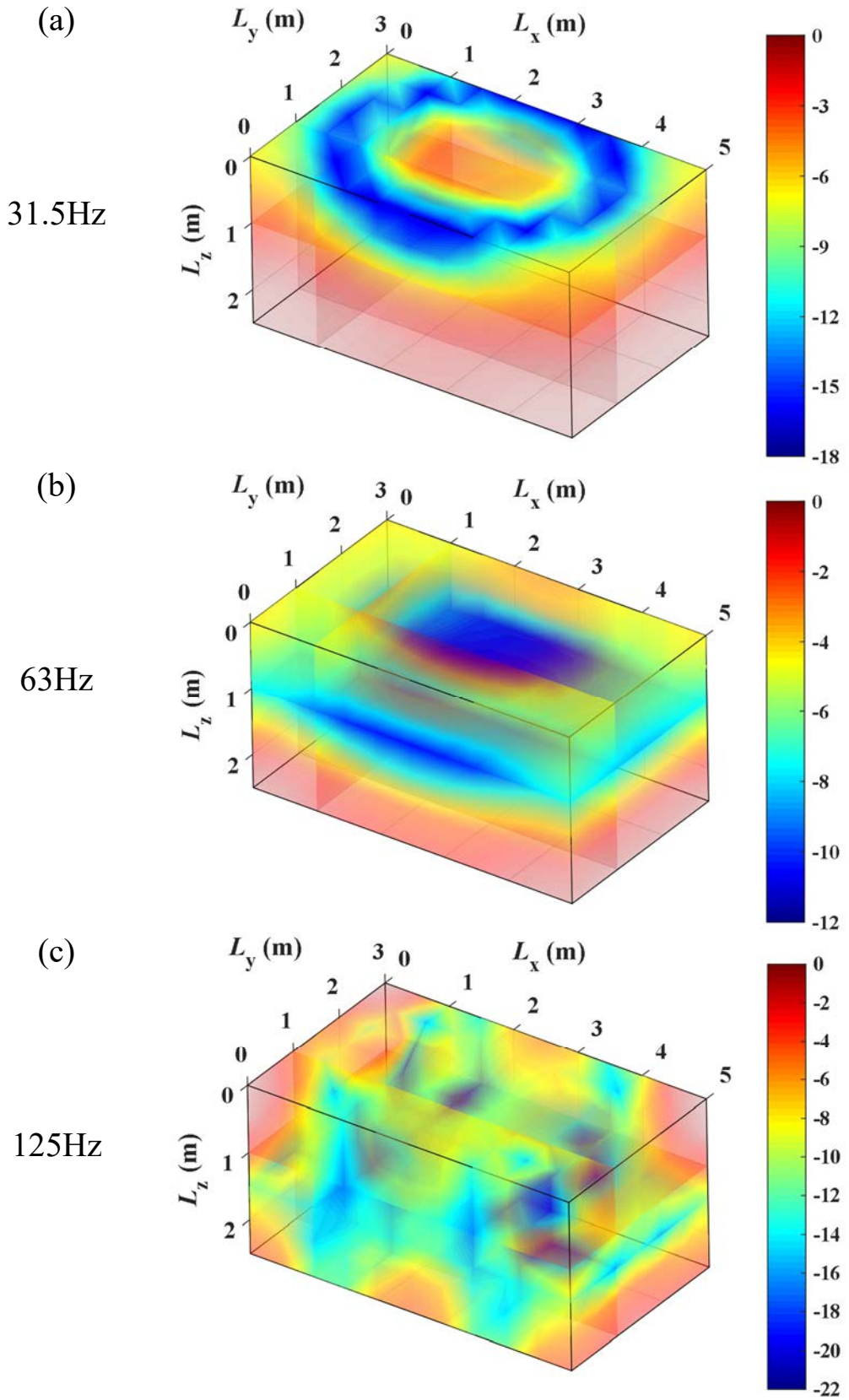

Figure 6-23. Sound pressure field in terms of $L_{p,Fmax}$ for model B (dB re the highest level in the room) for model B in the 31.5Hz (upper), 63 Hz (middle) and 125Hz (lower) octave bands.

Model C (25m^3)

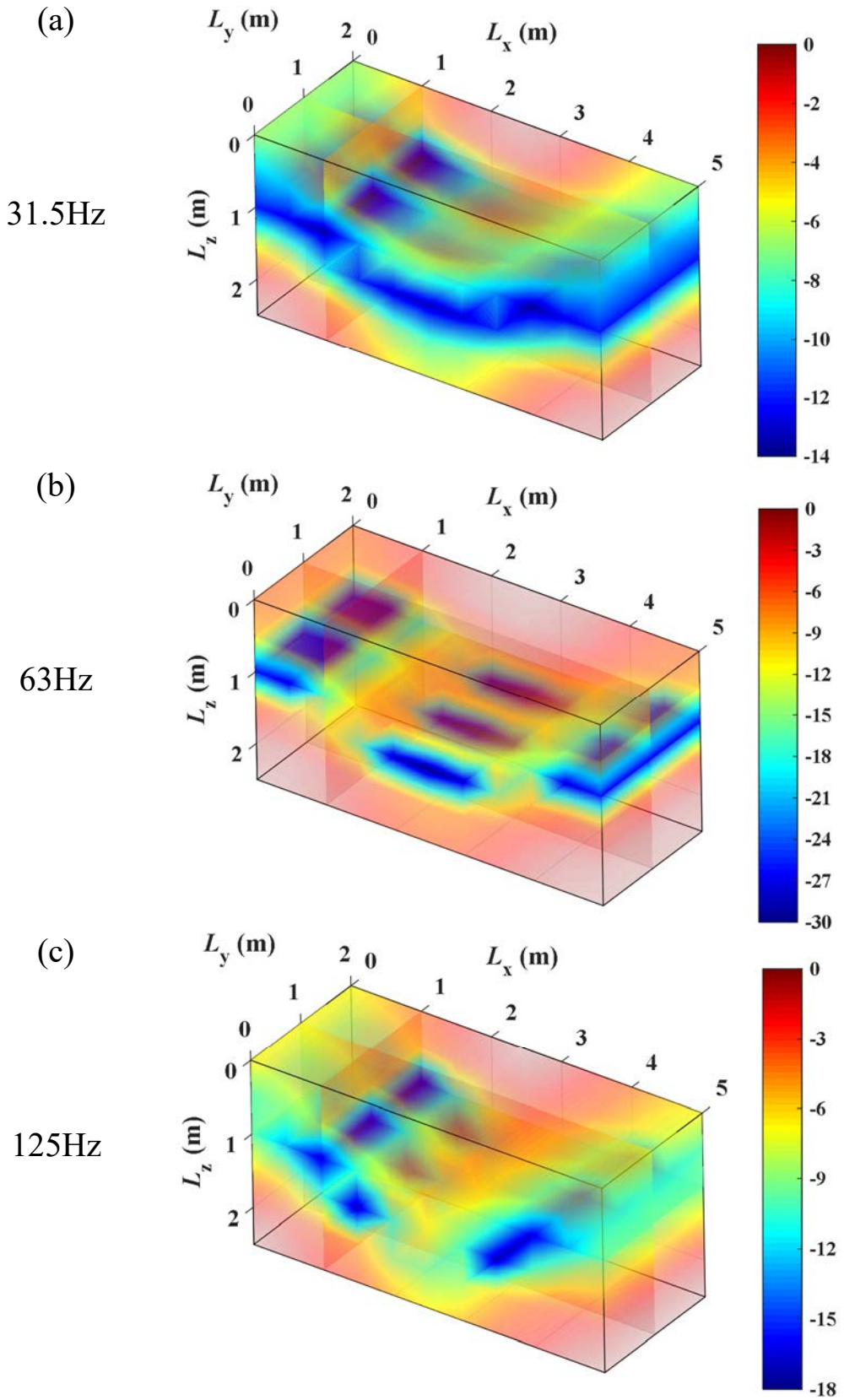

Figure 6-24. Sound pressure field in terms of $L_{p,Fmax}$ for model C (dB re the highest level in the room) for model C in the 31.5Hz (upper), 63 Hz (middle) and 125Hz (lower) octave bands.

Model D (15m^3)

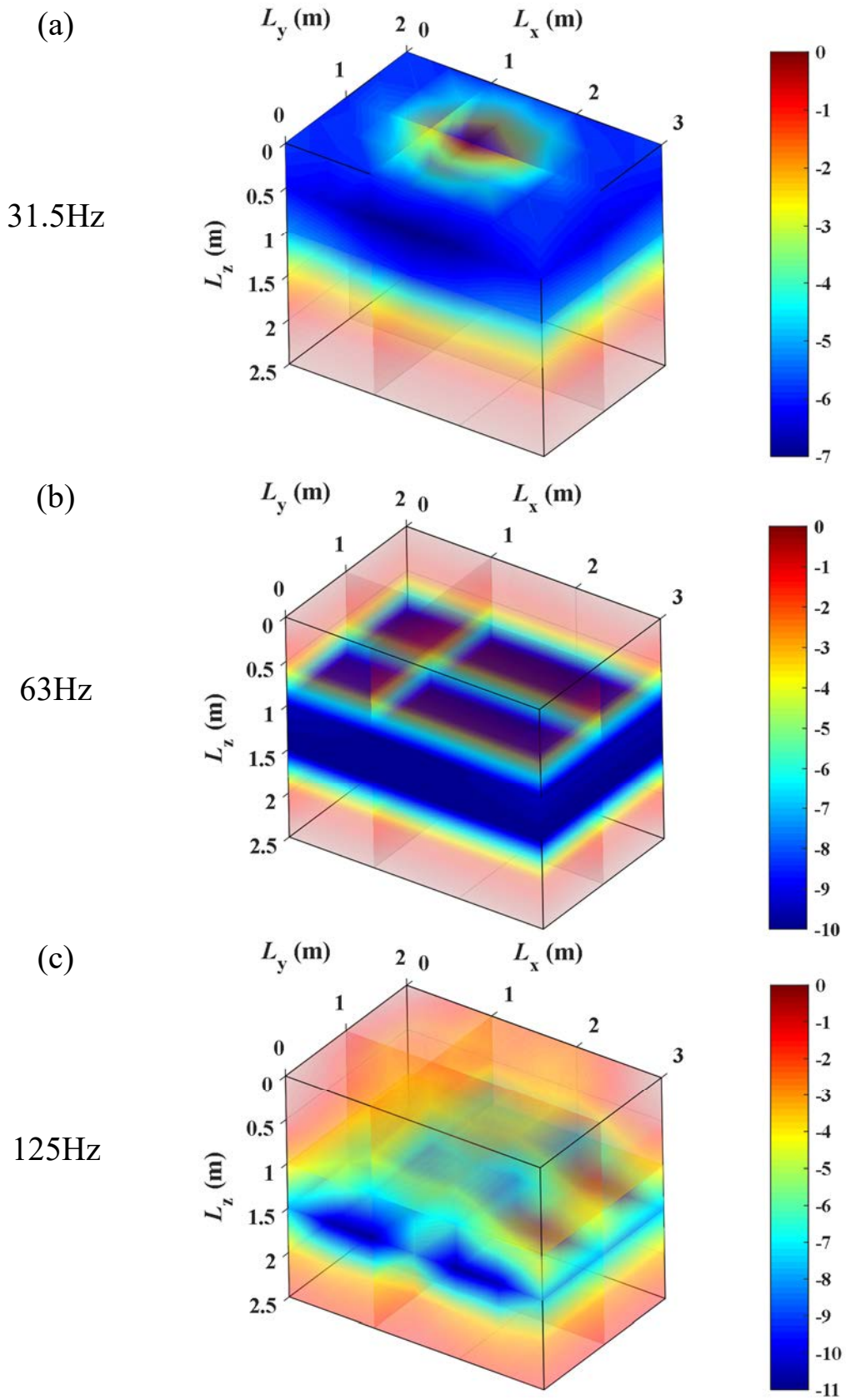

Figure 6-25. Sound pressure field in terms of $L_{p,Fmax}$ for model D (dB re the highest level in the room) for model D in the 31.5Hz (upper), 63 Hz (middle) and 125Hz (lower) octave bands.

6.5.3 I-INCE-J and MOCT-K microphone positions – vertical variation in $L_{p,Fmax}$

Section 1.2.2 described the different measurement procedures used for excitation and sampling of sound pressure used in Japan and Korea.

In this section these procedures are assessed using numerical experiments. Figure 6-26 summarises the excitation and measurement positions used in I-INCE-J and MOCT-K and also shows a grid with finer detail is used to assess the variation of $L_{p,Fmax}$ in the vertical direction at the measurement positions according to I-INCE-J and MOCT-K.

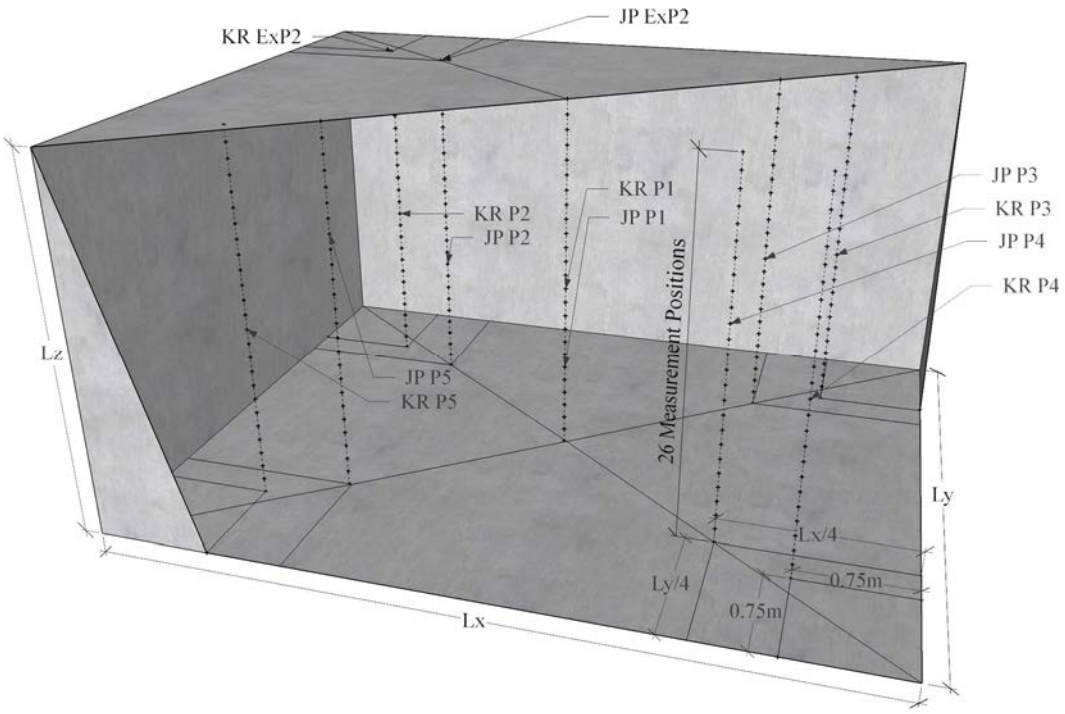

Figure 6-26. I-INCE-J and MOCK-K field measurement positions: excitation positions on the concrete slab and measurement positions in the room with 26 grid points in the vertical direction.

Figure 6-27 to Figure 6-30 shows the average $L_{p,Fmax}$ from five excitation positions in the vertical lines for the I-INCE-J and MOCT-K microphone positions which are directly underneath the excitation positions. The average $L_{p,Fmax}$ value is normalised to the highest value in the vertical line. Because of the symmetry that exists for the box-shaped room in these numerical experiments, Figure 6-27 to Figure 6-30 only shows the results for the 31.5 to 125Hz octave bands from microphone positions KR P1, JP P1, KR P2 and JP P2. Note that the values in Figure 6-22 to Figure 6-25 are not directly

comparable with those in Figure 6-27 to Figure 6-30 because the latter only considers one excitation position.

In general, the largest variations tend to occur for JP P1 and KR P1, but they occur in different frequency bands and at different heights. For Model A, the lowest value was -16.8dB which occurred at 125Hz at a height of 1.2m. For Model B, the lowest value was -14.4dB which occurred at 31.5Hz at a height of 0.6m. For Model C, the lowest value of -26dB occurred at 63Hz at a height of 1.1m and 1.5m. For Model D, the lowest value of -19.9dB occurred at 63Hz at a height of 1.2m.

It is not clear why the inclusion of P1 in the I-INCE-J and MOCT-K procedures is chosen because it is not representative of the central zone and it tends to give lower values than P2, P3, P4 and P5 (i.e. corner positions). In addition, it is unusual to have an excitation position at the centre of the floor with the receiver position at the centre point in the room. For this reason, the next section assesses whether the spatial average $L_{p,Fmax}$ which is determined from INCE-J and MOCT-K microphone positions give a reasonable estimate of the room-average $L_{p,Fmax}$.

Model A (50m^3)

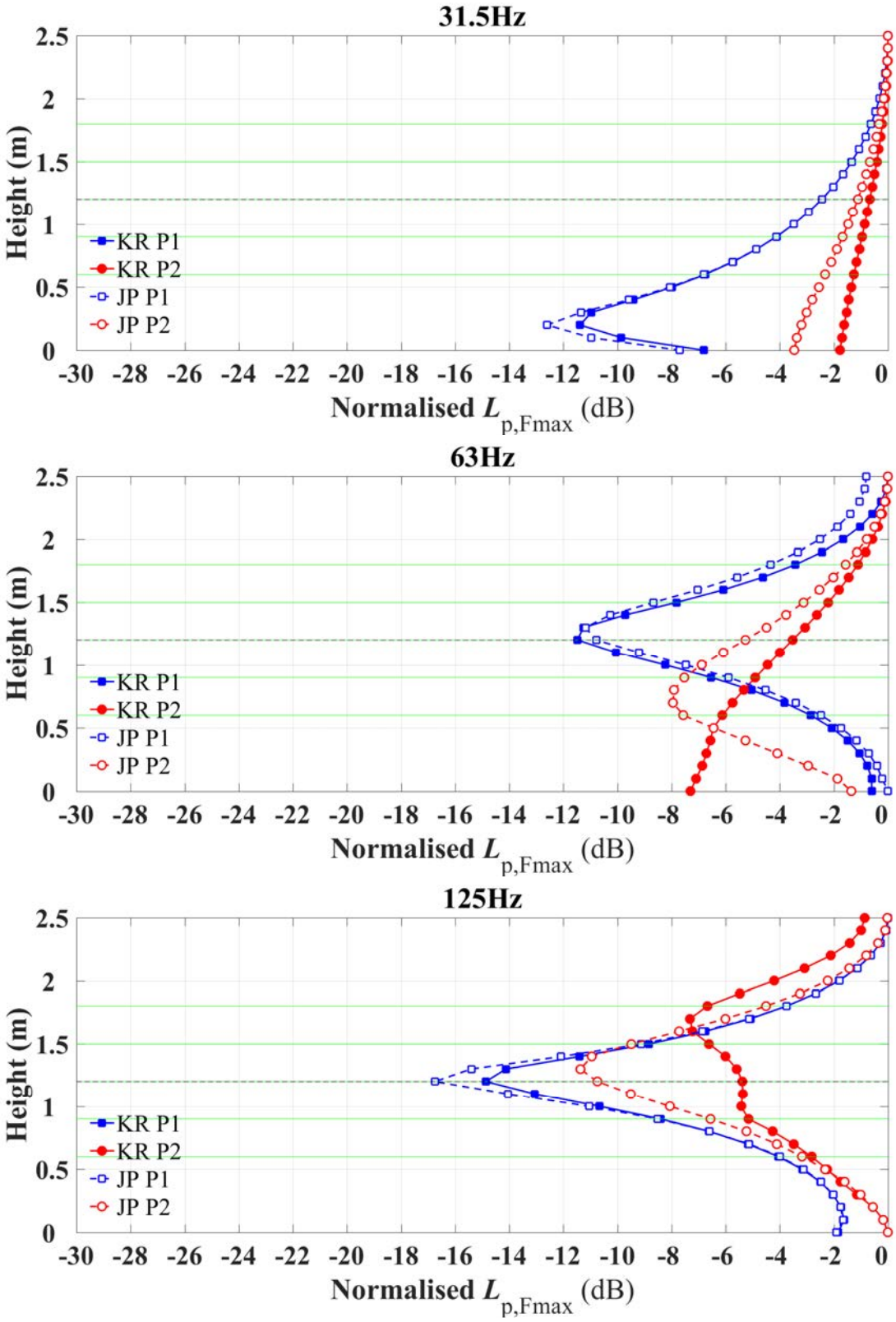

Figure 6-27. Spatial variation of normalised $L_{p,Fmax}$ in the vertical direction in model A. The black dashed horizonal line indicates the 1.2m height for MOCT-K and the green horizontal lines indicate the heights for I-INCE-J.

Model B (37.5m^3)

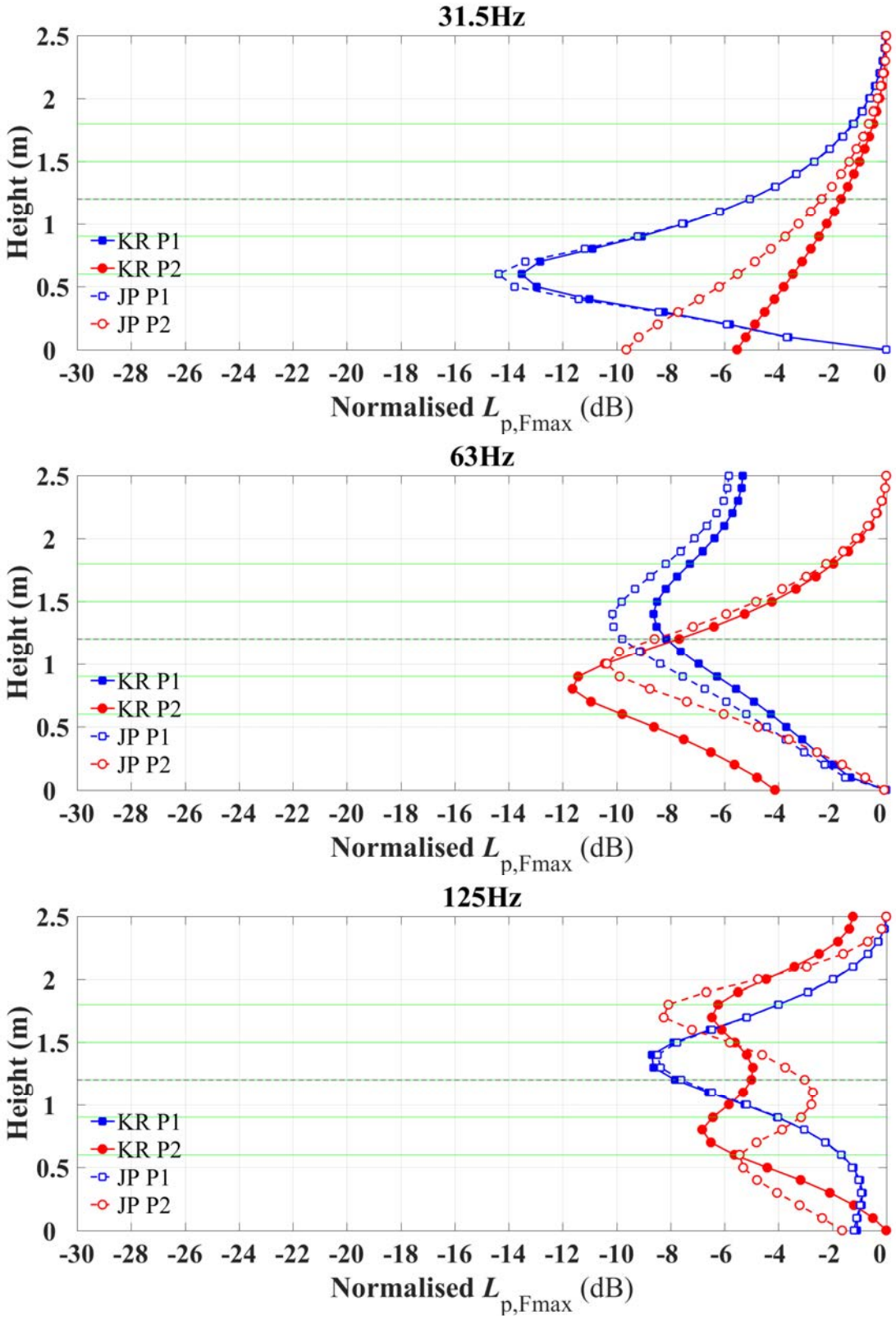

Figure 6-28. Spatial variation of normalised $L_{p,Fmax}$ in the vertical direction in model B. The black dashed horizonal line indicates the 1.2m height for MOCT-K and the green horizontal lines indicate the heights for I-INCE-J.

Model C (25m^3)

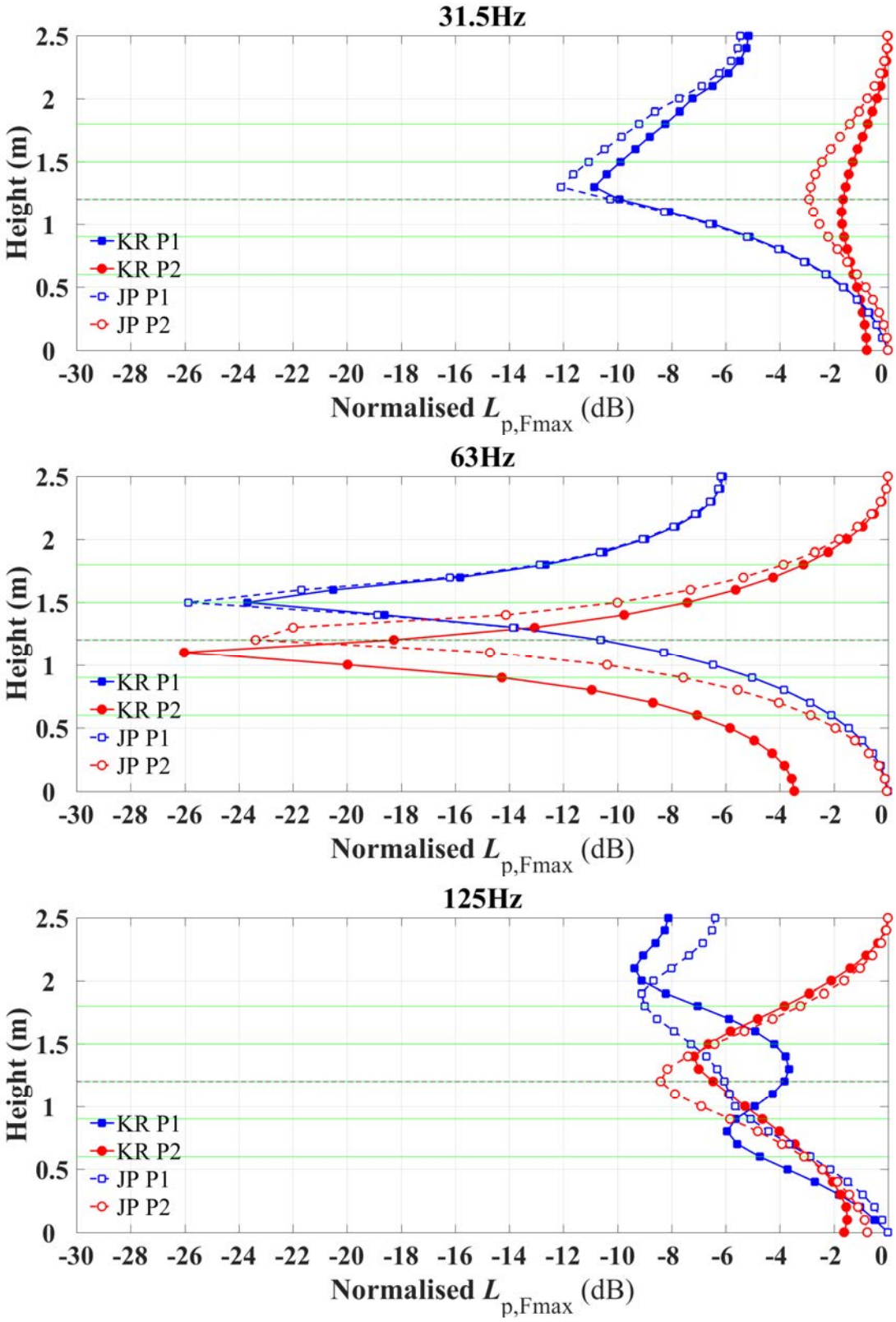

Figure 6-29. Spatial variation of normalised $L_{p,Fmax}$ in the vertical direction in model C. The black dashed horizonal line indicates the 1.2m height for MOCT-K and the green horizontal lines indicate the heights for I-INCE-J.

Model D (15m^3)

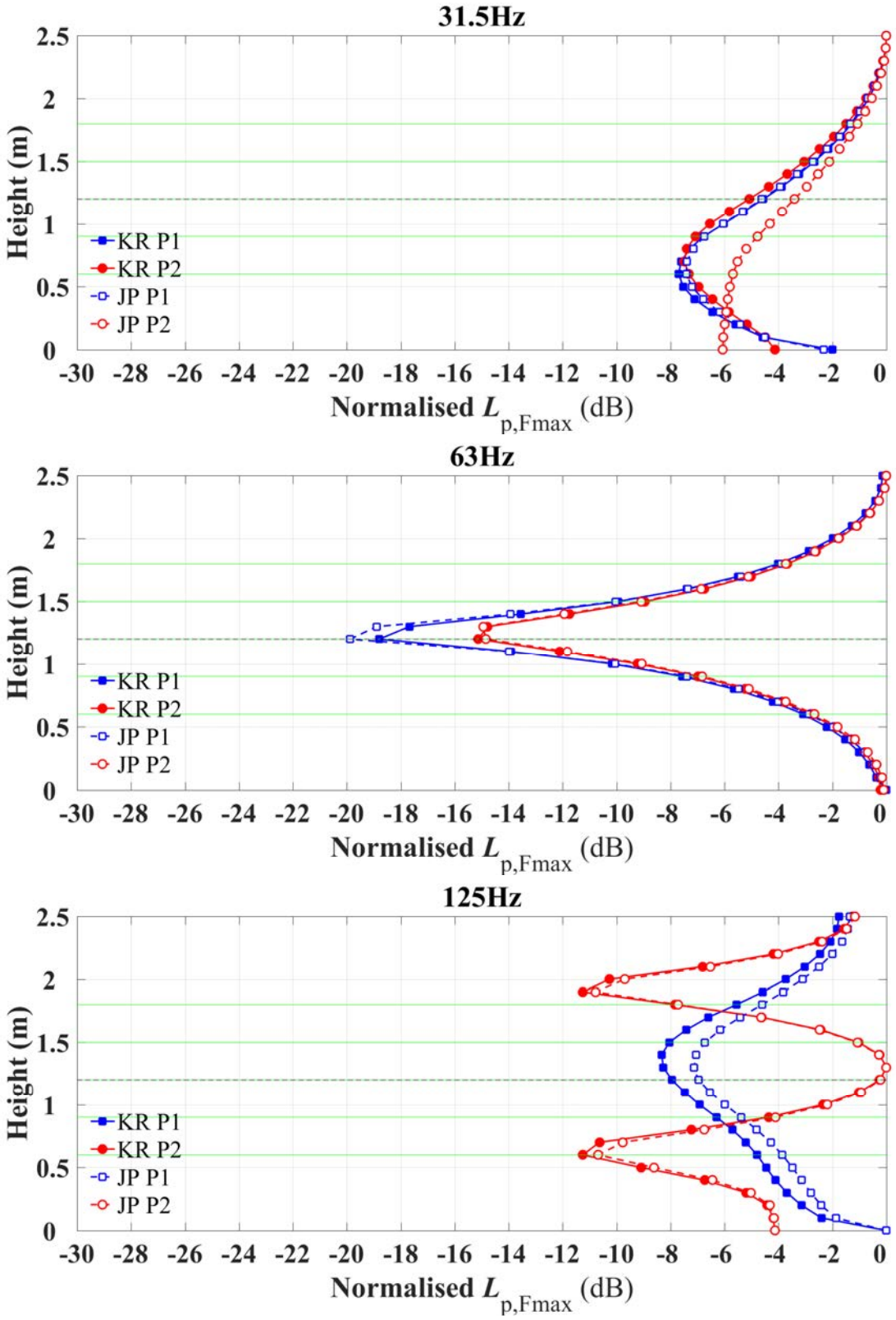

Figure 6-30. Spatial variation of normalised $L_{p,Fmax}$ in the vertical direction in model D. The black dashed horizonal line indicates the 1.2m height for MOCT-K and the green horizontal lines indicate the heights for I-INCE-J.

6.5.4 Comparison of I-INCE J, MOCT-K and ISO measurement procedures with the room-average sound pressure level

This section builds on the results in the previous section to assess the ability of different measurement procedure to estimate the room-average sound pressure level. Three measurement procedures of the floor impact sound insulation were discussed in section 1.2.1.4.

6.5.4.1 Low-frequency measurement procedure

The sound field cannot be considered as diffuse in the typical habitable room where volumes are below 25m^3. There are often less than five modes below 100Hz. In this case, the maximum difference between the lowest level and the highest level in the central zone of the room that is ~0.5m from the boundaries can be 17 to 28dB [115]. This was also seen in sections 6.5.2 and 6.5.3 where Model C and D showed up to a 30dB (see Figure 6-24) and 26dB (see Figure 6-29) difference in $L_{\mathrm{p,Fmax}}$ in the 63Hz octave band.

A low-frequency measurement procedure has previously been proposed by Hopkins and Turner [110] based on the study by Simmons [116]. The low-frequency procedure is to improve repeatability and reproducibility of the measurement of 50, 63 and 80Hz one-third octave bands with source and/or receiving room volumes less than 25m^3. Default low-frequency sound pressure level measurement for tapping machine for the field measurement is stated in ISO16283-2:2015 and these are an average of sound pressure in the central region of a room. The corner microphone position is taken from a minimum of four corners; two corners should be at ground level and two corners should be at ceiling level from the distance of 0.3 to 0.4m from each room boundary that forms the corner.

For the numerical experiment using the rubber ball, the same procedures are used, however, the frequency range is extended down to the 25Hz one-third octave band, and also applied to 31.5 and 63Hz octave bands.

The $L_{\mathrm{i,Corner,Fmax}}$ for each frequency band is then calculated using

$$L_{\mathrm{i,Fmax,corner},j} = 10\log_{10}\left(\frac{1}{n}\sum_{k=1}^{n} 10^{L_{\mathrm{i,Fmax,corner},j,k}/10}\right) \qquad (6.2)$$

where $L_{\mathrm{i,Fmax,corner},j}$ are Fast time-weighted maximum sound pressure levels at corner microphone positions in the room for rubber ball excitation position j with n microphone positions.

The low-frequency weighted energy-average sound pressure level in the 25, 31.5, 40, 50, 63 and 80Hz one-third octave bands, and 31.5 and 63Hz octave bands are calculated by combining L_{i} from the default procedure and $L_{\mathrm{i,Corner,Fmax}}$ from the low-frequency procedure using

$$L_{\mathrm{i,Fmax},j} = 10\log_{10}\left(\frac{1}{n}\sum_{k=1}^{n} 10^{L_{\mathrm{i,Fmax},j,k}/10}\right) \tag{6.3}$$

$$L_{\mathrm{i,LF,Fmax},j} = 10\log_{10}\left(\frac{10^{0.1L_{\mathrm{i,Fmax,Corner},j}} + \left(2 \times 10^{0.1L_{\mathrm{i,Fmax},j}}\right)}{3}\right) \tag{6.4}$$

In this thesis, two low-frequency weighted energy averages are calculated using either the highest corner level or the energy average of all eight corner levels in the cuboid room.

6.5.4.2 Results

The spatial-average $L_{\mathrm{p,Fmax}}$ in Figure 6-31 to Figure 6-34 has been calculated using the following approaches:

(1) Room-average: calculated from all points except those points on the boundaries,

(2) Central region: energy average of all points in the central region that are ≥0.5m from the boundaries (ISO 16283-2:2015 default procedure),

(3) I-INCE-J procedure,

(4) MOCT-K procedure,

(5) Low-frequency weighted energy average using highest corner level: the weighted energy average of the central region that is ≥0.5m from the boundaries and the highest of the eight corner positions that are 0.3m from each surface forming the corner (similar to the ISO 16283-2:2015 low-frequency procedure).

(6) Low-frequency weighted energy average using all eight corner levels: the weighted energy average of the central region that is ≥0.5m from the boundaries and the energy average of the eight corner positions that are 0.3m from each surface forming the corner (similar to the ISO 16283-2 low-frequency procedure).

For Models A, B, C and D, the central region always underestimates the room-average, and this was the reason that the I-INCE-J, MOCT-K, and ISO 16283-2:2015 procedures were developed. Ideally, an appropriate averaging and sampling procedure should give a close estimate of the room-average.

For one-third octave bands for Model A, the largest difference from the room average occurred with MOCT-K at 25Hz band by 8.1dB. Below 80Hz, the largest difference to the room average from each procedure were 3.1, 1.9, 8.1, -4.0 and 2.2dB for the procedures (2) to (6) respectively. The negative sign indicates an overestimation. For Model B, the largest difference to the room average was obtained from I-INCE-J at 125Hz band by 8.8dB. Below 80Hz, the largest differences from the room average were 2.6, 1.1, 4.7, -3.2 and 1.6dB for procedures (2) to (6) respectively. For Model C, the largest difference to the room average was obtained from I-INCE-J at 200Hz by 10.7dB. Below 80Hz the largest difference to the room average from each procedure were 1.8, 1.2, 2.7, -1.8 and 1.8dB for the procedures (2) to (6) respectively. For Model D, the largest difference to the room average was obtained from MOCT-K at 500Hz band by 8dB. Below 80Hz, the largest difference to the room average from each procedure were 1, 3.3, 2.2, -0.7 and 1.3dB for the procedures (2) to (6) respectively.

For octave bands for Model A, the largest difference from the room average occurred with MOCT-K at 31.5Hz by 5.2dB. Below 63Hz the largest differences from the room average were 2.1, 1.2, 5.2, -2.6 and -0.3dB for procedures (2) to (6) respectively. For Model B, the largest difference to the room average was obtained from I-INCE-J at 125Hz by 6.7dB. Below 63Hz, the largest difference to the room average from each procedure were 2.2, 1.0, 3.7, -2.1 and -0.4dB for the procedures (2) to (6) respectively. For Model C, the largest difference to the room average was obtained from MOCT-K at 500Hz by 4.6dB. Below 63Hz, the largest difference to the room average from each procedure were 2.2, 1.0, 3.7, -2.2 and -0.8dB for the procedures (2) to (6) respectively. For Model D, the largest difference to the room average was obtained from I-INCE-J

at 63Hz by 3.2dB. Below 63Hz, the largest difference to the room average from each procedure were 1, 3.2, 1.9, -1.9 and -0.8dB for the procedures (2) to (6) respectively.

Below 80Hz in one-third octave and 63Hz octave bands, the MOCT-K and I-INCE-J procedure tend to underestimate the room-average. For MOCT-K, this is due to the use of 1.2m height that coincides with nodal regions of room modes (see section 6.5.2 and 6.5.3). For I-INCE-J, use of fixed microphone position could eliminate underestimation in some Model (i.e. Model A), but this is not always the case. Measurements in a 62m^3 room from Yoo *et al.* [112] indicated that I-INCE-J and MOCT-K procedures produce underestimates, but that these were most significant with the MOCT-K procedure at 63Hz which is consistent with the findings in the current paper.

Use of procedure (5) which is closest (but not identical) to the low-frequency procedure in ISO 16283-2:2015 tends to overestimate the room-average in the 31.5, 63 and 125Hz bands for Models A, and B.

Use of procedure (6) which is close (but not identical) to the low-frequency procedure in ISO 16283-2:2015 tends to give the closest agreement with the room-average.
The result indicated that there is potential for the method that is similar to the ISO 16283-2:2015 low-frequency procedure that can be used for the rubber ball impact to measure $L_{p,Fmax}$ and to avoid the underestimation problems with I-INCE-J and MOCT-K.

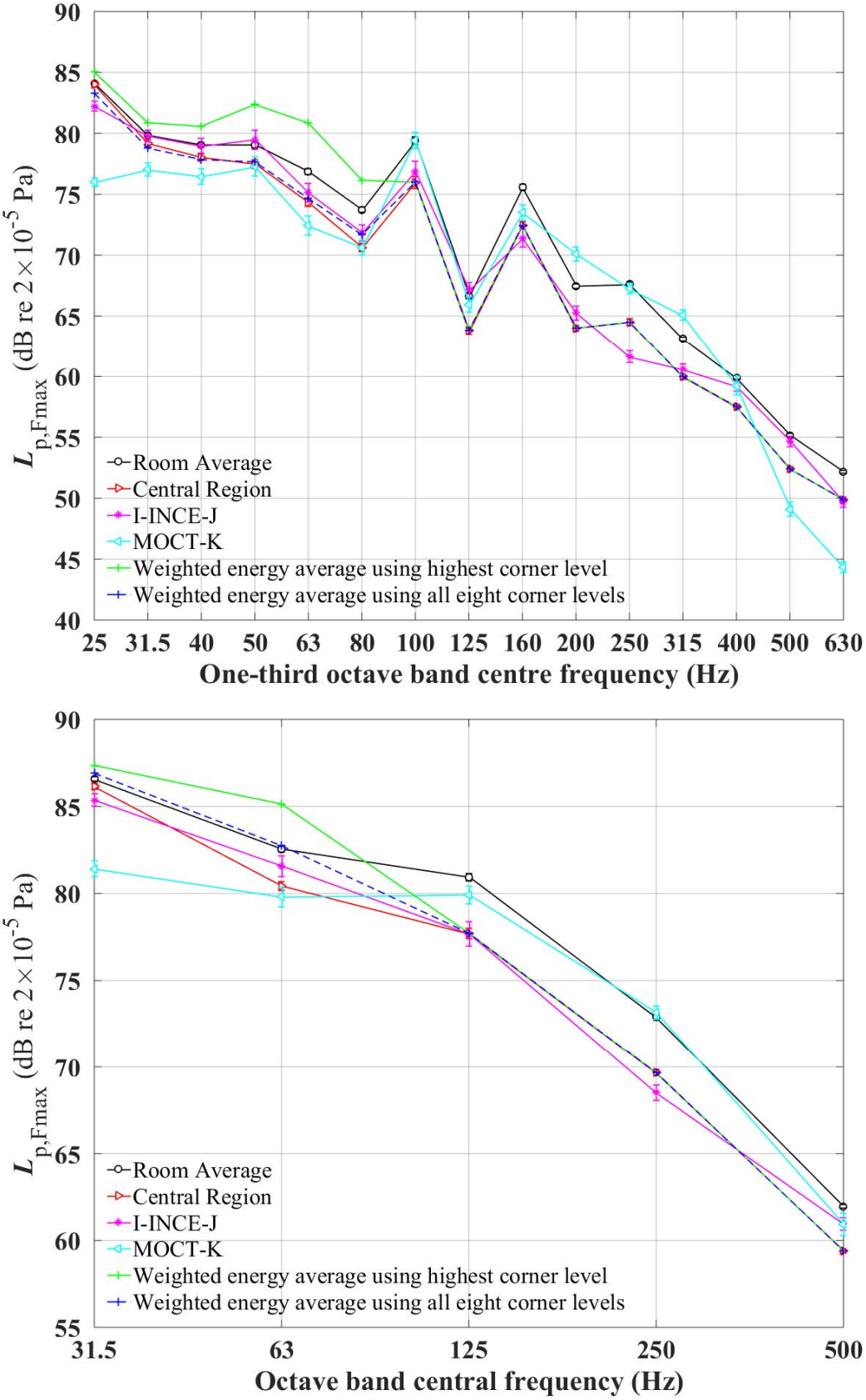

Figure 6-31. Spatial-average $L_{p,Fmax}$ from the room-average and different measurement procedures for T=1.5s for model A in one-third octave bands (upper) and in octave band (lower).

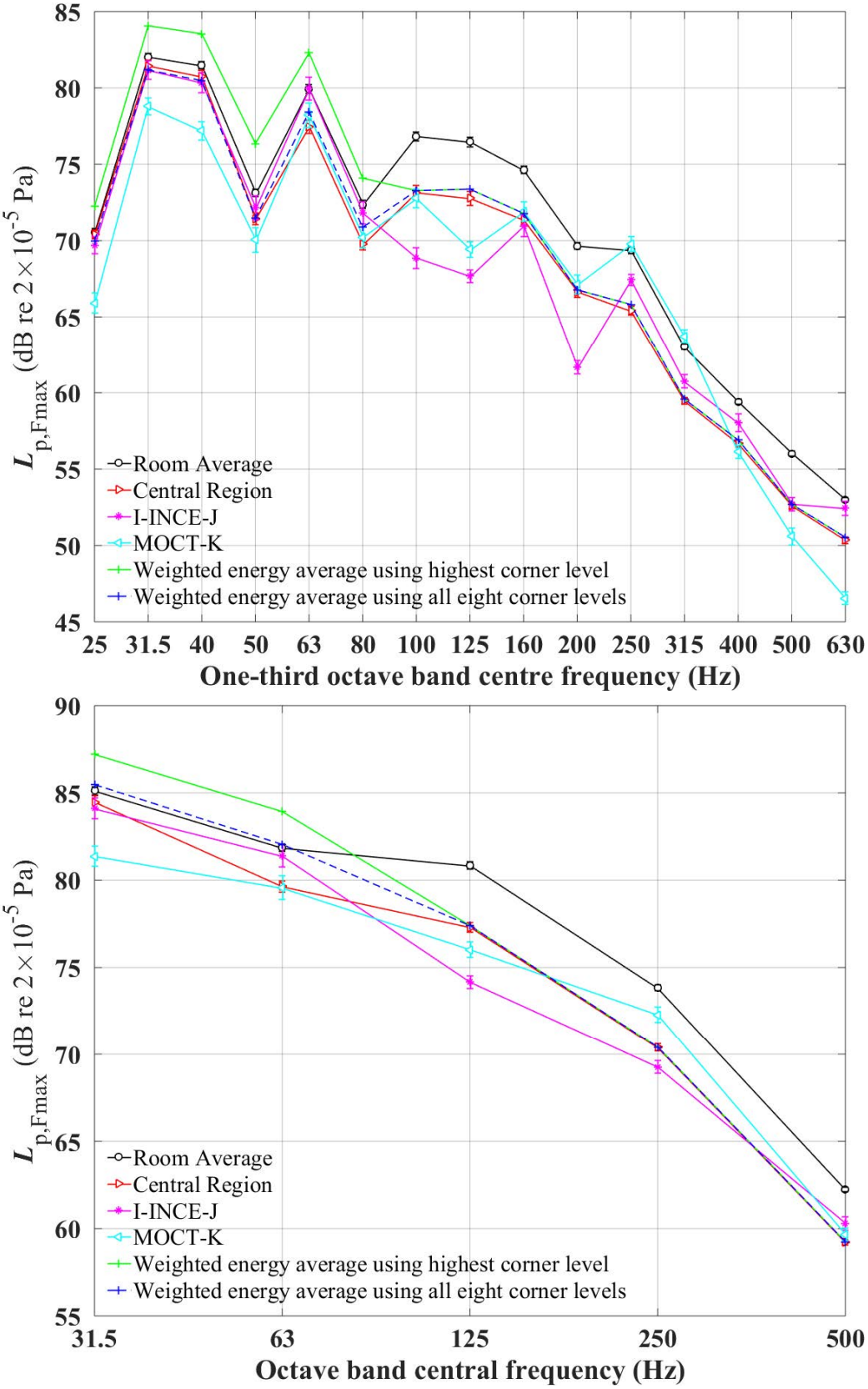

Figure 6-32. Spatial-average $L_{p,Fmax}$ from the room-average and different measurement procedures for T=1.5s for model B in one-third octave bands (upper) and in octave band (lower).

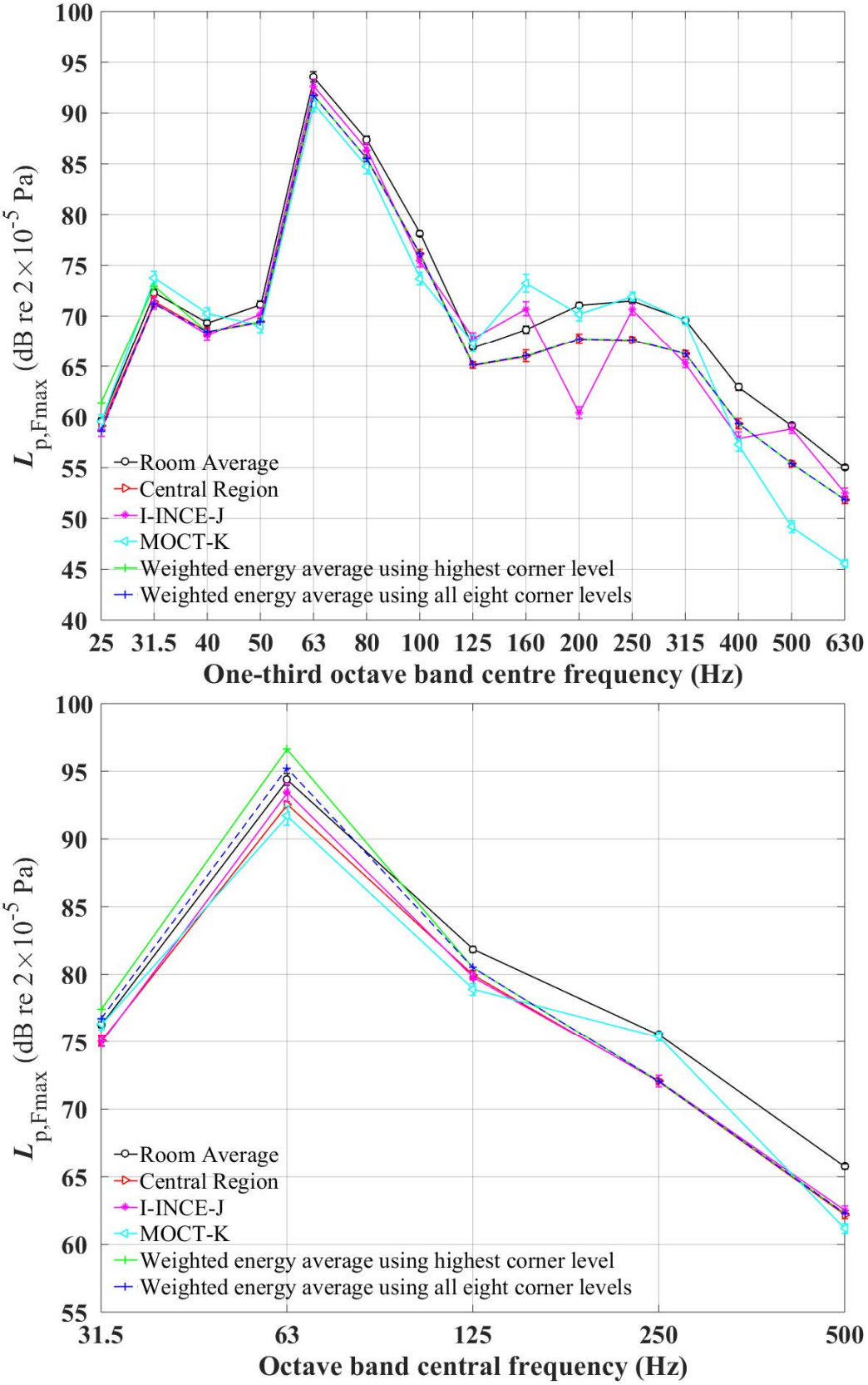

Figure 6-33. Spatial-average $L_{p,Fmax}$ from the room-average and different measurement procedures for T=1.5s for model C in one-third octave bands (upper) and in octave band (lower).

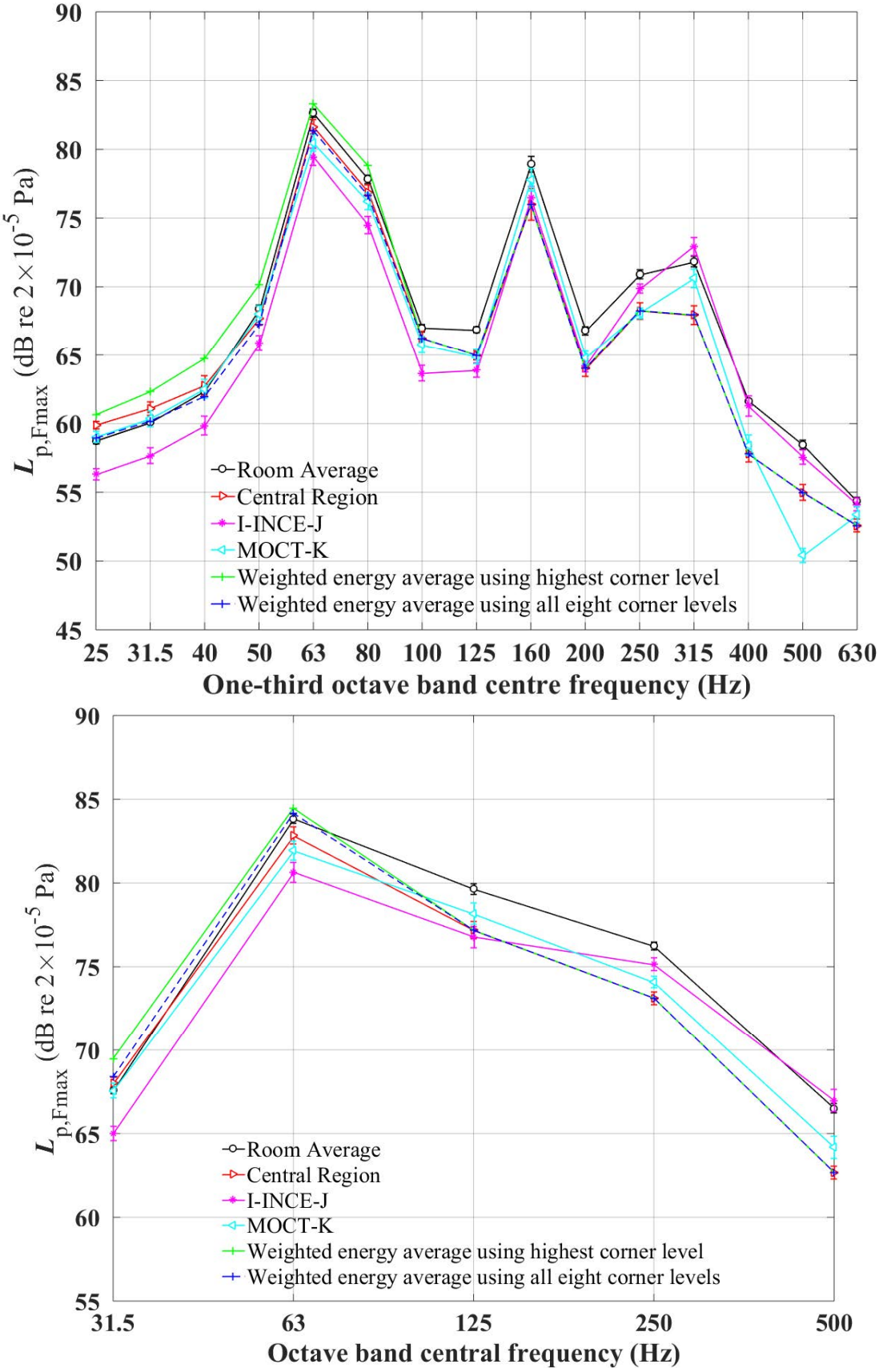

Figure 6-34. Spatial-average $L_{p,Fmax}$ from the room-average and different measurement procedures for T=1.5s for model D in one-third octave bands (upper) and in octave band (lower).

6.6 Summary

Experimental validation of the FEM model against TSEA and measurements indicated that the vibroacoustic interaction in the time domain between the excited plate and acoustic cavity was modelled within or overlap with the 95% confidence intervals of the measurement and FEM for most one-third octave bands, and 95% confidence intervals from the measurement overlapped FEM in octave bands. This allowed a set of numerical experiments to be carried out to assess the ability of TSEA to give reasonable estimates of $L_{p,Fmax}$ in the low-frequency range (≤125Hz band).

Numerical experiments were carried out for the ISO rubber ball impacting a 140mm concrete floor with different room volumes and different reverberation times. These showed that TSEA and FEM predict similar $L_{p,Fmax}$ in the low-frequency range; hence in many cases, it could be advantageous to use TSEA rather than FEM because it is quicker to create the model and run the simulation. TSEA is also able to give reasonable estimates in rooms with either high or low damping.

The measurement positions that are used to determine the spatial-average $L_{p,Fmax}$ have been investigated using FEM for the ISO rubber ball impacting a 140mm concrete floor with room volumes of 50, 37.5, 25 and 15 m^3 with a reverberation time of 1.5s. The spatial variation of $L_{p,Fmax}$ in the rooms was up to 26dB which is similar to that observed in airborne sound insulation measurements using steady-state signals with L_{eq}. The choice of measurement positions in the I-INCE-J and MOCT-K procedures seem difficult to justify because (a) the use of a central position (P1) in the room tends to cause the spatial-average $L_{p,Fmax}$ to underestimate the room-average $L_{p,Fmax}$ and (b) the MOCT-K procedure uses a microphone height that tends to coincide with low values of $L_{p,Fmax}$ in the room. An alternative approach to the I-INCE-J and MOCT-K procedures was investigated that was based on the low-frequency procedure in ISO 16283-2:2015 that is currently used for the ISO tapping machine. It was shown that this could avoid the underestimation problems with I-INCE-J and MOCT-K.

7. CONCLUSIONS AND FUTURE WORK

This section summarises the main finding of the chapters in this thesis and gives suggestions for future work.

7.1 Conclusions

The structural dynamics of the rubber ball have been experimentally assessed and results compared with lump parameter and FEM models. Using driving-point mobility measurements and EMA identified the fundamental frequency of the rubber ball as 78Hz. This value was used to estimate Young's modulus for the rubber which was required in the FEM model.

A SDOF mass-spring system model was used to predict the blocked force of the rubber ball dropped from 1m height directly onto the force plate. It was shown that the model could approximately predict the peak force and duration in the time domain, but the predicted force was non-zero force at t=0s which is not realistic. This is due to the lack of flexibility in the SDOF model with constant damping and spring stiffness. The predicted single event level from the SDOF model agreed with measurements and the limit values indicted in the JIS standard in the 31.5 and 63Hz octave bands but not at higher frequencies.

A FEM model was used to simulate the blocked force from a rubber ball drop onto a rigid concrete block. However, the predicted single event level did not meet the limit values given in JIS A 1418-2:2000 for the 31.5Hz octave band. However, it correctly predicted these limit values above the 31.5Hz octave band. After optimisation of the Young's modulus of the rubber ball, the agreement improved and a value of E=3.4×10^6 N/m^2 was determined for use in the FEM simulations.

The next stage was to use the force plate to measure the blocked force when the rubber ball impacted different locally reacting mass-spring systems. The dynamic stiffness of the resilient materials that formed these mass-spring systems was measured using a peak force similar to that applied by a rubber ball impact (≈1500N). The resilient materials were also tested with various input forces using small and large hammers (from 40N to 2500N). The results showed that the dynamic stiffness of the resilient material depended on the applied force. Hence, the models used a value determined at a force which was representative of the rubber ball impact.

The blocked force from a rubber ball impact on top of each mass-spring system was measured using a force plate. In the time domain, it was observed that the measured force had a single or double peak. The resilient materials were classified as Group A (relatively low stiffness and single peak) and Group B (relatively high stiffness and double peak). A TDOF mass-spring systems model was used to predict the time-varying force of the rubber ball dropped from 1m height onto the locally reacting mass-spring system that is on top of the force plate. The TDOF mass-spring system using measured dynamic stiffness and damping coefficient had a single peak. However, when the dynamic stiffness and damping coefficient were optimised, the double peak could be simulated. This indicates that there is potential to use the TDOF model to predict the blocked force from locally reacting mass-spring systems with relatively stiff springs. However, real floating floors are rarely locally reacting; hence an inverse form of TSEA (ITSEA) was devised and validated in this thesis to quantify the transient structure-borne sound power input from a heavy impact source into a heavyweight base floor with and without a floating floor. The aim was to incorporate the combination of heavy impact source and floating floor in TSEA models by using a laboratory-based experimental approach.

Using the rubber ball as a heavy impact source directly on a concrete base floor, there was reasonable agreement (i.e. <5dB) between the transient power input determined from force plate measurements and ITSEA; this provided an initial validation of the ITSEA approach. The next stage used the locally reacting, mass-spring systems to compare the normalised transient power input from force plate measurements with ITSEA on the same base floor. Again, reasonable agreement (i.e. <5dB) provided further evidence for the validity of the ITSEA approach.

The resulting TSEA model for a concrete base floor radiating into a receiving room used the normalised transient power input determined from ITSEA and the force plate measurement. This showed reasonable agreement (i.e. <5dB) with the measured $L_{p,Fmax}$ in the receiving room. Hence, the transient structure-borne sound power input from heavy impact sources into a concrete base floor with and without a floating floor can be determined using ITSEA.

Having demonstrated the validity of ITSEA to provide transient power input data for TSEA, the next stage was to consider its accuracy at low frequencies through comparison with numerical experiments using FEM in small volume rooms with various degrees of damping.

FEM simulation of test facilty A was compared with measurements and TSEA. The agreement between FEM and measurements was sufficient to validate the use of FEM for the numerical experiments. Comparisons between TSEA and FEM showed that they predict similar $L_{p,Fmax}$ in the low-frequency range and different room dampings; hence in many cases it could be advantageous to use TSEA rather than FEM because it is quicker to create the model and run the simulation. In addition, it was shown that TSEA could be used to predict $L_{p,Fmax}$ in a room with high or low damping.

Having validated FEM, numerical experiments were used to assess field measurement procedures for impact sound insulation from Japan, South Korea and International standards that are used with heavy impact sources. For the different field measurement procedures, the spatial variation of $L_{p,Fmax}$ in the rooms could be up to 26dB, which is similar to that observed in airborne sound insulation measurements using steady-state signals. The use of corner positions in the heavy/soft impact sound insulation measurement was investigated using FEM simulation. This was based on the low-frequency procedure in ISO 16283-2:2015 that is currently used for the ISO tapping machine. It was shown that this could avoid the underestimation problems with the measurement procedures in I-INCE-J and MOCT-K.

7.2 Future work

- TSEA for large floor slabs

  Nowadays in Japan, the use of large concrete slabs (60 to 80m^2) is common. However, TSEA has only been validated using 6 to 20m^2 floor slabs where it is reasonable to assume a reverberant vibration field. For large slabs this may be appropriate near 31.5Hz but not at 500Hz. Hence, comparisons of measurements and TSEA models are needed under controlled experimental conditions.

- TSEA for dry-floating floors (access floors)

  In Japan it is common to install floating floors such as an access floor for ease of access to pipes and cables. The current prediction model used in Japan is based on regression analysis and statistics with measurements being used for empirical corrections. Hence, it would be advantageous to assess the ITSEA approach for the access floor type of floating floor to move away from a reliance on empirical models.

- Use of the corner positions as the measurement positions in the test facility

  The FEM simulations in chapter 6 investigated the use of corner positions in the heavy/soft impact sound insulation measurement. The results indicated that the use of corner position could avoid the underestimation problems with I-INCE-J and MOCT-K. Hence, the next step would be to measure in the laboratory and field to validate the proposed approach.

REFERENCES

[1] J. Langdon, I.B. Buller, W.E. Scholes, Noise from neighbours and the sound insulation of party walls in houses, Sound Vib. 79 (1981) 205–228. doi:10.1016/0022-460X(81)90369-2.

[2] F.J. Langdon, I.B. Buller, W.W. Scholes, Noise from neighbours and the sound insulation of party floors and walls in flats, J. Sound Vib. 88 (1983) 243–270. doi:10.1016/0022-460X(83)90640-5.

[3] T. Kihlman, Fifty years of "Development " in sound insulation of dwellings, Noise Control Eng. J. 42 (1994) 47–52. doi:10.3397/1.2827860.

[4] C. Grimwood, Complaints about poor sound insulation between dwellings in England and Wales, Appl. Acoust. 52 (1997) 211–223. doi:10.1016/S0003-682X(97)00027-3.

[5] F. Ljunggren, C. Simmons, R. Öqvist, Correlation between sound insulation and occupants' perception – Proposal of alternative single number rating of impact sound, Appl. Acoust. 85 (2014) 57–68. doi:10.1016/j.apacoust.2014.04.003.

[6] F. Ljunggren, C. Simmons, R. Öqvist, Correlation between sound insulation and occupants' perception – Proposal of alternative single number rating of impact sound, part II, Appl. Acoust. 123 (2017) 143–151. doi:10.1016/j.apacoust.2017.03.014.

[7] S. Kimura, K. Inoue, M. So, K. Fujisawa, Analysis of occupancy evaluation and behaviour as to multi-family dwelling sound environment (in Japanese), J. Arch. Plann. Environ. Eng., AIJ,. 466 (1994) 1–8.

[8] J.Y. Jeon, Subjective evaluation of floor impact noise based on the model of ACF/IACF, J. Sound Vib. 241 (2001) 147–155. doi:10.1006/jsvi.2000.3286.

[9] J. Ryu, H. Sato, K. Kurakata, A. Hiramitsu, M. Tanaka, T. Hirota, Relation between annoyance and single-number quantities for rating heavy-weight floor impact sound insulation in wooden houses, J. Acoust. Soc. Am. 129 (2011) 3047–3055. doi:10.1121/1.3561660.

[10] S. Park, H. Kim, Development of analytical impact force models for floor impact vibration and acoustic numerical analysis, Appl. Sci. 6 (2016). doi:10.3390/app6050120.

[11] J. Ryu, H. Song, Y. Kim, Effect of the suspended ceiling with low-frequency resonant panel absorber on heavyweight floor impact sound in the building, Build. Environ. 139 (2018) 1–7. doi:10.1016/j.buildenv.2018.05.004.

[12] British Standards Institution, BS EN ISO 10140-3:2010+A1:2015. Acoustics – Laboratory measurement of sound insulation of building elements – Part 3: Measurement of impact sound insulation, (2014). doi:10.3403/30087653u.

[13] British Standards Institution, BS EN ISO 16283-2:2015 Acoustics – Field measurement of sound insulation in buildings and of building elements – Part 2: Impact sound insulation, (2014). doi:10.3403/30362054U.

[14] Japanese Standards Association, JIS A 1418-2:2000 Acoustics - Measurement of floor impact sound insulation of buildings - Part 2: Method using standard, (2000).

[15] Korean Standards Committee, KS F2810, Part 2: Method for field measurement of floor impact sound insulation. Part 2: Method using standard heavy impact sources (in Korean), (2001).

[16] M. Koyasu, Method for measurement of impact sound transmission through floor and related standards - The state-of-the-arts (in Japanese), J. INCEJ. 14 (1990) 4–7.

[17] J.H. Rindel, Sound insulation in buildings, 1st ed., CRC Press, Boca Raton, 2017. doi:10.1201/9781351228206.

[18] R. Lindahl, H.J. Sabine, Measurement of impact sound transmission through floors, J. Acoust. Soc. Am. 11 (1940) 379. doi:10.1121/1.1916052.

[19] F. Ingerslev, A.K. Nielsen, S.F. Larsen, The measuring of impact sound transmission through floors, J. Acoust. Soc. Am. 19 (1947) 981. doi:10.1121/1.1916650.

[20] D. Olynyk, Subjective judgments of footstep-noise transmission through floors, J. Acoust. Soc. Am. 38 (1965) 1035. doi:10.1121/1.1909834.

[21] B.G. Watters, Impact-noise characteristics of female hard-heeled foot traffic, J. Acoust. Soc. Am. 37 (1965) 619–630. doi:10.1121/1.1909381.

[22] R. Josse, How to assess the sound-reducing properties of floors to impact noise (footsteps), Appl. Acoust. 5 (1972) 15–20. doi:10.1016/0003-682X(72)90003-5.

[23] T.J. Schultz, Alternative test method for evaluating impact noise, J. Acoust. Soc. Am. 60 (1976) 645–655. doi:10.1121/1.381135.

[24] C. Hopkins, Sound Insulation, 1st ed., Butterworth-Heinemann, Oxford, UK, 2007. doi:10.4324/9780080550473.

[25] S. Kuga, A. Kouda, S. Kimura, M. Yasuoka, M. Tanemura, A study on the internal noise standard for the public housing. Part 1: Overall research plan and a questionnaire on the internal noise. (in Japanese), in: Archit. Inst. Japan Summ. Tech. Pap. Annu. Meet., 1971: pp. 25–26.

[26] S. Kuga, A. Kouda, S. Kimura, M. Yasuoka, Field measurement of the sound insulation performance of the wall and floor structure in the public housing. Part 2: A study on the internal noise standard for a public housing. (in Japanese), in: Archit. Inst. Japan Summ. Tech. Pap. Annu. Meet., 1971: pp. 23–24.

[27] S. Kuga, A. Kouda, S. Kimura, M. Yasuoka, Field measurements on the noise prevention effect of plumbing equipment. Part 3: A study on the internal noise standard for a public housing. (in Japanese), in: Archit. Inst. Japan Summ. Tech. Pap. Annu. Meet., 1971.

[28] S. Kimura, M. Yasuoka, On the measurement of impact sound insulation of floors (in Japanese), Proc. Acoust. Soc. Japan. (1971) 253–254.

[29] M. Yasuoka, A calculating method for the floor impact sound (in Japanese), Onkyo Gijuitsu. 6 (1977) 267–293.

[30] S. Kimura, JIS-Method for field measurement of impact sound level of floors (in Japanese), J. Acoust. Soc. Japan. 29 (1973) 598–602.

[31] M. Yasuoka, Method for determining floor impact sound insulation

performance (in Japanese), Kenchiku Gijutsu. (1978) 119–126.

[32] Japanese Standards Association, JIS A 1418:1978 Method for field measurement of floor impact sound level (in Japanese), (1978).

[33] Structure-borne WG., Acoustic environment committee, Environment engineering committee, AIJ., Structure-borne WG., Acoustic environment committee, Environment engineering committee, AIJ., The results of the literature survey on various problems for establishing the floor impact sound insulation performance standard of the Architectural Institute of Japan (in Japanese), 2013.

[34] A. Hiramitsu, Comparison of standard heavy/soft impact sources on the heavy-weight floor impact sound insulation, in: ICSV 25, 2018: pp. 1–8.

[35] S. Kimura, K. Inoue, Practical calculation of floor impact sound excited by heavy impact source, Appl. Acoust. 26 (1989) 263–292.

[36] H. Tachibana, H. Tanaka, M. Yasuoka, S. Kimura, Development of new heavy and soft impact source for the assessment of floor impact sound insulation of buildings, in: Internoise 1998, 1998.

[37] Floor impact sound insulation W.G., Architectural acoustic measurement sub-committee, Acoustic environment Committee, Environment enginerring committee, AIJ., Study on the force characteristics of heavy impact sound source for insulation of floors (in Japanese), J. Arch. Plann. Environ. Eng., AIJ,. 492 (1997) 249–255.

[38] Floor impact sound insulation W.G., Architectural acoustic measurement sub-committee, Acoustic environment Committee, Environment enginerring committee, AIJ., Study on the force characteristics of heavy impact sound source for insulation of floors part 2 (in Japanese), AIJ J. Technol Des. 6 (1998) 109–114.

[39] K. Inoue, Development of standard heavy impact source for measurement of floor impact sound (in Japanese), J. Acoust. Soc. Japan. 59 (2003) 267–273.

[40] Japanese Standards Association, JIS A 1419-2:2000 Acoustics - Rating of sound insulation in buildings and of building elements - Part 2: Floor impact sound insulation (in Japanese), (2000).

[41] K. Inoue, M. Yasuoka, H. Tachibana, Development of standard heavy impact source for measurement of floor impact sound (in Japanese), AIJ J. Technol Des No14. 14 (2001) 143–148.

[42] K. Yamamoto, S. Akao, M. Tanaka, Y. Urushido, M. Tano, K. Inadome, Y. Kozo, A. Shinichi, T. Manabu, Y. Urushido, T. Masanori, I. Koichi, A proposal for measurement of floor impact sound insulation of buildings using standard heavy impact sources (in Japanese), Proc. Meet. Inst. Noise Control Eng. Japan. (2004) 245–248.

[43] Ministry of Construction and Transportation, Ministry of Construction and Transportation Notice 2006-435: Threshold and management standard of the floor impact sound insulation for multi-family housing. (in Korean), (2006).

[44] T. Koga, M. Tano, K. Andow, A modified calculation method and its accuracy for floor impact sounds on large-span slabs from soft and heavy impact sources, in: Internoise 2000, 2000: pp. 1–5.

[45] S. Schoenwald, B. Zeitler, T. Nightingale, Influence of receive room properties on impact sound pressure level measured with heavy impact sources, 1st EAA - EUROREGIO 2010 Congr. Sound Vib. (2010) 1–8.

[46] T. Koga, Practical calculation of floor impact sound excited by heavy impact source, Internoise 2013. (2013) 3–6.

[47] Architectural Institute of Japan, Design of floor impact sound insulation for buildings (in Japanese), Gihoudou, 2009.

[48] T. Okano, S. Koyanagi, A quest for error factors in predicting heavy weight floor impact sound levels using measured data in existing residential buildings, Appl. Acoust. 76 (2014) 329–336. doi:10.1016/j.apacoust.2013.09.003.

[49] K. Masuda, H. Tanaka, Prediction of heavy impact sound level using mode shape function method, in: ICSV 25, Hiroshima, 2018: pp. 1–8.

[50] R.H. Lyon, R.G. DeJong, Statistical energy analysis of dynamical systems: theory and applications, 2nd ed., Butterworth-Heinemann, Newton, MA, 1995. doi:10.1016/C2009-0-26747-X.

[51] R.J.M. Craik, Sound transmission through buildings : using statistical energy analysis, 1st ed., Gower, Cambridge, 1996.

[52] J.E. Manning, K. Lee, Predicting mechanical shock transmission, Shock Vib. Bull. 37 (1968) 65–70.

[53] R.H. Lyon, Shock spectra for statistically modelled structures, Shock Vib. Bull. 40 (1969) 17–23.

[54] R. E. Powell, L.R. Quartararo, Statistical energy analysis of transient vibration, in: Proc. Am. Soc. Mech. Eng. (Winter Meet., Boston, US, 1987.

[55] M.L. Lai, A. Soom, Prediction of transient vibration envelopes using statistical energy analysis techniques, J. Vib. Acoust. 112 (1990) 127–137.

[56] M. Robinson, C. Hopkins, Prediction of maximum time-weighted sound and vibration levels using transient statistical energy analysis. Part 1: Theory and numerical implementation, Acta Acust. United with Acust. 100 (2014) 46–56. doi:10.3813/AAA.918685.

[57] M. Robinson, C. Hopkins, Prediction of maximum time-weighted sound and vibration levels using transient statistical energy analysis. Part 2: Experimental validation, Acta Acust. United with Acust. 100 (2014) 57–66. doi:10.3813/AAA.918686.

[58] R. Pinnington, Transient statistical energy analysis of an impulsively excited two oscillator system, J. Sound Vib. 189 (1996) 249–264. doi:10.1006/jsvi.1996.0018.

[59] R. Pinnington, D. Lednik, Transient energy flow between two coupled beams, J. Sound Vib. 189 (1996) 265–287. doi:10.1006/jsvi.1996.0019.

[60] M. Robinson, C. Hopkins, Prediction of maximum fast time-weighted sound pressure levels due to transient excitation from the rubber ball and human footsteps, Build. Environ. 94 (2015) 810–820. doi:10.1016/j.buildenv.2015.06.013.

[61] R.H. Lyon, G. Maidanik, Power flow between linearly coupled oscillators, J.

Acoust. Soc. Am. 34 (1962) 623. doi:10.1121/1.1918177.

[62] R.H. Lyon, Random noise and vibration in space vehicles, 1967.

[63] F.G. Leppington, E.G. Broadbent, K.H. Heron, The Acoustic Radiation Efficiency of Rectangular Panels, Proc. R. Soc. A Math. Phys. Eng. Sci. 382A (1982) 245–271. doi:10.1098/rspa.1982.0100.

[64] F.G. Leppington, E.G. Broadbent, K.H. Heron, Acoustic Radiation from Rectangular Panels with Constrained Edges, Proc. R. Soc. A Math. Phys. Eng. Sci. A393 (1984) 67–84. doi:10.1098/rspa.1984.0046.

[65] F.G. Leppington, K.H. Heron, E.G. Broadbent, S.M. Mead, Resonant and Non-Resonant Acoustic Properties of Elastic Panels. II. The Transmission Problem, Proc. R. Soc. A Math. Phys. Eng. Sci. 412 (1987) 309–337. doi:10.1098/rspa.1987.0091.

[66] F.G. Leppington, Acoustic radiation from plates into a wedge-shaped fluid region: application to the free plate problem, Proc. R. Soc. London. 452 (1996) 1745–1764. doi:10.1098/rspa.1996.0093.

[67] F.J. Fahy, Energy flow between oscillators: special case of point excitation, J. Sound Vib. 11 (1970) 481–483. doi:10.1016/S0022-460X(70)80012-8.

[68] D.A. Bies, S. Hamid, In situ determination of loss and coupling loss factors by the power injection method, J. Sound Vib. 70 (1980) 187–204. doi:10.1016/0022-460X(80)90595-7.

[69] A. Le Bot, Foundation of statistical energy analysis, 1st ed., Oxford University Press, Oxford, UK, 2015. doi:10.1002/9781118931158.

[70] L. Cremer, M. Heckl, Structure-borne sound: Structural vibrations and sound radiation at audio frequencies, 2nd ed., Springer-Verlag, Berlin, Heidelberg, 1985. doi:10.1007/978-3-662-10121-6.

[71] O.C. Zienkiewicz, R.L. Taylor, The finite element method for solid and structural mechanics, sixth, Butterworth Heinemann, Oxford, United Kingdom, 2005. doi:10.1016/B978-1-85617-634-7.00018-1.

[72] Dassault Systèmes Simulia Corp., Analysis User's Manual Volume 1: Introduction, Spatial modeling, execution and output, Abaqus, 2012.

[73] K.J. Bathe, E.L. Wilson, Numerical methods in finite element analysis, Prentice-Hall, Inc, Englewood Cliffs, New Jersey, 1976.

[74] K.J. Bathe, Conserving energy and momentum in nonlinear dynamics: A simple implicit time integration scheme, Comput. Struct. 85 (2007) 437–445. doi:10.1016/j.compstruc.2006.09.004.

[75] Dassault Systèmes Simulia Corp., Analysis User's Manual Volume 2: Analysis, Abaqus, 2012.

[76] Dassault Systèmes Simulia Corp., Theory Manual, Abaqus, 2012.

[77] Dassault Systèmes Simulia Corp., Analysis User's Manual Volume 4: Elements, Abaqus, 2012.

[78] N. Atalla, F. Sgard, Finite element and boundary methods in structural acoustics and vibration, 1st ed., CRC Press, Boca Raton, 2015. doi:10.1201/b18366.

[79] Dassault Systèmes Simulia Corp., Abaqus 6.12 ABAQUS/CAE User's Guide, 2012.

[80] H. Kuttruff, Room acoustics, 2nd ed., Applied Science Publishers Ltd, Barking, England, 1979. doi:10.1201/9781482286632.

[81] A. Brandt, Noise and vibration analysis: signal analysis and experimental procedures, 2011. doi:10.1002/9780470978160.

[82] British Standards Institution, IEC 61260-1:2014 Electroacoustics-Octave-band and fractional-octave-band filters Part 1:Specifications, (2011). doi:10.3403/30177581.

[83] British Standards Institution, BS EN 61672-2:2013+A1:2017 Electroacoustics - Sound level meters Part 2: Pattern evaluation tests, (2013).

[84] H. Tanaka, On the characteristics of heavy weight floor impact source (in Japanese), in: Summ. Tech. Pap. Annu. Meet., Architectural Institute of Japan, Kyushu, 1989: pp. 271–272.

[85] S. Schoenwald, B. Zeitler, T. Nightingale, Excitation of wood joist floors with the standard rubber ball, Internoise 2009. 6 (2009).

[86] S. Schoenwald, B. Zeitler, Floor excitation with the heavy soft impact source, Forum Acusticum 2011. (2011) 1–6.

[87] S. Schoenwald, B. Zeitler, T. Nightingale, Prediction of the blocked force at impact of Japanese rubber ball source, Acta Acust. United with Acust. 97 (2011) 590–598. doi:10.3813/AAA.918439.

[88] Percival, The impact and rebound of a football, Manchester Assoc. Eng. 1976–1977 (1977) 17–28.

[89] M. Hubbard, W.J. Stronge, Bounce of hollow balls on flat surfaces, Sport. Eng. (International Sport. Eng. Assoc. 4 (2001) 49–61. doi:10.1046/j.1460-2687.2001.00073.x.

[90] M. Nagurka, S. Huang, A mass-spring-damper model of a bouncing ball, Am. Control Conf. 2004. Proc. 2004. 1 (2004) 499–504. doi:10.23919/acc.2004.1383652.

[91] H. Lamb, On the vibrations of a spherical shell, Proc. London Math. Soc. s1-14 (1882) 50–56. doi:10.1112/plms/s1-14.1.50.

[92] W.E. Baker, Axisymmetric modes of vibration of thin spherical shell, J. Acoust. Soc. Am. 33 (1961) 1749–1758. doi:10.1121/1.1908562.

[93] A. Silbiger, Nonaxisymmetric modes of vibration of thin spherical shells, J. Acoust. Soc. Am. 34 (1962) 862. doi:10.1121/1.1918210.

[94] A. Kalnins, Effect of bending on vibrations of spherical shells, J. Acoust. Soc. Am. 36 (1964) 74–81. doi:10.1121/1.1918916.

[95] A.N. Robertson, F. Hemez, I.F. Salazar, T. Duffey, Model testing repeatability of a population of spherical shells, 2004. doi:10.2172/828954.

[96] Dassault Systèmes Simulia Corp., Benchmarks Manual, Abaqus, 2012.

[97] G.P. O'Hara, Mechanical properties of silicone rubber in a closed volume, Watervliet N.Y. 12189, 1983. doi:10.21236/ada138129.

[98] H. Itoh, K. Mihara, Y. Yamada, K. Ishikawa, Measurement of silicone rubber hardness by use of a quartz-crystal tuning-fork tactile sensor, Freq. Control Symp. Expo. 00 (2004) 571–574. doi:10.1109/FREQ.2004.1418522.

[99] Dassault Systèmes Simulia Corp., Analysis User's Manual Volume 3: Materials, Abaqus, 2012.

[100] C. Hopkins, M. Filippoupolitis, N. Ferreira, Prediction of Low-Frequency Radiation Efficiencies Using the Normal Mode Approach and Finite Element Methods, ICSV 22. (2015) 12–16.

[101] Engineering toolbox, Poisson's ratio, (2008). https://www.engineeringtoolbox.com/poissons-ratio-d_1224.html.

[102] British Standards Institution, BS EN 29052-1:1992, ISO 9052-1:1989 Acoustics. Method for the determination of dynamic stiffness. Materials used under floating floors in dwellings, (1992). doi:10.3403/00278634.

[103] Mathworks, Using LTI arrays for simulating multi-node dynamics, (2018). https://uk.mathworks.com/help/control/examples/using-lti-arrays-for-simulating-multi-mode-dynamics.html.

[104] M.R. Schroeder, New method of measuring reverberation time, J. Acoust. Soc. Am. 37 (1965) 409–412. doi:10.1121/1.1909343.

[105] British Standards Institution, BS EN ISO 354:2003 Acoustics - Measurement of sound absorption in a reverberation room, (2003). doi:10.3403/02824752.

[106] British Standards Institution, BS EN ISO 3382-1:2009 Acoustics - Measurement of room acoustic parameters. Part 1: Performance spaces (ISO 3382-1:2009), (2009). doi:10.1017/CBO9781107415324.004.

[107] F. Jacobsen, J.H. Rindel, Letters to the editor. Time reversed decay measurements, J. Sound Vib. 117 (1987) 187–190. doi:10.1016/0022-460X(87)90444-5.

[108] F. Jacobsen, A note on acoustic decay measurements, J. Sound Vib. 115 (1987) 163–170. doi:10.1016/0022-460x(87)90497-4.

[109] R.H. Lyon, R.G. DeJong, Theory and application of statistical energy analysis, 2nd ed., Newnes, 1990. doi:https://doi.org/10.1016/C2009-0-26747-X.

[110] C. Hopkins, P. Turner, Field measurement of airborne sound insulation between rooms with non-diffuse sound fields at low frequencies, Appl. Acoust. 66 (2005) 1339–1382. doi:10.1016/j.apacoust.2005.04.005.

[111] C. Hopkins, Revision of international standards on field measurements of airborne, impact and facade sound insulation to form the ISO 16283 series, Build. Environ. 92 (2015) 703–712. doi:10.1016/j.buildenv.2015.05.043.

[112] S.Y. Yoo, P.J. Lee, S.Y. Lee, J.Y. Jeon, Measurement of sound field for floor impact sounds generated by heavy/soft impact sources, Acta Acust. United with Acust. 96 (2010) 761–772. doi:10.3813/AAA.918330.

[113] A. Matsuoka, A. Shin-ichi, S. Nakazawa, K. Inadome, T. Hasome, Y. Urushido, T. Okano, T. Koga, M. Watanabe, Study on dispersion of floor impact sound level by difference of measurement position in room (in Japanese), Proc. Meet. Inst. Noise Control Eng. Japan. 9 (2001) 173–176.

[114] A. Matsuoka, K. Inadome, T. Koga, Dispersion of floor impact sound level on vertical direction in room (in Japanese), J. INCEJ. 25 (2001) 220–223.

[115] C. Hopkins, Sound insulation in buildings : linking theory and practice Laboratory sound insulation measurements : Errors in structural reverberation times for heavyweight, Acoust. 2012. (2012) 1557–1562.

[116] C. Simmons, TR 385 Measurement of sound pressure levels at low frequencies in rooms, Sweden, Borås, 1997.